Active hard mount vibration isolation for precision equipment

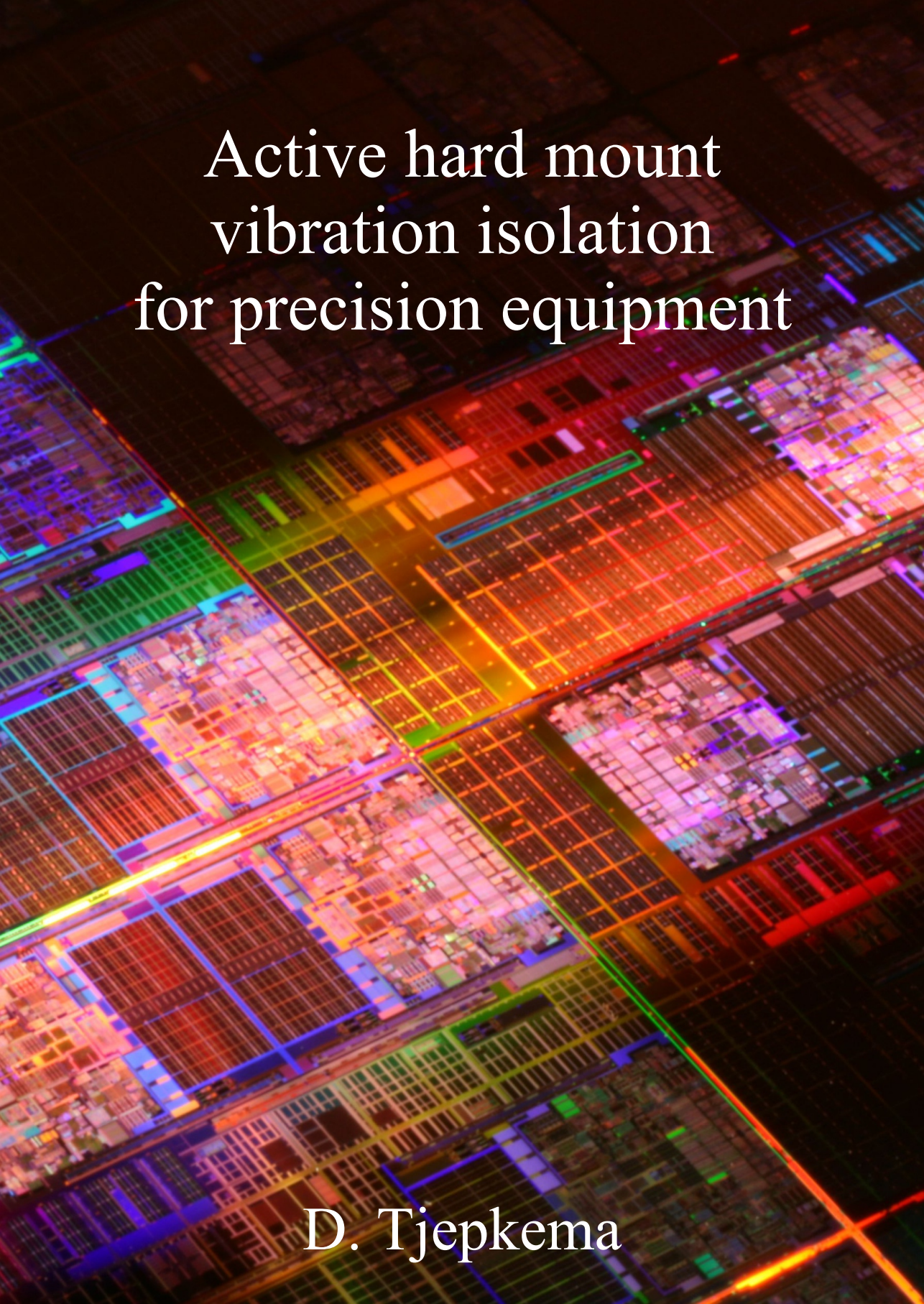

D. Tjepkema

ACTIVE HARD MOUNT VIBRATION ISOLATION FOR PRECISION EQUIPMENT

Actieve trillingsisolatie voor precisiemachines met een stijve ondersteuning

D. Tjepkema

Thesis committee:

prof. dr. F. Eising	University of Twente (Chairman)
prof. ir. H.M.J.R. Soemers	University of Twente (Promotor)
dr. ir. J van Dijk	University of Twente (Assistent promotor)
prof. dr. ir. A. Preumont	Universite Libre de Bruxelles
prof. ir. R.H. Munnig Schmidt	Delft University of Technology
prof. dr. ir. J.B. Jonker	University of Twente
prof. dr. ir. J. van Amerongen	University of Twente

This research was performed as part of Smart Mix project SSM06016 supported by the Dutch Ministry of Economic Affairs and the Dutch Ministry of Education, Culture and Science.

Active hard mount vibration isolation for precision equipment
D. Tjepkema

The cover shows a photo of an Intel 6-core microprocessor die codenamed “Dunnington”. It is based on the 45nm high-k process technology from 2008. Such a microprocessor can only be made using precision equipment in which a vibration isolator is applied.

Thesis University of Twente, Enschede - With summary in Dutch.
ISBN 978-90-365-3418-5

Printed by Print Service Ede

ACTIVE HARD MOUNT VIBRATION ISOLATION FOR PRECISION EQUIPMENT

PROEFSCHRIFT

ter verkrijging van
de graad van doctor aan de Universiteit Twente,
op gezag van de rector magnificus,
prof. dr. H. Brinksma,
volgens besluit van het College voor Promoties
in het openbaar te verdedigen
op vrijdag 2 november 2012 om 14.45 uur

door

Dirk Tjepkema

geboren op 23 maart 1983
te Leeuwarden

Dit proefschrift is goedgekeurd door de promotor:
prof. ir. H.M.J.R. Soemers

en de assistent-promotor:
dr. ir. J. van Dijk

Logic will get you from A to B. Imagination will take you everywhere.

Albert Einstein

Nomenclature

Notation

x	Scalar variable/signal (italic, lower case)
$\boldsymbol{x}$	Vector variable/signal (bold italic, lower case)
X	Scalar constant, Fourier/Laplace-transform, or SISO transfer function (italic, upper case)
$\boldsymbol{X}$	Vector of Fourier/Laplace-transforms (bold italic, upper case)
$\mathbf{X}$	Matrix constant, Fourier/Laplace-transforms, or MIMO transfer function (bold, upper case)
$\boldsymbol{x}_i$	ith element of vector $\boldsymbol{x}$
$\mathbf{X}_{ik}$	ikth entry of matrix $\mathbf{X}$
$\mathbf{X}(i,:)$	ith row of matrix $\mathbf{X}$
$\mathbf{X}(:,k)$	kth column of matrix $\mathbf{X}$
$\dot{\bullet}$	First derivative of $\bullet$ with respect to time
$\ddot{\bullet}$	Second derivative of $\bullet$ with respect to time
$\hat{\bullet}$	Estimate of the signal $\bullet$, or estimate of the dynamic system $\bullet$
$\overline{\bullet}$	Reduced matrix of $\bullet$
$\bullet(t)$	Continuous time signal
$\bullet(s)$	Laplace transformed variable, or continuous system
$\bullet(\omega)$	Fourier transformed variable, or value of $\bullet$ at ω
$\bullet(e^{\mathrm{j}\omega_f T_\mathrm{s}})$	Value of $\bullet$ at $e^{\mathrm{j}\omega_f T_\mathrm{s}}$
$\bullet(f)$	Value of $\bullet$ at $f = 2\pi\omega_f$
$\lvert\bullet\rvert$	Absolute value of $\bullet$
$\lvert\bullet\rvert_\mathrm{RMS}$	RMS value of $\bullet$
$\bullet^\mathrm{H}$	Complex conjugate (Hermitian) transpose of $\bullet$
$\bullet^\mathrm{T}$	Transpose of $\bullet$
$\bullet^{-1}$	Inverse of $\bullet$

diag(•)	Square matrix with the elements from the vector • on its diagonal and all other elements equal to zero
Re(•)	Real part of •
Im(•)	Imaginary part of •

Indices

$\bullet_f$	Index over (excited) frequencies
$\bullet_i$	Index over outputs or characteristic loci (CL)
$\bullet_k$	Index over inputs or experiments
$\bullet_l$	Index over polynomial coefficients, identified poles/modes

Abbreviations

BBN	Bolt, Beranek and Newman
cl	closed loop
CL	Characteristic loci
c.o.m.	Center of mass
comp	Compensated
disc	Discrete
CPSD	Cross power spectral density
cumPSD	Cumulative power spectral density
DFT	Discrete Fourier transform
DOF	Degree of freedom
e.c.	Elastic center
FRF	Frequency response function
HF	High-pass filter
LF	Low-pass filter
LS	Least squares
LSCF	Least squares complex frequency domain
MIMO	Multiple-input multiple-output
ol	open loop
PR	Pole residue
PSD	Power spectral density
red	Reduced
RFP	Rational fraction polynomial
RMS	Root mean square
SISO	Single-input single-output
SS	State-space

TEM	Transmission electron microscope
uncomp	Uncompensated
VC	Vibration Curve

Latin symbols

$\mathbf{A}, \mathbf{B}, \mathbf{C}, \mathbf{D}$	State-space model
A_f	Amplitude of sine in the multisine signal
$\mathbf{B}$	Input matrix
$\mathbb{C}$	Set of complex numbers
$C(s)$	Compliance transfer function (m/N)
$\mathbf{C}$	Output matrix
d	Axial damping constant of a leg (Ns/m)
d_1	Suspension damping (Ns/m)
d_2	Internal damping (Ns/m)
$D(s)$	Deformability transfer function (m/N)
$D_i(\omega_f)$	Denominator polynomial
$\mathbf{D}$	Damping matrix (Ns/m)
$\mathbf{D}_\mathrm{p}$	Parasitic damping matrix (Ns/m)
f	Frequency (Hz)
f_r	Resonance frequency of open loop suspension mode (Hz)
f_ref	Desired resonance frequency of suspension mode (Hz)
$F_i(s), \mathbf{F}(s)$	Filter (matrix)
F_a	Actuator force (N)
F_d	Disturbance force (N)
F_s	Measured force signal (N)
g	Gravity constant ($g = 9.81$ m/s^2)
$G(s), G_{\bullet_1\bullet_2}(s)$	Transfer function, transfer function between signal $\bullet_1$ and $\bullet_2$
h_m	Vertical distance between elastic center and center of mass
$H(s), H_\bullet(s)$	Controller transfer function
$H^\mathrm{d}(s), H^\mathrm{d}_\bullet(s)$	Diagonal controller transfer function
$\mathbf{I}_n$	$n \times n$ identity matrix
$\mathrm{j} = \sqrt{-1}$	Imaginary unit
$\mathbf{J}$	Jacobian matrix of the least squares problem
k	Axial stiffness of a leg (N/m)
k_1	Suspension stiffness (N/m)
k_2	Internal stiffness (N/m)
$k_\mathrm{a}, \mathbf{K}_\mathrm{a}$	Proportional gain (matrix) (kg)

k_f	Gain of force feedback controller using two-sensor control (-)
$k_\mathrm{p}, \mathbf{K}_\mathrm{p}$	Parasitic stiffness (matrix) (N/m)
k_s	Wire flexure stiffness (kg)
$k_\mathrm{v}, \mathbf{K}_\mathrm{v}$	Integral gain (matrix) (Ns/m)
$\mathbf{K}$	Stiffness matrix (N/m)
$L(s), L_\bullet(s)$	Loop gain transfer function
m	Number of inputs, outputs, and experiments
$m = m_1 + m_2$	Total payload mass (kg)
m_0	Floor mass (kg)
m_1	Payload 1 mass (kg)
m_2	Payload 2 mass (kg)
m_s	Coil mass (kg)
$\mathbf{M}$	Mass matrix (kg)
n	Order of the model for the system identification
n_d	Number of delays
n_f	Number of frequencies
n_l	Pole multiplicity
n_m	Number of kept modes for the system identification
n_r	Number of real poles
N	Number of samples for each experiment
N_p	Number of samples for each period
$N_i(\omega_f)$	Numerator polynomial
$\mathbf{O}$	Orthogonal matrix
p_i	Identified pole
P	Number of periods for each experiment
$P_{\bullet_1\bullet_2}(f)$	(Cross) power spectral density of signals $\bullet_1$ and $\bullet_2$
$\mathbf{P}$	Normal modal matrix
q	Degree of freedom
$\mathbf{Q}$	Mass normalized normal modal matrix
r	Distance between the vertical axis of symmetry and the point where a leg is attached to the payload
$r_\bullet$	$\bullet$-axis radius of gyration
$\mathbb{R}$	Set of real numbers
$\mathbf{R}_l$	Residue matrix of the lth mode
$\mathbf{R}$	Transformation matrix between vector of leg extensions $\boldsymbol{q}/\boldsymbol{q}_\mathrm{o}$ and vector of orthogonal coordinates $\boldsymbol{x}_\mathrm{ref}$
$T(s), \mathbf{T}(s)$	Transmissibility transfer function (matrix) (-)
$T_\mathrm{d}(s)$	Deformation transmissibility transfer function (–/s^2)
$T_\mathrm{ref}(s)$	Reference transmissibility transfer function (-)

T_s	Sample time (s)
$\mathbf{T}$	Transformation matrix
$\mathbf{T}^\mathrm{u}$	Input decoupling matrix
$\mathbf{T}^\mathrm{y}$	Output decoupling matrix
u	Input (excitation) signal
v	Noise signal
V	Strain energy
$W_i(\omega_f)$	Frequency dependent weighting function
$\Delta x = x_2 - x_1$	Internal deformation (m)
x	Multisine signal
x_i	Displacement of mass $i = 0, 1, 2$ (m)
$\boldsymbol{x}$	Orthogonal coordinates $\boldsymbol{x} = (x, y, \mathrm{z}, \theta_x \theta_y, \theta_z)^\mathrm{T}$
y	Output (response) signal
Δz	Static sagging due to gravity
z	Modal coordinate

Greek symbols

α	Factor
α_i	Angle between the three leg pairs and the x-axis ($i = 1, 2, 3$)
α_{il}	lth real-valued coefficient of denominator polynomial $D_i(\omega_\mathrm{f})$
β	Factor
β	Angle between axial direction of a leg and horizontal plane
β_{il}	lth real-valued coefficient of nominator polynomial $N_i(\omega_\mathrm{f})$
ϵ_ref	Desired lower transmissibility limit (-)
ζ_f	Damping ratio of second-order LF in controller (-)
ζ_l	Damping ratio of second-order HF in controller (-)
ζ_max	Maximum achievable damping ratio of internal mode (-)
ζ_n	Damping ratio of closed loop suspension mode (-)
ζ_r	Damping ratio of open loop suspension mode (-)
ζ_ref	Desired damping ratio of suspension mode (-)
$\lambda_i(s)$, $\lambda_i(\omega_f)$	Complex-valued eigenvalue
$\mathbf{\Lambda}(s)$, $\mathbf{\Lambda}(\omega_f)$	Complex-valued eigenvalue matrix
$\rho_\bullet$	Length $\bullet$ normalized with r (-)
$\sigma_\bullet$	Standard deviation of $\bullet$
σ_{li}	ith singular value of mode l
ϕ_f	Random phase of sine in multisine signal
$\mathbf{\Phi}(s)$, $\mathbf{\Phi}(\omega_f)$	Complex-valued modal matrix

ω, ω_f	Angular frequency (rad/s)
ω_i	Resonance frequency (rad/s)
ω_a	Anti-resonance frequency due to parasitic stiffness (rad/s)
$\omega_{\mathrm{a},F_\mathrm{s}}$	Anti-resonance frequency in force path (rad/s)
$\omega_{\mathrm{a},\ddot{x}_1}$	Anti-resonance frequency in acceleration path (rad/s)
ω_f	Corner frequency of second-order LF in controller (rad/s)
ω_l	Corner frequency of second-order HF in controller (rad/s)
ω_n	Resonance frequency of closed loop suspension mode (rad/s)
ω_p	Corner frequency of LF and HF filters for sensor fusion
ω_q	Corner frequency of additional HF filter for sensor fusion
ω_r	Resonance frequency of open loop suspension mode (rad/s)
ω_ref	Desired resonance frequency of suspension mode (rad/s)
$\omega_\mathrm{s} = \omega_{n_\mathrm{f}} T_\mathrm{s}/\pi$	Scaling factor
ω_z	High-frequency zero (rad/s)
$\Omega_l(\omega_f)$	Polynomial basis function
$\mathbf{\Omega}$	Eigenvalue matrix $\mathbf{\Omega} = \mathrm{diag}(\omega_1, \ldots, \omega_m)$

Table of contents

Introduction

Chapter 1

This chapter constitutes a general introduction to disturbance rejection in precision equipment. To guarantee the equipment's performance, disturbances have to be dealt with in an adequate way. Vibration isolators aim at reducing the effects of disturbances due to (floor) vibrations. This thesis describes the development of a so-called active hard mount vibration isolator. In this chapter, the research objective is discussed and an outline of the thesis is given.

1.1 Background

The continuous demand for higher accuracy and throughput is one of the most important challenges in the design of precision equipment. Examples of such equipment are wafer stepper lithography machines [20], atomic force microscopes [42], particle colliders [13], and space telescopes [19,47]. To guarantee the equipment's performance, the relative position of various components inside the equipment must be maintained to nanometer levels and internal deformations must be minimized. Even in controlled environments, the equipment is susceptible to environmental disturbances such as mechanical loads, thermal loads, electromagnetic radiation, humidity and contaminations. For example, mechanical loads result in vibrations of the equipment and therefore in internal deformations of the equipment, leading to a lower performance. Next to a robust equipment design, dedicated disturbance rejection systems may be applied to avoid or sufficiently reduce disturbances. Commonly used systems are vibration isolators, soundproof enclosures, servo-controlled positioning systems, and coolings systems. The focus of this thesis is on the development of a vibration isolator to reject disturbances due to mechanical loads.

In many industrial applications, the mechanical loads are due to floor vi-

brations that are entering the equipment by means of the mounts that suspend the equipment, see Fig. 1.1. Therefore, typical industrial vibration isolation systems focus on reducing the effects of floor vibrations [20]. These solutions can be considered as mechanical low-pass filters for the transmission of floor vibrations. Isolation is obtained above $\sqrt{2}$ times the system's suspension frequency, which is calculated as the square root of the suspension stiffness divided by the mass of the suspended equipment. Using a mount with low-stiffness springs (so-called soft mounts) results in low suspension frequencies (typically 0.5–2 Hz) and therefore in a low transmission of floor vibrations. An active control system is often added to artificially increase the damping of the suspension modes.

However, the low suspension stiffness introduces problems with leveling of the equipment and it increases its susceptibility to forces acting directly on it. These forces are due to for example acoustic excitation. Both problems can be circumvented by using mounts with high-stiffness springs (so-called hard mounts). Due to the higher stiffness, the suspension frequencies will be higher (typically 5–20 Hz). Therefore, the transmission of floor vibrations will also increase. An active control system is required to improve the response due to floor vibrations [8, 41]. Hence, the name active hard mounts.

In general, internal modes of the equipment are poorly damped. Excitation of these modes result in large internal deformations, leading to a lower performance of the the equipment. Therefore, it is desired to use the active control system to increase the damping of these modes as well.

1.2 Research objective

Although (active hard mount) vibration isolators that are able to simultaneously provide isolation from both floor vibrations and direct disturbance forces are not widely used yet, some examples can be found in [5, 25, 41]. However, none of these vibration isolators can be used to increase the damping of internal modes of the suspended equipment. Based on these facts, the research objective of this thesis is formulated as:

> *The development of an active hard mount vibration isolator for precision equipment that combines a high suspension stiffness with adequate isolation of both floor vibrations and direct disturbance forces as well as with sufficient damping of the suspension modes and internal modes of the suspended equipment.*

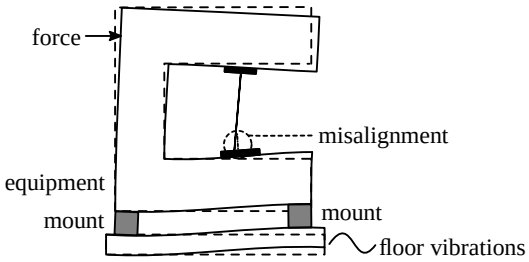

Fig. 1.1: Illustration of internal deformations in a precision equipment due to disturbances, leading to a lower performance of the equipment. The disturbances are mechanical loads due to floor vibrations and forces acting directly on the equipment..

This work is a continuation of research done by Van der Poel in 2010 [59]. The main contributions of his work are a set of guidelines for the mechanical design of an active hard mount vibration isolator as well as for the choice of sensors and actuators. Moreover, he has developed a control strategy based on a combination of feedback and feedforward control using accelerometers. He has validated this control strategy on an experimental setup of a one-axis active hard mount vibration isolation systems. However, the control strategy of Van der Poel requires a very high computational capacity, even for a one-axis vibration isolator. Therefore, it has been decided to not continue this control strategy. Instead, several novel control strategies have been derived.

1.3 Contributions

Active hard mount vibration isolation has already been covered in the thesis of Van der Poel [59]. In addition to this work, several contributions are made in this thesis. These can be summarized as follows:

- Two novel control strategies have been derived that are based on a combination of acceleration and force feedback. The combination of these types of feedback allows to improve the response due to floor vibrations and direct disturbance forces as well as to damp the internal modes.

- These control strategies are validated on an experimental setup of a one-axis active hard mount vibration isolator similar to the one used in [59].

- A demonstrator setup of a six-axes active hard mount vibration isolator is developed. It is used to verify the developed control strategies. Models

of the vibration isolator describing its dynamics have been derived as well.

- A novel method is presented for obtaining an identification model describing the dynamics of the demonstrator setup. The identification model can also be used to derive a modal controller.
- A modal controller is derived for the six-axes active hard mount vibration isolator and it is validated on the developed demonstrator setup.

1.4 Outline

In chapter 2 a background on vibration isolation in precision equipment is given. Several performance measures are defined and three performance objectives of active hard mount vibration isolators are formulated. In chapter 3 several control strategies for active hard mount vibration isolators will be derived that are based on acceleration feedback, force feedback or a combination of both. For each of these control strategies it is shown which of the three performance objectives can be realized. In chapter 4 the results are presented that are obtained with the real-time implementation of these control strategies on an experimental setup of a one-axis active hard mount vibration isolator. In chapter 5 the design of a demonstrator setup of a six-axes active hard mount vibration isolator is presented. It is used to verify the developed control strategies. Models of the vibration isolator describing its dynamics will be derived as well. In chapter 6 a novel method for the system identification of the developed demonstrator setup is presented that is used to validate the models of chapter 5. The obtained identification model can also be used to derive a modal controller. In chapter 7 a modal controller is designed for the six-axes active hard mount vibration isolator. It is shown how this modal controller can be used to extend the control strategies of chapter 3 from the one-axis vibration isolator to the six-axes vibration isolator. In chapter 8 the applicability of the modal controller is demonstrated by performing closed loop experiments on the developed demonstrator. In chapter 9 the conclusions of the various results presented in this thesis are summarized. Moreover, some recommendations for further research are given.

VIBRATION ISOLATION

2 Chapter

This chapter presents a background on vibration isolation in precision equipment. First, the characteristics of the various disturbance sources acting on the precision equipment are described. Next, the modeling of the vibration isolator and the used performance measures are presented. Also, the principles of passive and active vibration isolation are explained. The chapter concludes with the design and performance objectives of active hard mount vibration isolators.

2.1 Disturbances

In this thesis the focus is on disturbances due to mechanical loads. Two ways how these disturbances enter the equipment can be distinguished. This is illustrated in Fig. 1.1. *Direct* disturbances are forces acting directly on the equipment, causing vibrations. *Indirect* disturbances are forces acting on the equipment's support structure (often the floor) entering the equipment indirectly by means of the mounts that suspend the equipment. Indirect disturbances are often referred to as *floor vibrations*. In the following subsections, the characteristics of the direct and indirect disturbances are given.

2.1.1 Direct disturbances

Direct disturbance sources are application specific but may include: reaction forces on the equipment due to stage motion, forces transmitted through data and power cables, forces transmitted by cooling water systems, and acoustic excitation, see also [59] and the references therein. The disturbance forces are expected to be random of nature except for the reaction forces due to stage motion. Their levels are also application specific. In active vibration isolators,

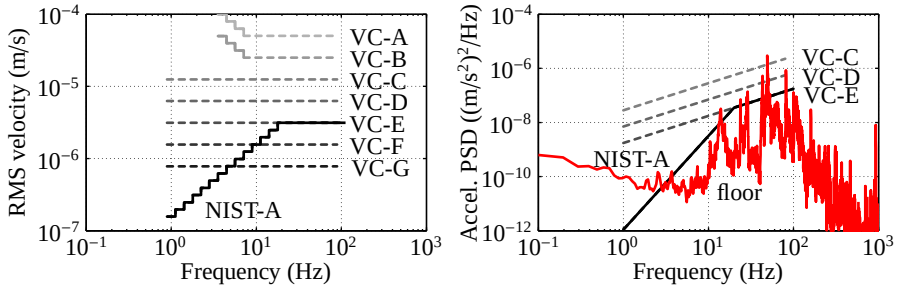

(a) VC-A to VC-G and NIST-A curves. (b) Power spectral density.

Fig. 2.1: (a) VC-A to VC-G and NIST-A curves expressed in RMS velocity units on a one-third octave frequency band. (b) Power spectral densities (PSDs) of the VC-C to VC-E and NIST-A curves in acceleration units together with an actual PSD of measured floor vibrations.

the noise generated by active components (actuators, sensors and their amplifiers) leads to random actuator forces. Hence, the active components have to be considered as direct disturbance sources as well.

2.1.2 Indirect disturbances

Indirect disturbances are caused by ground vibrations due to seismic activity and traffic, and disturbance sources inside the building in which the equipment is located (other machinery and human activity). The dynamics of the building in which the equipment is located, determines how the floor vibrations are observed at the equipment's mounts. Although the actual level of floor vibrations may vary over time and differ from site to site, measurements at many sites have revealed that most floor vibration spectra can be approximated by a flat spectrum when expressed as root mean square (RMS) velocity on a one-third octave frequency band from 1 to 80 Hz or from 4 to 80 Hz. Such a flat spectrum is also known as a Vibration Criterion (VC) curve or Bolt, Beranek and Newman (BBN) curve [16]. Several curves are specified suited for different environments, ranging from VC-A to VC-G, see Fig. 2.1(a). The VC-E curve (3.1 μm/s RMS per one-third octave in-between 1 and 80 Hz) is the quietest environment used for designing fabs, and it is suited for the most sensitive equipment. The VC-F and VC-G curves are only recommended for evaluation [2]. For use with nanotechnology, also the NIST-A curve (25 nm RMS per one-third octave in-between 1 and 20 Hz, VC-E in-between 20 and 100 Hz) is defined.

In this thesis, floor vibrations are evaluated using power spectral density (PSD) functions. Since floor vibrations are of a stochastic nature, the VC and

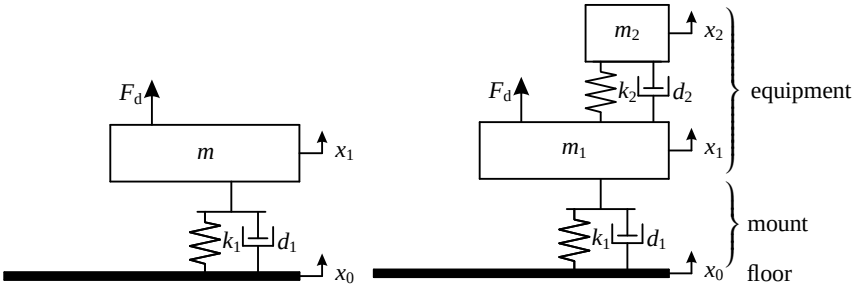

(a) Rigid body model. (b) Flexible body model.

Fig. 2.2: Models of a passive vibration isolator in which the equipment is represented by: (a) a rigid body; (b) a flexible body.

NIST curves can be converted to PSDs. The PSDs can also be used to evaluate the vibration isolator's performance, see section 2.2. For later use, the PSDs are expressed in acceleration units. Fig. 2.1(b) shows some of the curves together with a PSD of floor vibrations (in vertical direction) measured at the laboratory of Mechanical Automation and Mechatronics of the University of Twente, Enschede. The measurement approximates the NIST-A curve in the frequency range in-between 3 and 100 Hz. It is expected that below 3 Hz, sensor noise dominates over the actual floor vibration level [59]. Above 100 Hz, the acceleration level tends to decrease rapidly with increasing frequency. The total RMS value in-between 0 and 1 kHz of the measured floor vibrations is 1.7 mm/s^2 (0.17 mg). The same trends as in this measurement are also observed in the measurements published in [48, 59, 61], although with slightly higher acceleration levels. In [48] it is reported that at many sites horizontal and vertical vibration levels are alike, while rotational floor vibrations are in general small compared to translation.

2.2 Modeling and performance measures

In this section two basic models of a one-axis vibration isolator are introduced. These models are shown in Fig. 2.2. Both models use lumped masses, linear springs and viscous dampers to describe the dynamics of the equipment and the mount. The precision equipment is modeled as a rigid payload body with mass m (in Fig. 2.2(a)) or as a flexible payload body (in Fig. 2.2(b)). The flexible payload body consists of two bodies with mass m_1 and m_2 (where $m_1 + m_2 = m$) that are interconnected by spring k_2 and damper d_2, allowing

an internal deformation. The suspension or *mount* that connects the equipment to the floor is modeled as a parallel connection of spring k_1 and damper d_1. In both models, it is assumed that the floor motion x_0 is an independent input disturbance. This means that forces generated by the equipment's mounts do not influence floor motion x_0. This assumption is valid if the mass of the floor is much larger than the total mass of the equipment. A disturbance force F_d is included to represent the direct disturbance force acting on the equipment. In the model of Fig. 2.2(b), F_d is only acting on body m_1. In [59] it is shown that a force F_d acting on body m_2 has similar effects. The model of Fig. 2.2(a) is just a simplification of the model of Fig. 2.2(b), in which spring k_2 is considered infinitely stiff. With the simplified model it is easier to analyze the vibration isolator's performance when expressed in formulas.

The performance of the precision equipment is usually expressed in terms of an RMS value of the position error [5, 61]. This (dynamic) position error is due to the finite stiffness of spring k_2 in Fig. 2.2(b) and results in an internal deformation $\Delta x \equiv x_2 - x_1$ when a force is transmitted. In many applications the internal deformation cannot be measured directly. Instead, the acceleration $\ddot{x}_2$ of body m_2 which can be measured more easily, is used as a performance measure. These measures are related as follows. For frequencies below the resonance frequency of the internal mode, force F transmitted by spring k_2 is calculated as $F = m_2\ddot{x}_2$. If the influence of d_2 is neglected, the internal deformation is given by $\Delta x = F/k_2$. So, the expression for Δx becomes

$$\Delta x = \frac{m_2}{k_2}\ddot{x}_2. \tag{2.1}$$

By Eq. (2.1) it is observed that the RMS value of the internal deformation is proportional to the RMS value of $\ddot{x}_2$. For frequencies below the resonance frequency of the internal mode, the acceleration of bodies m_1 and m_2 is the same: $\ddot{x}_1 = \ddot{x}_2$. Therefore $\ddot{x}_1$ can be used as a performance measure as well.

It can be stated that the ultimate performance measure of the vibration isolator is the RMS value of the acceleration of the equipment, either $\ddot{x}_1$ or $\ddot{x}_2$ [61]. The RMS value $|\ddot{x}_i|_\mathrm{RMS}$ of $\ddot{x}_i$ in-between frequencies f_1 and f_2 is calculated as

$$|\ddot{x}_i|_\mathrm{RMS} = \sqrt{\int_{f_1}^{f_2} P_{\ddot{x}_i\ddot{x}_i}(\phi)\mathrm{d}\phi} \tag{2.2}$$

where $P_{\ddot{x}_i\ddot{x}_i}(f)$ refers to the single-sided PSD of x_i. The RMS value of the equipment's acceleration is due to the contributions of the various disturbance sources. Given the PSD $P_{w_jw_j}(f)$ of the disturbances w_j and assuming that the

disturbances are uncorrelated, $P_{\ddot{x}_i\ddot{x}_i}(f)$ is calculated as

$$P_{\ddot{x}_i\ddot{x}_i}(f) = \sum_j |TF_{ij}(f)|^2 P_{w_j w_j}(f) \tag{2.3}$$

where $TF_{ij}(f)$ is the transfer function from disturbance w_j to $\ddot{x}_i$. The disturbances are the floor vibrations, direct disturbance forces, and the noise contributions of the active components. Four performance transfer functions are defined: *transmissibility* $T(s)$, *compliance* $C(s)$, *deformation transmissibility* $T_\mathrm{d}(s)$, and *deformability* $D(s)$:

$$T(s) \equiv \frac{\ddot{X}_1(s)}{\ddot{X}_0(s)}, \qquad C(s) \equiv \frac{X_1(s)}{F_\mathrm{d}(s)}, \tag{2.4}$$

$$T_\mathrm{d}(s) \equiv \frac{\Delta X(s)}{\ddot{X}_0(s)}, \qquad D(s) \equiv \frac{\Delta X(s)}{F_\mathrm{d}(s)}, \tag{2.5}$$

where $s = \mathrm{j}\omega$ is the Laplace variable with $\omega = 2\pi f$. These transfer functions describe the equipment's acceleration responses $\ddot{X}_1(s)$ and internal deformation responses $\Delta X(s)$ due to floor acceleration $\ddot{X}_0(s)$ and direct disturbance force $F_\mathrm{d}(s)$. Here $\ddot{X}_i(s)$ is the Laplace transform of $\ddot{x}_i$. Eq. (2.1) is used to relate $\Delta X(s)$ to $\ddot{X}_2(s)$. The compliance is the equipment's displacement response $X_1(s)$ due to direct disturbance force $F_\mathrm{d}(s)$.

The ultimate performance of the vibration isolator depends on the level of the disturbances as well as the isolation performance of the isolator itself, which is determined by the four transfer functions. Therefore, these transfer functions are used to assess the isolator's performance using the different control strategies that are proposed in the next chapters.

2.3 Passive vibration isolation

A vibration isolator provides *passive isolation* if the mounts that suspends the equipment consist only of mechanical components. Passive electrical components, such as a *RL* circuit in combination with an electromagnetic transducer (voice coil actuator), may be included as well, but these are omitted in this thesis. The reader is referred to [45] for an example of such an isolator. *Active isolation* is provided if also active components, in fact actuators, sensors and a controller are incorporated in the mounts. The sensors and actuators require conditioning and power electronics respectively, which contain active electrical components, hence the name active isolation. Active vibration isolation is

discussed in the next sections, the mechanical design parameters for passive vibration isolation, in particular k_1 and d_1, are examined in this section.

Consider the rigid body model of Fig. 2.2(a). The equation of motion is

$$(ms^2 + d_1 s + k_1)X_1(s) = (k_1 + d_1 s)X_0(s) + F_\mathrm{d}(s). \tag{2.6}$$

The transmissibility and compliance can be calculated with Eq. (2.4) as

$$T(s) = \frac{k_1 + d_1 s}{ms^2 + d_1 s + k_1}, \tag{2.7}$$

$$C(s) = \frac{1}{ms^2 + d_1 s + k_1}. \tag{2.8}$$

Using $k_1/m = \omega_\mathrm{r}^2$ and $d_1/m = 2\zeta_\mathrm{r}\omega_\mathrm{r}$ Eqs. (2.7) and (2.8) can be rewritten as

$$T(s) = \frac{\omega_\mathrm{r}^2 + 2\zeta_\mathrm{r}\omega_\mathrm{r} s}{s^2 + 2\zeta_\mathrm{r}\omega_\mathrm{r} s + \omega_\mathrm{r}^2}, \tag{2.9}$$

$$C(s) = \frac{\omega_\mathrm{r}^2}{s^2 + 2\zeta_\mathrm{r}\omega_\mathrm{r} s + \omega_\mathrm{r}^2}\frac{1}{k_1}. \tag{2.10}$$

From Eq. (2.7) it is observed that the vibration isolator can be interpreted as a mechanical low-pass filter for floor vibrations with corner frequency $f_\mathrm{r} = 2\pi\omega_\mathrm{r} = 2\pi\sqrt{k_1/m}$ which is the resonance frequency of the vibration isolator. Given a certain mass m for the equipment, resonance frequency f_r, also referred to as the *suspension frequency*, is determined by suspension stiffness k_1. Vibration isolators with a low suspension frequency are also referred to as *soft mounts*. In a similar way *hard mounts* refer to vibration isolators with a high suspension frequency. The division, somewhat arbitrary, is chosen as $f_\mathrm{r} = 5$ Hz similar as in [59]. The magnitude responses of $T(s)$ and $C(s)$ are plotted in Fig. 2.3(a) and (b) for various values of ζ_r. It is observed in Fig. 2.3(a) that the isolator attenuates floor vibrations above $f = \sqrt{2}f_\mathrm{r}$, since all magnitudes are smaller than 1 above that frequency. A low transmissibility is obtained for a low value of suspension stiffness k_1. It is also visible that with a larger value of damping ratio ζ_r the amplification at resonance is lower at the cost of less attenuation at high frequencies. For $\zeta_\mathrm{r} = 0$, the high-frequency behavior of Eq. (2.9) approaches $1/s^2$, which means a roll-off rate of -40 dB/decade. For $\zeta_\mathrm{r} \neq 0$, the high-frequency behavior of Eq. (2.9) approaches $1/s$, which means a roll-off rate of only -20 dB/decade. This is caused by the terms $d_1 s$ and $2\zeta_\mathrm{r}\omega_\mathrm{r} s$ in the numerators of Eqs. (2.7) and (2.9). Hence, for a passive vibration isolator, the choice of the damper d_1 is a trade-off between amplification at resonance and high-frequency attenuation.

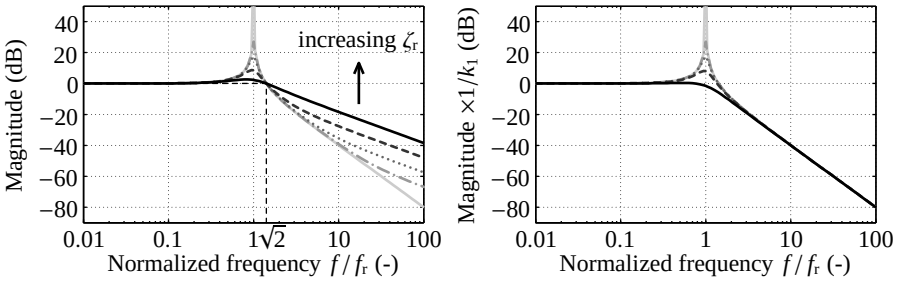

(a) Transmissibility $T(s)$. (b) Compliance $C(s)$.

Fig. 2.3: Transmissibility (a) and compliance (b) of a one-axis passive vibration isolator for various values of the damping ratio ζ_r.

Eq. (2.8) shows that the compliance can be interpreted as a second-order low-pass filter scaled with the inverse of the suspension stiffness k_1, see also Fig. 2.3(b). A low compliance is obtained for a high value of k_1. Hence, the choice for k_1 depends on the expected relative importance of floor vibrations versus direct disturbance forces. In most applications floor vibrations are the dominant sources of disturbances, so a low value of k_1 is preferred. However, a low suspension stiffness has some disadvantages including a longer settling time after direct disturbances (the settling transient is determined by the frequency and damping ratio of the suspension mode) and leveling problems due to gravity. The sagging due to gravity is calculated as

$$\Delta z = \frac{mg}{k_1} = \frac{g}{(2\pi f_r)^2}. \tag{2.11}$$

For a suspension frequency of $f_r = 1$ Hz, Δz is as large as 0.25 m(!). Hence, vibration isolators with such a low stiffness require additional leveling systems to compensate for this deflection.

The effect of increasing damping ratio ζ_r (by increasing d_1) is a reduced amplification at resonance without affecting the compliance, see Fig. 2.3(b).

Parameters k_1 and d_1 have a similar effect on $T_d(s)$ and $D(s)$ as on $T(s)$ and $C(s)$ respectively [59]. The effects of parameters m_1, m_2, k_2, and d_2 on the four transfer functions are not discussed in this thesis since these parameters have to do with the design of the equipment rather than with the design of the vibration isolator. The interested reader can read more about the effects of these parameters on the isolator's performance in [59].

The trade-offs that have to be made for the suspension stiffness k_1 and damper d_1 in passive vibration isolators pave the way for the need of active

vibration isolators. Moreover, active vibration isolators can be used for equipment with a high center of mass that suffer from unstable tilt modes due to a low suspension stiffness. Active vibration isolation is then used to stabilize these modes, see [20] for an example.

2.4 Active soft mount vibration isolation

A rigid body model of a one-axis active soft mount vibration isolator is shown in Fig. 2.4(a). The viscous damper which is present in the model of the passive vibration isolator of Fig. 2.2(a) is omitted. Instead, a force actuator F_a is present. The isolator can be equipped with several types of sensors, for example an accelerometer $\ddot{x}_1$ on payload body m or a force sensor F_s in the mount. Other types of sensors can be used as well, see [59] for an overview. In addition to a low-stiffness spring k_1 an additional spring k_p is included. This spring represents a parasitic stiffness path due to cables, etc. Parasitic stiffness is also present in multi-axes vibration isolators with non-ideal mounts. This will be discussed in chapter 5.

Two of the most widely used control strategies for active vibration isolators are integral acceleration feedback and integral force feedback, see [24], [45], and the references therein. Both strategies can be used to provide active damping. As an example integral acceleration feedback is illustrated. If the contribution of the parasitic stiffness k_p is neglected, the equation of motion is given by

$$(ms^2 + k_1)X_1(s) = k_1X_0(s) + F_d(s) + F_a(s). \tag{2.12}$$

The feedback control law is then defined by

$$F_a(s) = -\frac{k_v}{s}\ddot{X}_1(s), \tag{2.13}$$

where $-k_v/s$ is the feedback controller. Substituting Eq. (2.13) into Eq. (2.12) results in

$$T(s) = \frac{k_1}{ms^2 + k_vs + k_1}, \tag{2.14}$$

$$C(s) = \frac{1}{ms^2 + k_vs + k_1}, \tag{2.15}$$

for the closed loop transmissibility and compliance respectively. With this strategy an inertial damping force is provided that is proportional to the absolute velocity of the equipment. Since integral feedback gain k_v appears only in

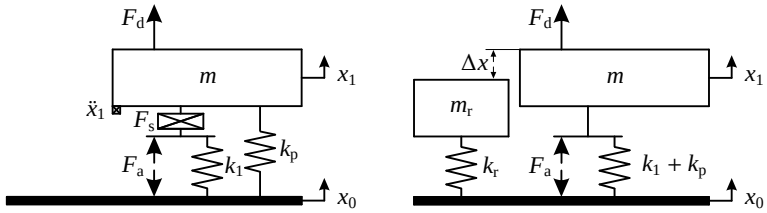

(a) Active vibration isolator. (b) Active vibration isolator with reference mass.

Fig. 2.4: Rigid body models of: (a) an active vibration isolator; (b) an active vibration isolator with a separate reference mass m_r.

the denominator of Eq. (2.14) and not in the numerator, the suspension mode can be damped without affecting the attenuation at high frequencies. This way of damping is usually referred to as *sky-hook* damping, since it can be interpreted as a virtual damper that is not placed between the equipment and floor but between the equipment and some inertial reference (the "sky") [29]. Integral force feedback results in the same transmissibility and compliance for the model of Fig. 2.4(a) if it is assumed that $k_p = 0$ [45, 46].

With active damping the performance of soft mount vibration isolators can be improved regarding the transmissibility, such that at high frequencies a roll-off rate of -40 dB/decade is obtained, while the amplification at resonance is lowered. However, the compliance is not improved, compare Eq. (2.15) to Eq. (2.8). This means that additional leveling systems are still required. Active hard mount vibration isolators, which are presented in the next section, aim for targeting both a low transmissibility and a low compliance without requiring an additional leveling system.

In the past decade, two alternative concepts [5, 63] for active soft mount vibration isolation have been introduced that are able to simultaneously realize a low transmissibility and a low compliance. Both make use of a separate reference body with mass m_r and a displacement sensor that measures the relative position between payload body m and reference body m_r. If body m_r is mounted on the floor with a low-stiffness spring k_r as in Fig. 2.4(b), body m_r is isolated from floor vibrations for frequencies above $\sqrt{2}$ times $2\pi\sqrt{k_r/m_r}$. An active control system is then used to keep the position of payload body m constant with respect to reference body m_r. So, body m is isolated from floor vibrations for frequencies above $\sqrt{2}$ times $2\pi\sqrt{k_r/m_r}$ as well. Hence, a low transmissibility is obtained.

Since the reference body is not exposed to direct disturbance forces that are acting on payload body m, the control system counteracts these forces, so a low

compliance can be obtained at the same time. Fig. 2.4(b) shows the concept of the Philips AIMS as described in [63]. If the reference body is mounted on payload body m instead of on the floor, the concept of the MECAL/TNO Hummingbird as described in [5] is obtained. Unfortunately, it has appeared to be very difficult to obtain a low suspension frequency for reference body m_r. Therefore, it has been decided not to use one of these concepts for the vibration isolator that is developed in this thesis. Instead, active hard mounts are used.

2.5 Active hard mount vibration isolation

The rigid body model of an active hard mount vibration isolator [8, 41, 59] is the same as for the active soft mount vibration isolator in Fig. 2.4(a) except spring k_1 is much stiffer. As a result the compliance is lower, see Eq. (2.10), and the sagging due to gravity is less, see Eq. (2.11), such that additional leveling systems are no longer required. However, the suspension frequency will be higher, resulting in a higher transmissibility. Hence, the feedback controller for the active hard mount vibration isolator does not only has to provide damping to the suspension mode but also has to lower the transmissibility. If the resonance frequency of the internal mode is relatively low and this mode is poorly damped, it is desired that the feedback controller provides damping to the internal mode as well. This is for example important in electron microscopes in which a poorly damped internal mode can be excited by acoustics (talking people, etc.).

So, the performance objectives for the active hard mount vibration isolator can be formulated as:

1. Lowering the transmissibility of floor vibrations to make it comparable to that of an ideal active soft mount vibration isolator.
2. Increasing the damping ratios of the internal modes.
3. Providing a stiff suspension to reduce the equipment's sensitivity for direct disturbances.

The transmissibility of the ideal active soft mount vibration isolator is chosen to be characterized by a suspension frequency of 1 Hz, a damping ratio of 70%, a roll-off rate of -40 dB/decade at frequencies above the suspension frequency, and a lower transmissibility limit of $2.5{\cdot}10^{-3} \approx -52$ dB at best. These values are based on high-end industrial soft mount vibration isolators which have suspension frequencies of 0.5–2 Hz, roll-off rates of at least

−30 dB/decade and at high frequencies, lower transmissibility limit ranging from −35 to −60 dB at best, see for example the websites of Halcyonics, Minus-K, and TMC [18, 39, 52]. The corresponding tranmssibility can be expressed as

$$T_{\text{ref}}(s) = \frac{\omega_{\text{ref}}^2}{s^2 + 2\zeta_{\text{ref}}\omega_{\text{ref}}s + \omega_{\text{ref}}^2} - \epsilon_{\text{ref}}, \tag{2.16}$$

where $\omega_{\text{ref}} = 2\pi f_{\text{ref}}$ with $f_{\text{ref}} = 1$ Hz, $\zeta_{\text{ref}} = 0.7$, and $\epsilon_{\text{ref}} = 2.5 \cdot 10^{-3}$. The damping ratio of the internal modes is desired to be as high as possible, but a value of at least 10% is aimed for. The stiffness of the suspension should be such that the active vibration isolator can be characterized as an active hard mount vibration isolator, which means that the suspension frequency is at least 5 Hz, see section 2.3. This means that the stiffness of the hard mount has to be more than 25 larger as compared to a soft mount with a suspension frequency of 1 Hz.

In the next chapter several feedback control strategies for the one-axis active hard mount vibration isolator are presented. These control strategies are based on acceleration feedback, force feedback, and combinations of acceleration and force feedback. The rigid and flexible body models of a vibration isolator that are presented in this chapter are used to evaluate the performance regarding the four performance transfer functions defined in section 2.2.

Control strategies for a one-axis vibration isolator

Chapter 3

Several feedback control strategies for one-axis hard mount vibration isolators for precision equipment are presented. Firstly, two strategies based on either acceleration or force feedback have been derived using a rigid body model of the vibration isolator. Secondly, these strategies are improved using a flexible body model, which allows to analyze the performance regarding internal deformations of the equipment. It is shown that with these strategies, it is not possible to simultaneously realize all three performance objectives mentioned in section 2.5. Therefore, two novel control strategies are developed that can be used to simultaneously realize all three performance objectives. One strategy is based on the sensor fusion of the accelerometer and force sensor signals. The other strategy is based on two-sensor control.

3.1 Introduction

The three performance objectives for active hard mount vibration isolators are stated in section 2.5. In section 3.2 it will be shown that these three objectives cannot be realized *simultaneously* by using only acceleration or force feedback. Therefore, a two-sensor control strategy is proposed to realize the three performance objectives simultaneously. The sensors that are used are an accelerometer and a force sensor. These sensors are chosen such that all parts of the vibration isolator, in fact suspension stiffness, actuators and sensors, can be located in the mount; there is no need for modification of the equipment's design. Other strategies, see for example [24], require placement of the actuators and sensors inside the equipment to target the damping of internal modes. This may not always be desirable.

Two-sensor controllers can be divided in two categories. For the first cat-

egory, which is discussed in section 3.3, both sensor signals are filtered first and then added using the same controller for the two sensor signals. This strategy is referred to as sensor fusion. For the second category, the two sensor signals are fed to two different controllers. This strategy will be discussed in section 3.4.

Two-sensor control strategies for vibration isolation based on the combination of absolute motion feedback (e.g. using a geophone or accelerometer) and force feedback have already been used in several applications. For example, Hauge and Campbell [19] used a two-sensor control strategy for vibration isolation in aerospace equipment to profit from the low-frequency performance of a geophone and the high-frequency robustness of a load cell. Among others, Gardonio et al. [15] studied the combination of velocity and force feedback to reduce the structural power transmission from a vibrating source to a receiving plate. The optimal controller was obtained by minimizing either the product of a velocity and a force signal or the weighted sum of the squares of both signals. A two-sensor control strategy based on sensor fusion was applied by Hua et. al. [26] and Ma and Ghasemi-Nejhad [36] to combine multiple signals in different frequency bands. However, all authors used two-sensor and sensor fusion control strategies to optimize for one performance objective only. In this thesis, these strategies are applied to realize two performance objectives simultaneously: lowering the transmissibility of floor vibrations and increasing the damping ratio of internal modes. The third objective, which is providing a stiff suspension, is realized by using hard mounts. The proposed strategies are explained for a one-axis vibration isolator.

To have a better understanding of two-sensor and sensor fusion control, the basic control strategies for a one-axis active hard mount vibration isolator based on either acceleration or force feedback are introduced first.

3.2 Acceleration and force feedback

This section is split into two parts. In the first part a rigid body model is considered to explain the basic control strategy for active vibration isolation. In the second part a flexible body model is used to discuss the effect of internal flexibilities of the equipment on the isolator's performance.

3.2.1 Rigid body model

Consider the rigid body model of the one-axis hard mount vibration isolator as shown in Figs. 3.1(a) and (b). These are similar to the model of Fig. 2.4(b). The

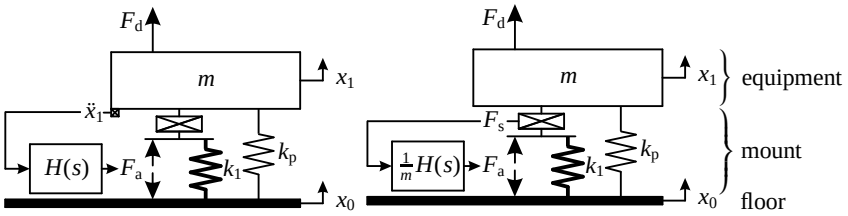

(a) Rigid body model using acceleration feedback. (b) Same model using force feedback.

Fig. 3.1: Model of the vibration isolator in which the equipment is represented by a rigid body, using: (a) acceleration feedback; (b) force feedback.

suspended equipment is modeled as a rigid payload body with mass m. The mount consists of a parallel connection of a spring k_1 and a force F_a generated by some actuator. An additional spring k_p is used to model parasitic stiffness caused by cables, etc. A disturbance force F_d is acting on the payload body. In the Laplace domain, the equation of motion is given by

$$(ms^2 + k_1 + k_p)X_1(s) = (k_1 + k_p)X_0(s) + F_a(s) + F_d(s). \tag{3.1}$$

The force actuator is controlled by $H(s)$ using the signal of either acceleration sensor $\ddot{x}_1$ or force sensor F_s. The acceleration signal is the absolute acceleration; the force sensor signal is the total internal force of the mount and is represented by:

$$F_s(s) = -k_1(X_1(s) - X_0(s)) + F_a(s). \tag{3.2}$$

Acceleration feedback is examined first, see Fig. 3.1(a). Negative proportional and integral acceleration feedback is proposed for controller $H(s)$ with gains k_a and k_v respectively:

$$H(s) = -(k_a + \frac{k_v}{s}). \tag{3.3}$$

According to [60], this is equivalent to adding virtual mass (to lower the suspension frequency of the vibration isolator) and artificial sky-hook damping, respectively. As already introduced in section 2.2, the performance of a vibration isolator is determined by the transmissibility $T(s)$ and the compliance $C(s)$ which are given by Eq. (2.4). Substituting Eq. (3.3) and $F_a(s) = H(s)\ddot{X}_1(s)$ into Eq. (3.1) gives the expressions for the transmissibility and compliance of the

closed loop system:

$$T(s) = \frac{k_1 + k_\mathrm{p}}{(m + k_\mathrm{a})s^2 + k_\mathrm{v}s + k_1 + k_\mathrm{p}}, \tag{3.4}$$

$$C(s) = \frac{1}{(m + k_\mathrm{a})s^2 + k_\mathrm{v}s + k_1 + k_\mathrm{p}}. \tag{3.5}$$

Indeed, the mass is virtually increased with k_a and sky-hook damping is realized by k_v. Stiffness k_1 can have any desired value.

Next, consider force feedback. By substituting Eq. (3.1) into Eq. (3.2), the force sensor signal can also be expressed as:

$$F_\mathrm{s}(s) = m\ddot{X}_1(s) + k_\mathrm{p}(X_1(s) - X_0(s)) - F_\mathrm{d}(s). \tag{3.6}$$

So, the force sensor is not only measuring the acceleration of body m, but also the contributions of k_p and F_d. If the contributions of k_p and F_d are neglected, it is observed that F_s and $\ddot{x}_1$ represent the same signals except for a gain m. Therefore, controller $H(s)$ of Eq. (3.3) is also suitable for force feedback, when it is scaled with $1/m$, see Fig. 3.1(b). By using $F_\mathrm{a}(s) = (1/m)H(s)F_\mathrm{s}(s)$ the transmissibility and compliance of the closed loop system are given by:

$$T(s) = \frac{k_1 + k_\mathrm{p} + (k_\mathrm{p}/m)(k_\mathrm{a} + k_\mathrm{v}/s)}{(m + k_\mathrm{a})s^2 + k_\mathrm{v}s + k_1 + k_\mathrm{p} + (k_\mathrm{p}/m)(k_\mathrm{a} + k_\mathrm{v}/s)}, \tag{3.7}$$

$$C(s) = \frac{1}{(m + k_\mathrm{a})s^2 + k_\mathrm{v}s + k_1 + k_\mathrm{p} + (k_\mathrm{p}/m)(k_\mathrm{a} + k_\mathrm{v}/s)} \frac{(m + k_\mathrm{a})s + k_\mathrm{v}}{ms}. \tag{3.8}$$

By comparing Eqs. (3.4) and (3.7), is is observed that the numerator and denominator terms in the expressions for the transmissibilities are dependent on the type of feedback. Therefore, the suspension frequencies are different for both types of feedback. Assuming $k_\mathrm{v} = 0$, the expressions for the suspension frequencies of the closed loop system are given by

$$\omega_\mathrm{n} = \sqrt{\frac{k_1 + k_\mathrm{p}}{m + k_\mathrm{a}}}, \tag{3.9}$$

for acceleration feedback, and

$$\omega_\mathrm{n} = \sqrt{\frac{k_1}{m + k_\mathrm{a}} + \frac{k_\mathrm{p}}{m}}, \tag{3.10}$$

for force feedback. When using acceleration feedback, the suspension frequency ω_n can be set to any desired value by choosing the appropriate value for k_a using Eq. (3.9). When using force feedback, the suspension frequency ω_n is limited by the factor k_p/m, so a large parasitic stiffness limits the performance, see also [60]. The relative damping can be set to any desired value by choosing the appropriate value for k_v:

$$\zeta_n = \frac{k_v}{2\omega_n(m + k_a)}. \tag{3.11}$$

So, in case of a significant parasitic stiffness, acceleration feedback performs better than force feedback regarding the transmissibility.

For the limit $s \to 0$ the static compliances can be calculated using Eq. (3.5) for acceleration feedback

$$C_{\ddot{x}_1}(s = 0) = \frac{1}{k_1 + k_p}, \tag{3.12}$$

and Eq. (3.8) for force feedback

$$C_{F_s}(s = 0) = \frac{1}{k_p}. \tag{3.13}$$

In a hard mount system it holds that $k_p \ll k_1$, such that the closed loop system using acceleration feedback has a much lower value for the static compliance. For force feedback the compliance tends to infinity if no parasitic stiffness is present, so the static stiffness will be even zero. Therefore, acceleration feedback also performs better than force feedback regarding the compliance.

3.2.2 Flexible body model

Next, consider the flexible body model as in Fig. 3.2(a), which is based on Fig. 2.2(b). This model describes the dynamics of the vibration isolator when the suspended equipment contains internal flexibilities. The equipment is represented by two payload bodies with masses m_1 and m_2, where $m_1 + m_2 = m$. These bodies are interconnected by a spring k_2. There is no physical damper d_2 modeled between bodies m_1 and m_2 since internal damping is often negligible. A disturbance force F_d is acting on body m_1.

Examine the model of Fig. 3.2(a) using the numerical values listed in Table 3.1. The values for the hard mount represent the experimental setup used for the control experiments. The parasitic stiffness k_p is chosen as 1% of the

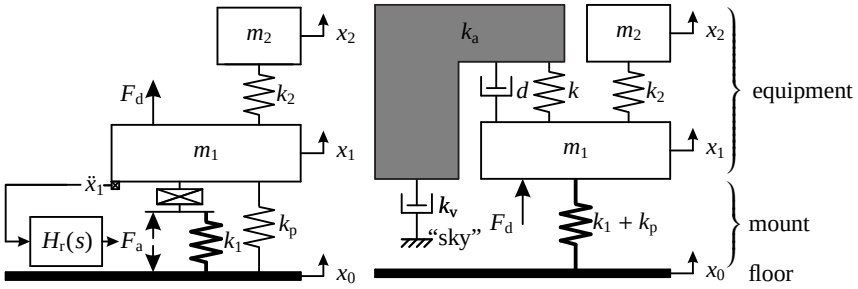

(a) Flexible body model. (b) Equivalent mechanical model.

Fig. 3.2: (a) Model of the vibration isolator in which the equipment is represented by a flexible body, using acceleration feedback. (b) Equivalent mechanical model with the same dynamics as the closed loop system of (a) using acceleration feedback with controller $H_r(s)$.

value of k_1. The system's suspension frequency is 13 Hz. The feedback gains of controller $H(s)$ of Eq. (3.3) are set to:

$$k_a = \frac{k_1}{\omega_n^2} - (m_1 + m_2), \tag{3.14}$$

$$k_v = 2\zeta_n \omega_n (m_1 + m_2 + k_a), \tag{3.15}$$

where, $\omega_n = 2\pi f_{ref}$ with $f_{ref} = 1$ Hz and $\zeta_n = \zeta_{ref} = 0.7$ are the desired suspension frequency and relative damping of the closed loop system. With these values the closed loop hard mount obtains the same transmissibility as the ideal active soft mount of Eq. (2.16) with $\epsilon_{ref} = 0$, a suspension frequency of 1 Hz, and 70% sky-hook damping, see section 2.5. The values for the soft mount in Table 3.1 represent this ideal active soft mount isolator. The gains of the controller for the soft mount isolator are $k_a = 0$ and k_v as in Eq. (3.15) with $\omega_n = 2\pi f_{ref}$ with $f_{ref} = 1$ Hz and $\zeta_n = \zeta_{ref} = 0.7$. The feedback strategies applied to the active hard mount are compared to the ideal active soft mount.

Acceleration feedback using sensor $\ddot{x}_1$ is analyzed first. The solid line in Fig. 3.3(a) shows the loop gain

$$L_{\ddot{x}_1}(s) = H(s) G_{\ddot{x}_1 F_a}(s) \tag{3.16}$$

that is formed by the controller $H(s)$ of Eq. (3.3) and plant transfer function $G_{\ddot{x}_1 F_a}(s)$ from actuator force to acceleration signal which can be derived from the equation of motion corresponding to Fig. 3.2(a):

$$G_{\ddot{x}_1 F_a}(s) = \frac{\ddot{X}_1(s)}{F_a(s)} = \frac{s^2(m_2 s^2 + k_2)}{(m_1 s^2 + k_1 + k_2 + k_p)(m_2 s^2 + k_2) - k_2^2}. \tag{3.17}$$

Table 3.1: Mass and stiffness properties of the hard and soft mounts.

	m_1 (kg)	m_2 (kg)	k_1 (N/m)	k_2 (N/m)	k_p (N/m)
hard mount	2.8	2.6	36 000	450 000	360
soft mount	2.8	2.6	213	450 000	0

$L_{\ddot{x}_1}(s)$ has two resonances at 13 and 93 Hz corresponding to the suspension and internal mode respectively, and one anti-resonance at 66 Hz. The frequency of the anti-resonance corresponds to the zeros of Eq. (3.17) and is

$$\omega_{a,\ddot{x}_1} = \sqrt{\frac{k_2}{m_2}}. \tag{3.18}$$

Since both plant and controller do not have high-frequency roll-off, the loop gain results in infinite closed loop bandwidth. This will cause stability problems in practical applications. By adding a second-order low-pass filter, the controller obtains high-frequency roll-off. The cut-off frequency ω_f of the filter is determined by the desired attenuation at high frequencies (above ω_f), which is expressed as $(\omega_n/\omega_f)^2$. An additional high-frequency zero ω_z is used to increase the phase margin around the high crossover frequency of the loop gain. A second-order high-pass filter with a corner frequency of $\omega_l = 2\pi{\cdot}0.1$ rad/s and relative damping ratio $\zeta_l = 0.7$ is added to prevent actuator saturation at low frequencies. The improved controller reads:

$$H_r(s) = -(k_a + \frac{k_v}{s})\frac{s^2}{s^2 + 2\zeta_l\omega_l s + \omega_l^2}\frac{\omega_f^2}{s^2 + 2\zeta_f\omega_f s + \omega_f^2}\frac{s + \omega_z}{\omega_z}. \tag{3.19}$$

The corner frequency is set to $\omega_f = 2\pi{\cdot}20$ rad/s to obtain above 20 Hz an attenuation of $(\omega_n/\omega_f)^2 = 1/20^2 = 2.5{\cdot}10^{-3}$, which is about −52 dB. With this value of ω_f, the high-frequency attenuation is equal to the desired value ϵ_{ref} of section 2.5. The damping of the low-pass filter can be set to any value, in this thesis $\zeta_f = 0.07$ is used. The lower the value of ζ_f, the more isolation is obtained at the frequency ω_f. The additional zero is placed at $\omega_z = 2\pi{\cdot}290$ rad/s. The resulting loop gain

$$L_{r,\ddot{x}_1}(s) = H_r(s)G_{\ddot{x}_1 F_a}(s) \tag{3.20}$$

is shown as the solid line in Fig. 3.3(b). The phase margin is about 60° at the crossover frequency of 524 Hz.

The dynamics of the closed loop system with loop gain $L_{r,\ddot{x}_1}(s)$ is comparable to the dynamics of the mechanical model shown in Fig. 3.2(b), if the values

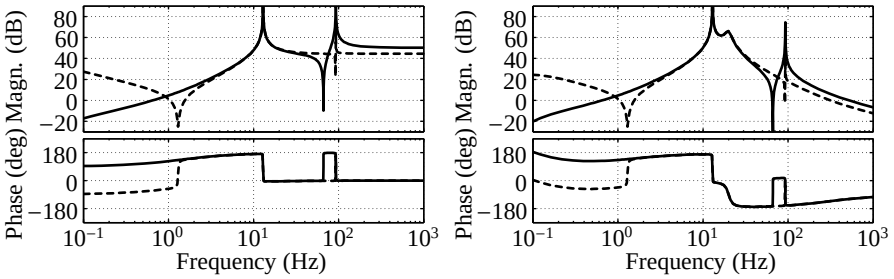

(a) Loop gains using controller $H(s)$. (b) Loop gains using controller $H_r(s)$.

Fig. 3.3: Loop gains of the hard mount using acceleration feedback ($L_{\ddot{x}_1}(s)$ and $L_{r,\ddot{x}_1}(s)$ ——) and force feedback ($L_{F_s}(s)$ and $L_{r,F_s}(s)$ - - - -) with: (a) controller $H(s)$; (b) controller $H_r(s)$.

of the stiffness, damping and mass are expressed in terms of the controller parameters of $H_r(s)$. So, the physical interpretation of this feedback strategy is that a virtual body with mass k_a is added to payload body m_1. It can be shown that the connection between bodies k_a and m_1 has stiffness $k = k_a\omega_f^2$ and viscous damping $d = 2\zeta_f\omega_f k_a - k_v$. A sky-hook damper k_v is attached to body k_a. For $H_r(s)$ a constraint $\omega_z(2\zeta_f\omega_f k_a - k_v) = k_a\omega_f^2$ is required to make the dynamics of both models in Figs. 3.2(a) and (b) completely equivalent. Fig. 3.2(b) can be interpreted as follows: at low frequencies, the suspended payload can be considered as a rigid body with mass $m_1 + m_2 + k_a$, connected to the floor with the stiff spring k_1 and connected to the "sky" with damper k_v. Above frequency ω_f, the contributions of mass k_a and damper k_v to the dynamics are decreasing. At high frequencies, the dynamics are equal to the original dynamics without k_a and k_v.

Next, force feedback is analyzed. The dashed lines in Figs. 3.3(a) and (b) display the loop gains

$$L_{F_s}(s) = \frac{1}{m_1 + m_2} H(s) G_{F_s F_a}(s), \tag{3.21}$$

$$L_{r,F_s}(s) = \frac{1}{m_1 + m_2} H_r(s) G_{F_s F_a}(s). \tag{3.22}$$

These are formed by force feedback controller, $1/(m_1 + m_2)H(s)$ or $1/(m_1 + m_2)H_r(s)$, and the transfer function $G_{F_s F_a}(s)$ from actuator force to force sensor signal:

$$G_{F_s F_a}(s) = \frac{F_s(s)}{F_a(s)} = \frac{(m_1 s^2 + k_2 + k_p)(m_2 s^2 + k_2) - k_2^2}{(m_1 s^2 + k_1 + k_2 + k_p)(m_2 s^2 + k_2) - k_2^2}. \tag{3.23}$$

Compared to the acceleration feedback loop gains, the high-frequency gain is lower and the anti-resonance has moved up to 92 Hz. This frequency can be approximated by:

$$\omega_{a,F_s} \approx \sqrt{\frac{k_2}{m_2}(1+\frac{m_2}{m_1})}. \tag{3.24}$$

The anti-resonance at 1.3 Hz is due to the presence of the parasitic spring k_p and its frequency can be approximated by

$$\omega_a \approx \sqrt{\frac{k_p}{m_1+m_2}}. \tag{3.25}$$

How k_p affects the control performance will be discussed below. From now on, controller $H_r(s)$ of Eq. (3.19) is used for both acceleration and force feedback. Note that the high-frequency zero ω_z in Eq. (3.19) which is added to increase the phase margin around the high crossover frequency, is optimized for acceleration feedback, resulting in a phase margin of 60°. For force feedback, the phase margin is only about 30°. This is because the crossover frequency for force feedback is lower than for acceleration feedback. However, it is assumed that this value for the phase margin is still sufficient. In [54] a control design is presented such that the acceleration and force feedback controllers have comparable high crossover frequencies and comparable phase margins around these high crossover frequencies.

3.2.3 Modeling results

Next to the transmissibility $T(s)$ and compliance $C(s)$ of Eq. (2.4), the isolator's performance is also determined by the deformation transmissibility $T_d(s)$ and deformability $D(s)$ of Eq. (2.5), which are the responses of the internal deformation $\Delta X(s)$ due to the disturbances $\ddot{X}_0(s)$ and $F_d(s)$. These four transfer functions are shown in Figs. 3.4(a)–(d). The dotted lines represent the responses of the open loop hard mount. The responses of an ideal active soft mount are given by the dash-dotted lines. The responses for the closed loop hard mount using acceleration feedback and the hard mount using force feedback are shown as the solid and dashed lines, respectively.

The transmissibilities of the closed loop hard mount using acceleration feedback and the ideal active soft mount are comparable in the frequency range up to 20 Hz, the frequency ω_f. Above this frequency the attenuation is more than 50 dB, see Fig. 3.4(a). The transmissibility of the closed loop hard mount using force feedback is higher than that of the ideal active soft mount. The higher transmissibility is because the force sensor is not able to compensate

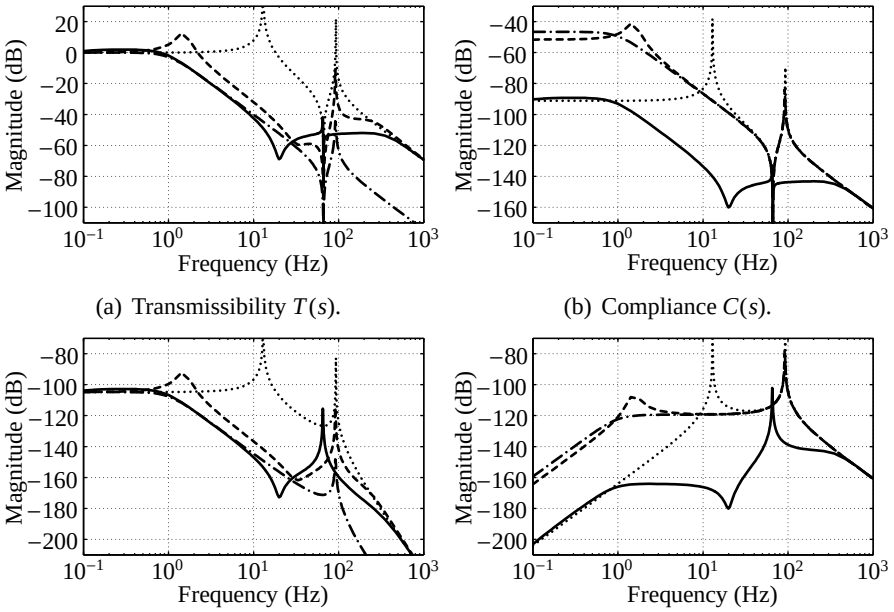

(a) Transmissibility $T(s)$.

(b) Compliance $C(s)$.

(c) Deformation transmissibility $T_{\mathrm{d}}(s)$.

(d) Deformability $D(s)$.

Fig. 3.4: Performance transfer functions: (a) transmissibility $T(s)$; (b) compliance $C(s)$; (c) deformation transmissibility $T_{\mathrm{d}}(s)$; (d) deformability $D(s)$.

- ····· open loop hard mount
- −·−·− ideal active soft mount with 70% sky-hook damping
- —— closed loop hard mount using acceleration feedback
- - - - closed loop hard mount using force feedback

for the vibration energy transmitted to the suspended payload by the parasitic stiffness k_{p} [60]. The zeros in the force feedback loop gain of Fig. 3.3(b) result in a poorly damped resonance peak at 1.5 Hz in the transmissibility. Around this frequency the loop gain is very small, so the controller is not able to alter the transmissibility compared to the open loop response. This results in a higher suspension frequency of the closed loop system, see also Eq. (3.10). Fig. 3.4(b) shows the compliances. Using acceleration feedback, the compliance at low frequencies is determined by the suspension stiffness k_1, resulting in a low value. In-between 1 and about 500 Hz, the compliance is even much lower than that of the open loop hard mount system. This means that in this frequency range the system's susceptibility to direct disturbance forces is much improved, which is an additional advantage of active hard mounts as compared to (active) soft mounts. Using force feedback, the compliance at low frequen-

cies is determined by the parasitic stiffness k_p and therefore 100 times higher compared to acceleration feedback. Figs. 3.4(c) and (d) show that the deformation transmissibility and the deformability using acceleration feedback are below those using force feedback for almost all frequencies. So, acceleration feedback outperforms force feedback regarding all four performance transfer functions.

However, both feedback strategies fail to increase the damping ratio of the internal mode. This is observed by the poorly damped resonance peaks in the closed loop responses of $\ddot{X}_2(s)$ in Figs. 3.4(c) and (d). The internal modes of the closed loop systems are lowered in frequency to almost the anti-resonance frequencies $\omega_{a,\ddot{x}_1}$ at 66 Hz for acceleration feedback and ω_{a,F_s} at 92 Hz for force feedback, respectively. Close to these anti-resonance frequencies, the loop gains have small magnitudes, see Fig. 3.3(b), so the control action has hardly any effect. As a consequence, the closed loop system cannot perform better than the open loop system (apparently, feedback makes it slightly worse). Therefore, the closed loop responses show resonance peaks at these frequencies.

To conclude, both sensor strategies fail to simultaneously achieve all three performance objectives. A trade-off has to be made between lowering the suspension frequency using the controller of Eq. (3.19) with acceleration feedback and adding damping to the internal mode using other control strategies, such as integral acceleration feedback [46]. The controller of Eq. (3.19) with force feedback cannot be used if a low compliance is desired.

In the next section, it is shown that all three performance objectives can be realized using a control strategy based on the sensor fusion of the accelerometer and force sensor signals.

3.3 Sensor fusion

In case of acceleration feedback, the internal resonance frequency of the closed loop system is close to the anti-resonance frequency in the corresponding loop gain. The controller of Eq. (3.19) cannot be used to increase the damping ratio of the internal mode, since the magnitude of the loop gain is very small in the vicinity of this anti-resonance. Because the force feedback loop gain has its anti-resonance at a much higher frequency (see Fig. 3.3(b)), it is suggested to use the force signal for the feedback controller in addition to the acceleration signal. Combining multiple sensor signals is referred to as sensor fusion. Similar as in [26] both signals are filtered by complementary filters first be-

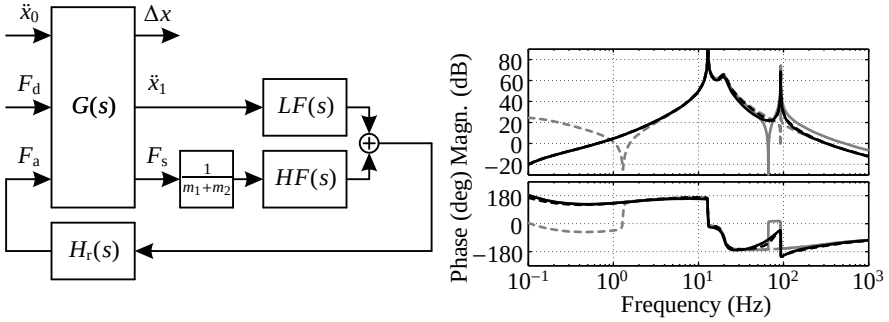

(a) Control scheme of sensor fusion. (b) Loop gains.

Fig. 3.5: (a) Control scheme of sensor fusion. (b) Loop gains of the hard mount using acceleration feedback ($L_{r,\ddot{x}_1}(s)$ ——), force feedback ($L_{r,F_s}(s)$ - - - -), sensor fusion ($L_{r,(\ddot{x}_1,F_s)}(s)$ - - - -), and sensor fusion with additional high-pass filter ($L_{r,(\ddot{x}_1,F_s)}(s)$ ——).

fore feeding them to the controller. Complementary filters are a low pass and high pass filter which transfer functions sum to one.

Regarding all performance transfer functions, acceleration feedback outperforms force feedback at low frequencies, while the high-frequency performance is similar. Therefore, it is proposed to filter the acceleration signal with a low-pass filter and the force signal with a high-pass filter. controller $H_r(s)$ of Eq. (3.19) is used together with first-order filters:

$$LF(s) = \frac{\omega_p}{s+\omega_p}, \qquad HF(s) = \frac{s}{s+\omega_p}. \tag{3.26}$$

Indeed, the sum of $LF(s)$ and $HF(s)$ is one. Filter pole $\omega_p = 2\pi{\cdot}56$ rad/s is chosen such that the damping ratio of the internal mode is maximized. How to choose ω_p to maximize this damping ratio will be explained at the end of this section. The control scheme of this strategy is shown in Fig. 3.5(a) and its loop gain

$$L_{r,(\ddot{x}_1,F_s)}(s) = H_r(s)(LF(s)G_{\ddot{x}_1F_a}(s) + \frac{1}{m_1+m_2}HF(s)G_{F_sF_a}(s)) \tag{3.27}$$

is shown in Fig. 3.5(b) as the dashed line. At frequencies below ω_p, the loop gain is equal to the acceleration feedback loop gain, at frequencies above ω_p it is equal to the force feedback loop gain. The anti-resonance in $L_{r,(\ddot{x}_1,F_s)}(s)$ is now well damped. The large amount of damping is possible because of the relatively large distance between the anti-resonance frequency in the acceleration path at 66 Hz and the anti-resonance frequency in the force path at 92 Hz.

Figs. 3.6(a)–(d) show the performance transfer functions. The black dashed lines represent the sensor fusion strategy. For reference, the transfer functions of Figs. 3.4(a)–(d) are repeated here in gray. The transmissibility and deformation transmissibility are comparable to those of the acceleration feedback system at low frequencies and to those of the force feedback system at high frequencies. It is visible in Figs. 3.6(c) and (d) that the damping ratio of the internal mode in the responses of $\ddot{X}_2(s)$ has much increased (to 20%). However, the low-frequency compliance and deformability are about 3 times higher than those of the acceleration feedback system. Apperently, the effect of the force feedback signal is still noticed at low frequencies. A higher frequency of filter pole ω_p would make these transfer functions more comparable to the acceleration feedback system at the cost of a smaller damping ratio of the internal mode.

Since at low frequencies only the acceleration signal is used for control, an additional high-pass filter can be added to the force sensor signal to make the force sensor at low frequencies even less important. The pole of the additional filter has to be smaller than ω_p to guarantee that the loop gain will hardly be affected by the presence of the filter pole ω_q. The new filters are

$$LF(s) = \frac{\omega_p}{s+\omega_p}, \qquad HF(s) = \frac{s}{s+\omega_p}\frac{s}{s+\omega_q}, \tag{3.28}$$

in which $\omega_q = \frac{1}{2}\omega_p$ is chosen. The loop gain and the resulting performance transfer functions are visible as the black solid lines in Fig. 3.5(b) and Fig. 3.6 respectively. The transmissibility and deformation transmissibility remain virtually the same, whereas the low-frequency compliance and deformability are now comparable to the acceleration feedback system up to 3 Hz. With respect to the open loop system, the susceptibility of the system using sensor fusion to direct disturbance forces is improved in the frequency range in-between 1 and 120 Hz. This is only slightly worse as compared to the acceleration feedback system.

The solid black lines in Fig. 3.6 demonstrate that the sensor fusion strategy using the controller of Eq. (3.19) and the filters of Eq. (3.28) makes it possible to simultaneously realize all three performance objectives. The performance of the vibration isolator is expressed in terms of high suspension stiffness k_1, desired closed loop suspension frequency ω_n and high-frequency attenuation (above ω_f) (calculated as $(\omega_f/\omega_n)^2$). Since in practical applications the control bandwidth is limited, the maximum achievable performance is related to the available bandwidth. A measure for bandwidth is the high-frequency crossover

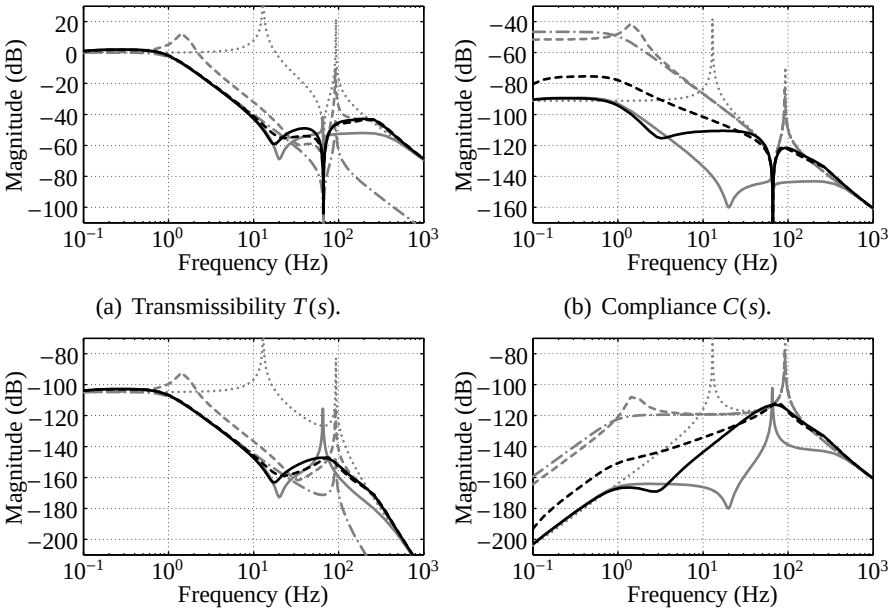

(a) Transmissibility $T(s)$.

(b) Compliance $C(s)$.

(c) Deformation transmissibility $T_{\mathrm{d}}(s)$.

(d) Deformability $D(s)$.

Fig. 3.6: Performance transfer functions: (a) transmissibility $T(s)$; (b) compliance $C(s)$; (c) deformation transmissibility $T_{\mathrm{d}}(s)$; (d) deformability $D(s)$.

- open loop hard mount
- ideal active soft mount with 70% sky-hook damping
- closed loop hard mount using acceleration feedback
- closed loop hard mount using force feedback
- closed loop hard mount using sensor fustion
- closed loop hard mount using sensor fusion and high-pass filter

in the loop gain $L_{\mathrm{r},(\ddot{x}_1,F_{\mathrm{s}})}(s)$. This crossover frequency can be estimated as:

$$\omega_{\mathrm{c}} \approx \alpha\omega_{\mathrm{f}}\sqrt{\frac{k_{\mathrm{a}}}{m_1+m_2}} \approx \alpha\frac{\omega_{\mathrm{f}}\omega_{\mathrm{r}}}{\omega_{\mathrm{n}}}. \tag{3.29}$$

Here $\omega_{\mathrm{r}} \approx \sqrt{k_1/(m_1+m_2)}$ is the open loop suspension frequency of the hard mount which is, for a given payload mass, determined by the suspension stiffness k_1. Furthermore, $\alpha = 1.2\ldots1.4$, depending on the location of the high-frequency zero ω_{z} in Eq. (3.19) relative to ω_{c}. From this it is concluded that the maximum achievable performance is a trade-off between the reduction of the suspension frequency $\omega_{\mathrm{r}}/\omega_{\mathrm{n}}$ and the high-frequency attenuation $(\omega_{\mathrm{f}}/\omega_{\mathrm{n}})^2$.

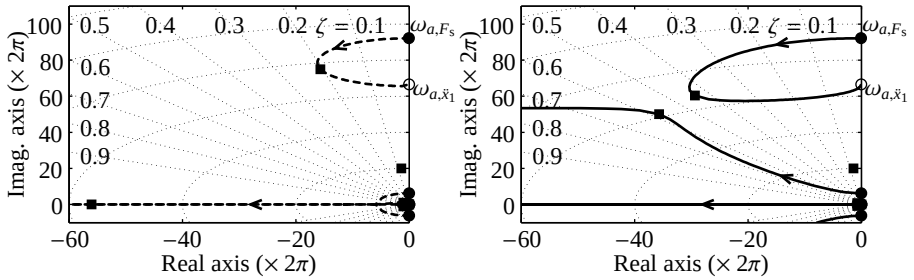

(a) Closed loop poles using filters (3.26). (b) Closed loop poles using filters (3.28).

Fig. 3.7: Closed loop poles of the hard mount when filter pole ω_p tends from 0 to ∞: (a) using sensor fusion and the filters of Eq. (3.26); (b) using sensor fusion and the filters (3.28). ∘ denote the zeros of $L_{r,\ddot{x}_1}(s)$; ● denote the zeros of $L_{r,F_s}(s)$; ■ denote the closed loop poles for which maximum damping of the internal mode is obtained.

3.3.1 Maximum achievable damping

The damping ratio of the internal mode in the model of Fig. 3.2(a) depends on the chosen value of filter pole ω_p. This is visualized in Fig. 3.7(a) where the closed loop poles of the hard mount system using the controller of Eq. (3.19) and the filters of Eq. (3.26) are plotted as branches of the "root locus" for ω_p varying from 0 to ∞. The branch corresponding to the internal mode traces a curve in the left-half of the complex plane. The curve starts approximately in $j\omega_{a,F_s}$ for $\omega_p = 0$ (this value corresponds to the system with force feedback only) and it ends approximately in $j\omega_{a,\ddot{x}_1}$ for $\omega_p = \infty$ (this value corresponds to the system with acceleration feedback only). Here ω_{a,F_a} and $\omega_{a,\ddot{x}_1}$ are the purely imaginary zeros of the transfer functions $G_{F_sF_a}(s)$ of Eq. (3.23) and $G_{\ddot{x}_1F_a}(s)$ of Eq. (3.17). These zeros correspond to the frequencies of the anti-resonances in the loop gains $L_{r,F_s}(s)$ and $L_{r,\ddot{x}_1}(s)$ respectively. The squares indicate the closed loop poles for which maximum damping of the internal mode is obtained. It is shown in appendix A that ω_p must be chosen as

$$\omega_p = \frac{m_1}{m_1+m_2}\omega_{a,F_s}\sqrt{\frac{\omega_{a,F_s}}{\omega_{a,\ddot{x}_1}}} = \frac{\omega_{a,\ddot{x}_1}}{\omega_{a,F_s}}\sqrt{\omega_{a,\ddot{x}_1}\omega_{a,F_s}}, \tag{3.30}$$

such that the anti-resonance frequency of $L_{r,(\ddot{x}_1,F_s)}(s)$ is equal to $\sqrt{\omega_{a,\ddot{x}_1}\omega_{a,F_s}}$. This value is obtained for $\omega_p = 2\pi{\cdot}56$ rad/s. The maximum achievable damping can be found as:

$$\zeta_{max} = \frac{1}{2}\left|\frac{\omega_{a,F_s}}{\omega_{a,\ddot{x}_1}} - 1\right|, \tag{3.31}$$

Substituting Eqs. (3.18) and (3.24) into Eq. (3.31) allows to rewrite Eq. (3.31) as $\zeta_{max} = \frac{1}{2}\sqrt{1+m_2/m_1} - \frac{1}{2} = 20\%$. So, the maximum achievable damping

depends on the mass ratio m_2/m_1 which is determined by the design of the suspended equipment. If m_2 is small compared to m_1, the maximum achievable damping will also be small. The higher ratio m_2/m_1 is, the higher the achievable damping. In general, for internal modes at very high frequencies, the mass ratio m_2/m_1 is very small, so it will not be possible to add much damping to these modes.

Fig. 3.7(b) shows the closed loop poles of the hard mount system using the controller of Eq. (3.19) and the filters of Eq. (3.28) for ω_p varying from 0 to ∞. It is observed that the maximum achievable damping has been increased to about 43%. This increase is due to the presence of the additional high-pass filter (with pole ω_q) in the force path. Approximate formulas for calculating the maximum achievable damping are more difficult to obtain and are therefore not derived.

3.4 Two-sensor control

In the previous section it is shown that the sensor fusion control strategy can be used to target on increasing the damping ratio of the internal mode while keeping the other two performance objectives stated in section 2.5. Sensor fusion control can be interpreted as a special case of two-sensor control in which the two controllers are the same (except for the complementary filters). In this section, the combination of acceleration and force feedback is discussed using different controllers for each sensor signal. It is shown how two-sensor control is used to minimize the internal deformation $\Delta X(s)$, rather than maximizing the damping ratio of the internal mode, without affecting the transmissibility and compliance. In the first subsection, a two-sensor control strategy is derived to target on increasing the damping ratio of the internal mode only. In the second subsection, the two-sensor control strategy is combined with the controllers from the previous section to satisfy all three performance objectives simultaneously.

3.4.1 Increasing the internal damping ratio

Consider the control scheme of Fig. 3.8(a) that corresponds to the flexible body model of Fig. 3.2(a). From single-input single-output control systems (either $\ddot{x}_1 = 0$ or $F_s = 0$) it is known that for the response of $\Delta X(s)$, the closed loop transfer function equals the open loop transfer function $G_{\Delta x \ddot{x}_0}(s) = \Delta X(s)/\ddot{X}_0(s)$ scaled with the sensitivity function $1/(1 + L(s))$ with the corresponding loop gain $L(s)$. In appendix B it is shown that the same relation holds

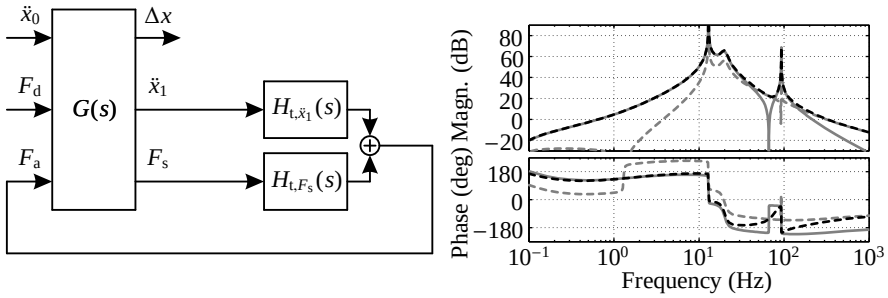

(a) Control scheme of two-sensor control. (b) Loop gains.

Fig. 3.8: (a) Control scheme of two-sensor control. (b) Loop gains of the hard mount using acceleration feedback ($L_{r,\ddot{x}_1}(s)LF(s)$ ——), force feedback ($L_{r,F_s}(s)HF(s)$ - - - -), and sensor fusion ($L_{r,(\ddot{x}_1,F_s)}(s)$ - - - -) with the filters of Eq. (3.26).

in case of two outputs:

$$\frac{\Delta X(s)}{\ddot{X}_0(s)} = \frac{1}{1 + L_{t,(\ddot{x}_1,F_s)}(s)} G_{\Delta x \ddot{x}_0}(s), \tag{3.32}$$

where $L_{t,(\ddot{x}_1,F_s)}(s)$ is the loop gain for the two-sensor controller, expressed as the sum of $L_{t,\ddot{x}_1}(s)$ and $L_{t,F_s}(s)$:

$$\begin{aligned} L_{t,(\ddot{x}_1,F_s)}(s) &= L_{t,\ddot{x}_1}(s) + L_{t,F_s}(s) \\ &= H_{t,\ddot{x}_1}(s) G_{F_{\ddot{x}_1 a}}(s) + H_{t,F_s}(s) G_{F_s F_a}(s), \end{aligned} \tag{3.33}$$

in which $H_{t,\ddot{x}_1}(s)$ and $H_{t,F_s}(s)$ are the acceleration and force feedback controllers respectively, that will be defined in this section.

From Eq. (3.32) it can be concluded that the resonance peak of the internal mode can be reduced in magnitude by realizing a high loop gain $L_{t,(\ddot{x}_1,F_s)}(s)$ in the frequency range where the internal mode must be damped. Therefore, $L_{t,(\ddot{x}_1,F_s)}(s)$ should ideally not contain any anti-resonance. An anti-resonance in $L_{t,(\ddot{x}_1,F_s)}(s)$ appears at a frequency for which $L_{t,\ddot{x}_1}(s)$ and $L_{t,F_s}(s)$ have the same magnitude but have opposite sign due to a 180° phase difference. So this situation must be prevented. In the ideal case, the loop gains $L_{t,\ddot{x}_1}(s)$ and $L_{t,F_s}(s)$ have the same phase over the complete frequency range, such that their sum is always maximized. In practice this is unrealistic because the plant must be precisely known to achieve this, so a model-based controller is required in that case. A method to circumvent a 180° phase difference without requiring a model-based controller is realizing a 90° phase difference between $L_{t,\ddot{x}_1}(s)$ and

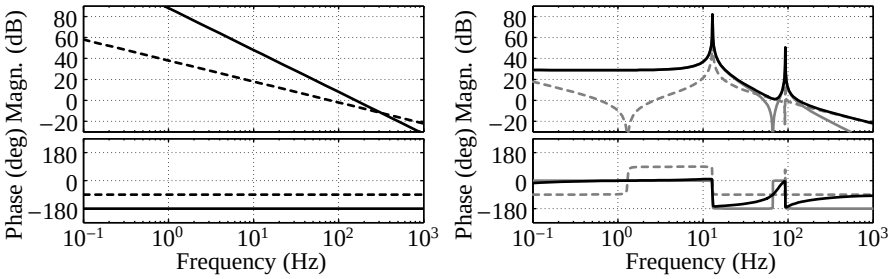

(a) Example of controllers $H_{\ddot{x}_1}(s)$ and $H_{F_s}(s)$.

(b) Loop gains.

Fig. 3.9: (a) Example of acceleration feedback controller ($H_{t,\ddot{x}_1}(s)$ ——) and force feedback controller ($H_{t,F_s}(s)$ - - - -) that are 90° out of phase. (b) Corresponding loop gains of the hard mount using acceleration feedback ($L_{t,\ddot{x}_1}(s)$ ——), force feedback ($L_{t,F_s}(s)$ - - - -), and two-sensor control ($L_{t,(\ddot{x}_1,F_s)}(s)$ ——).

$L_{t,F_s}(s)$. In the complex s-plane this is interpreted as the summation of two perpendicular vectors, which never results in a zero value.

An example of such acceleration feedback and force feedback controllers is given in Fig. 3.9(a). A roll-off rate of −40 dB/decade is applied for acceleration feedback and a roll-off rate of −20 dB/decade is applied for force feedback. Both controllers are 90° out of phase in the complete frequency range. The corresponding loop gain is shown in Fig. 3.9(b). In the frequency range between the anti-resonance in the acceleration path (66 Hz) and the anti-resonance in the force path (92 Hz), the phase difference of the loop gains is equal to +90°. Elsewhere the phase difference is −90°. From Fig. 3.9(b) it is observed that this method performs well since the summed loop gain for two-sensor control has no poorly damped anti-resonances anymore and the phase angle of the summed loop gain is in-between the phase angles of the separate loop gains.

Next to roll off rates of −40 and −20 dB/decade for acceleration and force feedback respectively, alternatives exist to achieve a 90° phase difference between the two controllers. For example, roll-off rates of −20 dB/decade for acceleration feedback and 0 dB/decade for force feedback could be used. The 90° phase difference is still achieved, but the force controller has no roll-off anymore, resulting in an infinite bandwidth. Another alternative could be using roll-off rates of −60 dB/decade for acceleration feedback and −40 dB/decade for force feedback, but this can lead to stability problems due a drop below the −180° phase line.

Therefore, it is suggested to use a roll-off rate of −40 dB/decade for ac-

celeration feedback and −20 dB/decade for force feedback. With this choice stability of the closed loop system is guaranteed in the frequency range where sensors and actuators are collocated. A property of collocated control is that variations in the phase angle due to internal modes are always in-between the angles ϕ and $\phi + 180°$ [45]. The system is designed such that for acceleration feedback $\phi = -180°$ and for force feedback $\phi = -90°$, see Fig. 3.9(b). This means that for collocated control the phase angles of the separate loop gains $L_{\mathrm{t},\ddot{x}_1}(s)$ and $L_{\mathrm{t},F_\mathrm{s}}(s)$ do not drop below −180°. The closed loop system with two-sensor control remains stable, since the phase angle of the summed loop gain is always in-between the phase angles of the separate loop gains, see Fig. 3.9(b). This can only be achieved with a higher roll-off rate for acceleration feedback than for force feedback. It can be shown that a higher roll-off rate for force feedback than for acceleration feedback results in a well damped anti-resonance, but the phase angle of the summed loop gain is no longer in-between the phase angles of the separate loop gains. Hence, closed loop stability cannot be guaranteed.

The control strategy based on sensor fusion is also an example in which the acceleration and force feedback controllers are 90° out of phase. This can be observed by plotting the individual loop gains, $L_{\mathrm{r},\ddot{x}_1}(s)LF(s)$ for acceleration feedback and $L_{\mathrm{r},F_\mathrm{s}}(s)HF(s)$ for force feedback using the complementary filters of Eq. (3.26). Fig. 3.8(b) shows the individual loop gains as well as the loop gain $L_{\mathrm{r},(\ddot{x}_1,F_\mathrm{s})}(s)$ for sensor fusion. At all frequencies, the phase difference between the individual loop gains is 90°. Since the loop gain of the acceleration feedback controller drops below −180°, closed loop stability for sensor fusion cannot be guaranteed. Sensor fusion loop gain $L_{\mathrm{r},(\ddot{x}_1,F_\mathrm{s})}(s)$ indicated by the black dashed line in Fig. 3.8(b) indeed drops below the −180° phase line in-between 93 and 120 Hz. However, the closed loop system based on sensor fusion is stable (since at the high crossover frequency the phase line is well above −180° such that there is sufficient phase margin), but it is not robustly stable. For example, a significant increase of the equipment's mass, results in a lower magnitude of the loop gain and therefore in a lower value of the high crossover frequency and less phase margin at this crossover frequency. The sensor fusion controller using the improved filters of Eq. (3.28) shows similar results. However, at low frequencies the phase difference between the acceleration feedback and force feedback loop gains is no longer 90° due to the presence of the additional high-pass filter in the force feedback controller. This is not a problem, since in the frequency range where damping of the internal mode is desired, the phase difference is 90° and damping can be achieved

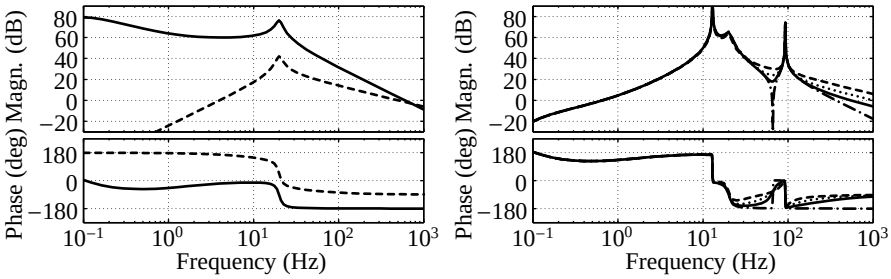

(a) Controllers of Eqs. (3.34) and (3.35). (b) Influence of k_f on the loop gain.

Fig. 3.10: (a) Acceleration feedback controller of Eq. (3.34) ($H_{t,\ddot{x}_1}(s)$ ——) and force feedback controller of Eq. (3.35) ($H_{t,F_s}(s)$ - - - -) with $k_f = 25$. (b) Influence of a varying k_f on the two-sensor control loop gain $L_{t,(\ddot{x}_1,F_s)}(s)$: -·-·- $k_f = 0$; —— $k_f = 25$; ····· $k_f = 50$; - - - - $k_f = 100$.

as already is shown in section 3.3.

3.4.2 Control design and modeling results

In Fig. 3.4 it is already shown that at low frequencies acceleration feedback performs better than force feedback. Therefore the first and third performance objective stated in section 2.5, are satisfied by using acceleration feedback. At high frequencies, where internal modes could occur, the two-sensor control strategy is used to satisfy the second objective. This strategy restricts the roll-off rates at high frequencies to −40 dB/decade (phase −180°) for the acceleration feedback controller and to −20 dB/decade (phase −90°) for the force feedback controller. Since the first performance objective determines the controller gains for acceleration feedback, it is suggested to use the highest roll-off rate for acceleration feedback, such that the resulting control bandwidth becomes not too high.

The acceleration feedback controller $H_r(s)$ of Eq. (3.19) can be used for two-sensor control if the zero at $\omega_z = 2\pi{\cdot}290$ Hz is removed. This zero must be removed to preserve the −40 dB/decade roll-off at high frequencies. The new acceleration feedback controller reads:

$$H_{t,\ddot{x}_1}(s) = -(k_a + \frac{k_v}{s})\frac{s^2}{s^2 + 2\zeta_l\omega_l s + \omega_l^2}\frac{\omega_f^2}{s^2 + 2\zeta_f\omega_f s + \omega_f^2}. \tag{3.34}$$

The force feedback controller $1/(m_1 + m_2)H_r(s)$ for single-sensor control is not suitable for two-sensor control, because it has no longer the role of adding virtual mass and sky-hook damping. At low frequencies the controller gain for force feedback must be limited to prevent distortion of the compliance (similar

as with the sensor fusion controllers using the filters of Eq. (3.26)). Therefore it suggested to use a second-order high-pass filter with a corner frequency of $\omega_f = 2\pi{\cdot}20$ rad/s and a small relative damping $\zeta_f = 0.07$. These values are identical to the values of the second-order low-pass filter in Eq. (3.19) to create the same behavior in the drop of the phase angle around 20 Hz and thus preserve the 90° phase difference. To realize the desired roll-off rate of −20 dB/decade at high frequencies an additional first-order low-pass filter with a corner frequency of $\omega_f = 2\pi{\cdot}20$ rad/s is placed. The result is the following force feedback controller:

$$H_{t,F_s}(s) = k_f \frac{s^2}{s^2 + 2\zeta_f\omega_f s + \omega_f^2} \frac{\omega_f}{s + \omega_f}. \tag{3.35}$$

The controllers of Eqs. (3.34) and (3.35) are plotted in Fig. 3.10(a).

The controller gain k_f can be tuned for any specific plant or application. It is suggested to choose k_f such that the loop gains $L_{t,F_s}(s)$ and $L_{t,\ddot{x}_1}(s)$ at the frequency of the anti-resonance in the acceleration path are of the same order of magnitude. These loop gains can be approximated using Eqs. (3.34) and (3.35) and Eqs. (3.17) and (3.23) as:

$$L_{t,\ddot{x}_1}(s \approx j\omega_{a,\ddot{x}_1}) \approx k_a \frac{\omega_f^2}{s^2} \frac{1}{m_1 + m_2}, \tag{3.36}$$

$$L_{t,F_s}(s \approx j\omega_{a,\ddot{x}_1}) \approx k_f \frac{\omega_f}{s}. \tag{3.37}$$

By demanding $|L_{t,F_s}(s \approx j\omega_{a,\ddot{x}_1})| = |\beta L_{t,\ddot{x}_1}(s \approx j\omega_{a,\ddot{x}_1})|$ with β a scale factor, the desired value of k_f can be calculated as:

$$k_f = \beta k_a \frac{\omega_f}{\omega_{a,\ddot{x}_1}} \frac{1}{m_1 + m_2} \approx \beta \frac{\omega_r^2 \omega_f}{\omega_n^2 \omega_{a,\ddot{x}_1}}, \tag{3.38}$$

where $\omega_r = \sqrt{k_1/(m_1 + m_2)}$. The influence of a k_f on the performance is illustrated in Fig. 3.11 using various scale factors $\beta = 0.5, 1$ and 2 resulting in $k_f = 25, 50$ and 100. The influence on the loop gain is illustrated in Fig. 3.10(b). It is observed that the anti-resonance in the loop gain at 66 Hz becomes more damped with increasing k_f, resulting in more damping of the internal mode, see Figs. 3.11(c) and (d). The obtained damping ratios of the internal mode range from 10% for $k_f = 25$ and 23% for $k_f = 100$. This increased damping is paid for by a higher value of the compliance at mid-frequencies, see Fig. 3.11(b), and a higher bandwidth, see Fig. 3.10(b). It is suggested to use

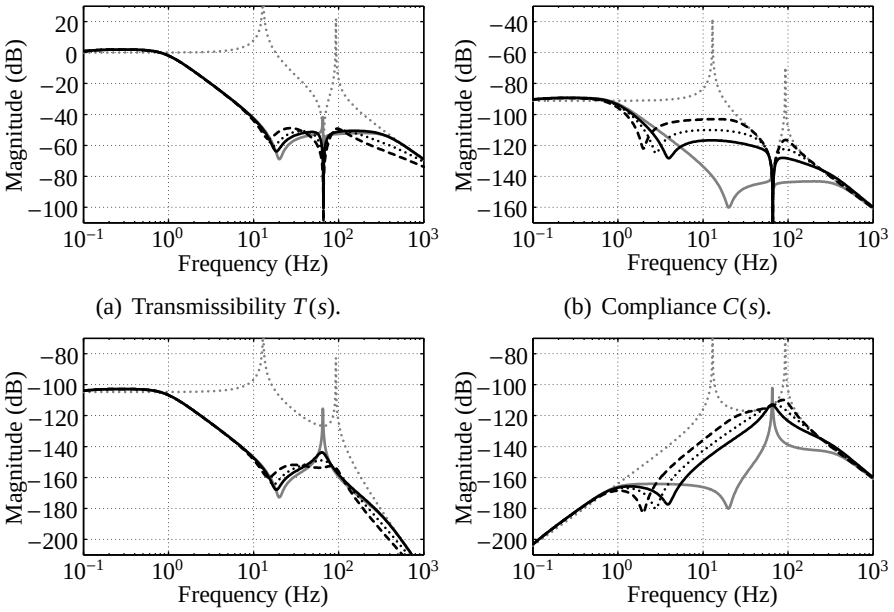

(a) Transmissibility $T(s)$.

(b) Compliance $C(s)$.

(c) Deformation transmissibility $T_d(s)$.

(d) Deformability $D(s)$.

Fig. 3.11: Performance transfer functions: (a) transmissibility $T(s)$; (b) compliance $C(s)$; (c) deformation transmissibility $T_d(s)$; (d) deformability $D(s)$.

- open loop hard mount
- closed loop hard mount using acceleration feedback
- closed loop hard mount using two-sensor control with $k_f = 25$
- closed loop hard mount using two-sensor control with $k_f = 50$
- closed loop hard mount using two-sensor control with $k_f = 100$

$\beta = 0.5$ such that $k_f = 25$, which results in a good trade-off between damping ratio, value of the compliance and bandwidth.

Similar to sensor fusion control, two-sensor control is based on different anti-resonance frequencies for acceleration feedback and force feedback. In section 3.3 it is already explained that the maximum achievable damping for the internal mode is determined by the ratio between the anti-resonance frequencies and depends on the mass ratio m_2/m_1 which should be not too small. Here m_1 and m_2 are the masses of the payload bodies in Fig. 3.2(a). So, two-sensor control is only beneficial over acceleration feedback for not too small ratios m_2/m_1. The compliance of the system using two-sensor control is comparable to that of the system using sensor fusion and is therefore improved with respect to the compliance of the active soft mount.

3.5 Conclusions

The performance objectives of active hard mount vibration isolators for precision equipment stated in section 2.5 can be realized simultaneously using sensor fusion or two-sensor control: obtaining a transmissibility of floor vibrations comparable to an ideal active soft mount (1 Hz suspension frequency and 70% sky-hook damping), increasing the damping ratio of the internal mode of the suspended equipment (20–43% for sensor fusion and 10–23% for two-sensor control) and increasing the suspension stiffness (>150 times larger than an ideal active soft mount). An additional advantage of these control strategies is that the system's susceptibility to direct disturbance forces is signficantly decreased in the frequency range in-between 0 and 120 Hz as compared to the ideal active soft mount.

It is not possible to realize all three performance objectives simultaneously by using either acceleration or force feedback. In case of proportional plus integral feedback, both feedback strategies are not capable of adding damping to an internal mode. Force feedback is also not suitable for the active hard mount vibration isolator, since the low-frequency compliance is determined by the parasitic stiffness and not by the suspension stiffness and is therefore much higher. It is shown that for the active hard mount vibration isolator in closed loop, the resonance frequency of an internal mode is significantly lower than in open loop. Therefore, it is even more important to increase its damping ratio to obtain a good performance.

For all control strategies it is explained how to choose the control parameters if the mass of the suspended payload and the stiffness of its suspension are known, and the desired values of the suspension frequency, damping ratio and high-frequency attenuation are specified. It is shown that the maximum achievable damping ratio for the internal mode is determined by the ratio of the anti-resonance frequencies for acceleration and force feedback.

The main contribution of this chapter is that, as compared to an ideal active soft mount vibration isolator, an active hard mount vibration isolator using sensor fusion or two-sensor control is able to realize the same transmissibility of floor vibrations, with a decreased susceptibility to direct disturbance forces, an increased suspension stiffness to prevent leveling problems of the suspended payload and the possibility to significantly increase the damping ratio of an internal mode.

Control experiments with a one-axis vibration isolator

Chapter 4

The results of the real-time implementation of the control strategies, described in chapter 3, on an experimental setup of a one-axis hard mount vibration isolator are presented. First, the experimental setup is described. The consequences of the differences in dynamics between the experimental setup and the models of chapter 3 are discussed. Secondly, the performance of the experimental setup is analyzed using the four performance transfer functions defined in section 4.3. It is explained how these transfer functions are calculated from the experimental data. Next, the experimental results are given and compared to the modeling results of chapter 3. Finally, the results are discussed.

4.1 Experimental setup

To test the real-time implementation of the various control strategies, the experimental setup depicted in Fig. 4.1 is used. It was already available from previous research [59]. The setup is designed to represent the flexible body model of Fig. 3.2(a) and consists of three moving bodies m_0, m_1 and m_2, which correspond to the floor and the two payload bodies of the equipment respectively. Each mass is provided with a linear guidance to allow motion in one direction only. The setup is mounted on a supporting frame and placed horizontally to circumvent the necessity of gravity compensation.

Floor body m_0 and body m_1 are connected by an active hard mount, consisting of a voice coil actuator which is able to generate a force F_a, and two flexible membranes used as a linear guidance of the coil. The out-of-plane stiffness of the membranes also provides for the desired suspension stiffness k_1. A voice coil actuator has been chosen over other types of actuators such as piezoelectric actuators, due to its linear characteristics. Bodies m_1 and m_2

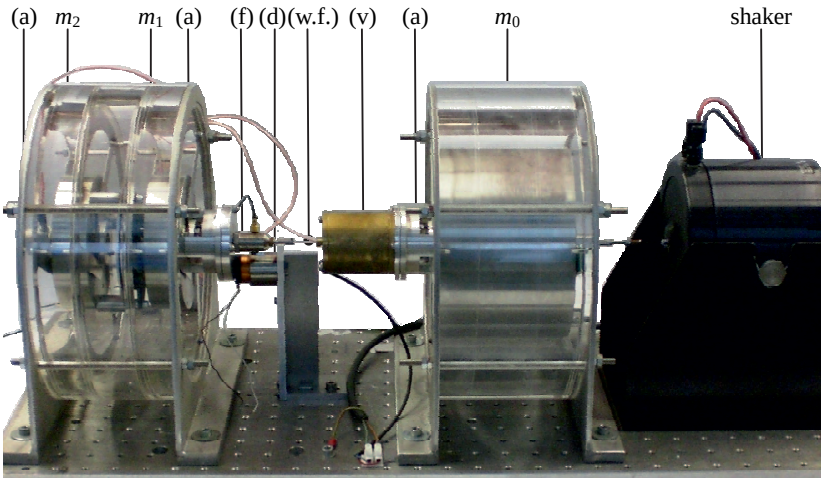

Fig. 4.1: Experimental setup with floor body m_0 that can be excited by a shaker, payload bodies m_1 and m_2 interconnected by a stiffness k_2, voice coil actuator (v) consisting of a stiffness k_1 and a parallel actuator force F_a, accelerometer (a), force sensor (f), wire flexure (w.f.), and additional voice coil actuator applying direct force F_d (d).

are connected by a compliant component which has stiffness k_2. Piezoelectric accelerometers are placed on each body to measure its acceleration. Between the voice coil actuator and body m_1, a piezoelectric force sensor is placed. A wire flexure is mounted between force sensor and coil to guarantee that only forces in the axial direction of the mount are transmitted onto body m_1. A shaker is used to excite the floor body. An additional voice coil actuator (without any guidance) is mounted on body m_1 to excite it with a direct force F_d. The voltage applied to this actuator is proportional to this force F_d within a bandwidth up to 1 kHz. The values for each mass and stiffness are already given in Table 3.1.

The linear guidances introduce additional parasitic stiffness paths. Therefore, the flexible body model of Fig. 3.2(a) is modified slightly such that the parasitic stiffness is no longer modeled by a spring between body m_1 and the floor, but by two springs k_p, connected at one side to a payload body (m_1 or m_2) and on the other side to the supporting frame, see Fig. 4.2(a). The value of the stiffness of each spring is $k_p = 4\,050$ N/m. In [55] it is shown that with this type of parasitic stiffness paths, the transmissibility and deformation transmissibility for force feedback differ at low frequencies from those presented in this thesis. This will also be illustrated in subsection 4.4.2 describing the experimental results for force feedback.

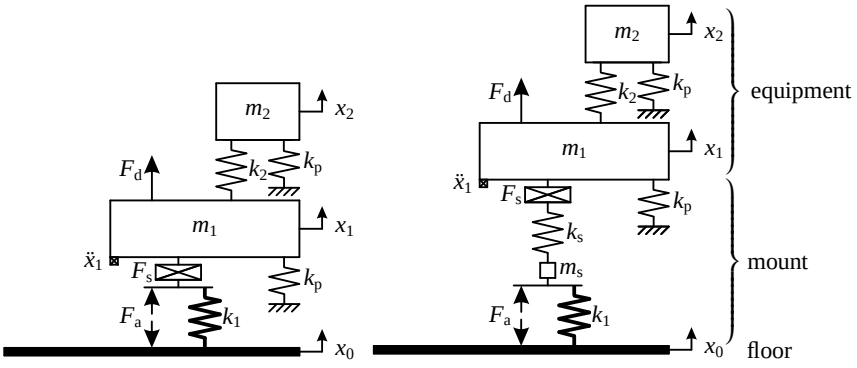

Fig. 4.2: Model of the vibration isolator in which the equipment is represented by a flexible body and: (a) the parasitic springs that represent the linear guidance of the payload bodies are included; (b) the dynamics due to the wire flexure is included as well.

4.2 Dynamics of the experimental setup

The flexible body model of the vibration isolator of Fig. 4.2(a) describes only the structural dynamics of the experimental setup. However, for the experimental setup also the actuator dynamics and the dynamics of the charge amplifiers for the accelerometer and force sensor are important. These include a first-order low-pass filter with a corner frequency of 390 Hz, due to the impedance of the voice coil actuator (its power amplifier is operated in velocity mode, not in current mode, to have a lower noise level), and a bandpass filter in the charge amplifiers with corner frequencies of 0.1 Hz and 3 kHz.

Fig. 4.3(a) shows the plant transfer function $G_{\ddot{x}_1 F_a}(s) = \ddot{X}_1(s)/F_a(s)$ of Eq. (3.17) corresponding to the structural dynamic model of Fig. 3.2(a) (dotted gray line) next to the plant transfer function corresponding to the electromechanical model describing both the structural dynamics and the actuator and amplifier dynamics (solid gray line). In addition to the structural dynamics of the flexible body model of Fig. 4.2(b), also the dynamics of the wire flexure contributes to the total dynamics of the electromechanical model. This wire flexure is mounted between the force sensor and the coil and can be modeled by a spring k_s between payload body m_1 and body m_s representing the mass of the coil, see Fig. 4.2(b). An additional mode due to the dynamics of the wire flexure appears, which resonance frequency of 1.3 kHz can be approximated by

$$\omega_s \approx \sqrt{\frac{k_s}{m_s}}, \text{ with } k_1 \ll k_s, \tag{4.1}$$

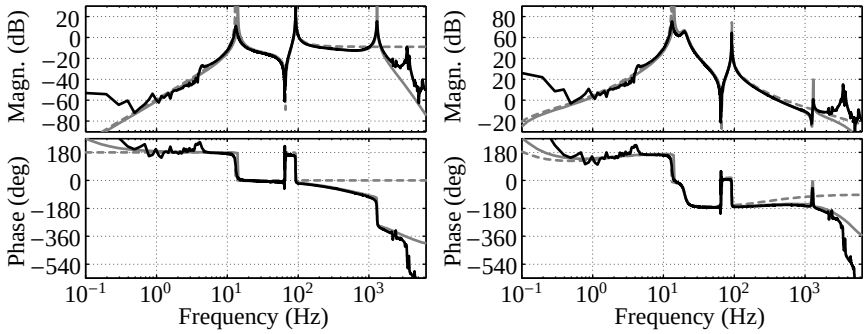

(a) Plant transfer functions. (b) Loop gains.

Fig. 4.3: (a) Plant transfer functions from actuator force to accelerometer signal for the structural dynamic model ($G_{\ddot{x}_1 F_a}(s)$ of Eq. (3.17) ----), for the electromechanical model including wire flexure dynamics (——), and for the FRF estimate (——). (b) Loop gains for the structural dynamic model with controller $H_r(s)$ of Eq. (3.19) ($L_{r,\ddot{x}_1}(s)$ of Eq. (3.20) ----), the electromechanical model with controller $H_r(s)$ multiplied by the filter $F_{ext}(s)$ of Eq. (4.2) (——), the FRF estimate with $H_r(s)$ multiplied by $F_{ext}(s)$ (——).

where the values of k_s and m_s are estimated as k_s =8·10^6 N/m and m_s = 0.125 kg. The wire flexure dynamics results in a loss of collocation between actuator and sensors, as is observed by the 180° phase drop in Fig. 4.3(a) at this resonance frequency. This may lead to instability of the closed loop system, due to crossing of the −180° phase line at the frequency where the magnitude of the loop gain is larger than one.

To prevent instability of the closed loop system, the controllers presented in chapter 3 need to be extended with a loop shaping filter. It consists of a skew notch filter to compensate for the resonance frequency and an additional zero ω_3 to compensate for the first-order low-pass filter formed by the impedance of the voice coil actuator. It is expressed as

$$F_{ext}(s) = \frac{s^2 + 2\zeta_1\omega_1 s + \omega_1^2}{s^2 + 2\zeta_2\omega_2 s + \omega_2^2}\frac{\omega_2^2}{\omega_1^2}\frac{s + \omega_3}{\omega_3}, \tag{4.2}$$

where $\omega_i = 2\pi f_i$ with f_1 = 1.25 kHz, f_2 = 7.5 kHz, and f_3 = 390 Hz, ζ_1 = 0.01, and ζ_2 = 0.7. Although the filter of Eq. (4.2) itself is non-proper, the resulting controllers to which this filter is added are proper, since all controllers are strictly proper. The second-order polynomial in the numerator of the skew notch filter of Eq. (4.2) causes a virtual anti-resonance in the loop gain such that there is a 180° phase lift before the 180° phase drop at 1.3 kHz. The denominator acts as a second-order low-pass filter to lower the control

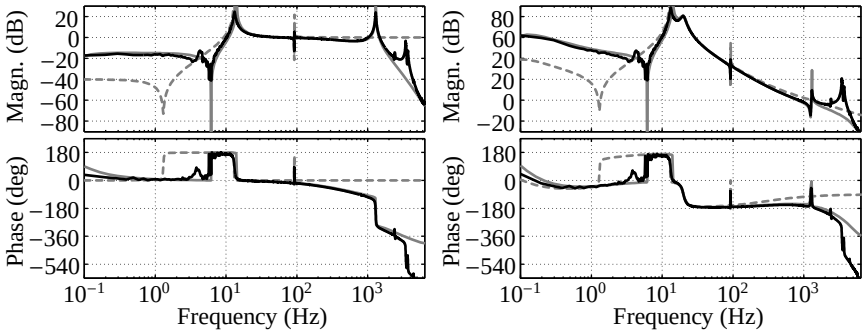

(a) Plant transfer functions. (b) Loop gains.

Fig. 4.4: (a) Plant transfer functions from actuator force to force sensor signal for the structural dynamic model ($G_{F_sF_a}(s)$ of Eq. (3.23) ----), for the electromechanical model including wire flexure dynamics (——), and for the FRF estimate (——). (b) Loop gains for the structural dynamic model with controller $1/(m_1 + m_2)H_r(s)$ ($L_{r,F_s}(s)$ of Eq. (3.22) ----), the electromechanical model with $1/(m_1 + m_2)H_r(s)$ multiplied by the filter $F_{ext}(s)$ of Eq. (4.2) (——), the FRF estimate with $1/(m_1 + m_2)H_r(s)$ multiplied by $F_{ext}(s)$ (——).

gain at high frequencies. So, the controllers used for the experiments are the controllers presented in chapter 3 multiplied by the filter of Eq. (4.2). The controllers are discretized and then implemented on a digital signal processor. The discrete controllers are running at a sample frequency of 12.8 kHz.

Fig. 4.3(b) shows the loop gain $L_{r,\ddot{x}_1}(s)$ of Eq. (3.20) for the structural dynamic model with controller $H_r(s)$ of Eq. (3.19) (gray dotted line) and the loop gain for electromechanical model with controller $H_r(s)$ multiplied by filter $F_{ext}(s)$ of Eq. (4.2) (gray solid line). It is visible that due to the bandpass filter of the charge amplifier there is less phase margin at the low and high crossover frequencies as expected based on the structural dynamic model of Fig. 3.2. Due to the filter of Eq. (4.2), the resonance peak at 1.3 kHz will not destabilize the system, because the crossing of the $-180°$ phase line is at a frequency where the magnitude of the loop gain is smaller than one.

An estimate of the frequency response function (FRF) between actuator force and accelerometer signal is also shown in Fig. 4.3(a) (black solid line). The FRF estimate is obtained by exciting the experimental setup with a random actuator force which is measured together with the resulting acceleration response. From this data, the FRF estimate is calculated as in [34]. The FRF estimate is resembled well by the electromechanical model in-between 3 Hz and 2 kHz, although the suspension mode in the FRF estimate is better damped than in the electromechanical model. The suspension frequency of the FRF es-

timate is a little lower than for the electromechanical model. This is because in the electromechanical model the floor motion is assumed as a rheonomic input, whereas in the experimental setup of Fig. 4.1 the actuator force is also acting on the floor. Therefore, the dynamics of the floor contribute to the dynamics of the experimental setup. Since the floor mass is 21.2 kg, which is much heavier than the total payload mass of 5.4 kg, the contribution of the floor dynamics is very low. Above 2 kHz additional high-frequency dynamics is present. Below 3 Hz, the FRF estimate is unreliable due to sensor noise. The loop gain formed by the FRF estimate with controller $H_{\mathrm{r}}(s)$ of Eq. (3.19) multiplied by filter $F_{\mathrm{ext}}(s)$ of Eq. (4.2) is shown in Fig. 4.3(b) (black solid line). It matches well with the loop gain for the electromechanical model.

The transfer functions from actuator force to force sensor signal show similar behavior. Fig. 4.4(a) shows transfer function $G_{F_{\mathrm{s}}F_{\mathrm{a}}}(s) = F_{\mathrm{s}}(s)/F_{\mathrm{a}}(s)$ of Eq. (3.23) corresponding to the structural dynamic model of Fig. 3.2(a) (dotted gray line) next to the transfer function corresponding to the electromechanical model which describes both the structural dynamics and the actuator and amplifier dynamics (solid gray line). The effect of increasing the value of the parasitic stiffness k_{p} from 320 N/m to two times 4 050 N/m is visible, because the anti-resonance frequency of the loop gain for the model of Fig. 4.2(a) is 6.2 Hz compared to 1.3 Hz for the flexible body model of Fig. 3.2(a). The FRF estimate of this transfer function is shown as well (black solid line). The corresponding loop gains obtained with controller $1/(m_1 + m_2)H_{\mathrm{r}}(s)$ of Eq. (3.19) are shown in Fig. 4.4(b).

4.3 Performance measures

During the experiments to determine the transmissibilities, the floor body is excited by the shaker such that the velocity spectrum of body m_0 is 25 μm/s RMS per one-third octave in-between 0.1 and 100 Hz. This is more or less comparable to VC-B curve excitation as defined by [16], see also Fig. 2.1(a). In-between 100 and 800 Hz, the acceleration spectrum of body m_0 is about 16 mm/s^2. This high excitation level is used to sufficiently excite the floor and payload bodies, such that the estimates of the performance transfer functions are not contaminated (too much) by sensor noise of the accelerometers. The realized acceleration level of the floor body is much higher than the expected acceleration level of a floor at a site. Therefore, it is not useful to calculate the RMS values of the payloads' acceleration levels as the ultimate performance measures. So, in this chapter the four performance transfer functions are the

only used performance measures. In chapter 8 a more realistic excitation level, comparable to a VC-D curve, is used for the control experiments with the six-axes vibration isolator.

The acceleration levels of each body m_i are measured and afterwards the power spectral densities (PSDs) $P_{\ddot{x}_i\ddot{x}_i}(f)$ and cross power spectral densities (CPSDs) $P_{\ddot{x}_i\ddot{x}_0}(f)$ are calculated. Here f is the frequency in Hz. The transmissibility is calculated as the CSD between payload body m_1 and floor body m_0 accelerations divided by the PSD of the floor body m_0 acceleration. Unfortunately, there is no sensor available to measure Δx directly, so the deformation transmissibility needs to be calculated in a different way. This is done using Eq. (2.1) which states that $\ddot{x}_2$ is related to Δx by a factor $k_2/m_2 = \omega^2_{\mathrm{a},\ddot{x}_1}$. So, the transmissibility and deformation transmissibility can be calculated as:

$$\hat{T}(f) = \frac{P_{\ddot{x}_1\ddot{x}_0}(f)}{P_{\ddot{x}_0\ddot{x}_0}(f)}, \tag{4.3}$$

$$\hat{T}_{\mathrm{d}}(f) = \frac{P_{\ddot{x}_2\ddot{x}_0}(f)}{P_{\ddot{x}_0\ddot{x}_0}(f)} \frac{1}{\omega^2_{\mathrm{a},\ddot{x}_1}}. \tag{4.4}$$

The relation between $\ddot{x}_2$ and Δx is only valid for the model of Fig. 3.2(a). In practical applications this approximation is not correct. In multi-axes vibration isolators, the transfer function estimates $P_{\ddot{x}_2\ddot{x}_0}(f)/P_{\ddot{x}_0\ddot{x}_0}(f)$ calculated from the measured accelerations on the floor and flexible body m_2, can be used directly. The height of a resonance peak can be used as a measure for the amount of damping added to the corresponding internal mode.

To determine the responses due to disturbance force F_{d}, body m_1 is excited using the additional voice coil actuator, while floor body m_0 has been fixated to the supporting frame of the experimental setup to reduce the influence of the floor dynamics on the responses due to F_{d}. A random signal is generated to apply a disturbance force of 0.3 N RMS. The compliance and deformability are estimated as:

$$\hat{C}(f) = \frac{P_{x_1F_{\mathrm{d}}}(f)}{P_{F_{\mathrm{d}}F_{\mathrm{d}}}(f)}, \tag{4.5}$$

$$\hat{D}(f) = \frac{P_{\ddot{x}_2F_{\mathrm{d}}}(f)}{P_{F_{\mathrm{d}}F_{\mathrm{d}}}(f)} \frac{1}{\omega^2_{\mathrm{a},\ddot{x}_1}}. \tag{4.6}$$

Here $P_{x_1F_{\mathrm{d}}}(f)$ is calculated by dividing $P_{\ddot{x}_1F_{\mathrm{d}}}(f)$ with $(2\pi f)^2$:

$$P_{x_1F_{\mathrm{d}}}(f) = \frac{P_{\ddot{x}_1F_{\mathrm{d}}}(f)}{(2\pi f)^2}. \tag{4.7}$$

which is equivalent to integrating $P_{\ddot{x}_1F_{\mathrm{d}}}(f)$ twice with respect to time.

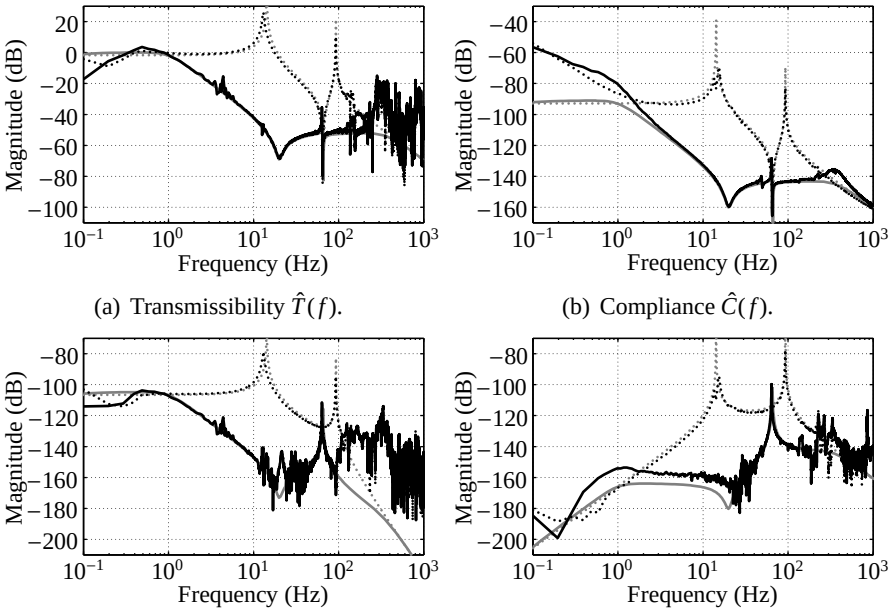

(a) Transmissibility $\hat{T}(f)$.

(b) Compliance $\hat{C}(f)$.

(c) Deformation transmissibility $\hat{T}_{\mathrm{d}}(f)$.

(d) Deformability $\hat{D}(f)$.

Fig. 4.5: Performance transfer functions in model and experiments: (a) transmissibility $\hat{T}(f)$; (b) compliance $\hat{C}(f)$; (c) deformation transmissibility $\hat{T}_{\mathrm{d}}(f)$; (d) deformability $\hat{D}(f)$.
- model: open loop hard mount
- model: closed loop hard mount using acceleration feedback
- experiment: open loop hard mount
- experiment: closed loop hard mount using acceleration feedback

4.4 Experimental results

The results of the experiments are presented in this section. The results of acceleration feedback using controller $H_{\mathrm{r}}(s)$ of Eq. (3.19) and force feedback using controller $1/(m_1 + m_2)H_{\mathrm{r}}(s)$ are shown first. The effect of the parasitic stiffness path introduced by the linear guidance of the payload bodies is also discussed. The results of sensor fusion using the filters of Eq. (3.28) are examined next. Finally, the results of two-sensor control are shown.

4.4.1 Acceleration feedback

Figs. 4.5(a)–(d) show the results of the acceleration feedback experiments. For reference, the open and closed loop response of the model are shown (in gray) as well. In Fig. 4.7(a) and (c) it can be seen that for the responses due to

floor motion, the experimental results coincide with the model results in the frequency range in-between 1 and 100 Hz. Below 1 Hz and above 250 Hz, the measured acceleration signals consist also of the contributions of actuator noise and sensor noise since the actual motion levels of the payload bodies are very small as well as vibrations transmitted onto the floor and payload bodies by means of the linear guidance. Therefore, above this frequency, the estimates of the transfer functions are not reliable. This can also be concluded from the corresponding coherence function which is displayed in Fig. C.1(a) of appendix C. Below 1 Hz and above 250 Hz, the coherence is much smaller than one. The peaks at 300 and 900 Hz in Figs. 4.5(a) and (c) may also be caused by local modes of the active hard mount. These are due to the in-plane stiffness of the membranes that are used in the active hard mount as a linear guidance of the voice coil as well as to provide for the suspension stiffness.

Figs. 4.5(c) and (d) show that the internal resonance peak of the closed loop system remains poorly damped. Fig. 4.5(b) shows that below 4 Hz the compliance cannot be estimated well, since the accelerometer noise dominates the payload's motion level at low frequencies and this noise is amplified because the compliance is obtained by filtering with $1/(2\pi f)^2$. The experimentally determined deformability differs from the modeled one in Fig. 4.5(d) for frequencies below 30 Hz. The difference is thought to be caused by a poor phase margin at low frequencies due to the second-order high-pass filters in the controller and charge amplifier. A poor phase margin also results in some amplification at the low and high crossover frequencies in the plot of the compliance of Fig. 4.5(b). Above 4 Hz for the compliance and above 30 Hz for the deformability, there is good agreement between the experimental and modeling results.

4.4.2 Force feedback

The experimental results of force feedback are shown in Figs. 4.6(a)–(d). Next to the modeling results obtained with the flexible body model of Fig. 3.2(a) (gray dashed lines), the modeling results obtained with the flexible body model of Fig. 4.2(a) are shown (gray solid lines). In the latter model the parasitic stiffness is modeled differently computed to the model of Fig. 3.2(a). Since for the model of Fig. 4.2(a) the value of the total parasitic stiffness is significantly higher ($2 \times 4\,050$ N/m instead of 360 N/m), the suspension frequency is much higher, see also Eq. (3.10). At low frequencies, the modeling results of the transmissibility and deformation transmissibility differ significantly. Below 4 Hz the transmissibility is even below one. This is due to the parasitic stiffness

path formed by the linear guidance of the payload bodies m_1 and m_2, see also [55]. This seems a good result since realizing a low transmissibility is one of the performance objectives. However, this type of parasitic stiffness path is usually not found in practical applications of vibration isolators, it is only present in the experimental setup of Fig. 4.1. Therefore, the modeling results obtained with the model of Fig. 3.2(a) are a better representation for the effect of force feedback on the performance transfer functions than the modeling results obtained with the model of Fig. 4.2(a).

It is visible that the experimental results match well with the modeling results obtained with the model of Fig. 4.2(a), in particular for the responses due to the direct disturbance force. However, it appears that the force sensor is not able to measure the vibrations of the setup's supporting frame that are transmitted by the linear guidance of the floor and payload bodies of the setup. As a result, the controller is not able to compensate for these vibrations, which results in some resonance peaks. This is observed in the responses due to floor vibrations which show some resonance peaks in-between 10 and 50 Hz, see Figs. 4.6(a) and (c). The coherence at the frequencies of these resonances is very low, see Figs. C.2(a) and (c) of appendix C.

4.4.3 Sensor fusion

Figs. 4.7(a)–(d) show the results of the sensor fusion experiments. The results match well with the modeling results. In Figs. 4.7(c) and (d) it is visible that the internal mode is well damped, since there are no peaks in the deformation transmissibility and deformability. The dip at 4.5 Hz and the peaks at 13 and 20 Hz in these plots are due to the dynamics of the supporting frame of the experimental setup. At these frequencies the correlation between floor and payload acceleration is small so the estimate is poor, see also Figs. C.3(a) and (c) of appendix C. The experimentally determined deformability differs from the modeled one at frequencies below 3 Hz. This is also because of a poor phase margin at the low crossover frequency. The experimental results proof that the sensor fusion strategy can be implemented real-time and that the desired goals are met.

4.4.4 Two-sensor control

Figs. 4.8(a)–(d) show the results of the two-sensor control experiments. The results match well with the modeling results using $k_f = 25$ for the force feedback controller gain in Eq. (3.38). The same remarks as for sensor fusion also apply for two-sensor control. In Figs. 4.8(c) and (d) it is visible that the peak

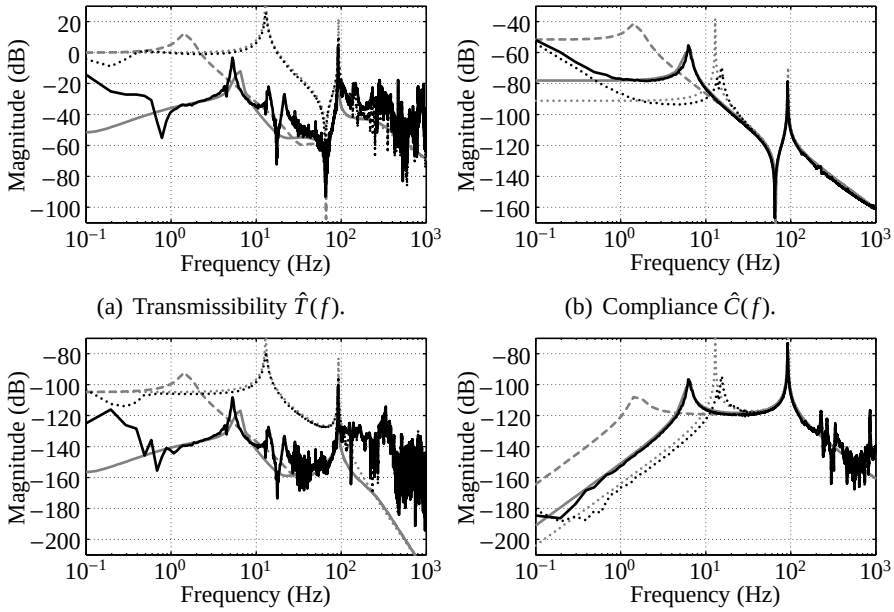

(a) Transmissibility $\hat{T}(f)$.

(b) Compliance $\hat{C}(f)$.

(c) Deformation transmissibility $\hat{T}_{\mathrm{d}}(f)$.

(d) Deformability $\hat{D}(f)$.

Fig. 4.6: Performance transfer functions in model and experiments: (a) transmissibility $\hat{T}(f)$; (b) compliance $\hat{C}(f)$; (c) deformation transmissibility $\hat{T}_{\mathrm{d}}(f)$; (d) deformability $\hat{D}(f)$.
- model of Fig. 3.2(a): open loop hard mount
- model of Fig. 3.2(a): closed loop hard mount using force feedback
- model of Fig. 4.2(a): closed loop hard mount using force feedback
- experiment: open loop hard mount
- experiment: closed loop hard mount using force feedback

at the frequency of the internal mode is a little higher than for sensor fusion, while Fig. 4.8(b) shows that the mid-frequency compliance is a little lower. The experimental results proof that the proposed two-sensor control strategy can be implemented real-time and that the desired goals are met.

4.5 Discussion

Precision equipment is usually mounted on very quiet floors, which motion levels are well below the VC-B curve. As a consequence, sensor and actuator noise may have a significant contribution to the overall performance of the vibration isolator. Ultra-low noise accelerometers have a limited usable bandwidth of <250 Hz [33]. However, this is no problem for the proposed sensor

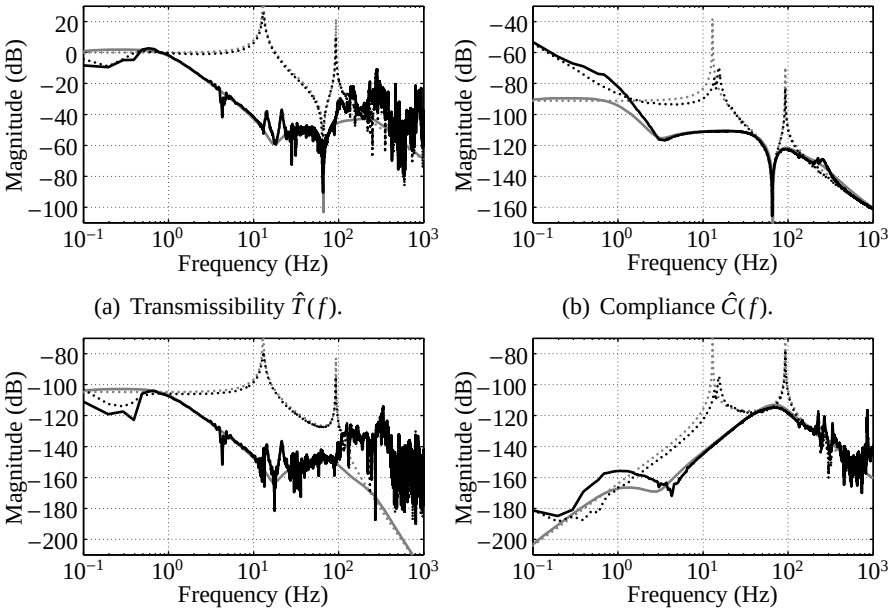

(a) Transmissibility $\hat{T}(f)$.

(b) Compliance $\hat{C}(f)$.

(c) Deformation transmissibility $\hat{T}_{\mathrm{d}}(f)$.

(d) Deformability $\hat{D}(f)$.

Fig. 4.7: Performance transfer functions in model and experiments: (a) transmissibility $\hat{T}(f)$; (b) compliance $\hat{C}(f)$; (c) deformation transmissibility $\hat{T}_{\mathrm{d}}(f)$; (d) deformability $\hat{D}(f)$.
- model: open loop hard mount
- model: closed loop hard mount using sensor fusion and high-pass filter
- experiment: open loop hard mount
- experiment: closed loop hard mount using sensor fusion and high-pass filter

fusion strategy, since the accelerometer signal is used only at low frequencies for control. Because force sensors have in general a much lower noise level than accelerometers [45], the high frequency performance of the sensor fusion strategy is not limited by the force sensor. Unfortunately, the high-frequency performance of the experimental setup of the one-axis vibration isolator cannot be measured well, because of the small motion levels of the payload bodies. This results in unreliable high-frequency estimates of the performance transfer functions as is shown in Figs. 4.5–4.8.

Instead of using an accelerometer a geophone can be used as well, since both sensors are measuring absolute motion. For the geophone, the feedback controller has to provide for a differentiating filter as well.

In chapter 3 it is already explained that force sensor are not able to compensate for the equipment's vibrations that are transmitted by means of parasitic

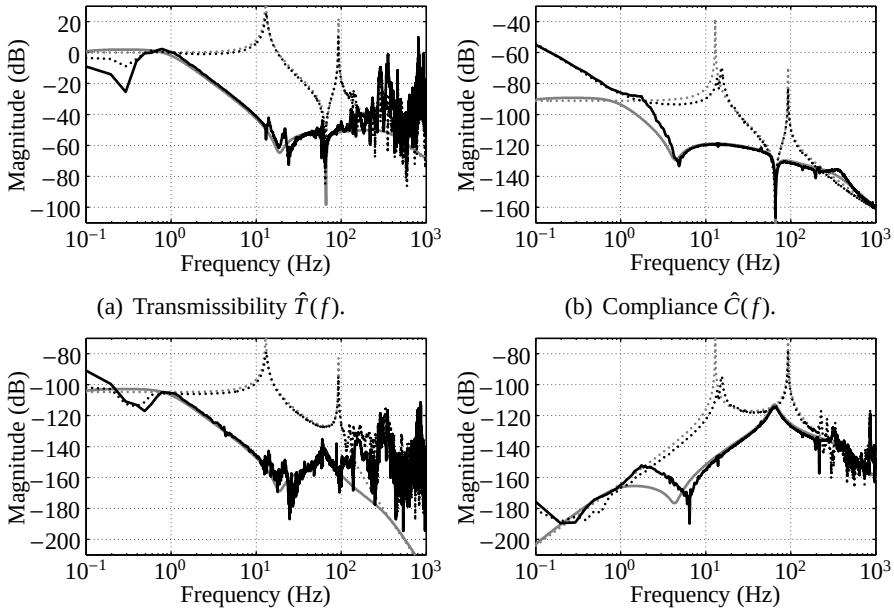

(a) Transmissibility $\hat{T}(f)$.

(b) Compliance $\hat{C}(f)$.

(c) Deformation transmissibility $\hat{T}_{\mathrm{d}}(f)$.

(d) Deformability $\hat{D}(f)$.

Fig. 4.8: Performance transfer functions in model and experiments: (a) transmissibility $\hat{T}(f)$; (b) compliance $\hat{C}(f)$; (c) deformation transmissibility $\hat{T}_{\mathrm{d}}(f)$; (d) deformability $\hat{D}(f)$.
model: open loop hard mount
model: closed loop hard mount using two-sensor control
experiment: open loop hard mount
experiment: closed loop hard mount using two-sensor control

stiffness paths. This is made visible in this chapter by the experimental results for force feedback, sensor fusion, and two-sensor control. The peaks in-between 10 and 50 Hz in the transmissibilities and deformation transmissibilities of Figs. 4.6–4.8 are due to motion transmitted by the linear guidance of the floor and payload bodies of the experimental setup which is not measured by the force sensor. Therefore, it is important to aim for a low value of the parasitic stiffness in the mount of the vibration isolator.

In section 2.5 it is stated that industrial vibration isolators (from suppliers such as Halcyonics, Minus-K, and TMC [18, 39, 52]) usually achieve −30 to −40 dB/decade roll-off above their suspension frequencies that are typically about 1 Hz. At high frequencies, the lower transmissibility limit ranges from −35 to −60 dB at best. Figs. 4.5(a)–4.8(a) show that the proposed strategies are capable of realizing the same performance of the transmissibility with a

low transmissibility limit of less than −40 dB at high frequencies. Except for the TMC STACIS™ [52] all other systems are soft mounts, which means that the proposed sensor fusion and two-control strategies will outperform these systems regarding the compliance, see Fig. 3.6(b). None of the industrial systems are capable of increasing the damping of internal modes of the suspended equipment, which is achieved in this thesis.

4.6 Conclusions

The control strategies presented in chapter 3 are successfully implemented on an experimental setup of a one-axis active hard mount vibration isolator. All three performance objectives for active hard mount vibration isolators stated in section 2.5 can be realized simultaneously for sensor fusion and two-sensor control: not only the transmissibility of floor vibrations is made comparable to that of an ideal soft mount, the susceptibility to direct disturbance forces is decreased, the suspension stiffness is increased, and the damping of the internal mode is significantly increased.

The experimental results match well with the modeling results in the frequency range from 1 to 250 Hz. Although, sensor and actuator noise make the estimates of the performance transfer functions less reliable below 1 Hz and above 250 Hz. It is observed that for all control strategies that use a force feedback controller, it is not possible to compensate for vibrations transmitted onto the suspended payload by means of parasitic stiffness paths. This results in a higher transmissibility and deformation transmissibility at some frequencies.

An important observation is that for a successful implementation of the control strategies, not only the structural dynamics of the vibration isolator has to be taken into account but also the dynamics of the actuator and charge amplifiers of the accelerometer and force sensor. In addition, the relevant high-frequency dynamics of the active hard mount is important. For the experimental setup, this dynamics is due to the wire flexure between the voice coil and force sensor, which results in a loss of collocation between actuator and sensors and can destabilize the closed loop system. Therefore, a loop shaping filter needs to be added to the controllers in chapter 3 to prevent instability of the closed loop system.

Design and modeling of a six-axes vibration isolator

Chapter 5

The design of a demonstrator setup of a six axes active hard mount vibration isolator is presented. A rigid body model describing the suspension dynamics of the isolator is derived. This model is used to get insight into how the six suspension modes depend on the mass and inertia properties of the payload, the stiffness of the suspension, and several other design parameters. For a better prediction of the isolator's performance including the effect of the payload's flexibilities, a flexible body model is presented. From that model, a reduced order model is derived. This model represents a more accurate representation of the suspension dynamics than the rigid body model.

5.1 Design

In three-dimensional space, any rigid body has six degrees of freedom (DOFs) with respect to another rigid body. To fully isolate two rigid bodies with respect to each other (in fact to isolate the suspended payload from the floor) six judiciously placed one-axis active vibration isolators are needed, each constraining one DOF. In this way, the suspension that connects the suspended payload to the floor is realized with an *exact-constrained* design [49]. This means that each DOF is constrained only one time. In an exact-constrained design, internal stresses and deformations of the equipment due to thermal loads, deformations of the suspension, and geometry variations due to part and assembly tolerances are minimized. To realize an exact-constrained design, each of the one-axis vibration isolators is designed to be relatively stiff in its axial direction and very compliant in the other directions. Several architectures for a generic six-axes isolator are possible, such as that of a standard Gough-Stewart platform [19, 47, 51] or that with three horizontally placed and three

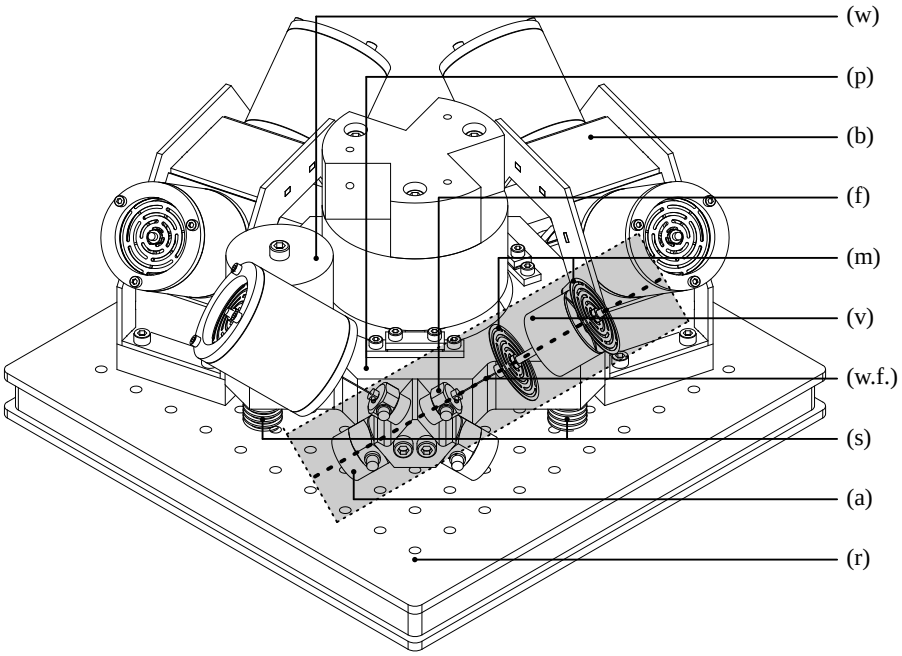

Fig. 5.1: Section view of the six-axes active vibration isolator with weight body (w), payload (p), bracket (b), force sensor (f), membranes (m), voice coil actuator (v), wire flexure (w.f.), pre-loaded low-stiffness springs (s), accelerometer (a), and rigid floor plate (r).

vertically placed isolators [5, 20, 61].

The six-axes vibration isolator presented in this chapter consists of six legs, arranged in three pairs of two, that suspend a payload (p) of about 10.9 kg. The payload is the consists of a rigid frame body and two flexible payload bodies. It mimics the precision equipment. Although the six legs are not mutually orthogonal as in a standard Gough-Stewart platform [51], it's configuration is still approximated. Fig. 5.1 shows the design of the six-axes vibration isolator. The gray box in Fig. 5.1 shows the most important components of a leg.

Each leg contains a voice coil actuator (v) which can provide a force in the axial direction of the leg. A force sensor (f) is placed between each actuator and the payload to measure the force in the leg and an accelerometer (a) is placed at the rigid frame body of the payload to measure it's acceleration. Both sensors are co-aligned with the actuator. The axial stiffness of the leg is due to two flexible membranes (m) that are used as a linear guidance for the voice coil. The six legs are connected to a rigid floor plate (r) by means of three brackets (b) (only two brackets are visible). The floor plate can be

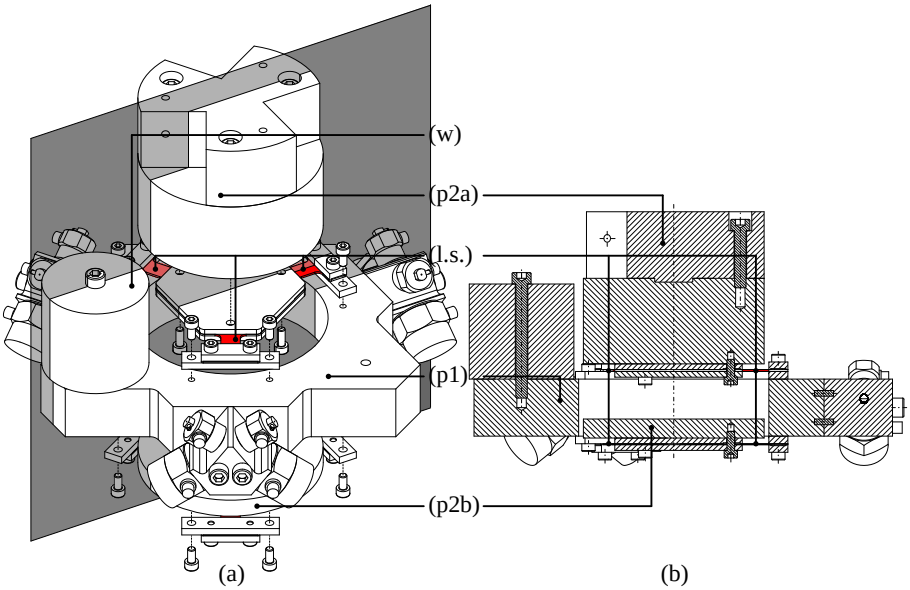

Fig. 5.2: (a) Exploded view and (b) section view of the payload with weight body (w), large flexible payload body (p2a), leaf springs (l.s.) (in red), rigid frame body (p1), and small flexible payload body (p2b).

excited using piezoelectric actuators, see chapter 8.

The maximum force of the used voice coil actuators is 10 N. To compensate for VC-D curve floor vibration levels, the six actuators together have to deliver a force equal to the payload's mass times a VC-D curve RMS acceleration level, which is about 4 mm/s^2 RMS (see section 2.1.2). This means an RMS force of only 40 mN, which is very small compared to the maximum actuator force. So, the actuator is capable of providing the required force level. The actuators are not used to compensate for the payload's sagging due to gravity. Instead, three preloaded low-stiffness springs (s) are used for gravity compensation and for preventing large deflections of the membranes and wire flexures. The preload is such that the gravitational force is compensated almost completely.

The payload consists of three bodies, see Fig. 5.2. The six legs are connected to a rigid frame body (p1) that weighs about 6.3 kg (including all sensors). A large flexible payload body (p2a) of 3.9 kg is connected to rigid frame body (p1) by means of three leaf springs (l.s.) (in red). In addition a small flexible payload body (p2b) of 0.7 kg is connected to rigid frame body (p1) by another three leaf springs. Due to these flexibilities, internal modes of the

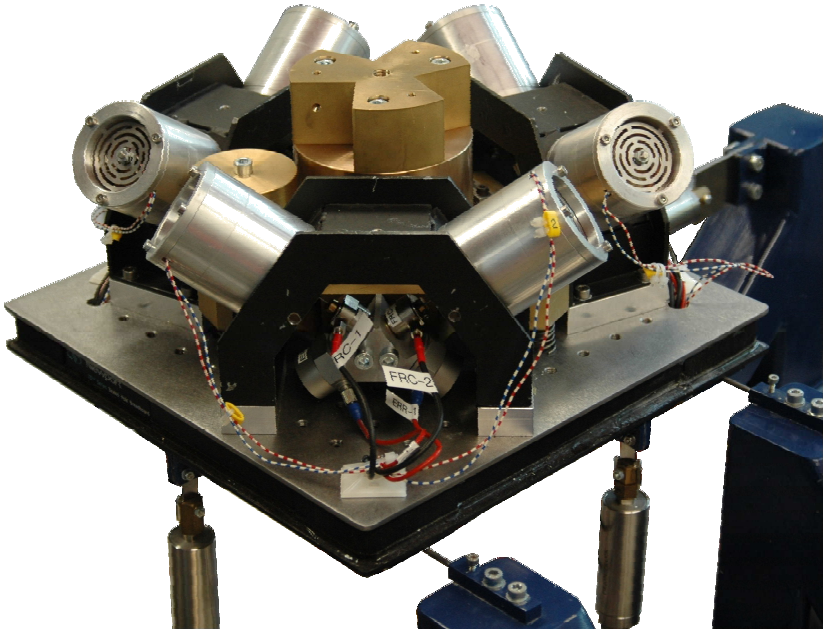

Fig. 5.3: The demonstrator setup of the six-axes active vibration isolator.

payload with resonance frequencies ranging from 75 to 360 Hz are obtained. In this way the internal modes of a precision equipment are mimicked. An additional weight body (w) is placed at one side of rigid frame body (p1) to break its symmetry. Although industrial vibration isolators used for suspending precision equipment are often designed to be symmetric, it is not always possible to realize this. Therefore, the weight is used to mimic an asymmetric payload.

Ideally, the bending and torsional stiffness of each leg should be zero, since the isolator's performance will be limited by the presence of this parasitic stiffness, see [19, 47] and chapter 3. Therefore, a wire flexure (w.f.) is added between each voice coil and the suspended payload. The wire flexure has a very high axial stiffness and at the same time a very low bending and torsional stiffness. Collocation between the voice coil actuator and both sensors is obtained up to the resonance frequency that is due to the wire flexure dynamics. Similar as for the wire flexure in the experimental setup of the one-axis vibration isolator, this resonance frequency is approximated as the square root of the axial stiffness of the wire flexure divided by the mass of the coil, see Eq. (4.1).

The six-axes active hard mount vibration isolator is designed to have six

suspension modes with resonance frequencies of about 10 Hz. More details about the design can be found in [21,44]. The realized demonstrator setup that is available in the laboratory of the department of Mechanical Automation and Mechatronics at the University of Twente is shown in Fig. 5.3.

5.2 Rigid body model

In this section a rigid body model is derived that describes the suspension dynamics of the six-axes vibration isolator. The model is used to understand how the six suspension modes are determined by the mass and stiffness properties of the isolator. In this section it is assumed that all legs are *ideal mounts* having the same axial stiffness and zero bending and torsional stiffness. Furthermore, it is assumed that all DOFs due to the internal flexibilities of the payload are negligible, so the payload is considered rigid for now. The stiffness and preload of the low-stiffness springs to compensate gravity, and the gravitational force itself are neglected. Finally, the payload is considered to be axisymmetric, so the additional weight body (w) in Fig. 5.2 is omitted.

At the payload a coordinate frame is located with the location and orientation as shown in Fig. 5.4. The origin of the frame is located in the elastic center (e.c.) of the payload. The elastic center is the point on the payload where a force exerted on that point in a certain direction results in a pure displacement of that point in the same direction. The payload motion can be expressed in the position and orientation coordinates $\boldsymbol{x}_{\text{ref}} = (x, y, z, \theta_x, \theta_y, \theta_z)^T$.

The stiffness matrix of the vibration isolator can be derived by writing the strain energy stored in the legs in terms of $\boldsymbol{x}_{\text{ref}}$ [45]. With the axial stiffness k of the legs, the strain energy is $V = \frac{1}{2} k \boldsymbol{q}^{\mathrm{T}} \boldsymbol{q}$, where $\boldsymbol{q} = (q_1, \ldots, q_6)^{\mathrm{T}}$ is the vector of leg extensions. A matrix $\mathbf{R}$ is defined that relates leg extensions $\boldsymbol{q}$ to coordinates $\boldsymbol{x}_{\text{ref}}$, such that $\boldsymbol{x}_{\text{ref}} = \mathbf{R}\boldsymbol{q}$. Matrix $\mathbf{R}$ depends on the configuration of the six-axes vibration isolator. For the design described in this thesis, the inverse of $\mathbf{R}$ is

$$\mathbf{R}^{-1} = \begin{bmatrix} -c\beta s\alpha_1 & c\beta c\alpha_1 & -s\beta & rs\beta s\alpha_1 & -rs\beta c\alpha_1 & rc\beta \\ c\beta s\alpha_1 & -c\beta c\alpha_1 & -s\beta & rs\beta s\alpha_1 & -rs\beta c\alpha_1 & -rc\beta \\ -c\beta s\alpha_2 & c\beta c\alpha_2 & -s\beta & rs\beta s\alpha_2 & -rs\beta c\alpha_2 & rc\beta \\ c\beta s\alpha_2 & -c\beta c\alpha_2 & -s\beta & rs\beta s\alpha_2 & -rs\beta c\alpha_2 & -rc\beta \\ -c\beta s\alpha_3 & c\beta c\alpha_3 & -s\beta & rs\beta s\alpha_3 & -rs\beta c\alpha_3 & rc\beta \\ c\beta s\alpha_3 & -c\beta c\alpha_3 & -s\beta & rs\beta s\alpha_3 & -rs\beta c\alpha_3 & -rc\beta \end{bmatrix}, \tag{5.1}$$

where α_1, α_2, and α_3 are the angles between the three leg pairs and the x-axis, $c\beta = \cos(\beta)$, $s\beta = \sin(\beta)$, etc. Design parameter β is the angle between the

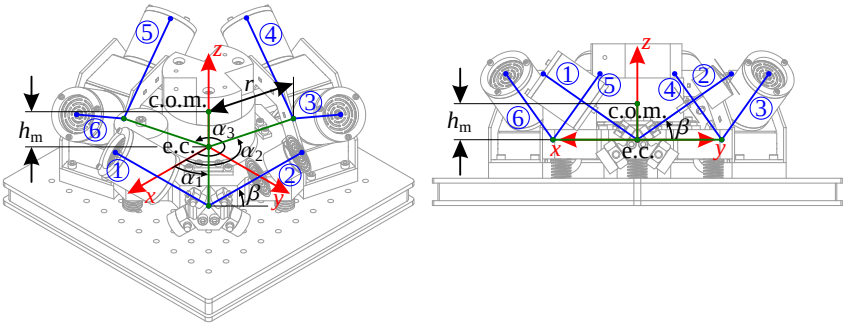

(a) Trimetric view. (b) Front view.

Fig. 5.4: Coordinate frame (x, y, z) located in the elastic center (e.c.). The six active hard mounts ①–⑥ are placed at an angle β with the horizontal plane.

axial direction of a leg and the horizontal plane, and design parameter r is the distance between the vertical axis of symmetry and the point where a leg is attached to the payload. In this thesis $\alpha_1 = \frac{1}{4}\pi$, $\alpha_2 = \frac{2}{3}\pi + \frac{1}{4}\pi$, and $\alpha_3 = \frac{4}{3}\pi + \frac{1}{4}\pi$ (see Fig. 5.4(a)). Using $\boldsymbol{q} = \mathbf{R}^{-1}\boldsymbol{x}_{\text{ref}}$ gives

$$V = \frac{1}{2}k\boldsymbol{q}^{\mathrm{T}}\boldsymbol{q} = \frac{1}{2}k\boldsymbol{x}_{\text{ref}}^{\mathrm{T}}\mathbf{R}^{-\mathrm{T}}\mathbf{R}^{-1}\boldsymbol{x}_{\text{ref}}, \tag{5.2}$$

which means that the stiffness matrix is

$$\mathbf{K} = k\mathbf{R}^{-\mathrm{T}}\mathbf{R}^{-1}. \tag{5.3}$$

This matrix turns out to be

$$\mathbf{K} = k\,\mathrm{diag}(3\mathrm{c}^2\beta, 3\mathrm{c}^2\beta, 6\mathrm{s}^2\beta, 3r^2\mathrm{s}^2\beta, 3r^2\mathrm{s}^2\beta, 6r^2\mathrm{c}^2\beta). \tag{5.4}$$

Since $\mathbf{K}$ is diagonal, the geometric center of the vibration isolator is also the elastic center. By choosing design parameter $\beta \approx 35°$ such that $\cos^2(\beta) = 2\sin^2(\beta) = \frac{2}{3}$, the stiffness matrix simplifies to $\mathbf{K} = k\,\mathrm{diag}(2, 2, 2, r^2, r^2, 4r^2)$. This means that the translational stiffness is the same in all directions while the rotational stiffness in torsion is four times greater than in bending.

If the payload is an axisymmetric rigid body having principal axes of inertia aligned with (x, y, z) and with center of mass (c.o.m.) displaced vertically from the elastic center of the six-axes isolator by amount h_{m}, the mass matrix

expressed in terms of $\boldsymbol{x}_{\text{ref}}$ is [51]

$$\mathbf{M} = m\begin{bmatrix} 1 & 0 & 0 & 0 & h_{\text{m}} & 0 \\ 0 & 1 & 0 & -h_{\text{m}} & 0 & 0 \\ 0 & 0 & 1 & 0 & 0 & 0 \\ 0 & -h_{\text{m}} & 0 & r_x^2 + h_{\text{m}}^2 & 0 & 0 \\ h_{\text{m}} & 0 & 0 & 0 & r_x^2 + h_{\text{m}}^2 & 0 \\ 0 & 0 & 0 & 0 & 0 & r_z^2 \end{bmatrix}, \tag{5.5}$$

where m is the total mass of the payload, and r_x, r_z are the x-axis and z-axis radii of gyration respectively.

With $\mathbf{M}$ and $\mathbf{K}$ the equation of motion describing the suspension dynamics of the vibration isolator can be expressed as

$$\mathbf{M}\ddot{\boldsymbol{x}}_{\text{ref}}(t) + \mathbf{K}\boldsymbol{x}_{\text{ref}}(t) = \mathbf{B}\boldsymbol{F}_{\text{a}}(t), \tag{5.6}$$

where $\boldsymbol{F}_{\text{a}} = (F_{\text{a1}}, \ldots, F_{\text{a6}})^{\text{T}}$ is the vector of actuator forces and $\mathbf{B}$ is the input matrix. Since the actuator forces $\boldsymbol{F}_{\text{a}}$ are in the direction of the leg extensions $\boldsymbol{q}$, it is easy to see that $\mathbf{B} = \mathbf{R}$. The natural frequencies of the isolator are calculated by solving the eigenvalue problem of the left hand side of Eq. (5.6)

$$\mathbf{M}^{-1}\mathbf{K} = \mathbf{P}\boldsymbol{\Omega}^2\mathbf{P}^{-1}, \tag{5.7}$$

where $\boldsymbol{\Omega} = \text{diag}(\omega_1, \ldots, \omega_6)$ with ω_l the lth suspension mode and $\mathbf{P}$ the normal modal matrix in which the lth column is the corresponding normal mode shape factor expressed in terms of $\boldsymbol{x}_{\text{ref}}$. From Eqs. (5.4) and (5.5) it is clear that the suspension modes are determined by design parameters β, r and h_{m} if the mass and inertia properties of the payload are given. It can be observed that the z-translation or "bounce" mode and the z-rotation or "torsional" mode are decoupled, with natural frequencies given by

$$\omega_3 = \sqrt{2}\omega_0, \qquad \omega_6 = \frac{2}{\rho_{\text{z}}}\omega_0, \tag{5.8}$$

where $\omega_0 = \sqrt{k/m}$ and $\rho_{\text{z}} = r_{\text{z}}/r$ is the z-axis radius of gyration normalized with radius r. For most cases of interest, $\rho_{\text{z}} < \sqrt{2}$ and therefore $\omega_6 > \omega_3$. The remaining four modes are bending coupled with shear (or horizontal translation). The natural frequencies corresponding to these bending and shear modes occur in two identical pairs and are given by the roots of the equation [45, 51]

$$(2 - \frac{\omega^2}{\omega_0^2})(1 - \rho_{\text{x}}^2\frac{\omega^2}{\omega_0^2}) - 2\rho_{\text{m}}^2\frac{\omega^2}{\omega_0^2} = 0, \tag{5.9}$$

where $\rho_x = r_x/r$ is the z-axis radius of gyration normalized with radius r and $\rho_m = h_m/r$ is the center of mass offset normalized with radius r. It can be seen that the modes will all be decoupled if the center of mass is located at the elastic center, hence $h_m = 0$ and $\rho_m = 0$. If in the ideal situation also the radii of gyration are $r_x = \frac{1}{2}\sqrt{2}r$ and $r_z = \sqrt{2}r$, all six suspension modes have the same natural frequency. However, these conditions are difficult to satisfy and in almost all situations there will be a frequency spread or *modal spread*. In [51] it is stated that for most axisymmetric payloads the natural frequency of the bounce mode is in-between the two pairs of bending and shear modes. The natural frequency of the torsional mode is usually the highest.

The six-axes active hard mount vibration isolator is designed such that the bounce mode is about 10 Hz. Using Eq. (5.8) with a 10.9 kg payload, the axial stiffness of the legs that is due to the membranes is chosen as $2{\cdot}10^4$ N/m. Radius r is 100 mm, the center of mass offset h_m is 56 mm, and the radii of gyration are $r_x = 125$ mm ($\rho_x = 1.25$) and $r_z = 117$ mm ($\rho_z = 1.17$). These distances differ from their ideal values, so there is coupling and there is a modal spread. With these values the resonance frequencies of the two pairs of bending and shear modes are 7.9 and 12.5 Hz, the bounce mode is 10.2 Hz and the torsional mode is 17.9 Hz.

In reality, the legs are *non-ideal mounts* since their bending and torsional stiffness are non-zero and additional parasitic stiffness due to cables may be present. This results in (weak) coupling and a non-diagonal stiffness matrix. Moreover, the low-stiffness springs that compensate the sagging due to gravity result in an increased stiffness in vertical direction. In addition, if the payload is not axisymmetric due to the additional weight body (w), the mass matrix will also be a full matrix. Hence, all six suspension modes will be coupled. As a result, the transmissibilities are also coupled. For example, payload motion in x-direction will be due to both floor translation in x-direction and floor rotation around the y-axis. To accurately predict the performance of the vibration isolator in terms of the transmissibilities, a linear finite element model of the vibration isolator describing input-output relations needs to be used. In the next section, the derivation of a finite element model is discussed.

5.3 Flexible body model

Within a finite element model of the vibration isolator, the flexible body dynamics of the payload itself and the payload's suspension can be included. So, the DOFs associated with these internal flexibilities are no longer neglected.

Table 5.1: Resonance frequencies of the suspensions modes for the derived models.

	rigid body model	flexible body model	reduced order model
bending and	7.9 Hz	7.6 Hz	7.6 Hz
shear modes	7.9 Hz	7.7 Hz	7.7 Hz
bounce mode	10.2 Hz	9.8 Hz	9.8 Hz
bending and	12.5 Hz	12.0 Hz	12.1 Hz
shear modes	12.5 Hz	12.8 Hz	12.8 Hz
torsional mode	17.9 Hz	16.7 Hz	16.7 Hz

The payload is modeled as being asymmetric and the bending and torsional stiffness of the legs is included. With the flexible body model, input-output relations can be obtained that are used to assess the performance of the active vibration isolator in terms of the transmissibilities and the stability of the closed loop system. The model has been developed using SPACAR, a non-linear finite element software package which can make computations of mechanical systems with interconnected rigid and flexible elements. The interested reader is referred to for example [28] and the references therein for more information about this software package.

The nonlinear finite element description used by SPACAR allows accurate modeling of the system dynamics with relatively few elements. Moreover, rigid and flexible elements can be used simultaneously. Geometrical nonlinear stiffness effects like preloading due to gravity are easily accounted for. Using the software package, linearized state-space representations for arbitrary inputs and outputs can be easily computed. These state-space systems are of low order due to the relatively small number of DOFs as compared to typical finite element models.

The three payload bodies in Fig. 5.2 are modeled with rigid elements. Their mass and inertia properties are derived from a CAD model. The two sets of three leaf springs that connect the payload bodies to each other are modeled with flexible elements. The rigid floor plate and the three brackets in Fig. 5.1 are also modeled with rigid elements. The legs are modeled with flexible elements that provide for the elastic properties of the membranes, back-EMF damping of the voice coil actuators and axial actuator forces. The force sensors, accelerometers and wire flexures are modeled with flexible elements as well. It is beyond the scope of this thesis to discuss the actual modeling in more detail. The reader is referred to [22, 28, 60] for more detailed descriptions on using SPACAR for the modeling of vibration isolators.

The SPACAR software package provides the system matrices corresponding to the six-axes vibration isolator. When the DOFs $\boldsymbol{q}$ consists of the leg

extensions as well as the axial and bending deformations of the leaf springs, the equations of motion are given by

$$\mathbf{M}\ddot{\boldsymbol{q}}(t) + \mathbf{D}\dot{\boldsymbol{q}}(t) + \mathbf{K}\boldsymbol{q}(t) = -\mathbf{M}_0\ddot{\boldsymbol{x}}_0(t) + \mathbf{B}\boldsymbol{F}_\mathrm{a}(t), \tag{5.10}$$

$$\boldsymbol{y}(t) = \mathbf{C}_{\boldsymbol{q}}\boldsymbol{q}(t) + \mathbf{C}_{\dot{\boldsymbol{q}}}\dot{\boldsymbol{q}}(t) + \mathbf{C}_{\ddot{\boldsymbol{q}}}\ddot{\boldsymbol{q}}(t), \tag{5.11}$$

where $\mathbf{M}$, $\mathbf{D}$, and $\mathbf{K}$ are the mass, damping, and stiffness matrices corresponding to DOFs $\boldsymbol{q}$ respectively, and $\mathbf{M}_0$ is the mass matrix corresponding to the vector of floor accelerometer signals $\ddot{\boldsymbol{x}}_0 = (\ddot{x}_{0,1}, \ldots, \ddot{x}_{0,6})^\mathrm{T}$. $\mathbf{B}$ is the input matrix and $\mathbf{C}_{\boldsymbol{q}}$, $\mathbf{C}_{\dot{\boldsymbol{q}}}$, and $\mathbf{C}_{\ddot{\boldsymbol{q}}}$ are the output matrices that relate the outputs $\boldsymbol{y}$ to DOFs $\boldsymbol{q}$ and their derivatives with respect to time. $\boldsymbol{F}_\mathrm{a} = (F_{\mathrm{a}1}, \ldots, F_{\mathrm{a}6})^\mathrm{T}$ is the vector with actuator forces and $\boldsymbol{y} = (\ddot{\boldsymbol{x}}_1^\mathrm{T}, \boldsymbol{F}_\mathrm{s}^\mathrm{T})^\mathrm{T}$ is the output vector. Herein, $\ddot{\boldsymbol{x}}_1 = (\ddot{x}_{1,1}, \ldots, \ddot{x}_{1,6})^\mathrm{T}$ is the vector with payload accelerometer signals and $\boldsymbol{F}_\mathrm{s} = (F_{\mathrm{s}1}, \ldots, F_{\mathrm{s}6})^\mathrm{T}$ is the vector with force sensor signals.

Using Eq. (5.7) the resonance frequencies and the mode shapes can be calculated. The first six modes represent the six suspension modes. Their resonance frequencies are in Table 5.1 compared to those of the rigid body model. The resonance frequencies of the two (approximate) pairs of bending and shear modes are 7.6 and 7.7 Hz, and 12.0 and 12.8 Hz, the bounce mode is 9.8 Hz and the torsional mode is 16.7 Hz. These frequencies differ slightly from the ones for the rigid body model. This is mainly due to the asymmetric payload.

5.3.1 Plant transfer function matrices

With Eq. (5.10) the plant transfer function matrix $\mathbf{G}_{\ddot{\boldsymbol{x}}_1\boldsymbol{F}_\mathrm{a}}(s)$ between actuator forces and payload accelerations is derived, such that $\ddot{\boldsymbol{X}}_1(s) = \mathbf{G}_{\ddot{\boldsymbol{x}}_1\boldsymbol{F}_\mathrm{a}}(s)\boldsymbol{F}_\mathrm{a}(s)$. In a similar way the transfer function matrix $\mathbf{G}_{\boldsymbol{F}_\mathrm{s}\boldsymbol{F}_\mathrm{a}}(s)$ is derived, such that $\boldsymbol{F}_\mathrm{s}(s) = \mathbf{G}_{\boldsymbol{F}_\mathrm{s}\boldsymbol{F}_\mathrm{a}}(s)\boldsymbol{F}_\mathrm{a}(s)$. Since $\mathbf{G}_{\ddot{\boldsymbol{x}}_1\boldsymbol{F}_\mathrm{a}}(s)$ and $\mathbf{G}_{\boldsymbol{F}_\mathrm{s}\boldsymbol{F}_\mathrm{a}}(s)$ each describe 36 transfer functions (from each of the six actuator forces to each of the six payload accelerations), only two typical transfer functions are displayed, being representative for the others.

Fig. 5.5(a) show the transfer functions $G_{\ddot{x}_{1,5}F_{\mathrm{a}5}}(s) = \ddot{X}_{1,5}(s)/F_{\mathrm{a}5}(s)$ (solid) and $G_{F_{\mathrm{s}5}F_{\mathrm{a}5}}(s) = F_{\mathrm{s}5}(s)/F_{\mathrm{a}5}(s)$ (dashed) from actuator 5 to sensor 5 corresponding to a co-aligned and (approximately) collocated actuator-sensor-pair. This is reflected by the plot of the phase angle that is in-between 180° and 0° [45] up to about 900 Hz, the frequency at which the collocation is lost (because of the local wire-flexure dynamics) and the plot shows a resonance peak. Fig. 5.5(b) show the transfer functions $G_{\ddot{x}_{1,1}F_{\mathrm{a}5}}(s) = \ddot{X}_{1,1}(s)/F_{\mathrm{a}5}(s)$ (solid) and $G_{F_{\mathrm{s}1}F_{\mathrm{a}5}}(s) = F_{\mathrm{s}1}(s)/F_{\mathrm{a}5}(s)$ (dashed) from actuator 5 to sensor 1

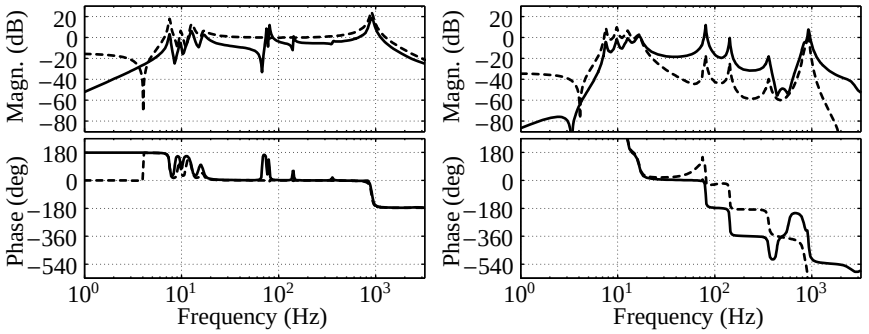

(a) $G_{\ddot{x}_{1,5}F_{a5}}(s)$ and $G_{F_{s5}F_{a5}}(s)$. (b) $G_{\ddot{x}_{1,1}F_{a5}}(s)$ and $G_{F_{s1}F_{a5}}(s)$.

Fig. 5.5: (a) Transfer functions $G_{\ddot{x}_{1,5}F_{a5}}(s)$ (——) and $G_{F_{s5}F_{a5}}(s)$ (- - - -) from actuator 5 to sensor 5; (b) Transfer functions $G_{\ddot{x}_{1,1}F_{a5}}(s)$ (——) and $G_{F_{s1}F_{a5}}(s)$ (- - - -) form actuator 5 to sensor 1.

corresponding to a non-collocated actuator-sensor pair. The phase angle is below 900 Hz no longer in-between 180° and 0°. So, Figs. 5.5(a) and (b) show clearly the difference between the transfer functions corresponding to collocated and non-collocated actuator-sensor-pairs. In both plots, some resonance peaks in-between 7.2 and 16.7 Hz are visible. These correspond to the suspension modes of the vibration isolator. The peaks in-between 75 and 360 Hz are due to internal flexibilities of the payload because of the leaf springs.

From the transfer function matrices $\mathbf{G}_{\ddot{\boldsymbol{x}}_1\boldsymbol{F}_a}(s)$ and $\mathbf{G}_{\boldsymbol{F}_s\boldsymbol{F}_a}(s)$ the so-called *characteristic loci* (CL) can be calculated. The CL are just the traces of the eigenvalues of transfer function matrix $\mathbf{G}_{\ddot{\boldsymbol{x}}_1\boldsymbol{F}_a}(s)$ or $\mathbf{G}_{\boldsymbol{F}_s\boldsymbol{F}_a}(s)$:

$$\mathbf{G}_{\bullet\bullet}(s) = \mathbf{\Phi}(s)\mathbf{\Lambda}(s)\mathbf{\Phi}^{-1}(s) \tag{5.12}$$

where $\mathbf{\Lambda}(s) = \text{diag}(\lambda_1(s), \ldots, \lambda_6(s))$ in which λ_i is the ith eigenvalue evaluated at each frequency $s = \text{j}\omega$. The CL of $\mathbf{G}_{\ddot{\boldsymbol{x}}_1\boldsymbol{F}_a}(s)$ are shown in Fig. 5.6. The plot of the CL of $\mathbf{G}_{\boldsymbol{F}_s\boldsymbol{F}_a}(s)$ is visible in Fig. 5.7. The eigenvalues can be calculated only if the transfer function matrix is square, which means that the number of inputs and outputs are equal. CL are normally used for checking the stability of multivariable systems using the generalized Nyquist stability criterion [37]. A nice property of the CL is that, while usually each mode appears as a resonance peak in multiple transfer functions contained in $\mathbf{G}_{\ddot{\boldsymbol{x}}_1\boldsymbol{F}_a}(s)$ or $\mathbf{G}_{\boldsymbol{F}_s\boldsymbol{F}_a}(s)$, it appears in only one of the CL as a resonance peak, see Figs. 5.6 and 5.7. Since there are more modes than CL, each of the CL may show more than one peak. The CL are a good representation of the dynamics of the vibration isolator.

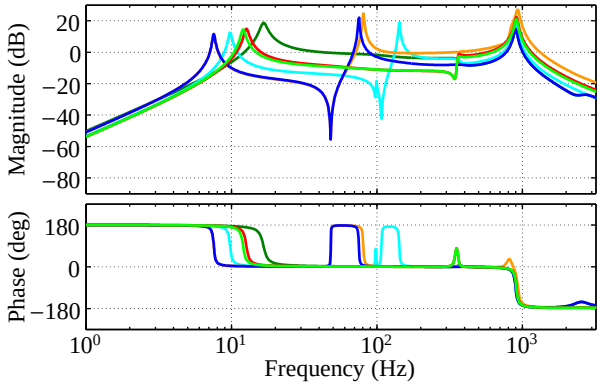

Fig. 5.6: Characteristic loci of the transfer function matrix $\mathbf{G}_{\ddot{x}_1 F_a}(s)$.

The dips in the CL of $\mathbf{G}_{F_s F_a}(s)$ in Fig. 5.7 are the anti-resonances due to parasitic stiffness, see also Eq. (3.25). Since the frequency of each anti-resonance is only about a factor 3 smaller than the frequency of the corresponding resonance (due to the axial stiffness of each leg), it is concluded that the parasitic stiffness is quiet large (about 14% of the axial stiffnees of each leg).

5.3.2 Transmissibility matrix

Eq. (5.10) can be used to calculate the transmissibility matrix $\mathbf{T}(s)$ which describes the relationship between the floor and payload accelerometer signals:

$$\ddot{\boldsymbol{X}}_1(s) = \mathbf{T}(s)\ddot{\boldsymbol{X}}_0(s). \tag{5.13}$$

Transmissibility matrix $\mathbf{T}(s)$ is used in chapter 7 to analyze the performance of the six-axes vibration isolator. Since $\ddot{\boldsymbol{x}}_0$ and $\ddot{\boldsymbol{x}}_1$ are measured in the axial directions of the sensors, $\mathbf{T}(s)$ is dependent on the choice and orientation of these sensors. If it is assumed that the inputs and outputs are transformed as

$$\ddot{\boldsymbol{X}}_{\text{floor}}(s) = \mathbf{R}_{\text{floor}}\ddot{\boldsymbol{X}}_0(s), \qquad \ddot{\boldsymbol{X}}_{\text{ref}}(s) = \mathbf{R}_{\text{ref}}\ddot{\boldsymbol{X}}_1(s), \tag{5.14}$$

where $\mathbf{R}_{\text{floor}}$ and $\mathbf{R}_{\text{ref}}$ are constant matrices defining geometric transformations and $\ddot{\boldsymbol{x}}_{\text{floor}}$ describes the motion of the frame attached rigidly to the floor, $\ddot{\boldsymbol{x}}_{\text{ref}}$ describes the motion of the frame attached rigidly to the payload. Substituting Eq. (5.14) into Eq. (5.13) yields

$$\ddot{\boldsymbol{X}}_{\text{ref}}(s) = \mathbf{R}_{\text{ref}}\mathbf{T}(s)\mathbf{R}_{\text{floor}}^{-1}\ddot{\boldsymbol{X}}_{\text{floor}}(s), \tag{5.15}$$

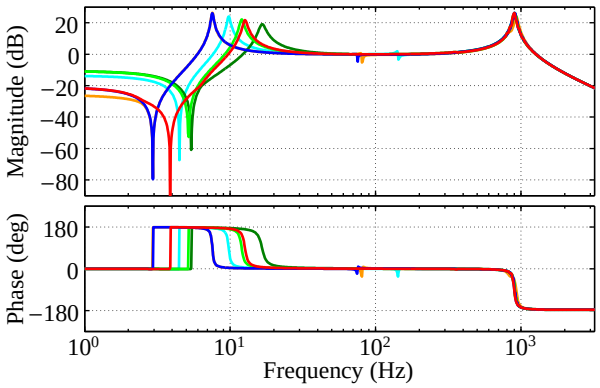

Fig. 5.7: Characteristic loci of the transfer function matrix $\mathbf{G}_{F_s F_a}(s)$.

which allows to define

$$\ddot{\boldsymbol{X}}_{\text{ref}}(s) = \mathbf{T}_{\text{ref}}(s)\ddot{\boldsymbol{X}}_{\text{floor}}(s), \tag{5.16}$$

where the transmissibility matrix $\mathbf{T}_{\text{ref}}(s)$ is defined as

$$\mathbf{T}_{\text{ref}}(s) = \mathbf{R}_{\text{ref}}\mathbf{T}(s)\mathbf{R}_{\text{floor}}^{-1}. \tag{5.17}$$

If both floor and payload have identical motions, $\ddot{\boldsymbol{x}}_{\text{floor}} = \ddot{\boldsymbol{x}}_{\text{ref}}$, $\mathbf{T}_{\text{ref}}(s)$ must be equal to $\mathbf{I}_6$ and $\mathbf{T}_{\text{ref}}(s)$ is the matrix generalization of a scalar transmissibility. This is achieved if $\ddot{\boldsymbol{x}}_{\text{floor}}$ and $\ddot{\boldsymbol{x}}_{\text{ref}}$ describe the motion of two reference frames located at the same point in space and with the same orientation. A natural location of this point is the elastic center of the vibration isolator with the orientation as in Fig. 5.4. This means $\mathbf{R}_{\text{ref}} = \mathbf{R}$ as in Eq. (5.1). An expression for $\mathbf{R}_{\text{floor}}$ is derived in chapter 8. With this choice, the llth entry of the transmissibility matrix $\mathbf{T}_{\text{ref}}(s)$ represents the payload's response (a pure translation or rotation in the direction of x, y or z) due to floor excitation in the same direction.

The equation of motion of Eq. (5.10) usually describes both the suspension dynamics of the vibration isolator and the flexible body dynamics of the payload. In chapter 7 a novel method for designing a modal controller will be presented. That method requires the mass, damping and stiffness matrices corresponding to a model describing only the suspension dynamics. Such a model can be obtained using for example a reduction method. This will be discussed in the next section.

5.4 Reduced order model

Consider the equation of motion of Eq. (5.10) and exclude the contribution of floor vibration $\ddot{\boldsymbol{x}}_0$. The DOFs $\boldsymbol{q}$ can be partitioned into a set (o) that is observed and controlled and a set (u) that is not observed and controlled. Set (o) is associated with the extensions of the legs, while set (u) is associated with the internal flexibilities of the payload. With this partition, Eq. (5.10) can be written as

$$\begin{bmatrix} \mathbf{M}_{oo} & \mathbf{M}_{ou} \\ \mathbf{M}_{uo} & \mathbf{M}_{uu} \end{bmatrix} \begin{Bmatrix} \ddot{\boldsymbol{q}}_o(t) \\ \ddot{\boldsymbol{q}}_u(t) \end{Bmatrix} + \begin{bmatrix} \mathbf{D}_{oo} & \mathbf{D}_{ou} \\ \mathbf{D}_{uo} & \mathbf{D}_{uu} \end{bmatrix} \begin{Bmatrix} \dot{\boldsymbol{q}}_o(t) \\ \dot{\boldsymbol{q}}_u(t) \end{Bmatrix} + \begin{bmatrix} \mathbf{K}_{oo} & \mathbf{K}_{ou} \\ \mathbf{K}_{uo} & \mathbf{K}_{uu} \end{bmatrix} \begin{Bmatrix} \boldsymbol{q}_o(t) \\ \boldsymbol{q}_u(t) \end{Bmatrix} = \begin{bmatrix} \mathbf{B}_o \\ \mathbf{B}_u \end{bmatrix} \boldsymbol{F}_a(t). \tag{5.18}$$

The equation of motion that describes only the suspension dynamics can be obtained using a reduction method, such as Guyan reduction [17]. Guyan reduction is a static method in which the forces associated with the not observed DOFs $\boldsymbol{q}_u$ are set to zero. Since the DOFs $\boldsymbol{q}_u$ are not controlled either, $\mathbf{B}_u = \mathbf{0}$. Solving the static equations of Eq. (5.10) with $\mathbf{B}_u = \mathbf{0}$ and $\ddot{\boldsymbol{q}}_u(t) = \dot{\boldsymbol{q}}_u(t) = \mathbf{0}$ gives

$$\boldsymbol{q}_u(t) = -\mathbf{K}_{uu}^{-1}\mathbf{K}_{uo}\boldsymbol{q}_o(t), \tag{5.19}$$

and a coordinate transformation is given as

$$\begin{Bmatrix} \boldsymbol{q}_o(t) \\ \boldsymbol{q}_u(t) \end{Bmatrix} = \begin{bmatrix} \mathbf{I}_6 \\ -\mathbf{K}_{uu}^{-1}\mathbf{K}_{uo} \end{bmatrix} \boldsymbol{q}_o(t) = \mathbf{T}\boldsymbol{q}_o(t). \tag{5.20}$$

With this transformation the reduced stiffness matrix can be calculated as

$$\bar{\mathbf{K}} = \mathbf{T}^T\mathbf{K}\mathbf{T} = \mathbf{K}_{oo} - \mathbf{K}_{ou}\mathbf{K}_{uu}^{-1}\mathbf{K}_{uo}. \tag{5.21}$$

Applying the same transformations to the damping and mass matrices results in the reduced damping and mass matrices $\bar{\mathbf{D}} = \mathbf{T}^T\mathbf{D}\mathbf{T}$ and $\bar{\mathbf{M}} = \mathbf{T}^T\mathbf{M}\mathbf{T}$, respectively. These are expressed as:

$$\bar{\mathbf{D}} = \mathbf{D}_{oo} - \mathbf{D}_{ou}\mathbf{K}_{uu}^{-1}\mathbf{K}_{uo} - \mathbf{K}_{ou}\mathbf{K}_{uu}^{-1}(\mathbf{D}_{uo} - \mathbf{D}_{uu}\mathbf{K}_{uu}^{-1}\mathbf{K}_{uo}), \tag{5.22}$$

$$\bar{\mathbf{M}} = \mathbf{M}_{oo} - \mathbf{M}_{ou}\mathbf{K}_{uu}^{-1}\mathbf{K}_{uo} - \mathbf{K}_{ou}\mathbf{K}_{uu}^{-1}(\mathbf{M}_{uo} - \mathbf{M}_{uu}\mathbf{K}_{uu}^{-1}\mathbf{K}_{uo}). \tag{5.23}$$

From Eq. (5.20) it is clear that Guyan reduction is a static reduction method, since the coordinate transformation only makes use of partitions of the stiffness matrix. The reduced mass, damping and stiffness matrices can be used to

Table 5.2: Modal matrix $\mathbf{\Phi}_o$ and resonance frequencies.

	7.6 Hz	7.7 Hz	9.8 Hz	12.1 Hz	12.8 Hz	16.7 Hz
x	−0.14	0.04	0.06	0.04	−0.01	0.00
y	0.04	−0.16	−0.02	−0.01	−0.04	0.01
z	0.01	−0.00	0.28	−0.02	0.00	−0.00
θ_x	0.26	0.95	0.25	0.26	0.97	0.00
θ_y	0.96	−0.25	0.93	0.96	−0.26	−0.00
θ_z	−0.00	−0.10	0.00	0.00	0.02	1.00

derive the modal controller as will be described in chapter 7. The equation of motion describing the rigid body dynamics is given by

$$\bar{\mathbf{M}}\ddot{\boldsymbol{q}}_o(t) + \bar{\mathbf{D}}\dot{\boldsymbol{q}}_o(t) + \bar{\mathbf{K}}\boldsymbol{q}_o(t) = \mathbf{B}_o\boldsymbol{F}_a(t). \tag{5.24}$$

The payload accelerations $\ddot{\boldsymbol{x}}_1$ are related to $\ddot{\boldsymbol{q}}_o$ by the output matrix $\mathbf{C}_o$:

$$\ddot{\boldsymbol{x}}_1(t) = \mathbf{C}_o\ddot{\boldsymbol{q}}_o(t). \tag{5.25}$$

Since $\bar{\mathbf{M}}$ is non-singular, pre-multiplying Eq. (5.24) by $\bar{\mathbf{M}}^{-1}$ allows to write the system as:

$$\ddot{\boldsymbol{q}}_o(t) + \bar{\mathbf{M}}^{-1}\bar{\mathbf{D}}\dot{\boldsymbol{q}}_o(t) + \bar{\mathbf{M}}^{-1}\bar{\mathbf{K}}\boldsymbol{q}_o(t) = \bar{\mathbf{M}}^{-1}\mathbf{B}_o\boldsymbol{F}_a(t) \tag{5.26}$$

If $\bar{\mathbf{D}}$ is a proportional damping matrix, the equation of motion of Eq. (5.26) can be decoupled using the modal transformation $\boldsymbol{q}_o = \mathbf{P}_o\mathbf{z}_o$ in which the columns of $\mathbf{P}_o$ are the normalized eigenvectors of $\bar{\mathbf{M}}^{-1}\bar{\mathbf{K}}$:

$$\bar{\mathbf{M}}^{-1}\bar{\mathbf{K}} = \mathbf{P}_o\mathbf{\Omega}_o^2\mathbf{P}_o^{-1}. \tag{5.27}$$

Pre-multiplying Eq. (5.26) by $\mathbf{P}_o^{-1}$ results in the modal decoupled equation of motion

$$\ddot{\boldsymbol{z}}_o(t) + \mathbf{\Xi}_o\dot{\boldsymbol{z}}_o(t) + \mathbf{\Omega}_o^2\boldsymbol{z}_o(t) = \mathbf{P}_o^{-1}\bar{\mathbf{M}}^{-1}\mathbf{B}_o\boldsymbol{F}_a(t), \tag{5.28}$$

where $\mathbf{\Xi}_o = \mathrm{diag}(\xi_{o1}, \ldots, \xi_{o6})$ and $\mathbf{\Omega}_o = \mathrm{diag}(\omega_{o1}, \ldots, \omega_{o6})$ with $\xi_{ol} = 2\zeta_{ol}\omega_{ol}$. Herein, ζ_{ol} and ω_{ol} are the damping ratio and the resonance frequency of the lth suspension mode of the vibration isolation system. The lth column of $\mathbf{P}_o$ is the corresponding normal mode shape vector.

The mode shapes vectors in $\mathbf{P}_o$ are expressed in terms of the DOFs $\boldsymbol{q}_o$. With the transformation matrix $\mathbf{R}$ of Eq. (5.1), the mode shapes can be expressed in terms of $\boldsymbol{x}_{\mathrm{ref}}$ as

$$\mathbf{\Phi}_o = \mathbf{R}\mathbf{P}_o. \tag{5.29}$$

The lth column of $\mathbf{\Phi}_o$ now expresses the lth mode shape in terms of $\boldsymbol{x}_{\text{ref}}$. Table 5.2 shows the mode shapes. It shows the coupling that is present in particular between translation in x-direction and rotation around the y-axis and visa versa. Because of the asymmetric payload, the third mode is not a perfect "bounce" mode, and the fourth and fifth mode have slightly different resonance frequencies.

In Table 5.1 the resonance frequencies of the suspension modes for the reduced order model are compared to those for the the other models. The frequencies for the flexible body model and reduced order model are almost identical, while these differ slightly from the ones for the rigid body model. Therefore, it is concluded that the reduced order model is a more accurate representation of the suspension dynamics than the rigid body model.

5.5 Conclusions

A demonstrator setup of a six-axes active hard mount vibration isolator is realized that is able to suspend a 10.9 kg payload. Under the assumptions that parasitic stiffness effects, internal flexibilities and asymmetry of the payload can be neglected, a rigid body model describing the suspension dynamics can be derived. This model shows how the six suspension modes are not only determined by the mass and inertia properties of the payload, and the axial stiffness of the legs, but also by several other design parameters of the suspension. These are the angle between the axial direction of a leg and the horizontal plane, the horizontal distance between the vertical axis of symmetry and the point where a leg is attached to the payload, and the vertical distance between the center of mass and the elastic center of the vibration isolator.

If these assumptions are not valid, a flexible body model should be used. With this model also the effect of the payload's flexibilities can be analyzed as well. From the flexible body model, a reduced order model can be derived using Guyan reduction. The reduced order model is a more accurate representation of the suspension dynamics than the rigid body model, since the bending and torsional stiffness of the legs, and the effect of an asymmetric payload are taken into account.

The main contribution of this chapter is that with the rigid body model and reduced order model, a model is available describing the suspension dynamics. The mass, damping and stiffness matrices can be derived from this model. These matrices are used to design the modal controller for the active hard mount vibration isolator described in chapter 7.

System identification of a six-axes vibration isolator

Chapter 6

In this chapter, an identification model describing the dynamics of the demonstrator setup of the six-axes active hard mount vibration isolator is obtained. This model can be compared to the models presented in chapter 5 to assess the stability of the vibration isolator in closed loop. A novel method for the system identification of such a system is developed. This method identifies a state-space model representing accelerance transfer functions. It requires the calculation of the so-called characteristic loci (CL). The CL are just the eigenvalues of the frequency response function matrix and can be calculated only if the system is square. This means that the number of inputs and outputs must be equal. It is shown that the reduced mass, damping and stiffness matrices can be calculated from the identified state-space model if the system is collocated. These matrices can be used to design the modal controller in chapter 7. The method is successfully applied to experimental data from the six-axes active hard mount vibration isolator. It is demonstrated that the method outperforms the widely used least squares complex frequency domain estimator for the identification of closely spaced poles.

The work in this chapter has been submitted for publication in revised form as: D. Tjepkema and J. van Dijk, "State-space identification of square structural dynamic systems using characteristic loci". Submitted 2012.

6.1 Introduction

Many methods are available for the system identification of structural dynamic systems. The goal of the identification model determines which method suits best. General system identification methods, e.g. based on predictive error models [34] or subspace identification [12], identify a model describing input-

output relations. Modal identification methods [4, 6, 11, 62] are dedicated to identify the resonance frequencies and mode shapes of a structural dynamic system. An advantage of modal identification methods over general system identification methods is that some basic knowledge about the nature of the system can be used to enforce constraints (e.g. the identified model has to be stable or reciprocal) without requiring an optimization algorithm [6]. Another advantage is that models obtained with modal identification methods usually contain only physical poles (poles corresponding to a mode of the system), whereas models obtained with general system identification methods also contain many mathematical poles (poles used to model the noise and which are due to over-modeling of the system).

None of the available methods from literature is able to accurately identify the modes of a system with a larger number of modes in a wide frequency range (describing multiple decades, e.g. 1–1 000 Hz) and with modes corresponding to multiple closely spaced poles, in particular at low frequencies (e.g. below 50 Hz). If it is tried to identify a model of such a system with existing methods, the multiple closely spaced poles are often identified as a single pole only. This is because the model has to describe a wide frequency range and the multiple closely spaced poles can hardly be distinguished from each other.

An example of such a system is the active hard mount vibration isolator for suspending precision equipment. Its six suspension modes are designed to be at low, closely spaced frequencies (e.g. 7.6–16.7 Hz), while the internal modes of the suspended equipment are in the mid and high frequency range (75–3 000 Hz). Another example is a multi-axes manipulator with a flexible linear guidance to accurately position a stage (e.g. a flexible x,y-table or a scanning mirror). The modes at low frequencies are in the direction of actuation, while the modes at mid and high frequencies are the internal modes. If high-bandwidth controllers are used to control such systems, an accurate identification model of the system is often desired.

In this chapter, a novel three-steps system identification method is proposed. It can be interpreted as a guideline for the system identification of square structural dynamics systems. With this method the (observable) modes of structural dynamic systems can be identified, including the modes corresponding to the multiple closely spaced poles at low frequencies.

The first step of the method is based on the framework of the least squares complex frequency domain (LSCF) estimator [4, 11, 62]. The LSCF estimator is using estimates of the frequency response functions (FRF estimates) to identify the system poles by curvefitting a model on all FRF estimates simulta-

neously. By using stabilization charts the system poles are divided into physical poles and mathematical poles. It will be shown that the LSCF estimator is not able to identify the modes corresponding to the closely space poles at low frequencies. In the proposed method the estimates of the so-called characteristic loci (CL) will be used to identify the poles instead of the FRF estimates. The CL estimates are just the eigenvalues of the FRF estimates evaluated at the same frequencies as the FRF estimates. The eigenvalues can be calculated only if the system is square, which means that the number of inputs and outputs is equal. In many controlled structural dynamic systems this requirement is fulfilled. CL are normally used for checking the stability of multivariable systems based on the generalized Nyquist stability criterion [37]. The advantage of the proposed method, which will be referred to as the CL estimator, is that, while usually each mode appears in multiple FRF estimates as a peak, it appears in only one of the CL estimates as a peak (if there are more modes than CL, each of the CL estimates may show multiple peaks). In this way, modes with closely spaced poles can be separated from each other and the system poles can be found by curvefitting a model on each of the CL estimates. Stabilization charts are then used to divide the system poles into physical poles and mathematical poles.

Once the physical poles have been found, a state-space model is derived in the second step using the pole/residue form as described in [6]. In that reference state-space models are derived for receptance transfer functions (displacement response due to force excitation). In this paper the framework of [6] is extended to derive a state-space model describing accelerance transfer functions (acceleration response due to force excitation), which is a non-trivial derivation. Therefore it has to be assumed the system is proportionally damped. This assumption can often be fulfilled in practice. The proposed method to derive a state-space model describing accelerance transfer functions differs from the one described in [50], since that method requires subspace identification and a non-linear optimization algorithm to enforce several constraints required to derive these accelerance transfer functions. The method described in [50] requires long calculation times, whereas the proposed method is very fast.

In the third step, a reduced order mass-damping-stiffness model can be derived from the identified state-space model, provided that the system contains some collocated actuator-sensor-pairs. Therefore, the methods described in [1, 3, 35] are combined. The obtained reduced mass, damping and stiffness matrices can be used for example to design the modal controller in chapter 7.

6.2 Outline

The system identification method described in this chapter involves three major steps. It is used to satisfy two goals. The first goal is to have an identification model available describing the dynamics of the demonstrator setup of the six-axes active hard mount vibration isolator. It can be compared to the flexible body model derived in chapter 5 and it can be used to assess closed loop stability. The second goal is to identify the reduced mass, damping and stiffness matrices that are used to design the modal controller in chapter 7.

The three-steps system identification method requires that FRF and CL estimates are available. Therefore, in section 6.3 a method is described how FRF estimates can be derived from measurement data of the six-axes active hard mount vibration isolator. From the FRF estimates the CL estimates can be calculated. The FRF and CL estimates are used as an identification model suitable for comparison purposes, in order to satisfy the first goal

The first step of the system identification method is presented in section 6.4. The CL estimator is used to curvefit a discrete-time model on each of the CL estimates. From these models, the system poles can be identified. It is shown how to distinguish between physical poles and mathematical poles, and how to compensate for physical poles that are due to non-structural dynamics, for example actuator/sensor dynamics or delays. A list of the individual steps is given.

The second step of the system identification method is presented in section 6.5. First, the pole/residue form as described in [6] is obtained using the identified physical poles and the FRF estimates. Next, the pole/residue form is converted to a state-space model describing accelerance transfer functions.

The third and last step of the system identification method is the derivation of the reduced mass, damping and stiffness matrices from this state-space model used to satisfy the second goal. The individual steps that are required are described in section 6.6.

Section 6.7 presents an illustrative example of the proposed system identification method using experimental data of the six-axes active hard mount vibration isolator. The identified poles using the CL estimator will be compared to the identified poles using the LSCF estimator from [4]. A short discussion is given in section 6.8. In section 6.9 the dynamics of the identification model is compared to that of the flexible body model described in chapter 5.

Throughout this chapter it is assumed that the system is square with m inputs and m outputs and, unless otherwise stated, with exclusively force excitations and acceleration responses for the inputs and outputs respectively. The pro-

posed system identification method is illustrated with some figures which are obtained with experimental data from the six-axes active hard mount vibration isolator.

6.3 Frequency response function estimates

This section describes a method to obtain FRF estimates for a structural dynamic system from (open loop) measurement data. The method is adopted from [65] and is summarized in subsection 6.3.1. The use of this method results in avoiding leakage effects and minimizing the variance of the FRF estimates. The FRF estimates are used to calculate the CL estimates as is shown in subsection 6.3.2. The CL estimates are used to identify the system poles in section 6.4. The FRF estimates will be used again in section 6.5 to derive the state-space model.

6.3.1 The estimation method

The structural dynamics of the square system is assumed to be given by

$$\boldsymbol{y}(t) = \mathbf{G}(q)\boldsymbol{u}(t) + \boldsymbol{v}(t), \tag{6.1}$$

where $\mathbf{G}(q)$ is the $m \times m$ multivariable discrete-time transfer operator, with q being the shift operator, and $\boldsymbol{v}(t)$ is the measurement noise. The input and outputs signals, $\boldsymbol{u}(t) \in \mathbb{R}^m$ and $\boldsymbol{y}(t) \in \mathbb{R}^m$, are measured at time instants $t_l = lT_\mathrm{s}, l = 1, \ldots, N$, with sample time T_s.

To avoid leakage effects the input signal $\boldsymbol{u}(t)$ is assumed to be N_p-periodic and an integer number of periods P of the steady state response is collected, giving $N = PN_\mathrm{p}$ samples for each experiment. The discrete Fourier transform (DFT) of the input signal reads

$$\boldsymbol{U}(\omega_f) = \frac{1}{\sqrt{N}} \sum_{l=1}^{N} \boldsymbol{u}(lT_\mathrm{s}) e^{\mathrm{j}\omega_f lT_\mathrm{s}}, \tag{6.2}$$

where only the N_p frequencies $\omega_f = (2\pi f)/(N_\mathrm{p}T_\mathrm{s})$, $f = 1, \ldots, N_\mathrm{p}$ are considered. Similar DFTs are obtained for the output signal $\boldsymbol{y}(t)$ and the measurement noise $\boldsymbol{v}(t)$. Giving periodic data, the following linear mapping holds

$$\boldsymbol{Y}(\omega_f) = \mathbf{G}(e^{\mathrm{j}\omega_f T_\mathrm{s}})\boldsymbol{U}(\omega_f) + \boldsymbol{V}(\omega_f), \tag{6.3}$$

where $\mathbf{G}(e^{\mathrm{j}\omega_f T_\mathrm{s}}) \in \mathbb{C}^{m\times m}$ is the FRF matrix. To extract $\mathbf{G}(e^{\mathrm{j}\omega_f T_\mathrm{s}})$ from input-output data, m different experiments are needed. The data vectors from m

experiments are collected into matrices where each column corresponds to one experiment. The input-output relation can then be written as

$$\mathbf{Y}(\omega_f) = \mathbf{G}(e^{\mathrm{j}\omega_f T_\mathrm{s}})\mathbf{U}(\omega_f) + \mathbf{V}(\omega_f), \tag{6.4}$$

where $\mathbf{Y}(\omega_f), \mathbf{U}(\omega_f), \mathbf{V}(\omega_f) \in \mathbb{C}^{m\times m}$. If $\mathbf{U}(\omega_f)$ has rank m, an estimate of $\mathbf{G}(e^{\mathrm{j}\omega_f T_\mathrm{s}})$ is given by the well-known H_1-estimator

$$\hat{\mathbf{G}}^{\mathrm{H}_1}(e^{\mathrm{j}\omega_f T_\mathrm{s}}) = \mathbf{Y}^{\mathrm{H}}(\omega_f)\mathbf{U}(\omega_f)[\mathbf{U}(\omega_f)\mathbf{U}(\omega_f)]^{-1}, \tag{6.5}$$

where $(\cdot)^{\mathrm{H}}$ denotes complex conjugate transpose. Due to the noise, this estimate will contain errors. The H_1-estimator is the best estimator if the output noise is much larger compared to the input noise (which is assumed zero in this chapter) [43].

If the system is excited using an orthogonal random phase multisine signal, the variance of the FRF estimates is minimized [65]. A scalar random phase multisine signal $x(t)$ can be written as

$$x(t) = \sum_{f=1}^{n_\mathrm{f}} A_f \cos(\omega_f t + \phi_f), \tag{6.6}$$

with amplitudes A_f, frequencies ω_f chosen from the grid $(2\pi f)/(N_\mathrm{p}T_\mathrm{s})$, $f = 1, \ldots, N_\mathrm{p}/2 - 1$ (N_p even), and random phase ϕ_f uniformly distributed in $[0, 2\pi)$. A random phase multisine signal is orthogonal if

$$\mathbf{U}(\omega_f) = X(\omega_f)\mathbf{O}, \tag{6.7}$$

with $\mathbf{O}$ an orthogonal matrix and $X(\omega_f)$ the DFT of $x(t)$ calculated in a similar way as Eq. (6.2). The optimal matrix $\mathbf{O}$, with constraints $|\mathbf{O}_{ik}| \leq 1$, is given by [65]

$$\mathbf{O}_{ik} = e^{\frac{2\pi\mathrm{j}}{m}(i-1)(k-1)}. \tag{6.8}$$

Under assumption that the noise $\mathbf{v}(t)$ is white, independent and identically distributed over the m different experiments, the estimate $\hat{\mathbf{G}}^{\mathrm{H}_1}(e^{\mathrm{j}\omega_f T_\mathrm{s}})$ is unbiased and if the orthogonal random phase multisine signal as in Eq. (6.7) is used, the variance of each entry in $\hat{\mathbf{G}}^{\mathrm{H}_1}(e^{\mathrm{j}\omega_f T_\mathrm{s}})$ can be written as

$$\sigma^2_{\hat{G}^{\mathrm{H}_1}_{ik}}(e^{\mathrm{j}\omega_f T_\mathrm{s}}) = \frac{\sigma^2_{V,ii}(\omega_f)}{m|U_k(\omega_f)|^2}, \tag{6.9}$$

in which $\sigma^2_{V,ii}(\omega_f)$ is the output variance for output i.

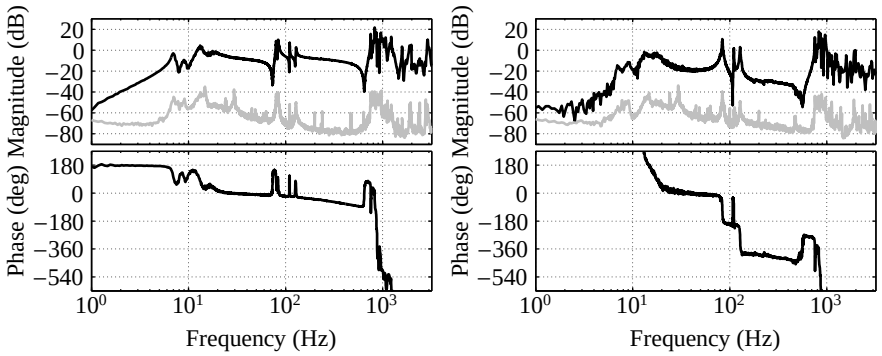

(a) $\hat{G}^{\mathrm{H}_1}_{55}(e^{\mathrm{j}\omega_f T_\mathrm{s}})$ and $\sigma_{\hat{G}^{\mathrm{H}_1}_{55}}(e^{\mathrm{j}\omega_f T_\mathrm{s}})$. (b) $\hat{G}^{\mathrm{H}_1}_{15}(e^{\mathrm{j}\omega_f T_\mathrm{s}})$ and $\sigma_{\hat{G}^{\mathrm{H}_1}_{15}}(e^{\mathrm{j}\omega_f T_\mathrm{s}})$.

Fig. 6.1: FRF estimates $\hat{G}^{\mathrm{H}_1}_{55}(e^{\mathrm{j}\omega_f T_\mathrm{s}})$ and $\hat{G}^{\mathrm{H}_1}_{15}(e^{\mathrm{j}\omega_f T_\mathrm{s}})$ (black lines), and their standard deviations $\sigma_{\hat{G}^{\mathrm{H}_1}_{55}}(e^{\mathrm{j}\omega_f T_\mathrm{s}})$ and $\sigma_{\hat{G}^{\mathrm{H}_1}_{15}}(e^{\mathrm{j}\omega_f T_\mathrm{s}})$ (gray lines) of the six-axes vibration isolator.

6.3.2 Characteristic loci

The CL estimates can be constructed from computing the eigenvalues from the square FRF matrix of Eq. (6.5) at each excited frequency ω_f

$$\hat{\mathbf{G}}^{\mathrm{H}_1}(e^{\mathrm{j}\omega_f T_\mathrm{s}}) = \hat{\mathbf{\Phi}}(\omega_f)\hat{\mathbf{\Lambda}}(\omega_f)\hat{\mathbf{\Phi}}^{-1}(\omega_f), \tag{6.10}$$

with

$$\hat{\mathbf{\Lambda}}(\omega_f) = \mathrm{diag}(\hat{\lambda}_1(\omega_f), \ldots, \hat{\lambda}_m(\omega_f)), \tag{6.11}$$

in which $\hat{\lambda}_i(\omega_f)$ is the ith eigenvalue of $\hat{\mathbf{G}}^{\mathrm{H}_1}(e^{\mathrm{j}\omega_f T_\mathrm{s}})$ and $\hat{\mathbf{\Phi}}(\omega_f)$ is the matrix with the corresponding eigenvector as the ith column. The CL estimates need to be sorted to obtain traces that are approximately continuous. Therefore, an algorithm is used which sorts the eigenvalues $(\hat{\lambda}_1(\omega_{f+1}), \ldots, \hat{\lambda}_m(\omega_{f+1}))^\mathrm{T}$ that are evaluated at frequency ω_{f+1} such that the total distance $\sum_{i=1}^{m} |\hat{\lambda}_i(\omega_{f+1}) - \hat{\lambda}_i(\omega_f)|$ is minimal with respect to the eigenvalues $(\hat{\lambda}_1(\omega_f), \ldots, \hat{\lambda}_m(\omega_f))^\mathrm{T}$ that are evaluated at frequency ω_f. In [14, 37] the sorting of the CL estimates is discussed in more detail.

Fig. 6.1(a) shows an example of the FRF estimate for one of the six co-oriented actuator-sensor-pairs of the six-axes vibration isolator. Fig. 6.1(b) shows an example of the FRF estimate for a non-co-oriented actuator-sensor-pair. It is visible that multiple closely spaced peaks are present at low frequencies (7–18 Hz) indicating modes with multiple closely spaced poles, while many resonance peaks are present in the range 700–3 200 Hz.

Fig. 6.2 shows the six CL estimates of the same system. It is observed that for each mode only one of the CL estimates shows as a peak (for example the

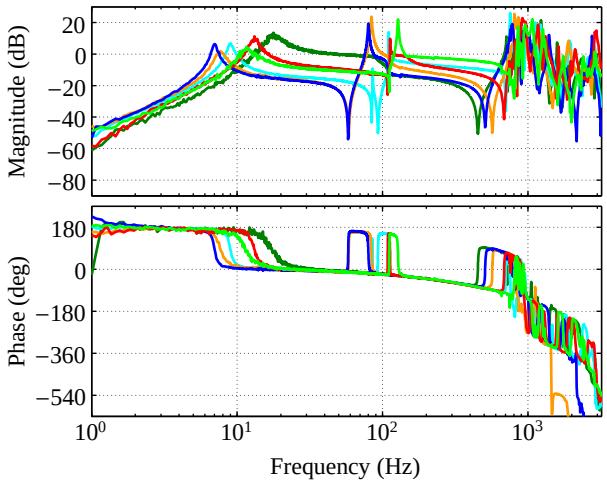

Fig. 6.2: The magnitude plots of the six CL estimates of the same system.

six peaks at low frequencies represent the six suspension modes of the vibration isolator). Since the number of peaks is larger than six, each of the CL estimates shows multiple peaks, where each peak appears at a different frequency. If multiple CL estimates show a peak at (approximately) the same frequency, this means that there are multiple modes with (approximately) the same resonance frequency. This can be expected in for example symmetric structural dynamic systems. The used sorting algorithm is capable of realizing CL estimates that, due to measurement noise, are only approximately continuous. This is reflected by the jumps between some of the CL estimates, see in-between 1 and 10 Hz in Fig. 6.2. However, it appears that this hardly affects the estimation of poles.

6.4 CL estimator

In the first step of the system identification method, the CL estimator is used to identify the system poles from the CL estimates. The individual steps that are required for this task are listed below.

1. On each of the m CL estimates, a discrete-time model, based on a rational fraction polynomial (RFP), is curvefitted. An RFP is a fraction of two rational polynomials. The numerator and denominator polynomial are both of order n. Since each mode appears in only one of the

CL estimates as a peak, the CL estimator requires m RFPs to identify all poles.

2. For each of the CL estimates, the coefficients of both polynomials are found as the solution of a least squares (LS) problem. A constrained on the coefficients has to be imposed, such that one of the coefficients of the denominator polynomial is fixed to 1.

3. The discrete system poles are calculated as the roots of each denominator polynomial and converted to continuous system poles. The continuous system poles are separated into stable and unstable poles. Stable poles are associated with physical poles, while unstable poles are associated with mathematical poles.

4. For each of the CL estimates, steps 2–4 are repeated n times for increasing model orders from 1 to n. The maximum order is set by the user. Steps 2–4 are repeated n times for varying the fixed coefficient of the denominator polynomial. It is shown that by doing these repetitions, the differences between physical and mathematical poles become more clear. For each of the CL estimates, the poles are plotted in a so-called stabilization chart for increasing the model order. The poles are also plotted in another stabilization chart for varying the fixed coefficient. The stabilization charts are used to distinguish between the (stable) physical poles and the (unstable) mathematical poles.

5. The stabilization charts are also used to distinguish between complex conjugated pole pairs, which are associated with structural dynamics, and real poles, which are associated with non-structural dynamics, for example actuator/sensor dynamics. It is shown how the FRF estimates can be compensated for poles due to non-structural dynamics as well as for delays.

6. The final step is that for each of the CL estimates the stable complex conjugated pole pairs are kept, resulting in a total number of n_m complex conjugated pole pairs. After sorting, the n_m resonance frequencies and n_m damping ratios are calculated from the n_m complex conjugated pole pairs, corresponding to n_m identified modes. In the next section, these are used together with the compensated FRF estimates to derive the state-space model.

Step 1. RFPs

The CL estimator uses a discrete-time model, which is based on an RFP, to be curvefitted on each of the CL estimates. The formulation is similar to the LSCF estimator described in [4, 11, 62]. The LSCF estimator uses a common-denominator model to be curvefitted on all FRF estimates in a least squares sense. Since all FRF estimates are used simultaneously, the common-denominator model is able to identify all poles in one shot. The CL estimator requires m RFPs to identify all poles. Each RFP is expressed as

$$\hat{\lambda}_i^{\text{RFP}}(\omega_f) = \frac{N_i(\omega_f)}{D_i(\omega_f)} = \frac{\sum_{l=0}^{n} \Omega_l(\omega_f)\beta_{il}}{\sum_{l=0}^{n} \Omega_l(\omega_f)\alpha_{il}}, \tag{6.12}$$

for $i = 1, \ldots, m$ and $f = 1, \ldots, n_\text{f}$ the index of the excited frequencies. α_{il} and β_{il} are the real-valued coefficients of the denominator polynomial $D_i(\omega_f)$ and numerator polynomial $N_i(\omega_f)$, that are to be estimated and are both of order n. Several choices are possible for the polynomial basis functions $\Omega_l(\omega_f)$. For a discrete-time model, the functions $\Omega_l(\omega_f)$ are usually given by $\Omega_l(\omega_f) = e^{\text{j}\omega_f T_\text{s} l}$ but a better choice is to use

$$\Omega_l(\omega_f) = e^{\text{j}\pi(\omega_f/\omega_\text{s})T_\text{s} l}, \tag{6.13}$$

with $\omega_\text{s} = \omega_{n_\text{f}} T_\text{s}/\pi$ a scaling factor and ω_{n_f} the highest excited frequency. With the latter choice, the FRF data is projected in the z-domain in the interval $[0, \pi)$, instead of only a part of it. This improves the numerical conditioning of the equations and only system poles in the range $[0, \omega_{n_\text{f}}]$ will be identified. Replacing the model $\hat{\lambda}_i^{\text{RFP}}(\omega_f)$ with the estimate $\hat{\lambda}_i(\omega_f)$ of Eq. (6.11) allows to rewrite Eq. (6.12) as

$$\sum_{l=0}^{n} \Omega_l(\omega_f)\beta_{il} - \sum_{l=0}^{n} \Omega_l(\omega_f)\hat{\lambda}_i(\omega_f)\alpha_{il} \approx 0. \tag{6.14}$$

Eq. (6.14) can be weighted with a frequency-dependent function $W_i(\omega_\text{f})$. The quality of the estimation is often improved using adequate weighting [43].

Step 2. LS problem

Since Eq. (6.14) is linear in the parameters, it can be reformulated as

$$[\mathbf{B}_i \ \mathbf{A}_i] \begin{Bmatrix} \boldsymbol{\beta}_i \\ \boldsymbol{\alpha}_i \end{Bmatrix} \approx \mathbf{0}, \tag{6.15}$$

with

$$\boldsymbol{\beta}_i = (\beta_{i0}, \beta_{i1}, \ldots, \beta_{in})^{\mathrm{T}}, \qquad \boldsymbol{\alpha}_i = (\alpha_{i0}, \alpha_{i1}, \ldots, \alpha_{in})^{\mathrm{T}},$$

$$\mathbf{B}_i = \begin{Bmatrix} \boldsymbol{B}_i(\omega_1) \\ \boldsymbol{B}_i(\omega_2) \\ \vdots \\ \boldsymbol{B}_i(\omega_{n_\mathrm{f}}) \end{Bmatrix}, \qquad \mathbf{A}_i = \begin{Bmatrix} \boldsymbol{A}_i(\omega_1) \\ \boldsymbol{A}_i(\omega_2) \\ \vdots \\ \boldsymbol{A}_i(\omega_{n_\mathrm{f}}) \end{Bmatrix},$$

$$\boldsymbol{B}_i(\omega_f) = W_i(\omega_\mathrm{f})(\Omega_0(\omega_f), \Omega_1(\omega_f), \ldots, \Omega_n(\omega_f)),$$

$$\boldsymbol{A}_i(\omega_f) = -\boldsymbol{B}_i(\omega_f)\hat{\lambda}_i(\omega_f).$$

Herein $\mathbf{J}_i = [\mathbf{B}_i \ \mathbf{A}_i]$ is the (complex) Jacobian matrix of the least squares (LS) problem with n_f rows and $2(n+1)$ columns. To solve the LS problem, the normal equations have to be constructed from the Jacobian matrix. Real-valued coefficients are obtained if the Jacobian matrix is transformed to a real-valued matrix. This can be formulated as $\mathbf{J}_{\mathrm{Re}}^{\mathrm{T}}\mathbf{J}_{\mathrm{Re}} = \mathrm{Re}(\mathbf{J}^{\mathrm{H}}\mathbf{J})$ or

$$\begin{bmatrix} \mathbf{H}_i & \boldsymbol{\Gamma}_i \\ \boldsymbol{\Gamma}_i^{\mathrm{T}} & \boldsymbol{\Delta}_i \end{bmatrix} \begin{Bmatrix} \boldsymbol{\beta}_i \\ \boldsymbol{\alpha}_i \end{Bmatrix} \approx \mathbf{0}, \tag{6.16}$$

with $\mathbf{H}_i = \mathrm{Re}(\mathbf{B}_i^{\mathrm{H}}\mathbf{B}_i)$, $\boldsymbol{\Gamma}_i = \mathrm{Re}(\mathbf{B}_i^{\mathrm{H}}\mathbf{A}_i)$, and $\boldsymbol{\Delta}_i = \mathrm{Re}(\mathbf{A}_i^{\mathrm{H}}\mathbf{A}_i)$. Elimination of the $\boldsymbol{\beta}_i \approx -\mathbf{H}_i^{-1}\boldsymbol{\Gamma}_i\boldsymbol{\alpha}_i$ yields

$$(\boldsymbol{\Delta}_i - \boldsymbol{\Gamma}_i^{\mathrm{T}}\mathbf{H}_i^{-1}\boldsymbol{\Gamma}_i)\boldsymbol{\alpha}_i \approx \mathbf{0}, \tag{6.17}$$

or $\mathbf{L}_i\boldsymbol{\alpha}_i \approx \mathbf{0}$ with $\mathbf{L}_i = \boldsymbol{\Delta}_i - \boldsymbol{\Gamma}_i^{\mathrm{T}}\mathbf{H}_i^{-1}\boldsymbol{\Gamma}_i$. The size of the square matrix $\mathbf{L}_i$ is $n+1$ which is smaller than the original normal equation Eq. (6.15). To obtain a nontrivial solution, a constraint has to be imposed on the coefficients to be estimated.

In [11] it is suggested to set the last coefficient of $\boldsymbol{\alpha}_i$ to 1 (i.e. $\alpha_{in} = 1$). This leads to stable physical poles and unstable mathematical poles, see [11] for the details on this observation. The LS solution of Eq. (6.17) is given by

$$\boldsymbol{\alpha}_i^{\mathrm{LS}} = \begin{Bmatrix} -[\mathbf{L}_i(1:n, 1:n)]^{-1}\mathbf{L}_i(1:n, n+1) \\ 1 \end{Bmatrix}. \tag{6.18}$$

There exist $n+1$ different LS solutions depending on which coefficient of $\boldsymbol{\alpha}_i$ is fixed. In [11] it is demonstrated that by varying the fixed coefficient from the lowest coefficient (α_{i0}) to the highest coefficient (α_{in}) the mathematical poles tend from stable to unstable, while the (stable) physical poles remain unchanged. Hence, setting $\alpha_{in} = 1$ facilitates the distinction between physical and mathematical poles.

Step 3. System poles

The discrete system poles corresponding to the ith CL estimate can be calculated as the roots of the denominator polynomial with coefficients $\boldsymbol{\alpha}_i$ from Eq. (6.18). Each discrete system pole p_{il}^{disc} can be transformed to a continuous system pole p_{il}^{cont} by the transformation

$$p_{il}^{\text{cont}} = \frac{\omega_s}{T_s} \ln(p_{il}^{\text{disc}}), \tag{6.19}$$

where scaling factor ω_s is needed to correct for the mapping if $\Omega_l(\omega_f) = e^{j\pi(\omega_f/\omega_s)T_s l}$ of Eq. (6.13) has been used for the polynomial basis functions instead of $\Omega_l(\omega_f) = e^{j\pi\omega_f/T_s l}$.

Step 4. Stabilization charts

The continuous system poles can be plotted for increasing the model order in a so-called stabilization chart. The computation of the poles for each model order can be done in an efficient way by solving Eq. (6.17) for submatrices of $\mathbf{L}_i$, see [62] for details. The continuous system poles can also be plotted for varying the fixed coefficient (i.e from $\alpha_{i0} = 1$ to $\alpha_{in} = 1$), see Figs. 6.3 and 6.4 for an example of both plots. Stable and unstable complex conjugated pole pairs are indicated with a black (+) and a red (·) respectively, while a black (o) and a red (o) indicate stable and unstable real poles. In agreement with [11] it is visible that physical poles are stable and their frequency locations remain unchanged for varying the model order or for varying the fixed coefficient, while mathematical poles are unstable and tend to scatter around in the stabilization charts. This is best visible for the complex conjugated pole pairs. For each of the CL estimates, the stable continuous system poles are kept. If desired, "accidentally stable" poles can be deleted by the user or "accidentally unstable" poles can be kept. In [62] an alternative method is presented to automatically select the poles.

Step 5. Non-structural dynamics

It is assumed that all complex conjugated pole pairs are due to the structural dynamics (each pole pair corresponds with one resonance frequency and one damping ratio). Stable real poles could be present as well, but in general these are due to the non-structural dynamics, for example actuator/sensor dynamics [6], hence the FRF estimates do not represent a system with true force excitations and true acceleration responses. If the same type of actuators/sensor

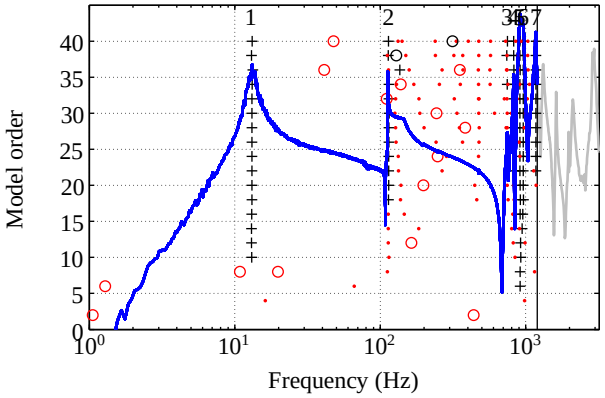

Fig. 6.3: Stabilization chart for the CL estimator with varying model orders, the poles are only shown for every second model order.

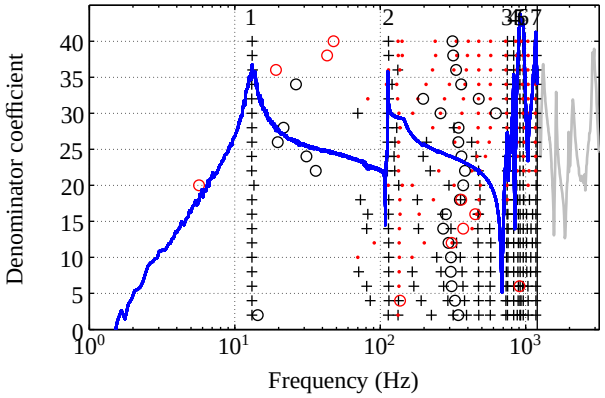

Fig. 6.4: Stabilization chart for the CL estimator with varying fixed denominator coefficients, the poles are only shown for every second model order.

is used for all inputs and outputs, each actuator/sensor pole should be present m times at approximately the same frequency. To let the FRF estimate represent a true structural dynamic system, it is suggested to compensate the FRF estimates for these real poles (e.g. by using an average value of the real poles). In a similar way, the FRF estimates can be compensated for delays by adding a integer number of delays such that the phase angle of the compensated FRF estimate is always (approximately) a multiple of 180°.

The compensated ikth FRF estimate reads

$$\hat{G}_{ik}^{\mathrm{comp}}(e^{\mathrm{j}\omega_f T_\mathrm{s}}) = \hat{G}_{ik}^{\mathrm{H}_1}(e^{\mathrm{j}\omega_f T_\mathrm{s}}) \sum_{l=1}^{n_\mathrm{r}} \frac{\mathrm{j}\omega_f + p_l^{\mathrm{real}}}{p_l^{\mathrm{real}}} e^{\mathrm{j}\omega_f T_\mathrm{s} n_\mathrm{d}}, \tag{6.20}$$

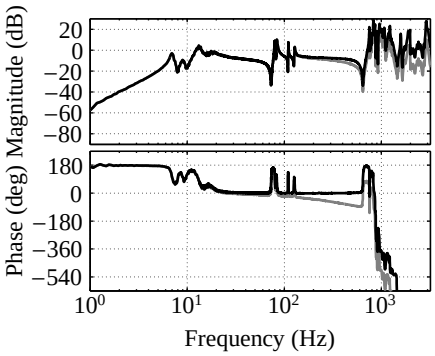

Fig. 6.5: Uncompensated FRF $\hat{G}_{55}^{\mathrm{H}_1}(e^{\mathrm{j}\omega_f T_s})$ (gray line) and compensated FRF $\hat{G}_{55}^{\mathrm{comp}}(e^{\mathrm{j}\omega_f T_s})$ (black line).

in which n_r and n_d are the number of real poles and delays respectively, with

$$p_l^{\mathrm{real}} = \frac{1}{m}\sum_{i=1}^{m} p_{il}^{\mathrm{real}}. \tag{6.21}$$

Fig. 6.5 shows an example of an uncompensated FRF estimate and a FRF in which is compensated for an actuator pole located at 331 Hz and one delay. It is observed that the phase angle of the compensated FRF estimate is always (approximately) a multiple of 180°.

Step 6. Resonance frequencies and damping ratios

From the total number of n_m continuous complex conjugated pole pairs that are kept and sorted the n_m damping ratios and n_m resonance frequencies are calculated:

$$\xi_l = -\frac{\mathrm{Re}(p_{2l-1}^{\mathrm{cont}})}{|p_{2l-1}^{\mathrm{cont}}|}, \qquad \omega_l = |p_{2l-1}^{\mathrm{cont}}|. \tag{6.22}$$

These correspond to n_m identified modes. In the next section the resonance frequencies and damping ratios are used to derive a state-space model.

6.5 Derivation of a state-space model

The second step of the system identification method is the derivation of a state-space model. Therefore several steps are involved:

1. The equation of motion describing the dynamics of a structural dynamic system can be written in the modal decoupled form if proportional damping is assumed. It is shown how this form can be written in the so-called pole/residue form.
2. A model having the structure of a pole/residue form is being curvefitted on each of the compensated FRF estimates. The poles are already known (the resonance frequencies and damping ratios are available from the previous section) and the entries of the residue matrices are found as the solution of a LS problem.
3. By the choice of the structure of the pole/residue form and by calculating a rank one approximation for each of the found residue matrices, the pole/residue form can be converted to a state-space model describing accelerance transfer functions.
4. If desired, the state-space model can be extended with the identified real poles and delays to include non-structural dynamics.

Step 1. Pole/residue form

Although the dynamics of the system has been considered to be a discrete system in the previous sections, the underlying dynamics is assumed to be that of a structural dynamic system which is described by

$$\begin{aligned} \mathbf{M}\ddot{\boldsymbol{q}}(t) + \mathbf{D}\dot{\boldsymbol{q}}(t) + \mathbf{K}\boldsymbol{q}(t) &= \mathbf{B}\boldsymbol{u}(t), \\ \boldsymbol{y}(t) &= \mathbf{C}\ddot{\boldsymbol{q}}(t). \end{aligned} \tag{6.23}$$

Herein, $\mathbf{M}$, $\mathbf{D}$ and $\mathbf{K}$ represent the mass, damping and stiffness matrices. $\boldsymbol{q}$ is the vector of the n_m degrees of freedom (DOFs) of the system. $\boldsymbol{u}$ is the input vector consisting of the excitation forces, $\boldsymbol{y}$ is the output vector containing the measured accelerations. $\mathbf{B}$ and $\mathbf{C}$ are the input and output matrices which relate the actuator forces and accelerations to the DOFs.

If $\mathbf{M}$ is non-singular, pre-multiplying Eq. (6.23) by $\mathbf{M}^{-1}$ gives

$$\ddot{\boldsymbol{q}}(t) + \mathbf{M}^{-1}\mathbf{D}\dot{\boldsymbol{q}}(t) + \mathbf{M}^{-1}\mathbf{K}\boldsymbol{q}(t) = \mathbf{M}^{-1}\mathbf{B}\boldsymbol{u}(t). \tag{6.24}$$

Assuming that $\mathbf{D}$ represents a proportional damping matrix, substituting the modal transformation $\boldsymbol{q} = \mathbf{P}\boldsymbol{z}$ into Eq. (6.24) and pre-multiplying by $\mathbf{P}^{-1}$ results in the modal decoupled equation of motion

$$\begin{aligned} \ddot{\boldsymbol{z}}(t) + \boldsymbol{\Xi}\dot{\boldsymbol{z}}(t) + \boldsymbol{\Omega}^2\boldsymbol{z}(t) &= \mathbf{P}^{-1}\mathbf{M}^{-1}\mathbf{B}\boldsymbol{u}(t), \\ \boldsymbol{y}(t) &= \mathbf{C}\mathbf{P}\ddot{\boldsymbol{z}}(t), \end{aligned} \tag{6.25}$$

in which $\mathbf{P}$ is the real-valued modal matrix corresponding to the eigenvalue problem of $\mathbf{M}^{-1}\mathbf{K}$, $\mathbf{\Xi} = \text{diag}(\xi_1, \cdots, \xi_{n_\text{m}})$, $\mathbf{\Omega} = \text{diag}(\omega_1, \cdots, \omega_{n_\text{m}})$, and $\xi_l = 2\zeta_l\omega_l$. ζ_l and ω_l are the damping ratio and resonance frequency of the lth mode respectively. The lth column of $\mathbf{P}$ is the corresponding normal mode shape vector.

The modal decoupled equation of motion of Eq. (6.25) can be expressed in the Laplace domain as

$$\begin{aligned}(\mathbf{I}_{n_\text{m}} s^2 + \mathbf{\Xi} s + \mathbf{\Omega}^2)\boldsymbol{Z}(s) &= \mathbf{P}^{-1}\mathbf{M}^{-1}\mathbf{B}\boldsymbol{U}(s), \\ \boldsymbol{Y}(s) &= -\mathbf{C}\mathbf{P}s^2\boldsymbol{Z}(s). \end{aligned} \tag{6.26}$$

This can be rewritten to

$$\boldsymbol{Y}(s) = \sum_{l=1}^{n_\text{m}} \frac{s^2\mathbf{C}\mathbf{P}(:,l)\mathbf{P}^{-1}\mathbf{M}^{-1}\mathbf{B}(:,l)}{s^2 + 2\zeta_l\omega_l s + \omega_l^2}\boldsymbol{U}(s), \tag{6.27}$$

where $\mathbf{CP}(:,l)$ is the lth column of matrix $\mathbf{CP}$ and $\mathbf{P}^{-1}\mathbf{M}^{-1}\mathbf{B}(:,l)$ the lth row of matrix $\mathbf{P}^{-1}\mathbf{M}^{-1}\mathbf{B}$. These vectors form a dyadic matrix, the residue matrix, such that Eq. (6.27) can be written in the so-called pole/residue form

$$\boldsymbol{Y}(s) = \sum_{l=1}^{n_\text{m}} \frac{s^2\mathbf{R}_l}{s^2 + 2\zeta_l\omega_l s + \omega_l^2}\boldsymbol{U}(s) = \mathbf{G}_\text{pr}(s)\boldsymbol{U}(s), \tag{6.28}$$

with

$$\mathbf{G}_\text{pr}(s) = \sum_{l=1}^{n_\text{m}} \frac{s^2\mathbf{R}_l}{s^2 + 2\zeta_l\omega_l s + \omega_l^2}, \tag{6.29}$$

and

$$\mathbf{R}_l = \mathbf{C}\mathbf{P}(:,l)\mathbf{P}^{-1}\mathbf{M}^{-1}\mathbf{B}(:,l). \tag{6.30}$$

The model of Eq. (6.29) is the correct pole/residue form to describe acceleration transfer functions.

Step 2. LS problem

Since in a causal system the input and output matrices $\mathbf{B}$ and $\mathbf{C}$, the mass matrix $\mathbf{M}$ and the normal modal matrix $\mathbf{P}$ are all real-valued, the residue matrices $\mathbf{R}_l$ are real-valued as well. The real-valued coefficients of these residue matrices can be estimated by solving for each FRF estimate a LS problem using the n_m

identified resonance frequencies and damping ratios from Eq. (6.22) and the compensated FRF estimates of Eq. (6.20):

$$\begin{bmatrix} \mathrm{Re}(\boldsymbol{\Phi}) \\ \mathrm{Im}(\boldsymbol{\Phi}) \end{bmatrix} \begin{Bmatrix} \hat{r}_{ik,1} \\ \hat{r}_{ik,2} \\ \vdots \\ \hat{r}_{ik,n_\mathrm{m}} \end{Bmatrix} - \begin{Bmatrix} \mathrm{Re}(\hat{\mathbf{G}}_{ik}^{\mathrm{comp}}) \\ \mathrm{Im}(\hat{\mathbf{G}}_{ik}^{\mathrm{comp}}) \end{Bmatrix} \approx \mathbf{0}, \tag{6.31}$$

with $\hat{r}_{ik,l}$ the ikth coefficient of $\hat{\mathbf{R}}_l$ and

$$\boldsymbol{\Phi} = \begin{Bmatrix} \boldsymbol{\Phi}(\omega_1) \\ \boldsymbol{\Phi}(\omega_2) \\ \vdots \\ \boldsymbol{\Phi}(\omega_{n_\mathrm{f}}) \end{Bmatrix}, \qquad \hat{\mathbf{G}}_{ik}^{\mathrm{comp}} = \begin{Bmatrix} \hat{G}_{ik}^{\mathrm{comp}}(e^{\mathrm{j}\omega_1 T_\mathrm{s}}) \\ \hat{G}_{ik}^{\mathrm{comp}}(e^{\mathrm{j}\omega_2 T_\mathrm{s}}) \\ \vdots \\ \hat{G}_{ik}^{\mathrm{comp}}(e^{\mathrm{j}\omega_{n_\mathrm{f}} T_\mathrm{s}}) \end{Bmatrix},$$

$$\boldsymbol{\Phi}(\omega_f) = (d_1(\omega_f), d_2(\omega_f), \ldots, d_{n_\mathrm{m}}(\omega_f)),$$

$$d_l(\omega_f) = \frac{-\omega_f^2}{\omega_l^2 - \omega_f^2 + \mathrm{j}2\zeta_l\omega_l\omega_f}.$$

Using the compensated FRF estimates usually results in better estimates of the residues that using the original FRF estimates, since all non-structural dynamics has been filtered out. The compensated FRF estimates should have a phase angle which is always a multiple of 180°, hence no phase lag because of first order filters or delays may occur.

Step 3. State-space model

The estimation method of the residues using Eq. (6.31) has been adopted from [6], however in this reference additional residual terms have been used to correct for out-of-band modes. Although the use of residual terms leads results in a better prediction of the frequencies of the anti-resonances, it leads to a different structure of Eq. (6.29), hence it no longer represents a true accelerance transfer function, particularly at very low and very high frequencies. Therefore, the use of residual terms has been omitted in this chapter. Note that Eq. (6.31) can only be used under assumption of proportional damping. The derivation of a state-space model describing accelerance transfer functions in case of non-proportional damping is not straightforward, since it requires a pole/residue model with $2n_\mathrm{m}$ first-order polynomials in the denominator instead of n_m second-order polynomials [6].

From Eqs. (6.27) and (6.28) it is observed that the true residue matrices should be dyadic, i.e. the product of a column vector and a row vector, so its rank should equal one. A singular value decomposition can be used to obtain a rank one approximation of the estimated residue matrices.

$$\begin{aligned} \hat{\mathbf{R}}_l &= \mathbf{U}_l \mathbf{\Sigma}_l \mathbf{V}_l^{\mathrm{T}}, \\ \hat{\mathbf{R}}_{11} &= \mathbf{U}_l(:,1)\sigma_{l1}\mathbf{V}_l(:,1)^{\mathrm{T}}, \end{aligned} \tag{6.32}$$

where $\mathbf{\Sigma}_l = \mathrm{diag}(\sigma_{l1}, \ldots, \sigma_{lm})$ the singular values. Here, $\hat{\mathbf{R}}_{l1}$ is the best rank one approximation of $\hat{\mathbf{R}}_l$. Introducing the notation

$$\hat{\mathbf{B}}(l,:) = \sqrt{\sigma_{l1}}\,\{\mathbf{V}_l(:,1)\}^{\mathrm{T}}, \qquad \hat{\mathbf{C}}(:,l) = \sqrt{\sigma_{l1}}\mathbf{U}_l(:,1), \tag{6.33}$$

leads to the estimates $\hat{\mathbf{B}}$ for $\mathbf{P}^{-1}\mathbf{M}^{-1}\mathbf{B}$ and $\hat{\mathbf{C}}$ for $\mathbf{CP}$. This constraint on the residues is called minimality [6]. The columns of $\hat{\mathbf{C}}$ are (the observable parts of) the mode shapes, while the rows of $\hat{\mathbf{B}}$ are called the participation factors. The estimates become more reliable if the second and subsequent singular values are much smaller compared to the first singular value. If an identified resonance frequency has a multiplicity $n_l > 1$, also the second and subsequent singular values and the corresponding columns of $\mathbf{U}_l$ and $\mathbf{V}_l$ have to be used to construct the n_l observable parts of mode shape and participation vectors for that pole. However, the resulting columns of $\hat{\mathbf{C}}$ will be an (unknown) linear combination of the true observable parts of the mode shapes.

If the true system represents a collocated (or reciprocal) system, the true residue matrices are symmetric [6]. To force the identified residue matrices to be symmetric, the symmetric parts of the residue matrices could be used to determine the singular values

$$(\hat{\mathbf{R}}_l + \hat{\mathbf{R}}_l^{\mathrm{T}})/2 = \mathbf{U}_l \mathbf{\Sigma}_l \mathbf{V}_l^{\mathrm{T}}, \tag{6.34}$$

such that $\mathbf{U}_l = \mathbf{V}_l$.

From Eqs. (6.29) and (6.33) a state-space model can be derived with actuator forces as inputs and the measured accelerations as outputs:

$$\begin{aligned} \dot{\boldsymbol{x}}_{\mathrm{ss}}(t) &= \mathbf{A}_{\mathrm{ss}}\boldsymbol{x}_{\mathrm{ss}}(t) + \mathbf{B}_{\mathrm{ss}}\boldsymbol{u}(t), \\ \boldsymbol{y}(t) &= \mathbf{C}_{\mathrm{ss}}\boldsymbol{x}_{\mathrm{ss}}(t) + \mathbf{D}_{\mathrm{ss}}\boldsymbol{u}(t), \end{aligned}$$

or

$$\mathbf{G}_{\mathrm{ss}}(s) = \mathbf{C}_{\mathrm{ss}}(s\mathbf{I}_{2n_{\mathrm{m}}} - \mathbf{A}_{\mathrm{ss}})^{-1}\mathbf{B}_{\mathrm{ss}} + \mathbf{D}_{\mathrm{ss}}, \tag{6.35}$$

with

$$\begin{aligned} \boldsymbol{x}_{\mathrm{ss}}(t) &= \begin{Bmatrix} \boldsymbol{z}(t) \\ \dot{\boldsymbol{z}}(t) \end{Bmatrix}, \\ \mathbf{A}_{\mathrm{ss}} &= \begin{bmatrix} \mathbf{0} & \mathbf{I}_{n_{\mathrm{m}}} \\ -\boldsymbol{\Omega}^2 & -\boldsymbol{\Xi} \end{bmatrix}, \qquad & \mathbf{B}_{\mathrm{ss}} &= \begin{bmatrix} \mathbf{0} \\ \hat{\mathbf{B}} \end{bmatrix}, \\ \mathbf{C}_{\mathrm{ss}} &= \begin{bmatrix} -\hat{\mathbf{C}}\boldsymbol{\Omega}^2 & -\hat{\mathbf{C}}\boldsymbol{\Xi} \end{bmatrix}, \qquad & \mathbf{D}_{\mathrm{ss}} &= [\hat{\mathbf{C}}\hat{\mathbf{B}}]. \end{aligned}$$

Step 4. Including non-structural dynamics

If desired the state-space model Eq. (6.35) can be extended with the identified real poles

$$\mathbf{G}_{\mathrm{ss}}^{\mathrm{uncomp}}(s) = \mathbf{G}_{\mathrm{ss}}(s) \sum_{l=1}^{n_{\mathrm{r}}} \frac{p_l^{\mathrm{real}}}{s + p_l^{\mathrm{real}}}, \tag{6.36}$$

and, after converting from the continuous domain to the discrete domain using the zero-order-hold transformation [38], the identified delays

$$\mathbf{G}_{\mathrm{disc}}^{\mathrm{uncomp}}(e^{\mathrm{j}\omega_f T_{\mathrm{s}}}) = \mathbf{G}_{\mathrm{ss}}^{\mathrm{uncomp}}(e^{\mathrm{j}\omega_f T_{\mathrm{s}}}) e^{-\mathrm{j}\omega_f T_{\mathrm{s}} n_{\mathrm{d}}}, \tag{6.37}$$

can be added to $\mathbf{G}_{\mathrm{disc}}^{\mathrm{uncomp}}(e^{\mathrm{j}\omega_f T_{\mathrm{s}}})$ which is the discretized transfer function of $\mathbf{G}_{\mathrm{disc}}^{\mathrm{uncomp}}(s)$.

6.6 Reduced mass, damping and stiffness matrices

In the third step of the system identification method the reduced mass, damping and stiffness matrices will be derived from the state-space model of Eq. (6.35). The expression "reduced" is used since the number of sensors (and actuators) m is in general smaller than the number of identified modes n_{m}.

The presented method is based on a combination of the various methods described in [1] and [3, 35]. It uses a partition of the modal matrix $\mathbf{P}$ that is available from the derived state-space model. The methods described in these references all have some limitations. Reference [1] is only usable if $\mathbf{P}$ represents a mass normalized modal matrix. Unfortunately, $\mathbf{P}$ is not directly available being scaled as a mass normalized modal matrix. In [3] a way of scaling $\mathbf{P}$ is described, but only for the case $m = n_{\mathrm{m}}$. Reference [35] only provides for the reduced stiffness matrix. Since none of these references present a method to derive the reduced stiffness matrix as well as the reduces mass and damping matrix for a state-space model with the structure of Eq. (6.35) and for the case

$m < n_m$, the methods in [1] and [3, 35] need to be combined. In this section, the combined method is described.

The various steps required for obtaining the reduced mass, damping and stiffness matrices are listed below:

1. It is shown that modal matrix $\mathbf{P}$ consists of an observable partition $\mathbf{P}_o$ and an unobservable partition $\mathbf{P}_u$. It is assumed that there are one or more collocated actuator-sensor-pairs and it is assumed that the observable parts of the input and output matrices are invertible and are known.

2. An arbitrary scaled modal matrix $\mathbf{P}$ can be converted to a mass scaled modal matrix $\mathbf{Q}$ by introducing an (unknown) diagonal and invertible scaling matrix $\mathbf{T}$. Modal matrices $\mathbf{P}$ and $\mathbf{Q}$ contain the same eigenvectors although differently scaled. Matrix $\mathbf{T}$ can be solved for, using the input and output matrices of a collocated actuator-sensor-pair that are available from the state-space model of Eq. (6.35). Once $\mathbf{T}$ is known, the observable partition of the mass normalized modal matrix, $\mathbf{Q}_o$, is calculated using again the input and output matrices available from the state-space model of Eq. (6.35).

3. Using $\mathbf{Q}_o$ and submatrices of the state-space model of Eq. (6.35), the reduced mass, damping and stiffness matrices are calculated similar as in [1].

Step 1. Observable partition of the modal matrix

Assume that the identified model of Eq. (6.35) and the true model of Eq. (6.23) represent the same structural dynamic system and that there is at least one collocated actuator-sensor-pair. This means that actuator i and sensor i are attached to the same DOF. Since $m < n_m$, only m DOFs of the total number of n_m DOFs can be observed and controlled. Therefore, DOFs $\boldsymbol{q}$ in Eq. (6.23) can be partitioned into a set (o) of m DOFs that are observed and controlled, and a set (u) of $n_m - m$ DOFs that are not observed and not controlled. This means that the true input and output matrices $\mathbf{B}$ and $\mathbf{C}$ can also be partitioned as [3]

$$\mathbf{C} = [\mathbf{C}_o \;\; \mathbf{C}_u], \qquad \mathbf{B} = \begin{bmatrix} \mathbf{B}_o \\ \mathbf{B}_u \end{bmatrix}, \tag{6.38}$$

where the unobservable parts have to be zero. Hence $\mathbf{C}_\mathrm{u} = \mathbf{0}$ and $\mathbf{B}_\mathrm{u} = \mathbf{0}$, such that the output is given by

$$\boldsymbol{y}(t) = [\mathbf{C}_\mathrm{o} \;\; \mathbf{C}_\mathrm{u}] \begin{Bmatrix} \ddot{\boldsymbol{q}}_\mathrm{o}(t) \\ \ddot{\boldsymbol{q}}_\mathrm{u}(t) \end{Bmatrix} = \mathbf{C}_\mathrm{o} \ddot{\boldsymbol{q}}_\mathrm{o}(t). \tag{6.39}$$

Matrices $\mathbf{B}_\mathrm{o}$ and $\mathbf{C}_\mathrm{o}$ have to be square. Since these matrices describe the geometric relation between DOFs $\boldsymbol{q}_\mathrm{o}$ and the input and output respectively, it can be assumed that these matrices are invertible and are known. This is a geometrical relation, so the assumption is easily fulfilled in many applications. In addition, the transformation $\boldsymbol{q} = \mathbf{P}\boldsymbol{z}$ can be partitioned as

$$\begin{Bmatrix} \boldsymbol{q}_\mathrm{o}(t) \\ \boldsymbol{q}_\mathrm{u}(t) \end{Bmatrix} = \begin{bmatrix} \mathbf{P}_\mathrm{o} \\ \mathbf{P}_\mathrm{u} \end{bmatrix} \boldsymbol{z}(t), \tag{6.40}$$

where $\mathbf{P}_\mathrm{o}$ and $\mathbf{P}_\mathrm{u}$ are partitions of the eigenvectors at the observed and unobserved DOFs, respectively.

Step 2. Observable partition of the mass scaled modal matrix

In Eq. (6.25) $\mathbf{P}$ is the modal matrix containing the eigenvectors of $\mathbf{M}^{-1}\mathbf{K}$. Since the eigenvectors can be arbitrary scaled, it is allowed to define

$$\mathbf{Q} = \mathbf{P}\mathbf{T}, \tag{6.41}$$

where $\mathbf{T} = \mathrm{diag}(t_1, \ldots, t_{n_\mathrm{m}})$ is a (unknown) diagonal and invertible scaling matrix such that $\mathbf{Q}$ contains the same eigenvectors as $\mathbf{P}$, except the columns of $\mathbf{Q}$ are scaled differently. The same partition as in Eq. (6.40) can be used for $\mathbf{Q}$. If a mass normalized scaling of $\mathbf{Q}$ is used, which means that $\mathbf{Q}$ is scaled such that

$$\mathbf{Q}^\mathrm{T}\mathbf{K}\mathbf{Q} = \boldsymbol{\Omega}^2, \qquad \mathbf{Q}^\mathrm{T}\mathbf{D}\mathbf{Q} = \boldsymbol{\Xi}, \qquad \mathbf{Q}^\mathrm{T}\mathbf{M}\mathbf{Q} = \mathbf{I}_{n_\mathrm{m}}, \tag{6.42}$$

the input matrix $\mathbf{P}^{-1}\mathbf{M}^{-1}\mathbf{B}$ and the output matrix $\mathbf{C}\mathbf{P}$ of Eq. (6.25) can be written as

$$\begin{aligned} \mathbf{P}^{-1}\mathbf{M}^{-1}\mathbf{B} &= \mathbf{T}\mathbf{Q}^{-1}\mathbf{Q}\mathbf{Q}^\mathrm{T}[\mathbf{I}_m \;\; \mathbf{0}]^\mathrm{T}\mathbf{B}_\mathrm{o} = \mathbf{T}\mathbf{Q}_\mathrm{o}^\mathrm{T}\mathbf{B}_\mathrm{o}, \\ \mathbf{C}\mathbf{P} &= \mathbf{C}_\mathrm{o}[\mathbf{I}_m \;\; \mathbf{0}]\mathbf{Q}\mathbf{T}^{-1} = \mathbf{C}_\mathrm{o}\mathbf{Q}_\mathrm{o}\mathbf{T}^{-1}, \end{aligned} \tag{6.43}$$

where $\mathbf{Q}_\mathrm{o}$ is the partition of $\mathbf{Q}$ at the observed DOFs similar as in Eq. (6.40). The identified approximations $\hat{\mathbf{B}}$ for $\mathbf{P}^{-1}\mathbf{M}^{-1}\mathbf{B}$ and $\hat{\mathbf{C}}$ for $\mathbf{C}\mathbf{P}$ of Eq. (6.33) result in

$$\hat{\mathbf{B}} = \mathbf{T}\mathbf{Q}_\mathrm{o}^\mathrm{T}\mathbf{B}_\mathrm{o} \;\Rightarrow\; \mathbf{Q}_\mathrm{o}^\mathrm{T} = \mathbf{T}^{-1}\hat{\mathbf{B}}\mathbf{B}_\mathrm{o}^{-1}, \tag{6.44}$$

$$\hat{\mathbf{C}} = \mathbf{C}_\mathrm{o}\mathbf{Q}_\mathrm{o}\mathbf{T}^{-1} \;\Rightarrow\; \mathbf{Q}_\mathrm{o} = \mathbf{C}_\mathrm{o}^{-1}\hat{\mathbf{C}}\mathbf{T}. \tag{6.45}$$

The unknown scaling matrix $\mathbf{T}$ can be solved for one of the collocated actuator-sensor-pairs using Eq. (6.44) and Eq. (6.45):

$$\mathbf{C}_\mathrm{o}^{-1}\hat{\mathbf{C}}(i,:)\mathbf{T}^2 = \mathbf{B}_\mathrm{o}^{-\mathrm{T}}\hat{\mathbf{B}}^\mathrm{T}(:,i). \tag{6.46}$$

For a true collocated system, Eq. (6.46) should result in the same value of $\mathbf{T}$ for all actuator-sensor-pairs. In practice, $\mathbf{T}$ can be obtained by taking the average $\mathbf{T}$ over all all actuator-sensor-pairs. Once $\mathbf{T}$ is known the observable partition $\mathbf{Q}_\mathrm{o}$ of the mode shape matrix can be calculated from either Eq. (6.44) or Eq. (6.45). The interested reader is referred to [3] for more information about this method. Note that if symmetrical residue matrices as in Eq. (6.34) are used to estimate the input and output matrices from Eq. (6.33), and $\mathbf{C}_\mathrm{o} = \mathbf{B}_\mathrm{o}^\mathrm{T}$, the left and right singular values are identical, hence $\mathbf{T} = \mathrm{diag}(\sigma_{11}, \ldots, \sigma_{n_\mathrm{m}1})$.

Step 3. Reduced order matrices

In [1] it is explained that if the mode shape matrix is scaled according to Eq. (6.42) and that the observable partition $\mathbf{Q}_\mathrm{o}$ of the mode shape matrix, eigenvalue matrix $\boldsymbol{\Omega}$, and modal damping matrix $\boldsymbol{\Xi}$ are known, the reduced mass, damping and stiffness matrices can be calculated. These matrices are identical to the so-called Guyan reduced mass, damping and stiffness matrices. These are obtained if the forces associated with the not observed DOFs $\boldsymbol{q}_\mathrm{u}(t)$ are set to zero, while the forces associated with the observed DOFs $\boldsymbol{q}_\mathrm{o}(t)$ are kept, see section 5.4 and [17]. The reduced matrices read

$$\bar{\mathbf{K}} = [\mathbf{Q}_\mathrm{o}\boldsymbol{\Omega}^{-2}\mathbf{Q}_\mathrm{o}^\mathrm{T}]^{-1}, \tag{6.47}$$

$$\bar{\mathbf{D}} = \bar{\mathbf{K}}\mathbf{Q}_\mathrm{o}\boldsymbol{\Omega}^{-2}\boldsymbol{\Xi}\boldsymbol{\Omega}^{-2}\mathbf{Q}_\mathrm{o}^\mathrm{T}\bar{\mathbf{K}}, \tag{6.48}$$

$$\bar{\mathbf{M}} = \bar{\mathbf{K}}\mathbf{Q}_\mathrm{o}\boldsymbol{\Omega}^{-4}\mathbf{Q}_\mathrm{o}^\mathrm{T}\bar{\mathbf{K}}. \tag{6.49}$$

There is a sign choice for the square roots when Eq. (6.46) is solved for the scaling factors in $\mathbf{T}$, however, this does not have any effect on the identified reduced matrices [3].

6.7 Illustrative example

The presented system identification method is illustrated with the system identification of the six-axes active hard mount vibration isolator of Fig. 5.3 which is described in the previous chapter. The goals of the system identification are to identify a model which describes the relevant dynamics and to identify the

reduced mass, stiffness and damping matrices that are used to design the modal controller in chapter 7.

Six different experiments were performed. For each experiment, the six input voltages were an orthogonal random phase multisine signal as described in section 6.3. The signal consisted of 2 136 sines with each a different frequency in the range 1–3 200 Hz, the same amplitude and a random phase, and it contained $N_p = 2^{16}$ samples per period. Each experiment contained $P = 5$ periods. Samples were recorded at a sample frequency of 6 400 Hz. The frequency grid the multisine signal was linear in the range from about 1 to 120 Hz and approximately logarithmic above 120 Hz. With this choice of the frequency grid a high frequency resolution at low frequencies is obtained while the number of FRF points was limited.

Using the framework described in section 6.3, the FRF estimates and their variances were calculated as well as the CL estimates. The FRF estimate $\hat{G}_{55}^{H_1}(e^{j\omega_f T_s})$ (corresponding to a collocated actuator-sensor-pair) and FRF estimate $\hat{G}_{15}^{H_1}(e^{j\omega_f T_s})$ (corresponding to a non-collocated actuator-sensor-pair) as well as their standard deviations were already shown in Figs. 6.1(a) and (b). The six corresponding CL estimates were presented in Fig. 6.2. The six peaks of the CL estimates in-between 7 and 18 Hz represent the six suspension modes of the system. It is visible that the second mode which can hardly be distinguished from the first mode is observable in a separate CL estimate. The system has six internal modes around 100 Hz and many more internal modes above 700 Hz.

From the CL estimates the poles were estimated with the CL estimator by curvefitting on each of the CL estimates an RFP of order 40 with the polynomial basis functions Eq. (6.13), see section 6.4. The weighting function is chosen as $W_i(\omega_f) = 1/(2\pi\omega_f)$. With this choice, the emphasis is on a more accurate identification of the low-frequency poles that correspond to the suspension modes of the vibration isolator. For the pole estimates, the CL estimates with frequencies up to only 1 200 Hz have been used. Although above this frequency many peaks are present in Fig. 6.2, it is thought that these peaks do not present relevant information for the goal of the system identification. If CL estimates with many frequencies above 1 200 Hz would be included, an accurate estimation of low-frequency poles becomes more difficult, even with this choice of the weighting function.

Using stabilization charts, the poles were separated into stable physical poles that were kept and unstable mathematical poles that were removed, see Figs. 6.3(a) and (b) for the stabilization charts corresponding to the the first CL

Table 6.1: Identified poles (continued on next page).

	CL estimator			LSCF estimator	
Mode	Freqency (Hz)	Damping (%)	CL	Frequency (Hz)	Damping (%)
1	7.0	3.5	6	7.0	3.6
2	7.7	6.4	1		
3	8.8	5.6	5	9.1[a]	1.2
4	12.1	6.5	4	13.1	2.4
5	13.2	5.4	3		
6	18.1	8.1	2	18.4	11.9
7	79.9	0.7	6	80.0	0.7
8	83.9	0.6	1	84.0	0.6
9	84.4	26.6	5		
10	109.8	0.2	5	110.2	0.2
11	114.1	0.6	3	112.7	0.2
12	127.3	0.3	4	127.9	0.6
13				133.6	0.5
14				182.0	0.0
15				225.1	0.6
16				456.3	1.0
17				658.9	0.0
18	710.0	0.0	2	714.2	0.4
19	748.6	0.8	3		
20	753.0	0.2	5	755.4	0.4
21	767.0	2.9	6	777.4	1.0
22	806.5	0.6	1	805.4	0.6

estimate. Based on the visual inspection of all stabilization charts, in total 14 “accidentally” stable poles were removed, and no “accidentally” unstable pole were kept. Each of the RFPs curvefitted on the CL estimates contained one stable real pole ranging from 264 to 404 Hz. It appeared that increasing the model order did not result in a larger number of stable poles or better estimates of the complex conjugated pole pairs, however it did have a large influence on the location of the real poles. This is because (poorly damped) complex conjugated pole pairs had a much larger influence on the fit of the LS estimator than the real poles.

In total 33 complex conjugated pole pairs and six real poles were identified using the CL estimator and their frequencies and damping ratios are given in Table 6.1. Their values were compared to the identified poles using the LSCF estimator of [4]. If the LSCF estimator would have been used with the FRF estimates for the complete frequency range of 1–1 200 Hz and a model order of 80 was chosen, only two of the six poles in-between 7 and 18 Hz, that represent the six suspension modes, were found at 9.3 and 17.2 Hz, see Fig. 6.6. To

Table 6.1: Identified poles (continued from previous page).

	CL estimator			LSCF estimator	
Mode	Frequency (Hz)	Damping (%)	CL	Frequency (Hz)	Damping (%)
23	813.4	0.5	2		
24	826.7	0.4	3	828.2	0.3
25	853.5	0.3	4		
26	854.8	0.9	1		
27	887.2	1.4	2	872.8	0.1
28	901.9	0.3	5	904.1	0.2
29	911.4	1.4	3		
30	916.6	0.4	6	931.7	0.1
31	956.7	1.0	4	950.9	0.3
33	960.0	1.3	1		
33	961.2	1.4	3	963.6	0.5
34	1 008.7	2.1	6	1 017.5	1.1
35	1 057.5	0.3	2	1 059.5	0.2
36	1 071.8	1.0	4	1 071.7	0.9
37	1 124.4	3.1	5	1 132.2	0.4
38	1 178.3	1.3	3	1 177.0	1.2
39	263.6	100.0	6		
40	313.9	100.0	3		
41	323.7	100.0	5		
42	331.2	100.0	1		
43	349.8	100.0	2		
44	403.6	100.0	4		

enable the identification of the poles at low frequencies, the FRF data was split into two pieces. First, the poles at low frequencies were identified using the FRF estimates in frequency range of 1–200 Hz, thereafter the poles at high frequencies were identified using the FRF estimates in the frequency range 200–1 200 Hz. The two sets of poles are displayed in one stabilization chart, see Fig. 6.7. The combined set of identified poles is also given in Table 6.1. For both data sets, a model of order 80 was curvefitted.

It is observed that both estimators identify approximately the same frequencies for most of the poles. The differences in identified damping ratios were larger, but this was probably due the low values of the damping ratios. The LSCF estimator was able to identify some additional poles in the frequency range in-between 130 and 650 Hz. These are poles which were identified as (unstable) mathematical poles using the CL estimator. However, it could be doubted whether some of these with the LSCF estimator identified poles should be considered as mathematical poles as well, see for example the poles at 225.1 and 456.3 Hz in Fig. 6.7. This was also illustrated by the plot of the CL

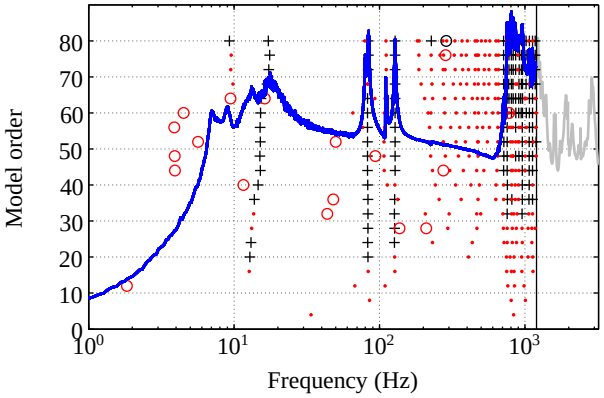

Fig. 6.6: Stabilization chart for the LSCF estimator with FRF estimates ranging from 1 to 1 200 Hz, the poles are only shown for every fourth model order.

estimates in Fig. 6.2, where it is visible that these poles do not result in poorly damped peaks. The LSCF estimator was able to identify only four of the six poles corresponding to the suspension modes, whereas the CL estimator identified all six poles. For the LSCF estimator, the pole at 9.1 Hz is considered as an "accidentally" unstable pole, and therefore marked with ([a]). In addition, the CL estimator identified a pole at 84.4 Hz with an unrealistic high value of the damping ratio. It can be doubted whether this is a true structural dynamic pole. The LSCF estimator was also not able to identify all poles in-between 700 and 1000 Hz, which are also closely spaced. Analysis of the vibration isolator revealed that these poles could be associated with structural dynamics within the actuators (due to the wire flexures). The LSCF estimator identified no real poles. It is concluded that both estimators can be used to identify the system poles, however the CL estimator outperforms the LSCF estimator in case of multiple closely spaced poles.

In the plot of the phase angle of the FRF estimates in Figs. 6.1(a) and (b), it is observed that above 100 Hz the system suffers from some phase lag. This is due to the presence of the real poles and some delays in the system. Analysis of the system revealed that the real poles were due to the inductance of the voice coil motors in the actuators and that the used electronics introduced a delay of about one sample time. By compensating the FRF estimates for the real poles by using Eq. (6.21) with the average value of 331 Hz and for the delay, the compensated FRF estimates were assumed to reflect only structural dynamics. This can also be concluded from Fig. 6.5 since the phase angle of the compensated FRF is always a multiple of 180°. It is visible that the collocation between actuator and sensor was lost above 900 Hz, since above

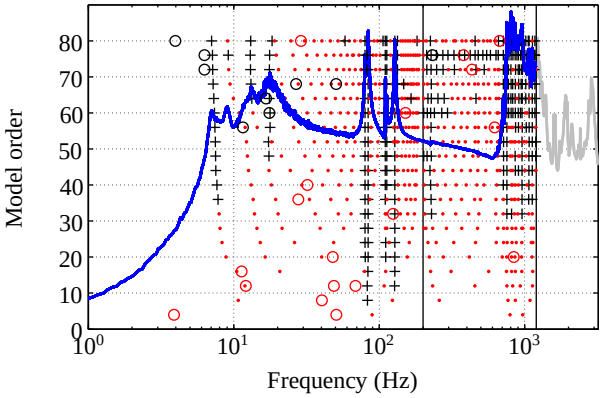

Fig. 6.7: Stabilization chart for the LSCF estimator with FRF estimates ranging from 1 to 200 Hz (left side of the vertical line) and FRF estimates ranging from 200 to 1 200 Hz (in-between the vertical lines), the poles are only shown for every fourth model order.

that frequency the phase angle is no longer in-between 0 and −180°. The implication of this is discussed below.

In a next step, for each of the 36 compensated FRF estimates the residues were calculated using Eq. (6.31). From the residues, the residue matrices were constructed for each of the complex conjugated pole pairs that were kept, and a rank one approximation was computed using a singular value decomposition. No poles with multiplicity > 1 were present, so the second and subsequent singular values were not needed in the calculation. The symmetry constraint Eq. (6.34) on the residue matrices was not used. The continuous state-space models for the compensated and uncompensated FRF estimates were calculated using Eqs. (6.35) and (6.36). The discrete state-space model including the one delay was computed from Eq. (6.37).

Figs. 6.8(a) and (b) show the (uncompensated) FRF estimates obtained with the H_1-estimator (red lines) of $\hat{G}_{55}^{H_1}(e^{j\omega_f T_s})$ for a collocated actuator-sensor-pair and $\hat{G}_{15}^{H_1}(e^{j\omega_f T_s})$ for a non-collocated actuator-sensor-pair as compared to the FRF computations of the discrete state-space model of Eq. (6.37) (blue lines). It is observed that the model fit for the collocated FRF seems slightly better than for the non-collocated FRF. This is because the non-collocated FRF $\hat{G}_{15}^{H_1}(e^{j\omega_f T_s})$ is more noisy below 5 Hz compared to the collocated FRF $\hat{G}_{55}^{H_1}(e^{j\omega_f T_s})$. This makes the non-collocated FRF estimate less reliable and therefore it becomes more difficult to fit a model on that FRF. The signal-to-noise ratio is also lower (compare the distance between the FRF estimates and its standard deviation). It is visible in Fig. 6.8(b) that the pole-residue model of Eq. (6.29) (black lines) fits slightly better than the state-space model fit of

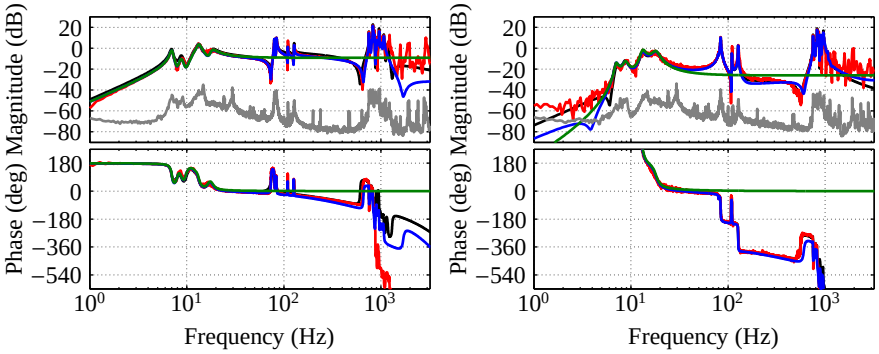

(a) FRF estimate $\hat{G}_{55}^{\mathrm{H}_1}(e^{\mathrm{j}\omega_f T_\mathrm{s}})$. (b) FRF estimate $\hat{G}_{15}^{\mathrm{H}_1}(e^{\mathrm{j}\omega_f T_\mathrm{s}})$.

Fig. 6.8: FRF estimates $\hat{G}_{55}^{\mathrm{H}_1}(e^{\mathrm{j}\omega_f T_\mathrm{s}})$ of a collocated actuator-sensor pair and $\hat{G}_{15}^{\mathrm{H}_1}(e^{\mathrm{j}\omega_f T_\mathrm{s}})$ of a non-collocated actuator-sensor-pair (red lines) and their standard deviations (gray lines), pole/residue model fits of Eq. (6.29) (black lines), state-space model fits of Eq. (6.37) (blue lines) and reduced state-space model fits (green lines).

Eq. (6.37). Note that the pole-residue model has also been compensated for the identified actuator pole and the delay. The worse fit of the state-space model is the price that has to be paid for using the rank one approximation of the residue matrices instead of using the full residue matrices. The fit below 130 Hz is still good. Since Fig. 6.8(b) shows one of the few worse fits of all 36 FRF estimates and the fit of Fig. 6.8(a) is excellent, it is concluded that the discrete state-space model of Eq. (6.37) fits the FRF estimates well. It is also concluded that the model represents accelerance transfer functions since the slope of the response at low frequencies is +40 dB/decade. The state-space models can for example be used for (closed loop) simulations but also to check the (observable partition of the) mode shapes which can be computed from Eq. (6.33).

As already was observed in Fig. 6.1(a), the collocation between actuator and sensor was lost above 900 Hz. Analysis of the system showed that this was due to the limited axial stiffness of the wire flexures that are mounted between each voice coil actuator and the corresponding accelerometer, see Fig. 5.1. It was also analyzed that the observed and controlled DOFs $\boldsymbol{q}_\mathrm{o}$ were due to the flexible membranes in the mounts, so these DOFs can be associated with the suspension modes. This means that DOFs $\boldsymbol{q}_\mathrm{o}$ appear at low frequencies (<20 Hz), while the DOFs due to the flexure stiffness, which are associated with the loss of collocation, appear at much higher frequencies (>900 Hz). Because of the large separation of frequencies, the loss of collocation will hardly affect the calculation of the reduced mass, damping and stiffness matrices, since these will represent the system's suspension dynamics only. It is assumed that the DOFs

$\boldsymbol{q}_o$ are in the axial direction of the mounts. Since the actuators and sensors also actuate and sense in the axial directions of the mounts, both input and output matrices have to be identity by geometric relations: $\mathbf{B}_o = \mathbf{C}_o = \mathbf{I}_m$. Using the framework of section 6.6 the reduced matrices were calculated. To check if these matrices represent the suspension dynamics a reduced state-space model was calculated as

$$\begin{aligned} \dot{\boldsymbol{x}}_{red}(t) &= \mathbf{A}_{red}\boldsymbol{x}_{red}(t) + \mathbf{B}_{red}\boldsymbol{u}(t), \\ \boldsymbol{y}(t) &= \mathbf{C}_{red}\boldsymbol{x}_{red}(t) + \mathbf{D}_{red}\boldsymbol{u}(t), \end{aligned} \tag{6.50}$$

with

$$\boldsymbol{x}_{red}(t) = \begin{Bmatrix} \boldsymbol{q}_o(t) \\ \dot{\boldsymbol{q}}_o(t) \end{Bmatrix},$$

$$\mathbf{A}_{red} = \begin{bmatrix} \mathbf{0} & \mathbf{I}_m \\ -\bar{\mathbf{M}}^{-1}\bar{\mathbf{K}} & -\bar{\mathbf{M}}^{-1}\bar{\mathbf{D}} \end{bmatrix}, \qquad \mathbf{B}_{red} = \begin{bmatrix} \mathbf{0} \\ \bar{\mathbf{M}}^{-1}\mathbf{B}_o \end{bmatrix},$$

$$\mathbf{C}_{red} = \begin{bmatrix} -\mathbf{C}_o\bar{\mathbf{M}}^{-1}\bar{\mathbf{K}} & -\mathbf{C}_o\bar{\mathbf{M}}^{-1}\bar{\mathbf{D}} \end{bmatrix}, \qquad \mathbf{D}_{red} = [\mathbf{C}_o\mathbf{B}_o].$$

The FRF estimates were also computed for the reduced model and shown in Figs. 6.8(a) and 6.8(b) (green lines). It is observed that the fits for low frequencies are good. Hence, the reduced mass, damping and stiffness matrices represent the suspension dynamics and can be used to design the modal controller in chapter 8 or to check the suspension mode shapes.

6.8 Discussion

Although the derivation of state-space models is done for acceleration transfer functions, the presented framework can also be used for receptance or mobility transfer functions (displacement or velocity response due to force excitation, respectively). Therefore, the s^2 in the output of Eq. (6.26) and in the numerators of Eqs. (6.27)–(6.29) has to be replaced with 1 and s for receptance and mobility transfer functions respectively, $-\omega_f^2$ in the numerator $d_l(\omega_f)$ of Eq. (6.31) has to be replaced with 1 and $\mathrm{j}\omega_f$ respectively, and the matrices $\hat{\mathbf{C}}_{ss}$ and $\hat{\mathbf{D}}_{ss}$ in Eq. (6.35) have to be replaced with $[\hat{\mathbf{C}} \;\; \mathbf{0}]$ and $[\mathbf{0} \;\; \hat{\mathbf{C}}]$ respectively and $\mathbf{0}$.

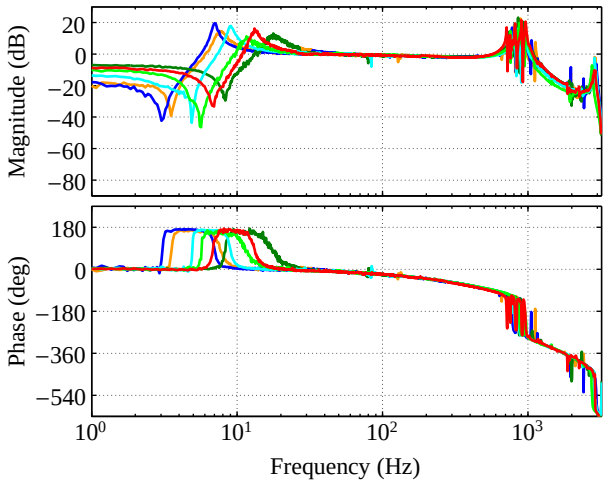

Fig. 6.9: The magnitude plots of the six CL estimates of the system with force response.

6.9 Comparison between identification and model

If the FRF estimates are compared with the FRF estimates of the acceleration responses due to force excitations for the flexible body model described in section 5.3, it is observed that the model FRF estimates resemble the FRF estimates well. This is for example visible by comparing Figs. 6.1(a) and (b) to Figs. 5.5(a) and (b) respectively. Except for small differences in damping ratios and small mismatches in the frequencies of the resonance peaks around 100 Hz, the FRF estimates and the modeled FRF estimates fit well for frequency up to 200 Hz. Since the effects of actuator dynamics and delays (see chapter 4), and high-frequency structural dynamics of the payload have not been included in the model, the differences between both sets of figures become larger above 200 Hz. If the CL estimates of Fig. 6.2 are compared with the modeled CL of Fig. 5.6, the same trends in the CL up to 200 Hz can be seen in both curves.

In this chapter, the force responses due to force excitations are not used for the system identification. However their FRF and CL estimates are also determined. The CL estimates are shown in Fig. 6.9. If this plot is compared with the plot of the modeled CL of Fig. 5.7, it is observed that both plots are alike, except for small differences in the low-frequency gain levels. These are due to errors for the values for the parasitic stiffness in the model.

By calculating the reduced stiffness matrix $\bar{\mathbf{K}}$ and mass matrix $\bar{\mathbf{M}}$, the modal matrix $\mathbf{P}_o$ can be calculated using Eq. (5.27). With the transformation matrix $\mathbf{R}$

Table 6.2: Modal matrix $\mathbf{\Phi}_o$ and resonance frequencies.

	7.0 Hz	7.7 Hz	8.7 Hz	12.2 Hz	13.2 Hz	18.1 Hz
x	−0.09	0.18	0.07	−0.01	0.03	0.02
y	0.14	0.08	0.10	−0.04	−0.01	0.00
z	0.05	0.06	−0.24	−0.01	0.01	0.01
θ_x	0.51	0.95	−0.06	0.99	−0.20	0.07
θ_y	0.84	−0.09	0.86	−0.08	0.96	0.20
θ_z	0.00	−0.23	0.42	−0.06	−0.22	0.98

of Eq. (5.1) as defined in section 5.2, the normal mode shapes can be expressed in terms of $\boldsymbol{x}_{\text{ref}}$ as modal matrix $\mathbf{\Phi}_o$ using Eq. (5.29). Table 6.2 shows these mode shapes, which are quiet similar to the modeled mode shapes of Table 5.2.

6.10 Conclusions

A novel three-steps method for the system identification of square structural dynamic systems is proposed. It is successfully applied to experimental data from the six-axes active hard mount vibration isolator.

In the first step, estimates of the CL are used for the identification of system poles. These are obtained from FRF estimates. It is shown that the use of CL estimates allows to separate modes with closely spaced poles from each other. A way to distinguish mathematical poles from physical poles is presented and it is explained how to compensate for non-structural dynamics due to actuator/sensor dynamics and delays. It is demonstrated that the proposed method outperforms the widely used LSCF estimator for the identification of closely spaced system poles.

In the second step, a model of the pole/residue form is being curvefitted on each of the FRF estimates. It is shown that this model has the correct structure to identify a state-space model describing accelerance transfer functions. Therefore, proportional damping has to be assumed.

In the third step the reduced mass, damping and stiffness matrices are obtained. It is shown how these matrices can be calculated if there is at least one collocated actuator-sensor-pair.

The main contribution of this chapter is that an identification model is available describing the dynamics of the demonstrator setup, which can be compared to the flexible body model derived in chapter 5, and that the reduced mass, damping and stiffness matrices can be used to design the modal controller in chapter 7.

Control strategies for a six-axes vibration isolator

Chapter 7

A novel method for designing a modal controller for the six-axes active hard mount vibration isolator is proposed, such that for each suspension mode not only its suspension frequency and damping ratio but also its mode shape can be tuned. The modal controller is based on either acceleration or force feedback. It is shown how the modal controller can be used to extend the control strategies of chapter 3 that are based on sensor fusion and two-sensor control, from the one-axis vibration isolator to the six-axes vibration isolator.

7.1 Introduction

In chapter 2 the deformation transmissibility is introduced as a measure of how floor vibrations lead to an internal deformation of the suspended equipment. The RMS value of the internal deformation determines the performance of the equipment. In many applications the allowable internal deformation is different for each direction. Since a deformation transmissibility is direction dependent, a different deformation transmissibility for each direction is required. A different transmissibility for each direction is required as well.

An example of such an application is a wafer stepper lithography machine [20]. An internal deformation in horizontal direction leads to a position error of the image that is exposed on the wafer, while a deformation in vertical direction leads to a focus error of the lens during exposure. A nanometer accuracy level is required for the position error, whereas the focus error may be much larger. Since in section 2.1 it is stated that vibration levels of the floor in horizontal and vertical direction are similar, the horizontal transmissibility has to be much lower than the vertical transmissibility.

Despite all efforts made by a design engineer of a six-axes vibration isolator,

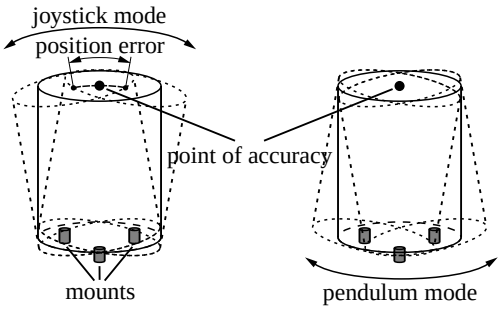

(a) Joystick mode of a TEM. (b) Pendulum mode of a TEM.

Fig. 7.1: (a) Joystick mode of a TEM, suspended by a vibration isolator with three mounts, leading to a relatively large position error at the point of accuracy. (b) Pendulum mode of a TEM leading to an (almost) zero position error at the point of accuracy.

its suspension modes are often coupled. This is for example the case in a vibration isolator suspending a symmetric payload with a high center of mass and a small footprint, such as a transmission electron microscope (TEM). This is also the case in a vibration isolator suspending an asymmetric payload, such as in the demonstrator setup described in chapter 5. If its suspension modes are coupled, the transmissibilities are coupled as well. This means that the transmissibilities show multiple resonance peaks. In combination with a large modal spread, this may lead to high transmissibilities for some directions.

This chapter presents a novel method for designing a modal controller for the six-axes active hard mount vibration isolator, in order to decouple its suspension mode shapes. This means that the transmissibilities can be decoupled as well. As a result, lower transmissibilities can be obtained. The design of the modal controller is such that for each suspension mode, not only its suspension frequency and damping ratio, but also its mode shape can be tuned. The modal controller consists of proportional and integral gain matrices which are used to add virtual mass and virtual damping. This is the same control strategy as for the one-axis active hard mount vibration isolator that is discussed in chapter 3, and it is referred to as *mode shaping modal control*. The possibility of tuning the suspension mode shapes provides an additional tool for designers of active vibration isolators to obtain the desired isolation performance.

Mode shaping modal control can be used for example to tune (some of) the suspension mode shapes of a vibration isolator suspending a TEM. Typically, two of the suspension modes correspond to rotation around two perpendicular axes in the plane of mounting at the bottom of the TEM, see Fig. 7.1(a). These

two modes are referred to as “joystick” modes. Since the point where the suspended payload needs to have its highest accuracy, the so-called *point of accuracy* (in this example the specimen port of the TEM) is usually located at the top of the TEM, the joystick modes lead to a relatively large position error at the point of accuracy, see again Fig. 7.1(a). Therefore it is desired to change the two joystick modes into two modes that correspond to rotation around two perpendicular axes which intersect in the point of accuracy, see Fig. 7.1(b). These two modes are referred to as “pendulum” modes. The pendulum modes result in an (almost) zero position error at the point of accuracy.

Whereas the control strategies described in chapter 3 require that the mass of the suspended payload and the stiffness of its suspension (damping is neglected) have to be known in order to choose the control parameters, mode shaping modal control requires that the mass, damping and stiffness matrices of a model describing the suspension dynamics of the vibration isolator have to be known. These matrices are available from either the reduced order model of section 5.4 or the identified reduced order model of section 6.6. With these matrices the suspension modes of the vibration isolator in open loop can be calculated. The desired suspension frequencies, damping ratios and mode shapes of the vibration isolator in closed loop have to be specified as well. With mode shaping modal control it is possible to obtain a different suspension frequency and a different damping ratio for each suspension mode.

7.2 Outline

Mode shaping modal control can be used with acceleration and force feedback as well as with sensor fusion and two-sensor control. First, the design of the modal controller for each of these control strategies is presented. Next, the modeling results are discussed.

In section 7.3 it is explained how the suspension mode shapes can be calculated from the mass, damping and stiffness matrices of a model of the vibration isolator describing its suspension dynamics. It is suggested to express the suspension mode shapes in terms of the coordinates of a reference frame located at the point of accuracy, which is the point where the suspended payload needs to have its highest accuracy. In subsection 5.3.2 it is already shown that the transmissibilities can also be expressed in therms of these coordinates.

In section 7.4 mode shaping modal control for acceleration and force feedback is discussed. First, it is explained how the proportional and integral gain matrices of the modal controller for acceleration feedback can be calculated. It

is shown how the obtained modal controller can be rewritten in order to decouple the system's plant, such that the multiple-input multiple-output (MIMO) tuning problem reduces to a single-input single-output (SISO) problem. As a result the MIMO (modal) controller reduces to a number of SISO controllers, stored at the diagonal entries of a diagonal controller. The SISO controllers are used to individually tune the suspension frequency and damping ratio of each suspension mode. Additional filtering can be added to each SISO controller. Next, the desired suspension frequencies, damping ratios and mode shapes of the vibration isolator in closed loop are specified. Finally, the modal controller for force feedback is derived.

Mode shaping modal control for sensor fusion and two-sensor control are discussed in sections 7.5 and 7.6. It is shown how to choose the control parameters for these control strategies to maximize the damping ratios of the internal modes of the suspended payload.

In section 7.7 the modeling results obtained with mode shaping modal control for acceleration feedback, sensor fusion and two-sensor control are shown. The achievable isolation performance regarding the transmissibility and deformation transmissibility is discussed. The compliance and deformability are not derived, since the third performance objective stated in section 2.5, which is providing a stiff suspension, has already been realized by using active hard mounts. The lowest suspension frequency is 7.0 Hz which is higher than the required suspension frequency of at least 5 Hz, see chapter 5.

7.3 Suspension mode shapes

To derive the mode shaping modal controller, the mass, damping and stiffness matrices of a model describing the suspension dynamics of the vibration isolator have to be known. These matrices are available from either the reduced order model of section 5.4 or the identified reduced order model of section 6.6. It is shown that with these matrices the suspension modes of the vibration isolator in open loop can be calculated and can be expressed in the coordinates of a reference frame located at the point of accuracy.

Reduced order model

The equation of motion corresponding to the reduced order model of Eq. (5.24) can be written in the Laplace domain as

$$(\bar{\mathbf{M}}s^2 + \bar{\mathbf{D}}s + \bar{\mathbf{K}})\boldsymbol{Q}_{\mathrm{o}}(s) = \mathbf{B}_{\mathrm{o}}\boldsymbol{F}_{\mathrm{a}}(s), \tag{7.1}$$

where $\boldsymbol{Q}_{\mathrm{o}}(s)$ is Laplace transformed vector of degrees of freedom (DOFs) $\boldsymbol{q}_{\mathrm{o}}$ that are associated with the suspension dynamics. $\boldsymbol{F}_{\mathrm{a}}$ is the vector of actuator forces. $\boldsymbol{B}_{\mathrm{o}}$ is the input matrix that relates actuator forces $\boldsymbol{F}_{\mathrm{a}}$ to DOFs $\boldsymbol{q}_{\mathrm{o}}$. The subscript "o" is used to indicate that the suspension dynamics is related to the observable and controllable DOFs, see also sections 5.4 and 6.6.

In case of acceleration feedback, the vector of accelerometer signals $\ddot{\boldsymbol{x}}_1$ is related to DOFs $\boldsymbol{q}_{\mathrm{o}}$ by the output matrix $\boldsymbol{C}_{\mathrm{o}}$ as

$$\ddot{\boldsymbol{X}}_1(s) = \mathbf{C}_{\mathrm{o}} s^2 \boldsymbol{Q}_{\mathrm{o}}(s). \tag{7.2}$$

To derive the mode shaping modal controller, it is assumed that the reduced mass, damping and stiffness matrices $\bar{\mathbf{M}}$, $\bar{\mathbf{D}}$ and $\bar{\mathbf{K}}$ as well as the input and output matrices $\mathbf{B}_{\mathrm{o}}$ and $\mathbf{C}_{\mathrm{o}}$ are known and invertible. These matrices are obtained from either the reduced order model of section 5.4 using Eqs. (5.21)–(5.23) or the identified reduced order model of section 6.6 using Eqs. (6.47)–(6.49). Pre-multiplying Eq. (7.2) by $\bar{\mathbf{M}}^{-1}$ gives

$$(\mathbf{I}_6 s^2 + \bar{\mathbf{M}}^{-1}\bar{\mathbf{D}} s + \bar{\mathbf{M}}^{-1}\bar{\mathbf{K}})\boldsymbol{Q}_{\mathrm{o}}(s) = \bar{\mathbf{M}}^{-1}\mathbf{B}_{\mathrm{o}}\boldsymbol{F}_{\mathrm{a}}(s). \tag{7.3}$$

If $\bar{\mathbf{D}}$ is a proportional damping matrix, the equation of motion of Eq. (7.3) can be decoupled using the modal transformation $\boldsymbol{q}_{\mathrm{o}} = \mathbf{P}_{\mathrm{o}}\mathbf{z}_{\mathrm{o}}$ in which the columns of $\mathbf{P}_{\mathrm{o}}$ are the normalized eigenvectors of $\bar{\mathbf{M}}^{-1}\bar{\mathbf{K}}$:

$$\bar{\mathbf{M}}^{-1}\bar{\mathbf{K}} = \mathbf{P}_{\mathrm{o}}\boldsymbol{\Omega}_{\mathrm{o}}^2\mathbf{P}_{\mathrm{o}}^{-1}. \tag{7.4}$$

Here $\boldsymbol{\Omega}_{\mathrm{o}} = \mathrm{diag}(\omega_{\mathrm{o}1}, \ldots, \omega_{\mathrm{o}6})$ with $\omega_{\mathrm{o}l}$ the suspension frequency of the lth suspension mode of the vibration isolator in open loop. The lth column of $\mathbf{P}_{\mathrm{o}}$ is the corresponding suspension mode shape. Pre-multiplying Eq. (7.3) by $\mathbf{P}_{\mathrm{o}}^{-1}$ results in the modal decoupled equation of motion

$$(\mathbf{I}_6 s^2 + \boldsymbol{\Xi}_{\mathrm{o}} s + \boldsymbol{\Omega}_{\mathrm{o}}^2)\boldsymbol{Z}_{\mathrm{o}}(s) = \mathbf{P}_{\mathrm{o}}^{-1}\bar{\mathbf{M}}^{-1}\mathbf{B}_{\mathrm{o}}\boldsymbol{F}_{\mathrm{a}}(s), \tag{7.5}$$

where $\boldsymbol{\Xi}_{\mathrm{o}} = \mathrm{diag}(\xi_{\mathrm{o}1}, \ldots, \xi_{\mathrm{o}6})$ and $\xi_{\mathrm{o}l} = 2\zeta_{\mathrm{o}l}\omega_{\mathrm{o}l}$ with $\zeta_{\mathrm{o}l}$ the damping ratio of the lth suspension mode of the vibration isolator.

Point of accuracy

The suspension mode shapes, which are the columns of modal matrix $\mathbf{P}_{\mathrm{o}}$, are expressed in terms of the DOFs $\boldsymbol{q}_{\mathrm{o}}$. It is desired to express these mode shape in terms of the translations (x, y, z) and rotations $(\theta_x, \theta_y, \theta_z)$ of a reference frame located at the so-called *point of accuracy*, which is the point where the

suspended equipment needs to have its highest accuracy, and oriented such that the three orthogonal axes of the reference frame are in the directions in which the highest accuracy is defined. This can be done using a transformation matrix **R**:

$$\mathbf{\Phi}_{\mathrm{o}} = \mathbf{R}\mathbf{P}_{\mathrm{o}}. \tag{7.6}$$

The lth column of modal matrix $\mathbf{\Phi}_{\mathrm{o}}$ now expresses the lth mode shape in terms of $\boldsymbol{x}_{\mathrm{ref}} = (x, y, z, \theta_x, \theta_y, \theta_z)^{\mathrm{T}}$. In subsection 5.3.2 it is shown that the transmissibilities can also be expressed in terms of $\boldsymbol{x}_{\mathrm{ref}}$.

7.4 Mode shaping modal control: acceleration and force feedback

The mode shaping modal controller for acceleration and force feedback is derived in this subsection. Therefore, some information from the previous section is required: the mass, damping and stiffness matrices as well the input and output matrices. The desired suspension frequencies, damping ratios and suspension mode shapes are defined in this section.

Throughout this section, the subscript “o” indicates a property (suspension frequency, damping ratio, modal matrix, etc.) of the vibration isolator in open loop, the subscript “n” indicates a desired property of the vibration isolator in closed loop.

7.4.1 Acceleration feedback

The mode shaping modal controller for acceleration feedback consists of proportional and integral gain matrices. In this subsection it is shown how these are calculated using the information from the previous section. Next, it is shown that there exist an input and output decoupling matrix that (approximately) decouple the system’s plant, such that a diagonal controller is obtained. Each diagonal entry is a SISO controller that is used to individually tune the suspension frequency and damping ratio of each suspension mode. It is shown that additional filtering can be added to each SISO controller individually. This filtering can be used to add roll-off to the modal controller, to prevent actuator saturation at low frequencies and to shape the loop. Finally, the desired suspension frequencies, damping ratios and mode shapes of the vibration isolator in closed loop are specified.

Proportional and integral gain matrices

The control strategy based on negative proportional plus integral acceleration feedback as proposed in [55, 60] and used in chapter 3.2.1 is used here as well. The controller reads

$$\mathbf{H}_{\ddot{x}_1}(s) = -(\mathbf{K}_a + \frac{\mathbf{K}_v}{s}), \tag{7.7}$$

where $\mathbf{K}_a$ and $\mathbf{K}_v$ are the proportional and integral gain matrices. This controller adds virtual mass $\mathbf{K}_a$ and virtual sky-hook damping $\mathbf{K}_v$ to the suspended payload. Note that the suspension frequencies and mode shapes of the vibration isolator in open loop depend on the mass matrix $\bar{\mathbf{M}}$ and stiffness matrix $\bar{\mathbf{K}}$, see Eq. (7.4). So, by adding virtual mass by $\mathbf{K}_a$, not only the suspension frequencies, but also the mode shapes of the vibration isolator in closed loop can be altered, since the shapes depend on the distribution of the virtual mass $\mathbf{K}_a$ in space. Using the feedback equation $\boldsymbol{F}_a(s) = \mathbf{H}_{\ddot{x}_1}(s)\ddot{\boldsymbol{X}}_1(s)$ with Eqs. (7.2) and (7.7), results in

$$\boldsymbol{F}_a(s) = -(\mathbf{K}_a s^2 + \mathbf{K}_v s)\mathbf{C}_o \boldsymbol{Q}_o(s). \tag{7.8}$$

The equation of motion of the vibration isolator in closed loop is given by substituting Eq. (7.8) into Eq. (7.1):

$$\begin{aligned}(\bar{\mathbf{M}}s^2 + \bar{\mathbf{D}}s + \bar{\mathbf{K}})\boldsymbol{Q}_o(s) &= -\mathbf{B}_o(\mathbf{K}_a s^2 + \mathbf{K}_v s)\mathbf{C}_o \boldsymbol{Q}_o(s),\\ \Rightarrow [(\bar{\mathbf{M}} + \mathbf{B}_o\mathbf{K}_a\mathbf{C}_o)s^2 + (\bar{\mathbf{D}} + \mathbf{B}_o\mathbf{K}_v\mathbf{C}_o)s + \bar{\mathbf{K}}]\boldsymbol{Q}_o(s) &= 0.\end{aligned} \tag{7.9}$$

Eq. (7.9) is the matrix generalization of the denominators of Eqs. (3.4) and (3.5). Assuming that $(\bar{\mathbf{M}} + \mathbf{B}_o\mathbf{K}_a\mathbf{C}_o)^{-1}$ exists and defining

$$\mathbf{K}_n = (\bar{\mathbf{M}} + \mathbf{B}_o\mathbf{K}_a\mathbf{C}_o)^{-1}\bar{\mathbf{K}}, \tag{7.10}$$

$$\mathbf{D}_n = (\bar{\mathbf{M}} + \mathbf{B}_o\mathbf{K}_a\mathbf{C}_o)^{-1}(\bar{\mathbf{D}} + \mathbf{B}_o\mathbf{K}_v\mathbf{C}_o), \tag{7.11}$$

allows to rewrite Eq. (7.9) as

$$(\mathbf{I}_6 s^2 + \mathbf{D}_n s + \mathbf{K}_n)\boldsymbol{Q}_o(s) = \mathbf{0}. \tag{7.12}$$

The desired solution of Eq. (7.12) is obtained by demanding $\mathbf{K}_n$ and $\mathbf{D}_n$ to be:

$$\mathbf{K}_n = \mathbf{P}_n\boldsymbol{\Omega}_n^2\mathbf{P}_n^{-1}, \tag{7.13}$$

$$\mathbf{D}_n = \mathbf{P}_n\boldsymbol{\Xi}_n\mathbf{P}_n^{-1}. \tag{7.14}$$

The columns of $\mathbf{P}_n$ are the eigenvectors of $\mathbf{K}_n$ expressed in terms of $\boldsymbol{q}_o$, $\boldsymbol{\Omega}_n = \mathrm{diag}(\omega_{n1}, \ldots, \omega_{n6})$ and $\boldsymbol{\Xi}_n = \mathrm{diag}(\xi_{n1}, \ldots, \xi_{n6})$ with $\xi_{nl} = 2\zeta_{nl}\omega_{nl}$. Herein, ω_{nl}

and ζ_{nl} are the desired closed loop suspension frequency and damping ratio of the lth suspension mode that can be set by the control engineer. The lth column of modal matrix $\mathbf{P}_n$ is the desired normal mode shape vector expressed in terms of $\boldsymbol{q}_o$. The desired suspension frequencies and damping ratios of the desired mode shapes are also the resonance frequencies and damping ratios of the desired transmissibilities. The values of the desired suspension frequencies and damping ratios are related to the desired isolation performance of the vibration isolator.

The role of $\mathbf{P}_n$ is that the added virtual mass is distributed to specific virtual locations at the payload, such that the normal mode shapes are altered and become the desired mode shapes. The mode shapes can be expressed in terms of $\boldsymbol{x}_{ref}$ using

$$\boldsymbol{\Phi}_n = \mathbf{R}\mathbf{P}_n. \tag{7.15}$$

The columns of $\boldsymbol{\Phi}_n$ can be chosen arbitrarily, provided that $\boldsymbol{\Phi}_n$ is full rank. A choice for $\boldsymbol{\Phi}_n$ is made at the end of this subsection. From Eq. (7.15) it is observed that $\mathbf{P}_n$ has to be chosen as

$$\mathbf{P}_n = \mathbf{R}^{-1}\boldsymbol{\Phi}_n. \tag{7.16}$$

Since in Eq. (7.14), $\mathbf{D}_n$ is demanded to be a modal damping matrix, Eq. (7.12) can be rewritten into the modal decoupled equations of motion using the transformation $\boldsymbol{q}_o = \mathbf{P}_n\boldsymbol{z}_n$:

$$(\mathbf{I}_6 s^2 + \boldsymbol{\Xi}_n s + \boldsymbol{\Omega}_n^2)\boldsymbol{Z}_n(s) = \mathbf{0}. \tag{7.17}$$

Proportional gain matrix $\mathbf{K}_a$ is found by substituting Eq. (7.13) into Eq. (7.10):

$$\begin{aligned}\mathbf{P}_n\boldsymbol{\Omega}_n^2\mathbf{P}_n^{-1} &= (\bar{\mathbf{M}} + \mathbf{B}_o\mathbf{K}_a\mathbf{C}_o)^{-1}\bar{\mathbf{K}} \\ \Rightarrow \mathbf{K}_a &= \mathbf{B}_o^{-1}(\bar{\mathbf{K}}\mathbf{P}_n\boldsymbol{\Omega}_n^{-2}\mathbf{P}_n^{-1} - \bar{\mathbf{M}})\mathbf{C}_o^{-1}.\end{aligned} \tag{7.18}$$

Integral gain matrix $\mathbf{K}_v$ is found by substituting Eq. (7.14) into Eq. (7.11):

$$\begin{aligned}\mathbf{P}_n\boldsymbol{\Xi}_n\mathbf{P}_n^{-1} &= (\bar{\mathbf{M}} + \mathbf{B}_o\mathbf{K}_a\mathbf{C}_o)^{-1}(\bar{\mathbf{D}} + \mathbf{B}_o\mathbf{K}_v\mathbf{C}_o) \\ \Rightarrow \mathbf{K}_v &= (\mathbf{B}_o^{-1}\bar{\mathbf{M}} + \mathbf{K}_a\mathbf{C}_o)\mathbf{P}_n\boldsymbol{\Xi}_n\mathbf{Q}_n^{-1}\mathbf{C}_o^{-1} - \mathbf{B}_o^{-1}\bar{\mathbf{D}}\mathbf{C}_o^{-1}.\end{aligned} \tag{7.19}$$

Substituting Eq. (7.18) into Eq. (7.19) results in

$$\mathbf{K}_v = \mathbf{B}_o^{-1}(\bar{\mathbf{K}}\mathbf{P}_n\boldsymbol{\Omega}_n^{-2}\boldsymbol{\Xi}_n\mathbf{P}_n^{-1} - \bar{\mathbf{D}})\mathbf{C}_o^{-1}. \tag{7.20}$$

Note that if $\mathbf{D}_n$ is nonzero, the mode shapes of the system become complex. However, by demanding $\mathbf{D}_n$ to be a proportional damping matrix, which is

done in this thesis, the complex mode shapes can be transformed to normal mode shapes again.

Since the flexible body dynamics of the vibration isolator usually appears at high frequencies, it will have hardly any effect on the suspension frequencies and corresponding mode shapes of the vibration isolator in closed loop. Therefore, the controller designed on the reduced order model of Eq. (7.1) describing the suspension dynamics is still valid for the flexible body model of Eq. (5.10) in section 5.3 describing both the suspension dynamics and flexible body dynamics. However, the flexible body dynamics is influenced significantly by the controller since a large amount of virtual mass $\mathbf{K}_a$ is added.

In appendix D it is shown that the mode shaping modal controller, which is a centralized controller (each actuator interacts will all sensors), can be simplified to a centralized controller (each actuator interacts only with its collocated sensor and for each actuator-sensor-pair the same controller is used). However, with this centralized controller it is no longer possible to individually tune the suspension frequency and damping ratio of each mode.

Decoupling

It is shown that there exist an input and output decoupling matrix that (approximately) decouple the system's plant, such that the mode shaping modal controller for acceleration feedback of Eq. (7.27) reduces to an (approximate) diagonal controller. Each diagonal entry is a SISO controller that can be used to individually tune the suspension frequency and damping ratio of each suspension mode.

Eqs. (7.18) and (7.20) can be rewritten such that the proportional plus integral controller of Eq. (7.27) is expressed in the Laplace domain as

$$\begin{aligned}\mathbf{H}_{\ddot{x}_1}(s) = \mathbf{B}_o^{-1}\bar{\mathbf{K}}\mathbf{P}_n[\boldsymbol{\Omega}_n^{-2} - \mathbf{P}_n^{-1}\bar{\mathbf{K}}^{-1}\bar{\mathbf{M}}\mathbf{P}_n \\ +(\boldsymbol{\Omega}_n^{-2}\boldsymbol{\Xi}_n - \mathbf{P}_n^{-1}\bar{\mathbf{K}}^{-1}\bar{\mathbf{D}}\mathbf{P}_n)\frac{1}{s}]\mathbf{P}_n^{-1}\mathbf{C}_o^{-1}.\end{aligned} \tag{7.21}$$

The terms $\bar{\mathbf{K}}^{-1}\bar{\mathbf{M}}$ and $\bar{\mathbf{K}}^{-1}\bar{\mathbf{D}}$ in Eq. (7.21) can also be expressed as

$$\begin{aligned}\bar{\mathbf{K}}^{-1}\bar{\mathbf{M}} &= (\bar{\mathbf{M}}^{-1}\bar{\mathbf{K}})^{-1} \\ &= (\mathbf{P}_o\boldsymbol{\Omega}_o^2\mathbf{P}_o^{-1})^{-1} = \mathbf{P}_o\boldsymbol{\Omega}_o^{-2}\mathbf{P}_o^{-1}\end{aligned} \tag{7.22}$$

$$\begin{aligned}\bar{\mathbf{K}}^{-1}\bar{\mathbf{D}} &= \bar{\mathbf{K}}^{-1}\bar{\mathbf{M}}\bar{\mathbf{M}}^{-1}\bar{\mathbf{D}} = (\bar{\mathbf{M}}^{-1}\bar{\mathbf{K}})^{-1}\bar{\mathbf{M}}^{-1}\bar{\mathbf{D}} \\ &= (\mathbf{P}_o\boldsymbol{\Omega}_o^2\mathbf{P}_o^{-1})^{-1}\mathbf{P}_o\boldsymbol{\Xi}_o\mathbf{P}_o^{-1} \\ &= \mathbf{P}_o\boldsymbol{\Omega}_o^{-2}\mathbf{P}_o^{-1}\mathbf{P}_o\boldsymbol{\Xi}_o\mathbf{P}_o^{-1} = \mathbf{P}_o\boldsymbol{\Omega}_o^{-2}\boldsymbol{\Xi}_o\mathbf{P}_o^{-1}\end{aligned} \tag{7.23}$$

Defining the matrices

$$\mathbf{T}^{\mathrm{u}} = \mathbf{B}_{\mathrm{o}}^{-1}\bar{\mathbf{K}}\mathbf{P}_{\mathrm{n}}, \tag{7.24}$$

$$\mathbf{T}^{\mathrm{y}}_{\ddot{\mathbf{x}}_1} = \mathbf{P}_{\mathrm{n}}^{-1}\mathbf{C}_{\mathrm{o}}^{-1}, \tag{7.25}$$

and using Eqs. (7.22) and (7.23), allows to rewrite Eq. (7.21) as

$$\begin{aligned}\mathbf{H}_{\ddot{\mathbf{x}}_1}(s) = \mathbf{T}^{\mathrm{u}}[&\boldsymbol{\Omega}_{\mathrm{n}}^{-2} - \mathbf{P}_{\mathrm{n}}^{-1}\mathbf{P}_{\mathrm{o}}\boldsymbol{\Omega}_{\mathrm{o}}^{-2}\mathbf{P}_{\mathrm{o}}^{-1}\mathbf{P}_{\mathrm{n}} \\ &+(\boldsymbol{\Omega}_{\mathrm{n}}^{-2}\boldsymbol{\Xi}_{\mathrm{n}} - \mathbf{P}_{\mathrm{n}}^{-1}\mathbf{P}_{\mathrm{o}}\boldsymbol{\Omega}_{\mathrm{o}}^{-2}\boldsymbol{\Xi}_{\mathrm{o}}\mathbf{P}_{\mathrm{o}}^{-1}\mathbf{P}_{\mathrm{n}})\frac{1}{s}]\mathbf{T}^{\mathrm{y}}_{\ddot{\mathbf{x}}_1}.\end{aligned} \tag{7.26}$$

For the choice $\boldsymbol{\Phi}_{\mathrm{n}} = \boldsymbol{\Phi}_{\mathrm{o}}$ such that $\mathbf{P}_{\mathrm{n}} = \mathbf{P}_{\mathrm{o}}$, the part of Eq. (7.26) in-between the square brackets is diagonal, hence the matrices $\mathbf{T}^{\mathrm{u}}$ and $\mathbf{T}^{\mathrm{y}}_{\ddot{\mathbf{x}}_1}$ decouple the system's plant and a diagonal control structure is possible. This is illustrated in Fig. 7.2. The plant transfer function matrix $\mathbf{G}_{\ddot{\mathbf{x}}_1\boldsymbol{F}_s}(s)$ is pre-multiplied with $\mathbf{T}^{\mathrm{u}}$ and post-multiplied with $\mathbf{T}^{\mathrm{y}}_{\ddot{\mathbf{x}}_1}$ which results in a decoupled plant as observed by a diagonal controller $\mathbf{H}^{\mathrm{d}}(s)$.

The part in-between the square brackets in Eq. (7.21) is approximately diagonal if the off-diagonal terms in $\mathbf{P}_{\mathrm{n}}^{-1}\mathbf{P}_{\mathrm{o}}\boldsymbol{\Omega}_{\mathrm{o}}^{-2}\mathbf{P}_{\mathrm{o}}^{-1}\mathbf{P}_{\mathrm{n}}$ and $\mathbf{P}_{\mathrm{n}}^{-1}\mathbf{P}_{\mathrm{o}}\boldsymbol{\Omega}_{\mathrm{o}}^{-2}\boldsymbol{\Xi}_{\mathrm{o}}\mathbf{P}_{\mathrm{o}}^{-1}\mathbf{P}_{\mathrm{n}}$ are much smaller compared to the diagonal terms in $\boldsymbol{\Omega}_{\mathrm{n}}^{-2}$ and $\boldsymbol{\Omega}_{\mathrm{n}}^{-2}\boldsymbol{\Xi}_{\mathrm{n}}$ respectively. This approximation is valid if the mode shapes for the open loop system and the desired mode shapes for the closed loop system do not differ too much or if $\boldsymbol{\Omega}_{\mathrm{n}} \ll \boldsymbol{\Omega}_{\mathrm{o}}$ and $\boldsymbol{\Omega}_{\mathrm{n}}^{-2}\boldsymbol{\Xi}_{\mathrm{n}} \gg \boldsymbol{\Omega}_{\mathrm{o}}^{-2}\boldsymbol{\Xi}_{\mathrm{o}}$, which is the case for hard mount vibration isolators. Then Eq. (7.26) can be approximated as

$$\mathbf{H}_{\ddot{\mathbf{x}}_1}(s) \approx \mathbf{T}^{\mathrm{u}}\mathbf{H}^{\mathrm{d}}(s)\mathbf{T}^{\mathrm{y}}_{\ddot{\mathbf{x}}_1}, \tag{7.27}$$

where the diagonal controller is

$$\mathbf{H}^{\mathrm{d}}(s) = \mathbf{K}^{\mathrm{d}}_{\mathrm{a}} + \frac{\mathbf{K}^{\mathrm{d}}_{\mathrm{v}}}{s} \tag{7.28}$$

with diagonal matrices

$$\begin{aligned}\mathbf{K}^{\mathrm{d}}_{\mathrm{a}} &= \boldsymbol{\Omega}_{\mathrm{n}}^{-2} - \mathrm{diag}(\mathbf{P}_{\mathrm{n}}^{-1}\mathbf{P}_{\mathrm{o}}\boldsymbol{\Omega}_{\mathrm{o}}^{-2}\mathbf{P}_{\mathrm{o}}^{-1}\mathbf{P}_{\mathrm{n}}), \\ \mathbf{K}^{\mathrm{d}}_{\mathrm{v}} &= \boldsymbol{\Omega}_{\mathrm{n}}^{-2}\boldsymbol{\Xi}_{\mathrm{n}} - \mathrm{diag}(\mathbf{P}_{\mathrm{n}}^{-1}\mathbf{P}_{\mathrm{o}}\boldsymbol{\Omega}_{\mathrm{o}}^{-2}\boldsymbol{\Xi}_{\mathrm{o}}\mathbf{P}_{\mathrm{o}}\mathbf{P}_{\mathrm{n}}),\end{aligned}$$

or alternatively, using Eqs. (7.22) and (7.23)

$$\mathbf{K}^{\mathrm{d}}_{\mathrm{a}} = \boldsymbol{\Omega}_{\mathrm{n}}^{-2} - \mathrm{diag}(\mathbf{P}_{\mathrm{n}}^{-1}\bar{\mathbf{K}}^{-1}\bar{\mathbf{M}}\mathbf{P}_{\mathrm{n}}), \tag{7.29}$$

$$\mathbf{K}^{\mathrm{d}}_{\mathrm{v}} = \boldsymbol{\Omega}_{\mathrm{n}}^{-2}\boldsymbol{\Xi}_{\mathrm{n}} - \mathrm{diag}(\mathbf{P}_{\mathrm{n}}^{-1}\bar{\mathbf{K}}^{-1}\bar{\mathbf{D}}\mathbf{P}_{\mathrm{n}}). \tag{7.30}$$

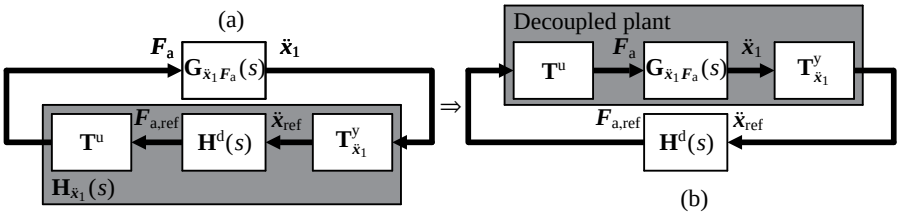

Fig. 7.2: Two ways to represent the control schemes for acceleration feedback: (a) the plant "observed" by controller $\mathbf{H}_{\ddot{x}_1}(s)$ is coupled; (b) the plant "observed" by controller $\mathbf{H}^d_{\ddot{x}_1}(s)$ is decoupled. $\ddot{\boldsymbol{x}}_{ref}$ and $\boldsymbol{F}_{a,ref}$ represent the payload accelerations and actuator forces in the modal (decoupled) coordinates $\ddot{\boldsymbol{x}}_{ref}$.

The diagonal entries of $\mathbf{H}^d(s)$ are SISO controllers that can be used to individually tune the suspension frequency and damping ratio of each suspension mode.

In Fig. 7.2, the modal (decoupled) coordinates describe the motion of the reference frame $\boldsymbol{x}_{ref}$. Therefore, $\ddot{\boldsymbol{x}}_{ref}$ and $\boldsymbol{F}_{a,ref}$ are the payload accelerations and actuator forces expressed in terms of $\boldsymbol{x}_{ref}$, whereas $\ddot{\boldsymbol{x}}_1$ and $\boldsymbol{F}_a$ are the payload accelerations and actuator forces expressed in terms of DOFs $\boldsymbol{q}_o$ associated with the leg extensions.

Additional filtering

The diagonal controller of Eq. (7.28) allows to add additional filtering to each SISO controller stored at the diagonal entries of $\mathbf{H}^d(s)$. The parameters of these filters can be different for each SISO controller. This allows to individually tune the isolation performance for each suspension mode.

The plant transfer function matrix $\mathbf{G}_{\ddot{x}_1 F_s}(s)$ is an acceleration response due to force excitation. The transfer functions corresponding to collocated actuator-sensor-pairs have no roll-off. Since the mode shaping modal controller for acceleration feedback presented in this section does not have roll-off either, the resulting loop gains will lead to infinite closed loop bandwidth. This will cause stability problems in practical applications. Therefore it is suggested to add second-order high pass filters to the diagonal controller $\mathbf{H}^d(s)$ resulting in high frequency roll-off. This approach is similar to the one-axis controller as proposed in chapter 3.2.2.

The improved diagonal controller reads

$$\mathbf{H}^d_r(s) = \mathbf{H}^d(s)\mathbf{F}_r(s), \tag{7.31}$$

where $\mathbf{F}_\mathrm{r}(s) = \mathrm{diag}(F_{\mathrm{r}1}(s), \ldots, F_{\mathrm{r}6}(s))$ with

$$F_{\mathrm{r}l}(s) = \frac{s^2}{s^2 + 2\zeta_{\mathrm{l}l}\omega_{\mathrm{l}l}s + \omega_{\mathrm{l}l}^2} \frac{\omega_{\mathrm{f}l}^2}{s^2 + 2\zeta_{\mathrm{f}l}\omega_{\mathrm{f}l}s + \omega_{\mathrm{f}l}^2} \frac{s + \omega_{\mathrm{z}l}}{\omega_{\mathrm{z}l}} F_{\mathrm{ext}}(s). \tag{7.32}$$

The corner frequency for filter $F_{\mathrm{r}l}(s)$ determines the attenuation at high frequencies of the lth mode, see section 3.2.2. The attenuation of the lth mode is expressed as $(\omega_{\mathrm{n}l}/\omega_{\mathrm{f}l})^2$. The damping ratio $\zeta_{\mathrm{f}l}$ for the second-order filter can be set arbitrarily by the control engineer. An additional high-frequency zero $\omega_{\mathrm{z}l}$ is used to increase the phase margin around the high crossover frequency of the loop gain. A second-order high-pass filter with corner frequency $\omega_{\mathrm{l}l}$ and relative damping $\zeta_{\mathrm{l}l}$ is used to prevent actuator saturation at low frequencies.

Due to the wire flexure dynamics a loss in collocation between actuator and sensor (see sections 4.2 and 5.3) occurs around 900 Hz and therefore a loop shaping filter $F_{\mathrm{ext}}(s)$ can be used. Similar as in section 4.2, it consists of a skew notch filter

$$F_{\mathrm{ext}}(s) = \frac{s^2 + 2\zeta_1\omega_1 s + \omega_1^2}{s^2 + 2\zeta_2\omega_2 s + \omega_2^2} \frac{\omega_2^2}{\omega_1^2}, \tag{7.33}$$

where $\omega_i = 2\pi f_i$ with $f_1 = 800$ Hz, $f_2 = 3$ kHz, $\zeta_1 = 0.05$, and $\zeta_2 = 0.4$.

Desired suspension frequencies, damping ratios and mode shapes

The mode shaping modal controllers that will be used to derive the modeling results of section 7.7 are obtained using the mass, damping and stiffness matrices $\bar{\mathbf{M}}$, $\bar{\mathbf{D}}$ and $\bar{\mathbf{K}}$ available from the reduced order model of section 5.4. The input and output matrices $\mathbf{B}_\mathrm{o}$ and $\mathbf{C}_\mathrm{o}$ are also known and equal to identity, since the actuators and sensors are co-aligned with DOFs $\boldsymbol{q}_\mathrm{o}$ associated with the leg extensions: $\mathbf{B}_\mathrm{o} = \mathbf{C}_\mathrm{o} = \mathbf{I}_6$. The point of accuracy is chosen as the elastic center of the vibration isolator. This means that transformation matrix $\mathbf{R}$ can be calculated using Eq. (5.1). A coordinate frame (x, y, z) is defined, such that its origin is located at the point of accuracy and its orientation is as in Fig. 5.4. The suspension frequencies and (open loop) suspension mode shapes expressed in terms of the coordinates of this reference frame are already given in Table 5.2.

The specification of the desired isolation performance regarding the transmissibilities is not straightforward. Since the desired suspension modes are related to the desired transmissibilities, the choice for the desired mode shapes as well as the desired suspension frequencies and damping ratios is not straightforward either. The isolation performance of industrial vibration isolators is

Table 7.1: Control parameters for the mode shaping modal controller.

l	mode shape	ω_{nl} (rad/s)	ζ_{nl} (-)	ω_{fl} (rad/s)	ζ_{fl} (-)
1	x	$2\pi\cdot3$	0.4	$2\pi\cdot45$	0.07
2	y	$2\pi\cdot3$	0.4	$2\pi\cdot45$	0.07
3	z	$2\pi\cdot1$	0.4	$2\pi\cdot22.5$	0.07
4	θ_x	$2\pi\cdot2.5$	0.4	$2\pi\cdot37.5$	0.07
5	θ_y	$2\pi\cdot2.5$	0.4	$2\pi\cdot37.5$	0.07
6	θ_z	$2\pi\cdot2$	0.4	$2\pi\cdot30$	0.07

usually expressed in terms of horizontal and vertical transmissibilities. To be able to express the isolation performance of the six-axes active hard mount vibration isolator described in this thesis, in terms of horizontal and vertical transmissibilities as well, its desired suspension mode shapes are chosen as pure translations and rotations of the point of accuracy in the directions of x, y and z. Hence, modal matrix $\mathbf{\Phi}_{\mathrm{n}} = \mathbf{I}_6$.

The chosen values for the suspension frequency $\omega_{\mathrm{n}l}$ and damping ratio $\zeta_{\mathrm{n}l}$ corresponding to the lth suspension mode are listed in Table 7.1. The corner frequencies and damping ratios of the second-order low-pass filters of Eq. (7.32) are also listed. By comparing the desired suspension frequencies and mode shapes of the vibration isolator in closed loop to the open loop suspension frequencies and mode shapes listed in Table 5.2, it is observed that for example the mode of the (approximate) z-translation has to be lowered from 9.8 to 1 Hz.

With these values the desired performance objective given in section 2.5 regarding the transmissibility cannot be realized for each direction. In the next chapter it is shown that with the developed demonstrator setup of the six-axes active hard mount vibration isolator it is not possible to realize a higher performance due to hardware limitations. However, the efficacy of the mode shaping modal controller can still be demonstrated with the values listed in Table 7.1. The remaining parameters of the filter $\mathbf{F}_{\mathrm{r}}(s)$ of Eq. (7.32) are chosen $\omega_{zl} = 2\pi\cdot100$ rad/s, $\omega_{ll} = 2\pi\cdot0.1$ rad/s and $\zeta_{ll} = 0.7$ for all l. $F_{\mathrm{ext}}(s)$ is given as in Eq. (7.33).

To check closed loop stability, the generalized Nyquist criterion is used [37]. This can be done by plotting the characteristic loci (CL) of the corresponding loop gain matrix. The loop gain matrix is obtained by cutting the loop in Fig. 7.2 at the position of $\boldsymbol{F}_{\mathrm{a}}$ and replacing $\mathbf{H}_{\ddot{\mathbf{x}}_1}(s)$ with $\mathbf{H}_{\mathrm{r},\ddot{\mathbf{x}}_1}(s)$. For acceleration feedback, this matrix reads

$$\mathbf{L}_{\mathrm{r},\ddot{\mathbf{x}}_1}(s) = \mathbf{H}_{\mathrm{r},\ddot{\mathbf{x}}_1}(s)\mathbf{G}_{\ddot{\mathbf{x}}_1\boldsymbol{F}_{\mathrm{s}}}(s) = \mathbf{T}^{\mathrm{u}}\mathbf{H}^{\mathrm{d}}_{\mathrm{r}}(s)\mathbf{T}^{\mathrm{y}}_{\ddot{\mathbf{x}}_1}\mathbf{G}_{\ddot{\mathbf{x}}_1\boldsymbol{F}_{\mathrm{a}}}(s). \tag{7.34}$$

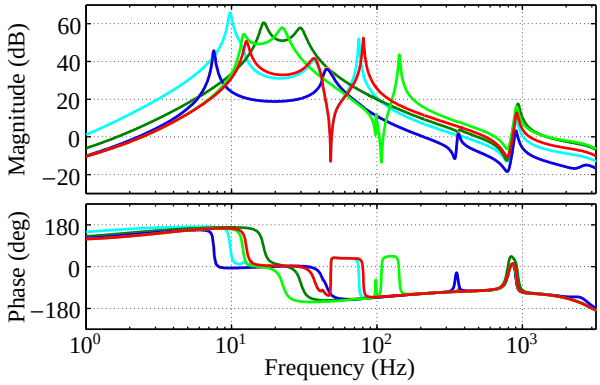

Fig. 7.3: Characteristic loci of loop gain matrices $\mathbf{L}_{\mathrm{r},\ddot{\boldsymbol{x}}_1}(s)$ for acceleration feedback.

The CL of the plant transfer function matrix $\mathbf{G}_{\ddot{\boldsymbol{x}}_1 \boldsymbol{F}_\mathrm{a}}(s)$ are shown in Fig. 5.6. The CL of loop gain matrix $\mathbf{L}_{\mathrm{r},\ddot{\boldsymbol{x}}_1}(s)$ are shown in Fig. 7.3. It is observed that the phase angles of all CL do not cross the $-180°$ line. This means that the closed loop is stable.

7.4.2 Force feedback

In this subsection the mode shaping modal controller for force feedback is derived. The mode shaping modal controller for force feedback will only be used to derive the mode shaping modal controllers for sensor fusion and two-sensor control. This is because in chapter 3 it is demonstrated that force feedback is outperformed by acceleration feedback regarding all performance transfer functions. Therefore it has been decided that the modeling results obtained with the mode shaping modal controller for force feedback will not be analyzed in section 7.7.

The vibration isolator is also equipped with force sensors. These are located in the legs and co-aligned with accelerometers, see Fig. 5.1. Therefore, the relation between the measured forces $\boldsymbol{F}_\mathrm{s}$ and the DOFs $\boldsymbol{q}_\mathrm{o}$ can be derived as

$$\boldsymbol{F}_\mathrm{s}(s) = \mathbf{C}_\mathrm{o}[-(k + ds)\boldsymbol{Q}_\mathrm{o}(s) + \mathbf{B}_\mathrm{o}\boldsymbol{F}_\mathrm{a}(s)], \tag{7.35}$$

using the same output matrix $\mathbf{C}_\mathrm{o}$ as for the measured accelerometer signals. In Eq. (7.35), k and d represent the axial stiffness and damping of a leg, assumed being equal for all legs. $-(k + ds)\boldsymbol{Q}_\mathrm{o}(s) + \mathbf{B}_\mathrm{o}\boldsymbol{F}_\mathrm{a}(s)$ is the total force in the leg, which is the sum of the elastic restoring force in the spring, the force associated with dissipated energy, and the actuator force $\mathbf{B}_\mathrm{o}\boldsymbol{F}_\mathrm{a}(s)$. Since the

vibration isolator has been designed to be approximately exact constrained, the main contributions to the total reduced stiffness and damping matrices $\bar{\mathbf{K}}$ and $\bar{\mathbf{D}}$ are due to the axial stiffness k and damping d. The remaining contributions are due to flexibilities of the wire flexures in the mounts. These add a small parasitic stiffness $\bar{\mathbf{K}}_\mathrm{p}$ and damping $\bar{\mathbf{D}}_\mathrm{p}$. Then the equation of motion of Eq. (7.1) describing the suspension dynamics, can be written as

$$[\bar{\mathbf{M}}s^2 + (\bar{\mathbf{D}}_\mathrm{p} + d)s + (\bar{\mathbf{K}}_\mathrm{p} + k)]\boldsymbol{Q}_\mathrm{o}(s) = \mathbf{B}_\mathrm{o}\boldsymbol{F}_\mathrm{a}(s). \tag{7.36}$$

If the parasitic contributions $\bar{\mathbf{K}}_\mathrm{p}$ and $\bar{\mathbf{D}}_\mathrm{p}$ are neglected (this is common in case of force feedback [45]), Eq. (7.36) can be substituted into Eq. (7.35) to obtain

$$\boldsymbol{F}_\mathrm{s}(s) = \mathbf{C}_\mathrm{o}\bar{\mathbf{M}}s^2\boldsymbol{Q}_\mathrm{o}(s) = \mathbf{C}_\mathrm{o}\bar{\mathbf{M}}\mathbf{C}_\mathrm{o}^{-1}\ddot{\boldsymbol{X}}_1(s) \tag{7.37}$$

where Eq. (7.2) has been used. Eq. (7.37) describes the approximate relation between the measured accelerations $\ddot{\boldsymbol{x}}_1$ and measured forces $\boldsymbol{F}_\mathrm{s}$, which is just the transformed mass matrix $\mathbf{C}_\mathrm{o}\bar{\mathbf{M}}\mathbf{C}_\mathrm{o}^{-1}$. Therefore, if all entries of $\ddot{\boldsymbol{x}}_1$ in the previous subsection are replaced with $\mathbf{C}_\mathrm{o}\bar{\mathbf{M}}^{-1}\mathbf{C}_\mathrm{o}^{-1}\boldsymbol{F}_\mathrm{s}$, a similar controller for force feedback as Eq. (7.21) can be derived. This controller does the same job as Eq. (7.21), despite the error introduced by neglecting the contributions of $\bar{\mathbf{K}}_\mathrm{p}$ and $\bar{\mathbf{D}}_\mathrm{p}$. The controller reads

$$\mathbf{H}_{\boldsymbol{F}_\mathrm{s}}(s) = \mathbf{K}_\mathrm{a} + \frac{\mathbf{K}_\mathrm{v}}{s} \tag{7.38}$$

with the gain matrices

$$\mathbf{K}_\mathrm{a} = \mathbf{B}_\mathrm{o}^{-1}(\bar{\mathbf{K}}\mathbf{P}_\mathrm{n}\boldsymbol{\Omega}_\mathrm{n}^{-2}\mathbf{P}_\mathrm{n}^{-1} - \bar{\mathbf{M}})\bar{\mathbf{M}}^{-1}\mathbf{C}_\mathrm{o}^{-1}, \tag{7.39}$$

$$\mathbf{K}_\mathrm{v} = \mathbf{B}_\mathrm{o}^{-1}(\bar{\mathbf{K}}\mathbf{P}_\mathrm{n}\boldsymbol{\Omega}_\mathrm{n}^{-2}\boldsymbol{\Xi}_\mathrm{n}\mathbf{P}_\mathrm{n}^{-1} - \bar{\mathbf{D}})\bar{\mathbf{M}}^{-1}\mathbf{C}_\mathrm{o}^{-1}. \tag{7.40}$$

This controller can be written as an approximate diagonal controller in a similar way as for acceleration feedback:

$$\mathbf{H}_{\boldsymbol{F}_\mathrm{s}}(s) \approx \mathbf{T}^\mathrm{u}\mathbf{H}^\mathrm{d}(s)\mathbf{T}^\mathrm{y}_{\boldsymbol{F}_\mathrm{s}} \tag{7.41}$$

with $\mathbf{H}^\mathrm{d}(s)$ as in Eq. (7.28), and output decoupling matrix

$$\mathbf{T}^\mathrm{y}_{\boldsymbol{F}_\mathrm{s}} = \mathbf{P}_\mathrm{n}^{-1}\bar{\mathbf{M}}^{-1}\mathbf{C}_\mathrm{o}^{-1}. \tag{7.42}$$

Additional filtering can be added to the mode shaping modal controller for force feedback in a similar way as to the mode shaping modal controller for acceleration feedback. The control parameters listed in Table 7.1 can be used as well.

In the next sections, the mode shaping modal controllers for acceleration and force feedback derived in section are used to derive the mode shaping modal controllers for sensor fusion and two-sensor control.

7.5 Mode shaping modal control: sensor fusion

It is shown how the input and output decoupling matrices of Eqs. (7.24), (7.25) and (7.42) can be used to extend the sensor fusion control strategy as in section 3.3 from the one-axis vibration isolator to the six-axes vibration isolator. Therefore, the loop gain matrices are needed. Loop gain matrix $\mathbf{L}_{\mathrm{r},\ddot{\mathbf{x}}_1}(s)$ for acceleration feedback is given by Eq. (7.34), that for force feedback is given by

$$\mathbf{L}_{\mathrm{r},\boldsymbol{F}_\mathrm{s}}(s) = \mathbf{H}_{\mathrm{r},\boldsymbol{F}_\mathrm{s}}(s)\mathbf{G}_{\boldsymbol{F}_\mathrm{s}\boldsymbol{F}_\mathrm{a}}(s) = \mathbf{T}^{\mathrm{u}}\mathbf{H}^{\mathrm{d}}_{\mathrm{r}}(s)\mathbf{T}^{\mathrm{y}}_{\boldsymbol{F}_\mathrm{s}}\mathbf{G}_{\boldsymbol{F}_\mathrm{s}\boldsymbol{F}_\mathrm{a}}(s). \tag{7.43}$$

The CL of the plant transfer function matrix $\mathbf{G}_{\boldsymbol{F}_\mathrm{s}\boldsymbol{F}_\mathrm{a}}(s)$ are shown in Fig. 5.6. Loop gain matrix $\mathbf{L}_{\mathrm{r},\ddot{\mathbf{x}}_1}(s)$ is obtained by cutting the loop in Fig. 7.2 at the position of $\boldsymbol{F}_\mathrm{a}$ and replacing $\mathbf{H}_{\ddot{\mathbf{x}}_1}(s)$ with $\mathbf{H}_{\mathrm{r},\ddot{\mathbf{x}}_1}(s)$. The loop gain matrix for force feedback is derived in the same way. By cutting the loop in Fig. 7.2 at the position of $\boldsymbol{F}_{\mathrm{a,ref}}$, the decoupled loop gain matrix for acceleration feedback is obtained. The decoupled loop gain matrix for force feedback is derived in the same way. The decoupled loop gain matrices are calculated by pre-multiplying Eqs. (7.34) and (7.43) with the inverse of $\mathbf{T}^{\mathrm{u}}$ and post-multiplying with $\mathbf{T}^{\mathrm{u}}$:

$$\mathbf{L}^{\mathrm{d}}_{\mathrm{r},\ddot{\mathbf{x}}_1}(s) = \mathbf{T}^{\mathrm{u}-1}\mathbf{H}_{\mathrm{r},\ddot{\mathbf{x}}_1}(s)\mathbf{G}_{\ddot{\mathbf{x}}_1\boldsymbol{F}_\mathrm{a}}(s)\mathbf{T}^{\mathrm{u}} = \mathbf{H}^{\mathrm{d}}_{\mathrm{r}}(s)\mathbf{T}^{\mathrm{y}}_{\ddot{\mathbf{x}}_1}\mathbf{G}_{\ddot{\mathbf{x}}_1\boldsymbol{F}_\mathrm{a}}(s)\mathbf{T}^{\mathrm{u}}, \tag{7.44}$$

$$\mathbf{L}^{\mathrm{d}}_{\mathrm{r},\boldsymbol{F}_\mathrm{s}}(s) = \mathbf{T}^{\mathrm{u}-1}\mathbf{H}_{\mathrm{r},\boldsymbol{F}_\mathrm{s}}(s)\mathbf{G}_{\boldsymbol{F}_\mathrm{s}\boldsymbol{F}_\mathrm{a}}(s)\mathbf{T}^{\mathrm{u}} = \mathbf{H}^{\mathrm{d}}_{\mathrm{r}}(s)\mathbf{T}^{\mathrm{y}}_{\boldsymbol{F}_\mathrm{s}}\mathbf{G}_{\boldsymbol{F}_\mathrm{s}\boldsymbol{F}_\mathrm{a}}(s)\mathbf{T}^{\mathrm{u}}. \tag{7.45}$$

It is clear that $\mathbf{T}^{\mathrm{y}}_{\ddot{\mathbf{x}}_1}\mathbf{G}_{\ddot{\mathbf{x}}_1\boldsymbol{F}_\mathrm{a}}(s)\mathbf{T}^{\mathrm{u}}$ and $\mathbf{T}^{\mathrm{y}}_{\boldsymbol{F}_\mathrm{s}}\mathbf{G}_{\boldsymbol{F}_\mathrm{s}\boldsymbol{F}_\mathrm{a}}(s)\mathbf{T}^{\mathrm{u}}$ must represent the decoupled plant matrices. $\mathbf{L}^{\mathrm{d}}_{\mathrm{r},\ddot{\mathbf{x}}_1}(s)$ and $\mathbf{L}^{\mathrm{d}}_{\mathrm{r},\boldsymbol{F}_\mathrm{s}}(s)$ are diagonal loop gain matrices. Their diagonal entries are plotted in Fig. 7.4. The solid gray lines represent acceleration feedback, the dashed gray lines force feedback.

The resonance peaks below 20 Hz in the loop gains in Fig. 7.4 are due to the suspension modes, the resonance peaks in-between 75 and 360 Hz are due to the internal modes of the payload, see also section 5.3.1. Each peak at 900 Hz is due to the wire flexure dynamics (see also section 5.3.1), and each dip at 800 Hz is due to the skew notch filter $F_{\mathrm{ext}}(s)$ of Eq. (7.33) that is used in the controllers. Each resonance peak corresponding to an internal mode is preceded by an anti-resonance dip in the loop gain. This is similar to the one-axis vibration isolator, see Fig. 3.5 in section 3.3. In that section, sensor fusion is applied by low-pass filtering of the loop gain for acceleration feedback and high-pass filtering of the loop gain for force feedback. It is described that the maximum achievable damping ratio depends on the ratio between the frequencies of the anti-resonances in the acceleration and force paths, see Eq. (3.31). The corresponding filter pole can be found using Eq. (3.30).

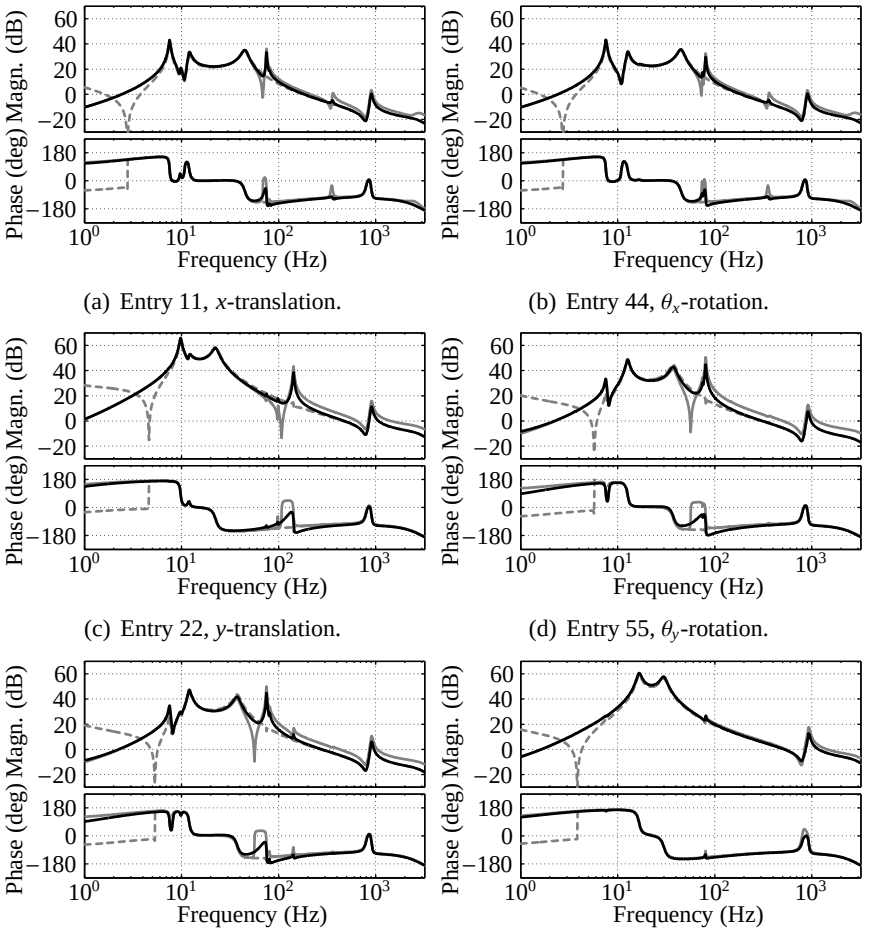

(a) Entry 11, x-translation.

(b) Entry 44, θ_x-rotation.

(c) Entry 22, y-translation.

(d) Entry 55, θ_y-rotation.

(e) Entry 33, z-translation.

(f) Entry 66, θ_z-rotation.

Fig. 7.4: Diagonal entries of decoupled loop gain matrices $\mathbf{L}^{\mathrm{d}}_{\mathrm{r},\ddot{\mathbf{x}}_1}(s)$ (——) for acceleration feedback, $\mathbf{L}^{\mathrm{d}}_{\mathrm{r},\boldsymbol{F}_\mathrm{s}}(s)$ (- - - -) for force feedback, and $\mathbf{L}^{\mathrm{d}}_{\mathrm{r},(\ddot{\mathbf{x}}_1,\boldsymbol{F}_\mathrm{s})}(s)$ (——) for sensor fusion.

Fig. 7.4 shows only one clear anti-resonance for each entry of the loop gain matrix. The frequency of the anti-resonance in the force path is almost on the frequency of the corresponding resonance. The frequencies of the anti-resonances are used to determine the filter poles for the six-axes sensor fusion controller. Each filter pole is calculated as

$$\omega_{\mathrm{pl}} = \frac{\omega_{\mathrm{al},\ddot{x}_1}}{\omega_{\mathrm{al},F_\mathrm{s}}} \sqrt{\omega_{\mathrm{al},\ddot{x}_1}\omega_{\mathrm{al},F_\mathrm{s}}}, \tag{7.46}$$

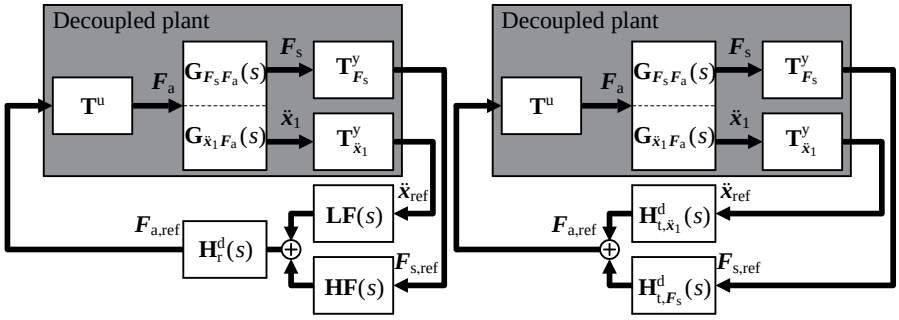

(a) Control scheme of sensor fusion. (b) Control scheme of two-sensor control.

Fig. 7.5: Control schemes for: (a) sensor fusion; (b) two-sensor control. The plant "observed" by the diagonal controllers is decoupled. $\ddot{\boldsymbol{x}}_{\mathrm{ref}}$, $\boldsymbol{F}_{\mathrm{s,ref}}$ and $\boldsymbol{F}_{\mathrm{a,ref}}$ represent the payload accelerations, leg forces and actuator forces in the modal (decoupled) coordinates $\ddot{\boldsymbol{x}}_{\mathrm{ref}}$.

Table 7.2: Frequencies of the anti-resonances and poles, and controller gains.

l	mode shape	$\omega_{\mathrm{al},\ddot{x}_1}$ (rad/s)	$\omega_{\mathrm{al},F_{\mathrm{s}}}$ (rad/s)	ω_{pl} (rad/s)	k_{fl} (-)
1	x	$2\pi\cdot$ 68.5	$2\pi\cdot$ 75.1	$2\pi\cdot$64.4	$9.3\cdot10^{-3}$
2	y	$2\pi\cdot$ 72.9	$2\pi\cdot$ 80.9	$2\pi\cdot$69.2	$8.7\cdot10^{-3}$
3	z	$2\pi\cdot$107.4	$2\pi\cdot$142.4	$2\pi\cdot$93.3	$2.7\cdot10^{-3}$
4	θ_x	$2\pi\cdot$ 56.4	$2\pi\cdot$ 80.6	$2\pi\cdot$47.2	$1.3\cdot10^{-3}$
5	θ_y	$2\pi\cdot$ 56.4	$2\pi\cdot$ 75.1	$2\pi\cdot$48.9	$1.3\cdot10^{-3}$
6	θ_z	$2\pi\cdot$ 79.7	$2\pi\cdot$ 81.4	$2\pi\cdot$78.9	$1.2\cdot10^{-3}$

where $\omega_{\mathrm{al},\ddot{x}_1}$ and $\omega_{\mathrm{al},F_{\mathrm{s}}}$ are the frequencies of the anti-resonances in the llth entry of the corresponding loop gain matrices. The used values are displayed in Table 7.2. Note that the ratio between the frequencies of the anti-resonances for the 66th entry, the torsional mode, is almost 1, see Fig. 7.4(f), so it is expected that not much damping can be added to this mode. The filter matrices can be defined as

$$\mathbf{LF}(s) = \mathrm{diag}(LF_1(s), \ldots, LF_6(s)), \text{ with } LF_l(s) = \frac{\omega_{\mathrm{pl}}}{s + \omega_{\mathrm{pl}}}, \tag{7.47}$$

$$\mathbf{HF}(s) = \mathrm{diag}(HF_1(s), \ldots, HF_6(s)), \text{ with } HF_l(s) = \frac{s}{s + \omega_{\mathrm{pl}}}. \tag{7.48}$$

The sensor fusion controllers are then defined as

$$\mathbf{H}^{\mathrm{SF}}_{\mathrm{r},\ddot{\boldsymbol{x}}_1}(s) = \mathbf{T}^{\mathrm{u}}\mathbf{H}^{\mathrm{d}}_{\mathrm{r}}(s)\mathbf{LF}(s)\mathbf{T}^{\mathrm{y}}_{\ddot{\boldsymbol{x}}_1}, \tag{7.49}$$

$$\mathbf{H}^{\mathrm{SF}}_{\mathrm{r},\boldsymbol{F}_{\mathrm{s}}}(s) = \mathbf{T}^{\mathrm{u}}\mathbf{H}^{\mathrm{d}}_{\mathrm{r}}(s)\mathbf{HF}(s)\mathbf{T}^{\mathrm{y}}_{\boldsymbol{F}_{\mathrm{s}}}, \tag{7.50}$$

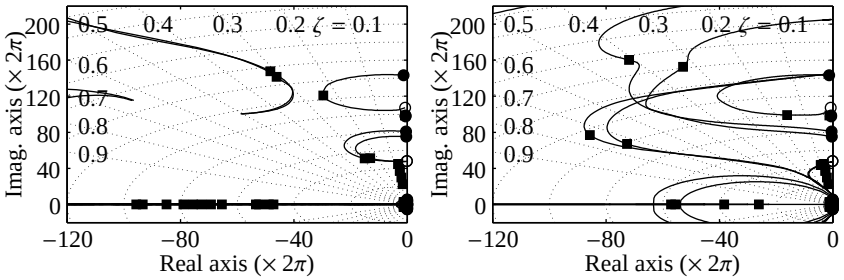

(a) Sensor fusion. (b) Two-sensor control.

Fig. 7.6: Closed loop poles of the hard mount when filter pole ω_{pl} tends from 0 to ∞ for: (a) sensor fusion; (b) two-sensor control. ○ denote the transmission zeros of $\mathbf{L}_{\mathrm{r},\ddot{x}_1}(s)$; ● denote the transmission zeros of $\mathbf{L}_{\mathrm{r},\boldsymbol{F}_\mathrm{s}}(s)$; ■ denote the closed loop poles for which maximum damping of the internal mode is obtained.

and the resulting sensor fusion loop gain matrix is then given by

$$\begin{aligned}\mathbf{L}_{\mathrm{r},(\ddot{x}_1,\boldsymbol{F}_\mathrm{s})}(s) &= \mathbf{H}^{\mathrm{SF}}_{\mathrm{r},\ddot{\mathbf{x}}_1}(s)\mathbf{G}_{\ddot{\mathbf{x}}_1\boldsymbol{F}_\mathrm{a}}(s) + \mathbf{H}^{\mathrm{SF}}_{\mathrm{r},\boldsymbol{F}_\mathrm{s}}(s)\mathbf{G}_{\boldsymbol{F}_\mathrm{s}\boldsymbol{F}_\mathrm{a}}(s)\\ &= \mathbf{T}^{\mathrm{u}}\mathbf{H}^{\mathrm{d}}_{\mathrm{r}}(s)(\mathbf{LF}(s)\mathbf{T}^{\mathrm{y}}_{\ddot{\mathbf{x}}_1}\mathbf{G}_{\ddot{\mathbf{x}}_1\boldsymbol{F}_\mathrm{a}}(s) + \mathbf{HF}(s)\mathbf{T}^{\mathrm{y}}_{\boldsymbol{F}_\mathrm{s}}\mathbf{G}_{\boldsymbol{F}_\mathrm{s}\boldsymbol{F}_\mathrm{a}}(s)). \quad (7.51)\end{aligned}$$

This is illustrated in Fig. 7.5(a). Loop gain matrix $\mathbf{L}_{\mathrm{r},(\ddot{x}_1,\boldsymbol{F}_\mathrm{s})}(s)$ is obtained by cutting the loop at the position of $\boldsymbol{F}_\mathrm{a}$. The diagonal loop gain matrix for sensor fusion is calculated by cutting the loop at the position of $\boldsymbol{F}_{\mathrm{a,ref}}$, in a similar way as for acceleration and force feedback:

$$\mathbf{L}^{\mathrm{d}}_{\mathrm{r},(\ddot{\mathbf{x}}_1,\boldsymbol{F}_\mathrm{s})}(s) = \mathbf{H}^{\mathrm{d}}_{\mathrm{r}}(s)(\mathbf{LF}(s)\mathbf{T}^{\mathrm{y}}_{\ddot{\mathbf{x}}_1}\mathbf{G}_{\ddot{\mathbf{x}}_1\boldsymbol{F}_\mathrm{a}}(s) + \mathbf{HF}(s)\mathbf{T}^{\mathrm{y}}_{\boldsymbol{F}_\mathrm{s}}\mathbf{G}_{\boldsymbol{F}_\mathrm{s}\boldsymbol{F}_\mathrm{a}}(s))\mathbf{T}^{\mathrm{u}}. \quad (7.52)$$

Their diagonal entries are shown in Fig. 7.4 as the solid black lines. It is observed that the anti-resonances corresponding to the internal modes are better damped.

The maximum achievable damping ratios depend on the ratio between the frequencies of the (undamped) anti-resonances. These frequencies are equal to the magnitudes of the so-called *transmission zeros* in the loop gain matrices $\mathbf{L}_{\mathrm{r},\ddot{x}_1}(s)$ and $\mathbf{L}_{\mathrm{r},\boldsymbol{F}_\mathrm{s}}(s)$. Transmission zeros correspond to the suspension frequencies of a substructure constrained by the sensors and actuators [40]. By varying the filter poles $\omega_{\mathrm{p}l}$ from 0 to ∞, the closed loop poles can be plotted as branches of the "root locus", similar as in Fig. 3.7 for the one-axis vibration isolator. This is illustrated in Fig.7.6(a) that shows these curves. For each mode, the curve starts in $s = \mathrm{j}\omega_{\mathrm{a}l,\boldsymbol{F}_\mathrm{s}}$ and ends in $s = \mathrm{j}\omega_{\mathrm{a}l,\ddot{x}_1}$, where $\omega_{\mathrm{a}l,\boldsymbol{F}_\mathrm{s}}$ and $\omega_{\mathrm{a}l,\ddot{x}_1}$ are the frequency of the anti-resonances corresponding to the lth mode. It is visible that the torsional mode around 107 Hz remains poorly damped.

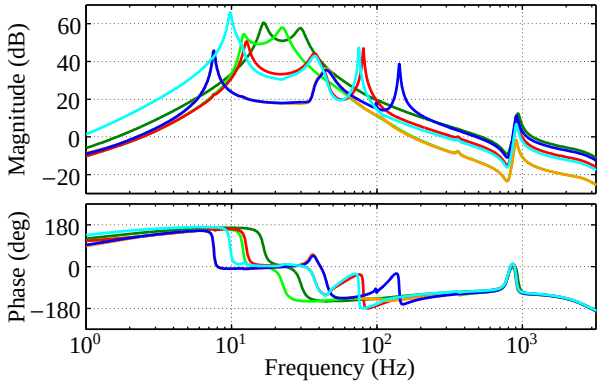

Fig. 7.7: Characteristic loci of loop gain matrix $\mathbf{L}_{\mathrm{r},(\ddot{\boldsymbol{x}}_1,\boldsymbol{F}_\mathrm{s})}(s)$ for sensor fusion.

The squares indicate the closed loop poles using the filter poles of Table 7.2. It is clear that the distances between the realized damping ratios and the maximum achievable damping ratios are small. The reason that the distances are not zero, is because the input and output decoupling matrices do not decouple the internal modes exactly, they only decouple the suspension modes.

To check closed loop stability for the sensor fusion control strategy, the CL of the loop gain matrix $\mathbf{L}_{\mathrm{r},(\ddot{\boldsymbol{x}}_1,\boldsymbol{F}_\mathrm{s})}(s)$ of Eq. (7.51) are plotted in Fig. 7.7. It is observed that the phase angles of all CL do not cross the -180° line, except for the light blue and red CL that just hit the -180° in-between 70 and 100 Hz. In that frequency range the magnitude of these CL is well above 0 dB, so closed loop stability is achieved. The high magnitude is due to the high values for ω_{fl}. If lower values are used, the light blue and red CL may cross the 0 dB line in the frequency range where the phase angle is below -180°. In that case closed loop stability is not achieved.

So, sensor fusion can only be applied successfully if the magnitudes of the CL are crossing the 0 dB in the frequency range where the phase angles are above -180°. This requires a high control bandwidth. The highest crossover frequency of the CL is a measure of the required control bandwidth. In Fig. 7.7 it is visible that the highest crossover frequency of the CL is above 1 kHz.

7.6 Mode shaping modal control: two-sensor control

In a similar way as for the sensor fusion control strategy, the input and output decoupling matrices can be used to decouple the plant and design a diagonal

two-sensor controller. This is illustrated in Fig. 7.5(b). The proposed controller for acceleration feedback reads

$$\mathbf{H}_{\mathrm{t},\ddot{\boldsymbol{x}}_1}(s) = \mathbf{T}^{\mathrm{u}}\mathbf{H}_{\mathrm{t}}^{\mathrm{d}}(s)\mathbf{T}^{\mathrm{y}}_{\ddot{\boldsymbol{x}}_1}, \text{ with } \mathbf{H}_{\mathrm{t}}^{\mathrm{d}}(s) = \mathbf{H}^{\mathrm{d}}(s)\mathbf{F}_{\mathrm{t}}(s), \tag{7.53}$$

where $\mathbf{F}_{\mathrm{t}}(s) = \mathrm{diag}(F_{\mathrm{t}1}(s), \ldots, F_{\mathrm{t}6}(s))$ with

$$F_{tl}(s) = \frac{s^2}{s^2 + 2\zeta_{ll}\omega_{ll}s + \omega_{ll}^2}\frac{\omega_{\mathrm{f}l}^2}{s^2 + 2\zeta_{\mathrm{f}l}\omega_{\mathrm{f}l}s + \omega_{\mathrm{f}l}^2}F_{\mathrm{ext}}(s). \tag{7.54}$$

So, $\mathbf{H}_{\mathrm{t},\ddot{\boldsymbol{x}}_1}(s)$ is the same controller as $\mathbf{H}_{\mathrm{r},\ddot{\boldsymbol{x}}_1}(s)$ except for the contribution of the high-frequency zero $\omega_{\mathrm{z}l}$. This approach is similar to the two-sensor control strategy used for the one-axis vibration isolator described in section 3.4. The proposed controller for force feedback is derived in a similar way as

$$\mathbf{H}_{\mathrm{t},\boldsymbol{F}_{\mathrm{s}}}(s) = \mathbf{T}^{\mathrm{u}}\mathbf{H}^{\mathrm{d}}_{\mathrm{t},\boldsymbol{F}_{\mathrm{s}}}(s)\mathbf{T}^{\mathrm{y}}_{\boldsymbol{F}_{\mathrm{s}}}, \tag{7.55}$$

with

$$\mathbf{H}^{\mathrm{d}}_{\mathrm{t},\boldsymbol{F}_{\mathrm{s}}}(s) = \mathrm{diag}(H^{\mathrm{d}}_{\mathrm{t}1,F_{\mathrm{s}}}(s), \ldots, H^{\mathrm{d}}_{\mathrm{t}6,F_{\mathrm{s}}}(s)). \tag{7.56}$$

Instead of using $\mathbf{H}_{\mathrm{t}}^{\mathrm{d}}(s)$, a different diagonal controller $\mathbf{H}^{\mathrm{d}}_{\mathrm{t},\boldsymbol{F}_{\mathrm{s}}}(s)$ is used for force feedback. This controller is the same as the force feedback controller used for the one-axis vibration isolator. Its diagonal elements are given by

$$H^{\mathrm{d}}_{\mathrm{t}l,F_{\mathrm{s}}}(s) = k_{\mathrm{f}l}\frac{s^2}{s^2 + 2\zeta_{\mathrm{f}l}\omega_{\mathrm{f}l}s + \omega_{\mathrm{f}l}^2}\frac{\omega_{\mathrm{f}l}}{s + \omega_{\mathrm{f}l}}F_{\mathrm{ext}}(s). \tag{7.57}$$

The filter parameters $\omega_{\mathrm{f}l}$ and $\zeta_{\mathrm{f}l}$ are given in Table 7.1. The controller gains $k_{\mathrm{f}l}$ can be set by the control engineer. Therefore, the following procedure is suggested. First, the decoupled loop gain matrices $\mathbf{L}^{\mathrm{d}}_{\mathrm{t},\ddot{\boldsymbol{x}}_1}(s)$ and $\mathbf{L}^{\mathrm{d}}_{\mathrm{t},\boldsymbol{F}_{\mathrm{s}}}(s)$ are calculated for acceleration and force feedback. Next, $k_{\mathrm{f}l}$ is chosen such that the llth entries of $\mathbf{L}^{\mathrm{d}}_{\mathrm{t},\ddot{\boldsymbol{x}}_1}(s)$ and $\mathbf{L}^{\mathrm{d}}_{\mathrm{t},\boldsymbol{F}_{\mathrm{s}}}(s)$ have approximately the same magnitude at the frequency of the anti-resonances in the acceleration path, so $|L^{\mathrm{d}}_{tll,\ddot{x}_1}(s = \mathrm{j}\omega_{\mathrm{a}l,\ddot{x}_1})|$ $= |\beta L^{\mathrm{d}}_{tll,F_{\mathrm{s}}}(s = \mathrm{j}\omega_{\mathrm{a}l,\ddot{x}_1})|$. An approximate formula for calculating $k_{\mathrm{f}l}$ can be derived as

$$k_{\mathrm{f}l} = \beta\frac{1}{\omega_{\mathrm{n}l}^2}\frac{\omega_{\mathrm{f}l}}{\omega_{\mathrm{a}l,\ddot{x}_1}}. \tag{7.58}$$

This expression is equal to the expression of Eq. (3.38) for the one-axis vibration isolator except for the term ω_{r}^2 in Eq. (3.38), which is accounted for in the input and output decoupling matrices. The used values are given in Table 7.2, where a value of $\beta = 0.5$ similar as in section 3.4 is used.

By varying the gains k_{fl} for the force feedback controller from 0 to ∞ and keeping the acceleration feedback controller as in Eq. (7.53), the resulting closed loop poles can be plotted as branches of the "root locus" in a similar way as for sensor fusion. The plot is shown in Fig. 7.6(b). The squares indicate the location of the closed loop poles for the controller gains of Table 7.2. It is clearly visible that large damping ratios can be obtained for the internal modes, even larger than for sensor fusion. Another advantage is that drops of the phase angles of the corresponding CL below the -180° do not occur, hence closed loop stability can be guaranteed.

7.7 Modeling results and discussion

In this section the achievable performance of the active vibration isolator is analyzed for the various presented control strategies. These are mode shaping modal control for acceleration feedback, sensor fusion and two-sensor control. Mode shaping modal control for force feedback is not analyzed, because in chapter 3 it is demonstrated that force feedback is outperformed by the other control strategies, in particular in case of a relative high parasitic stiffness. In section 5.3.1 it is shown that for the designed vibration isolator, the parasitic stiffness is large. Hence, it can be expected that mode shaping modal control for force feedback is also outperformed by the other control strategies using mode shaping modal control.

The performance is analyzed using the transmissibilities. For each control strategy, the transmissibility matrix $\mathbf{T}_{\text{ref}}(s)$ of Eq. (5.17) is calculated. This matrix describes the motion of reference frame $\boldsymbol{x}_{\text{ref}}(s)$ attached rigidly to the payload, due to motion of the frame $\boldsymbol{x}_{\text{floor}}(s)$ attached rigidly to the floor. The payload consists of three bodies, see Fig. 5.2: payload body (p1) on which the accelerometers and force sensors used for feedback are attached, and a large and small flexible payload body (p2a) and (p2b). If reference frame $\boldsymbol{x}_{\text{ref}}(s)$ is attached to payload body (p1), matrix $\mathbf{T}_{\text{ref}}(s)$ can be interpreted as the matrix extension of the scalar transmissibility $T(s)$. If an additional reference frame $\boldsymbol{x}_{\text{d,ref}}(s)$ is attached to flexible payload body (p2b), matrix $\mathbf{T}_{\text{d,ref}}(s)$ can be interpreted as the matrix extension of the scalar deformation transmissibility $T_{\text{d}}(s)$. Hence, $\mathbf{T}_{\text{d,ref}}(s)$ is the deformation transmissibility matrix. The llth element of each matrix represents the payload's response (a pure translation or rotation in the direction of x, y or z) due to floor excitation in the same direction.

The diagonal entries of $\mathbf{T}_{\text{ref}}(s)$ are plotted in Fig. 7.8. Since the off-diagonal

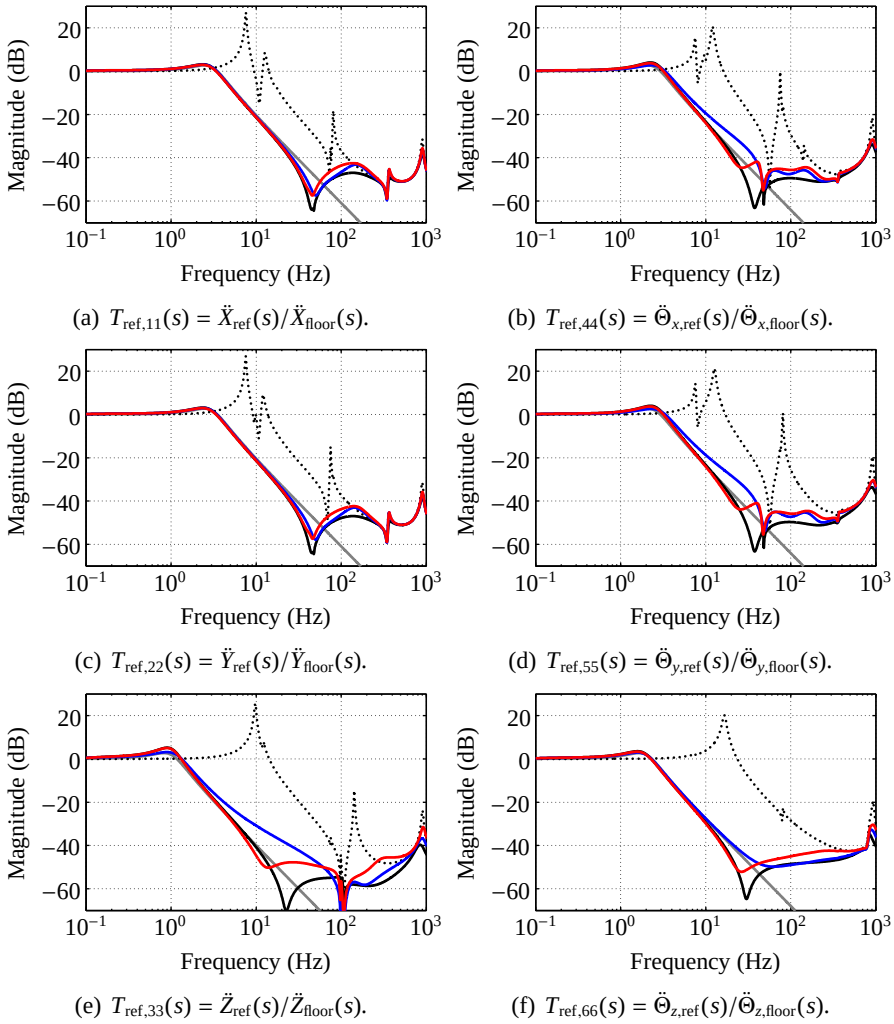

(a) $T_{\text{ref},11}(s) = \ddot{X}_{\text{ref}}(s)/\ddot{X}_{\text{floor}}(s)$.

(b) $T_{\text{ref},44}(s) = \ddot{\Theta}_{x,\text{ref}}(s)/\ddot{\Theta}_{x,\text{floor}}(s)$.

(c) $T_{\text{ref},22}(s) = \ddot{Y}_{\text{ref}}(s)/\ddot{Y}_{\text{floor}}(s)$.

(d) $T_{\text{ref},55}(s) = \ddot{\Theta}_{y,\text{ref}}(s)/\ddot{\Theta}_{y,\text{floor}}(s)$.

(e) $T_{\text{ref},33}(s) = \ddot{Z}_{\text{ref}}(s)/\ddot{Z}_{\text{floor}}(s)$.

(f) $T_{\text{ref},66}(s) = \ddot{\Theta}_{z,\text{ref}}(s)/\ddot{\Theta}_{z,\text{floor}}(s)$.

Fig. 7.8: Diagonal entries of transmissibility matrix $\mathbf{T}_{\text{ref}}(s)$.
- reference transmissibility
- open loop
- closed loop using acceleration feedback
- closed loop using sensor fusion
- closed loop using two-sensor control

entries are much smaller compared to the diagonal entries, these are not shown. Next to the closed loop results, also the open loop transmissibilities are displayed (black dotted lines). The transmissibilities for acceleration feedback

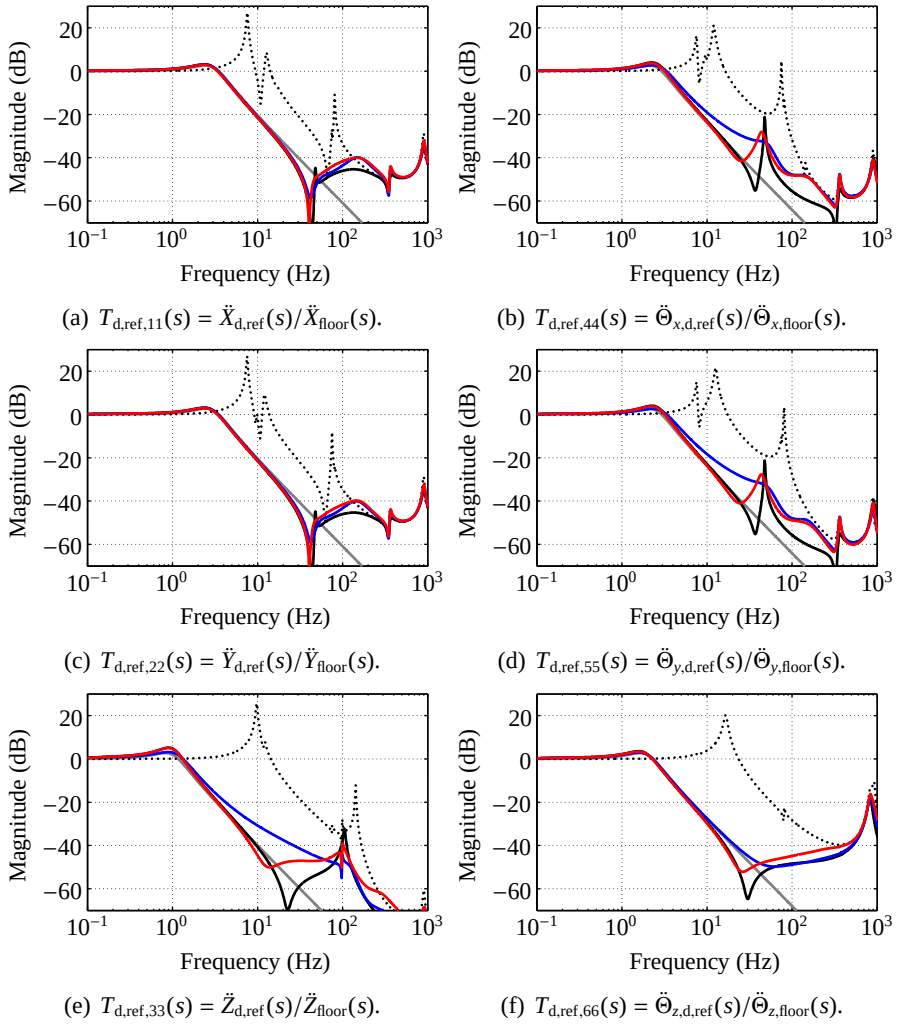

(a) $T_{\mathrm{d,ref},11}(s) = \ddot{X}_{\mathrm{d,ref}}(s)/\ddot{X}_{\mathrm{floor}}(s)$.

(b) $T_{\mathrm{d,ref},44}(s) = \ddot{\Theta}_{x,\mathrm{d,ref}}(s)/\ddot{\Theta}_{x,\mathrm{floor}}(s)$.

(c) $T_{\mathrm{d,ref},22}(s) = \ddot{Y}_{\mathrm{d,ref}}(s)/\ddot{Y}_{\mathrm{floor}}(s)$.

(d) $T_{\mathrm{d,ref},55}(s) = \ddot{\Theta}_{y,\mathrm{d,ref}}(s)/\ddot{\Theta}_{y,\mathrm{floor}}(s)$.

(e) $T_{\mathrm{d,ref},33}(s) = \ddot{Z}_{\mathrm{d,ref}}(s)/\ddot{Z}_{\mathrm{floor}}(s)$.

(f) $T_{\mathrm{d,ref},66}(s) = \ddot{\Theta}_{z,\mathrm{d,ref}}(s)/\ddot{\Theta}_{z,\mathrm{floor}}(s)$.

Fig. 7.9: Diagonal entries of deformation transmissibility matrix $\mathbf{T}_{\mathrm{d,ref}}(s)$.
- reference transmissibility
- open loop
- closed loop using acceleration feedback
- closed loop using sensor fusion
- closed loop using two-sensor control

(black solid lines), sensor fusion (blue solid lines) and two-sensor control (red solid lines) are shown. In Figs. 7.8(a)–(d) it is visible that due to coupling of the suspension modes, the open loop transmissibilities in horizontal directions

(both translations and rotations) are high. The desired suspension frequencies and damping ratios of the closed loop suspension modes are achieved. This is observed by the transmissibility curves. Each of the curves coincides with the curve of a *reference transmissibility* (gray solid lines) up to at least the frequency where an attenuation of −30 dB is obtained (except for sensor fusion). Each of the reference transmissibilities is a second-order low-pass filter constructed using the desired suspension frequency for the corner frequency of the filter and the corresponding damping ratio. It also indicates that the desired mode shapes are realized. If the transmissibility curves would not coincide with the curves of the second-order low-pass filters, this would mean that the desired mode shapes are not realized. This is the case for sensor fusion. Because of a high parasitic stiffness, not all of the desired mode shapes can be realized, especially the vertical mode, see Fig. 7.8(e). There is a small amplification at each resonance, but this is because a damping ratio of only 40% is used. For the vertical transmissibility in Fig. 7.8(e) there is a little more amplification at resonance. This is due to the pole at 0.1 Hz in the second-order high-pass filter which is relatively close to the desired suspension frequency of 1 Hz for the vertical transmissibility.

The diagonal entries of $\mathbf{T}_{\mathrm{d,ref}}(s)$ are plotted if Fig. 7.9 and show similar results as for $\mathbf{T}_{\mathrm{ref}}(s)$. In case of acceleration feedback, three deformation transmissibilities (for horizontal rotations and vertical translation) show resonance peaks in-between 40 and 100 Hz corresponding to poorly damped internal modes, that cannot be damped using acceleration feedback, see Figs. 7.9(b), (d) and (e). In case of sensor fusion and two-sensor control, the damping ratios of these modes can be increased, although only a little bit, at the price of less attenuation in the surrounding frequency range. It is remarkable that with acceleration feedback also three internal modes can be damped, see the other three deformation transmissibilities (for horizontal translations and vertical rotation) in Figs. 7.9(a), (c) and (f). For these modes, sensor fusion and two-sensor control do not improve the performance.

7.8 Conclusions

A method for designing a mode shaping modal controller for the six-axes active hard mount vibration isolator is presented. With this controller, for each suspension mode not only its suspension frequency and damping ratio, but also its mode shape can be tuned. The mode shapes can be chosen arbitrarily, provided that the modal matrix containing the mode shape vectors is of full rank.

It is suggested to choose the mode shapes as the translations and rotations of a reference frame located in the point of accuracy, which is the point where the suspended payload needs to have a high accuracy. The mode shaping shaping modal controller can be used with both acceleration and force feedback, although for force feedback it is required that parasitic stiffness and damping is small and negligible.

There exist an input and output decoupling matrix that (approximately) decouple the system's plant. This is the case if the mode shapes of the open loop system and the desired mode shapes of the closed loop system do not differ too much or the desired suspension frequencies of the closed loop system are much lower than the suspension frequencies of the open loop system. Then, the mode shaping modal controller reduces to a diagonal controller where each of the diagonal entries is a SISO controller. This allows to use additional filtering for each SISO controller individually. Additional filtering is required to set the desired high-frequency attenuation of each mode and, if necessary, to stabilize the control loop.

The input and output decoupling matrices can be used to combine the mode shaping modal control design with sensor fusion or two-sensor control. In this way, it is possible to simultaneously shape the suspension modes and increase the damping ratios of the internal modes of the suspended payload. Design methods are presented to maximize these damping ratios without affecting the realized suspension modes.

By analyzing the performance regarding the transmissibilities and deformation transmissibilities, it is demonstrated that the desired suspension frequencies and damping ratios can be realized using mode shaping modal control for acceleration feedback, sensor fusion or two-sensor control. The desired mode shapes can be realized as well, except for sensor fusion control, because its performance is affected by the presence of a large parasitic stiffness. For the same reason, it is recommended not to use mode shaping modal control for force feedback. It is shown that for sensor fusion, the closed loop system can become unstable in case of a low control bandwidth. With sensor fusion or two-sensor control, the damping ratios of all internal modes can be increased at the price of less attenuation at high frequencies compared to acceleration feedback. It is remarkable that with acceleration feedback, the damping ratios of some internal modes can be increased as well. Therefore, acceleration feedback and two-sensor control are the two most promising control strategies for using mode shaping modal control.

Control experiments with a six-axes vibration isolator

Chapter 8

The results of the real-time implementation of the control strategies described in chapter 7 on the demonstrator setup of the six-axes active hard mount vibration isolator are presented. First, the experimental procedure is described. Next, it is shown that due to hardware limitations it is not possible to obtain a stable closed loop using the control parameters of Tables 7.1 and 7.2. Therefore, the control designs need to be modified such that a stable closed loop is possible. For the modified control designs, the performance is analyzed using the identified transmissibility and deformation transmissibility matrices, and the obtained RMS accelerations levels of the payload.

8.1 Experimental procedure

The demonstrator setup of the six-axes active hard mount vibration isolator is mounted on a rigid floor plate, see also Fig. 5.3. It is available at the laboratory of Mechanical Automation and Mechatronics of the University of Twente, Enschede. In Fig. 2.1(b) it is shown that the floor vibrations measured at this laboratory are very small, even below the level of the VC-E curve. To prevent that the measurements used to analyze the performance suffer from measurement noise of the accelerometers, the motion level of the floor plate needs to be increased.

Therefore, the floor plate is equipped with several piezoelectric actuators. Six piezoelectric actuators are needed to excite all six degrees of freedom (DOFs) of the floor plate. Unfortunately, only four piezoelectric actuators are available, such that only four DOFs of the floor plate can be excited. The consequence of this restriction is discussed later on in this chapter. Three of the piezoelectric actuators are placed vertically and one is placed horizontally.

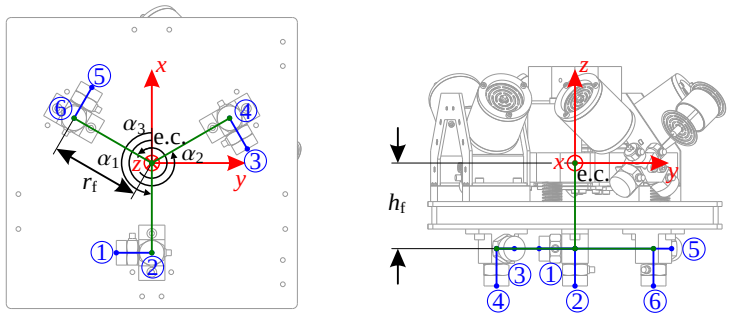

(a) Bottom view of the floor plate. (b) Front view of the vibration isolator.

Fig. 8.1: Coordinate frame (x, y, z) which origin is located at the elastic center (e.c.) and the location of the accelerometers ①–⑥ at the floor plate.

These are visible in Fig. 5.3 except for one of the vertically placed piezoelectric actuators. In this way the floor plate is allowed to have (small) translations in x- and z-direction and (small) rotations around the x- and y-axes. The floor plate's translation in y-direction and its rotation around the z-axis are constrained. The motion is expressed in the coordinates of the reference frame $\boldsymbol{x}_{\text{ref}} = (x, y, z, \theta_x, \theta_y, \theta_z)^{\text{T}}$ attached to the suspended payload and oriented as in Fig. 5.4. The point of accuracy at which the origin of the reference frame is located, is the elastic center of the vibration isolator.

The floor plate is equipped with six accelerometers, see Fig. 8.1. Their signals $\ddot{\boldsymbol{x}}_0$ are measured in the axial direction of the accelerometers. A transformation matrix $\mathbf{R}_{\text{floor}}$ allows to transform $\ddot{\boldsymbol{x}}_0$ to $\ddot{\boldsymbol{x}}_{\text{floor}}$, which describes the motion of a reference frame attached to the floor with the same location and orientation as $\ddot{\boldsymbol{x}}_{\text{ref}}$, see Eq. (5.14) in subsection 5.3.2. The inverse of $\mathbf{R}_{\text{floor}}$ is

$$\mathbf{R}_{\text{floor}}^{-1} = \begin{bmatrix} \text{s}\alpha_1 & -\text{c}\alpha_1 & 0 & h_\text{f}\text{c}\alpha_1 & h_\text{f}\text{s}\alpha_1 & r_\text{f} \\ 0 & 0 & 1 & -r_\text{f}\text{s}\alpha_1 & r_\text{f}\text{c}\alpha_1 & 0 \\ \text{s}\alpha_2 & -\text{c}\alpha_2 & 0 & h_\text{f}\text{c}\alpha_2 & h_\text{f}\text{s}\alpha_2 & r_\text{f} \\ 0 & 0 & 1 & -r_\text{f}\text{s}\alpha_2 & r_\text{f}\text{c}\alpha_2 & 0 \\ \text{s}\alpha_3 & -\text{c}\alpha_3 & 0 & h_\text{f}\text{c}\alpha_3 & h_\text{f}\text{s}\alpha_3 & r_\text{f} \\ 0 & 0 & 1 & -r_\text{f}\text{s}\alpha_3 & r_\text{f}\text{c}\alpha_3 & 0 \end{bmatrix}, \tag{8.1}$$

where α_1, α_2, and α_3 are the angles between the three accelerometer pairs and the x-axis, $\text{c}\alpha_i = \cos(\alpha_i)$ and $\text{s}\alpha_i = \sin(\alpha_i)$. Length r_f is the distance between the vertical axis of symmetry and the point where an accelerometer is attached to the floor plate, length h_f is the distance between the point of accuracy and the point where a horizontally placed accelerometer is attached to the floor

plate. In this thesis $\alpha_1 = \pi$, $\alpha_2 = \frac{2}{3}\pi + \pi$, and $\alpha_3 = \frac{4}{3}\pi + \pi$ (see Fig. 8.1(a)).

By exciting the floor plate using random input signals for the four piezoelectric actuators, the floor plate's motion and the payload's response are measured as $\ddot{\boldsymbol{x}}_0$ and $\ddot{\boldsymbol{x}}_1$ respectively. Using Eq. (5.14), $\ddot{\boldsymbol{x}}_0$ and $\ddot{\boldsymbol{x}}_1$ are transformed to $\ddot{\boldsymbol{x}}_{\text{floor}}$ and $\ddot{\boldsymbol{x}}_{\text{ref}}$ respectively. This allows to calculate the power spectral densities (PSDs) $P_{\ddot{x}_{\text{floor},k}\ddot{x}_{\text{floor},k}}(f)$ and cross power spectral densities (CPSDs) $P_{\ddot{x}_{\text{ref},i}\ddot{x}_{\text{floor},k}}(f)$. The ikth entry of the transmissibility matrix $\hat{\mathbf{T}}_{\text{ref}}(f)$ can be calculated as

$$\hat{T}_{\text{ref},ik}(f) = \frac{P_{\ddot{x}_{\text{ref},i}\ddot{x}_{\text{floor},k}}(f)}{P_{\ddot{x}_{\text{floor},k}\ddot{x}_{\text{floor},k}}(f)}. \tag{8.2}$$

This way of calculating the entries of $\hat{\mathbf{T}}_{\text{ref}}(f)$ requires only one experiment to identify all entries. In [47] an alternative method is described, however this requires six different experiments to identify all entries. Therefore, the method used in this thesis is preferred.

Large flexible payload body (p2a), visible in Fig. 5.2, can also be equipped with accelerometers. Their signals $\ddot{\boldsymbol{x}}_{\text{d}}$ can be transformed to $\ddot{\boldsymbol{x}}_{\text{d,ref}}$ using a transformation matrix $\mathbf{R}_{\text{d,ref}}$ that is calculated in a similar way as Eq. (8.1). Next, the CPSDs $P_{\ddot{x}_{\text{d,ref},i}\ddot{x}_{\text{floor},k}}(f)$ can be calculated. This allows to identify the entries of the deformation transmissibility matrix of $\hat{\mathbf{T}}_{\text{d,ref}}(f)$ as

$$\hat{T}_{\text{d,ref},ik}(f) = \frac{P_{\ddot{x}_{\text{d,ref},i}\ddot{x}_{\text{floor},k}}(f)}{P_{\ddot{x}_{\text{floor},k}\ddot{x}_{\text{floor},k}}(f)}. \tag{8.3}$$

Unfortunately, only one accelerometer is available for the measurements on the large flexible payload body (p2a), while there are six needed to identify all elements of accelerometer signals $\ddot{\boldsymbol{x}}_{\text{d}}$. Therefore, six experiments are performed in which during each experiment the additional accelerometer is mounted at a different location at the large flexible payload body (p2a). For each experiment, approximately the same excitation signals for the floor plate are used.

The floor plate is excited such that the PSDs of its acceleration levels are more or less comparable to that of a VC-D curve, which is the second quietest environment used for designing fabs. In Fig. 8.2(a) it is shown that the PSDs of its acceleration level for x- and z-translation are indeed comparable to that of a VC-D curve, except for two peaks at 30 and 50 Hz. These are due to flexible modes of the table on which the floor plate is mounted on. It is discussed in section 2.1.2 that above 100 Hz the acceleration level of fab floors tends to decrease rapidly. This is also visible in Fig. 8.2(a), although some peaks in-between 100 and 300 Hz are present. Since the y-translation of the floor plate cannot be excited, the PSD of its acceleration level is a little lower. The PSDs

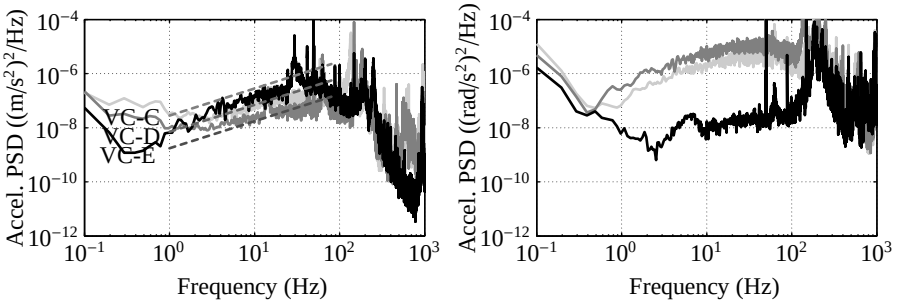

(a) VC-C to VC-E curves. (b) PSDs of *x*-, *y*- and *z*-rotations.

Fig. 8.2: (a) Power spectral densities (PSDs) of measured floor translations in acceleration units compared to PSDs of the VC-C to VC-E curves. (b) PSDs of measured floor rotations. *x*-direction ( ); *y*-direction ( ); *z*-direction ( ).

of the acceleration levels for rotation show similar results, see Fig. 8.2(b). The rotation around the *z*-axis cannot be excited as well, therefore its PSD is lower as compared to the PSDs for the other rotations.

8.2 Closed loop stability

In section 6.9 it is shown that the identification model and flexible body model of the six-axes vibration isolator have comparable dynamics at least up to a frequency of 200 Hz. Above that frequency, the effects of actuator dynamics and high-frequency structural dynamics of the suspended payload, which have not been included in the model, cause some differences. However, it is thought that the controllers designed in the previous chapter on the flexible body model can be implemented on the demonstrator setup of the six-axes active hard mount vibration isolator with only minor modifications.

The first modification is that not the reduced stiffness, damping and mass matrices $\bar{\mathbf{M}}$, $\bar{\mathbf{D}}$ and $\bar{\mathbf{K}}$ available from the reduced order model of section 5.4, are used to design the mode shaping modal controller, but those obtained from the identified reduced order model of section 6.6. The second modification is that filter $F_{\text{ext}}(s)$ of Eq. (7.33) is replaced by

$$F_{\text{ext}}(s) = \frac{s^2 + 2\zeta_1\omega_1 s + \omega_1^2}{s^2 + 2\zeta_2\omega_2 s + \omega_2^2}\frac{\omega_2^2}{\omega_1^2}\frac{s + \omega_3}{\omega_3}, \tag{8.4}$$

where, $\omega_i = 2\pi f_i$ with $f_1 = 800$ Hz, $f_2 = 3$ kHz and $f_3 = 390$ Hz, $\zeta_1 = 0.05$, and $\zeta_2 = 0.4$. This filter compensates not only for the dynamics of the wire

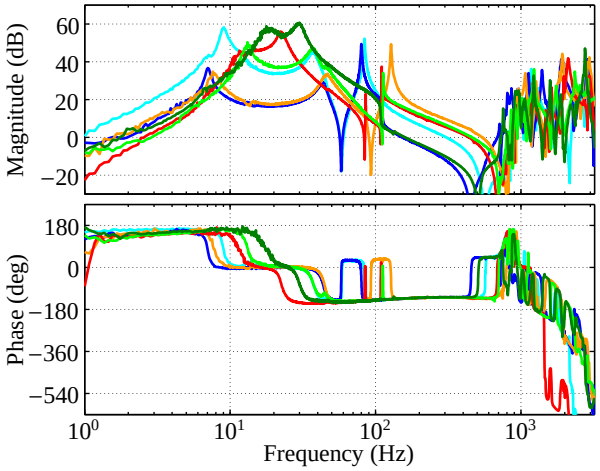

Fig. 8.3: Characteristic loci of loop gain matrices $\mathbf{L}_{\mathrm{r},\ddot{\mathbf{x}}_1}(s)$ for acceleration feedback without using the modified control parameters and filter $F_{\mathrm{ext}}(s)$ of Eq. (8.4).

flexures by using a skew notch filter as in Eq. (7.33), but also for the first-order low-pass filter formed by the impedance of the voice coil actuator. It is similar to the filter used in section 4.2.

Closed loop stability can be checked using the generalized Nyquist criterion [37]. This is done by plotting the characteristic loci (CL) of the loop gain matrix for the corresponding controller. Each loop gain matrix is calculated using the estimates of the frequency response functions from actuator forces to accelerometer or force sensor signals. These are obtained in chapter 6. The CL for acceleration feedback are plotted in Fig. 8.3. At high frequencies the magnitudes of the CL are still above 0 dB. This means that an infinite control bandwidth is obtained. Unfortunately, the phase angles of the CL all cross the $-180°$ phase line at a certain frequency, resulting in an unstable closed loop.

The instability is due to the high-frequency structural dynamics of the payload that is not taken into account in the flexible body model. This dynamics is causing a large increase of the magnitudes of the loop gains in the high-frequency range where collocation between actuator and sensor is lost. In contrast to the one-axis vibration isolator, the notch filter in $F_{\mathrm{ext}}(s)$ of Eq. (8.4) is not effective in compensating for the loss in collocation in the six-axes vibration isolator. The plots of the CL of sensor fusion and two-sensor control show similar results. Therefore, the designed demonstrator setup is not suitable to use with high-bandwidth control strategies, such as those derived in chapter 7.

8.3 Modified control parameters

To stabilize the system, the control bandwidth needs to be lowered. Hence, the achievable isolation performance is also lower. Loop shaping filters are used to shape the controllers such that closed loop stability is obtained while the performance is maximized. The details of the loop shaping filters are given in appendix E. Acceleration feedback is considered first. Sensor fusion and two-sensor control are discussed next.

8.3.1 Acceleration feedback

To lower the control bandwidth, the control parameters need to be changed. First, the corner frequencies of the second-order low-pass filters in $\mathbf{F}_r(s)$ of Eq. (7.32) are lowered by a factor 3 as compared to the values listed in Table 7.1. This results in a lower isolation performance of the vibration isolator, since the high-frequency attenuation is depending on the values of these corner frequencies. By lowering these values, the magnitudes of all CL are below 0 dB in the frequency range in-between 200 and 400 Hz. This is in-between the frequencies of the internal modes and the modes due to the high-frequency structural dynamics. Next, a loop shaping filter is constructed such that the phase angles of all CL are crossing the -180° phase line in-between 200 and 400 Hz.

The CL of the loop gain matrix using the modified control parameters and the loop shaping filter are plotted in Fig. 8.4. It is observed that closed loop stability is obtained, since the phase angles of the CL cross the -180° phase line at a frequency where the corresponding magnitudes are smaller than 0 dB and the phase angles are all below -180° at the six highest crossover frequencies. However, the phases margins at the the crossover frequencies in-between 30 and 300 Hz are very small. The phase margins at the six lowest crossover frequencies in-between 1 and 3 Hz are also small. This is due to the second-order high-pass filters in the controller and charge amplifiers for the accelerometers, both with corner frequencies of 0.1 Hz (see section 4.2). By increasing the damping ratios of the suspension modes or lowering their suspension frequencies, the phase margins at the lowest crossover frequencies become even smaller. That is the reason that damping ratios of only 40% are used.

To illustrate what the achievable performance is, the transmissibility and deformation transmissibility matrices are calculated using the modified acceleration feedback controller on the flexible body model. Their diagonal entries are shown in Figs. E.4 and E.5 of appendix E as the black lines. It is observed that in-between 30 and 300 Hz, there are some resonance peaks in both

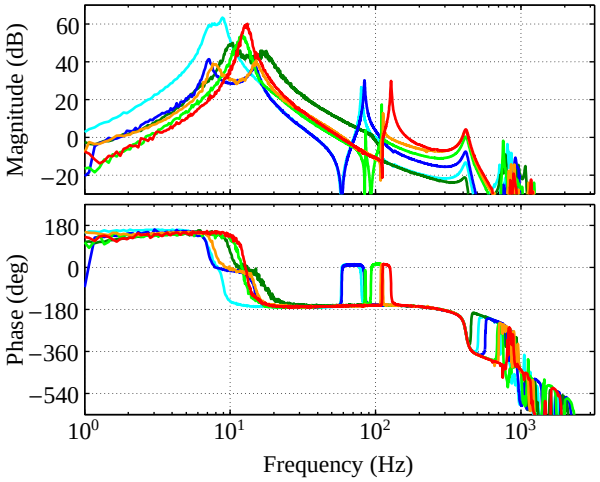

Fig. 8.4: Characteristic loci of loop gain matrices $\mathbf{L}_{\mathrm{r},\ddot{x}_1}(s)$ for acceleration feedback using the modified control parameters and filter $F_{\mathrm{ext}}(s)$ of Eq. (E.1).

the transmissibilities and deformation transmissibilities of the closed loop system. These are due to the small phase margins at the crossover frequencies in-between 30 and 300 Hz. The small phase margins also cause the amplification of the closed loop (deformation) transmissibility for the z-rotation in-between 80 and 400 Hz, as compared to the open loop one, see Figs. E.4(e) and E.5(e). However, with the modified control settings it is still possible to achieve lower transmissibility limits ranging from −20 to −35 dB.

8.3.2 Sensor fusion and two-sensor control

The same approach as for acceleration feedback is used for sensor fusion and two-sensor control. The corner frequencies of the second-order low-pass filters in $\mathbf{F}_{\mathrm{r}}(s)$ of Eq. (7.32) are lowered by a factor 3 as compared to the values listed in Table 7.1 and a loop shaping filter is constructed.

The CL of the loop gain matrices of sensor fusion and two-sensor control using the modified control parameters and the loop shaping filter are plotted in Figs. 8.5 and 8.6. It is observed that closed loop stability is obtained, since the phase angles of the CL cross the -180° phase line at a frequency where the corresponding magnitudes are smaller than 0 dB and the phase angles are all below -180° at the six highest crossover frequencies. The phase margins at the the crossover frequencies in-between 30 and 300 Hz are somewhat larger than for acceleration feedback. It is observed that the anti-resonances in-between 60

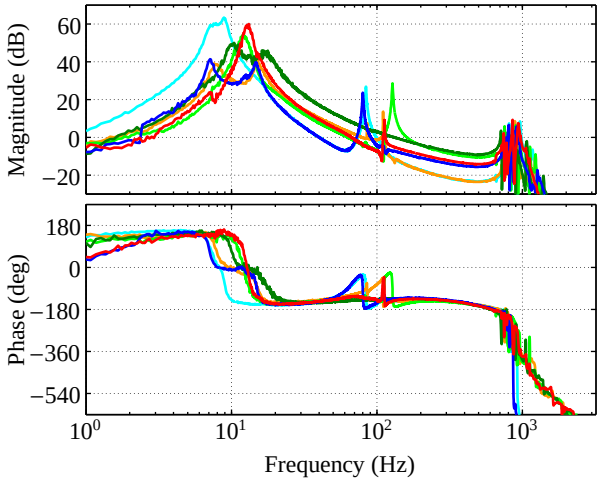

Fig. 8.5: Characteristic loci of loop gain matrices $\mathbf{L}_{\mathrm{r},\ddot{x}_1}(s)$ for sensor fusion using the modified control parameters and filter $F_{\mathrm{ext}}(s)$ of Eq. (E.2).

and 120 Hz are also better damped than for acceleration feedback. Therefore, it is expected that the damping ratios of the internal in-between 75 and 300 Hz can be increased.

To illustrate what the achievable performance is, the transmissibility and deformation transmissibility matrices are calculated using the modified feedback controllers for sensor fusion and two-sensor control on the flexible body model. Their diagonal entries are shown in Figs. E.4 and E.5 of appendix E as the blue and red lines. It is observed that the peaks in-between 30 and 300 Hz in the transmissibilities and deformation transmissibilities of the closed loop system, are (much) lower compared to acceleration feedback, in particular for two-sensor control. This is because of the larger phase margins at the crossover frequencies in-between 30 and 300 Hz. Note that there is no amplification of the closed loop (deformation) transmissibility for the z-rotation in-between 80 and 400 Hz, compared to the open loop one. With the modified control settings for sensor fusion and two-sensor control, it is possible to achieve a slightly better performance than for acceleration feedback.

8.4 Experimental results

The performance is analyzed in this section. Therefore the identified transmissibility and deformation transmissibility matrices are used. Since the measured

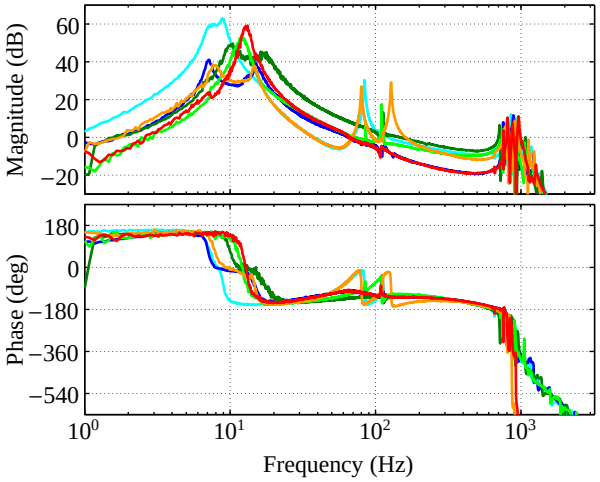

Fig. 8.6: Characteristic loci of loop gain matrices $\mathbf{L}_{\mathrm{r},\tilde{x}_1}(s)$ for two-sensor control using the modified control parameters and filter $F_{\mathrm{ext}}(s)$ of Eq. (E.2).

acceleration levels of the excited rigid floor plate are comparable to that of a VC-D curve, it is useful to calculate the RMS acceleration levels of the payload as well and to use these as the ultimate performance measure of the vibration isolator. The results are presented for acceleration feedback, sensor fusion and two-sensor control.

8.4.1 Acceleration feedback

The diagonal entries of the identified transmissibility matrix are plotted in Fig. 8.7. The gray solid lines represent the open loop, the black solid lines the closed loop using acceleration feedback. The coupling of the suspension modes is well visible in the open loop transmissibility of the *x*-translation of Fig. 8.7(a), because multiple resonance peaks are visible (at about 8 and 13 Hz). In-between 1 and 100 Hz, the transmissibilities of the closed loop match well with those of the black lines in Fig. E.4 obtained with the flexible body model, except for the *z*-rotation, see Fig. 8.7(f). Since the *z*-rotation cannot be excited using the piezoelectric actuators of the floor plate, see section 8.1, it is not possible to obtain a reliable identification of this transmissibility. This can also be concluded from the corresponding coherence function which is displayed in Fig. 8.8(b). It is much smaller than the coherence function for the transmissibility of the *z*-translation shown in Fig. 8.8(a).

Above 100 Hz, the measured accelerations also consist of the contributions

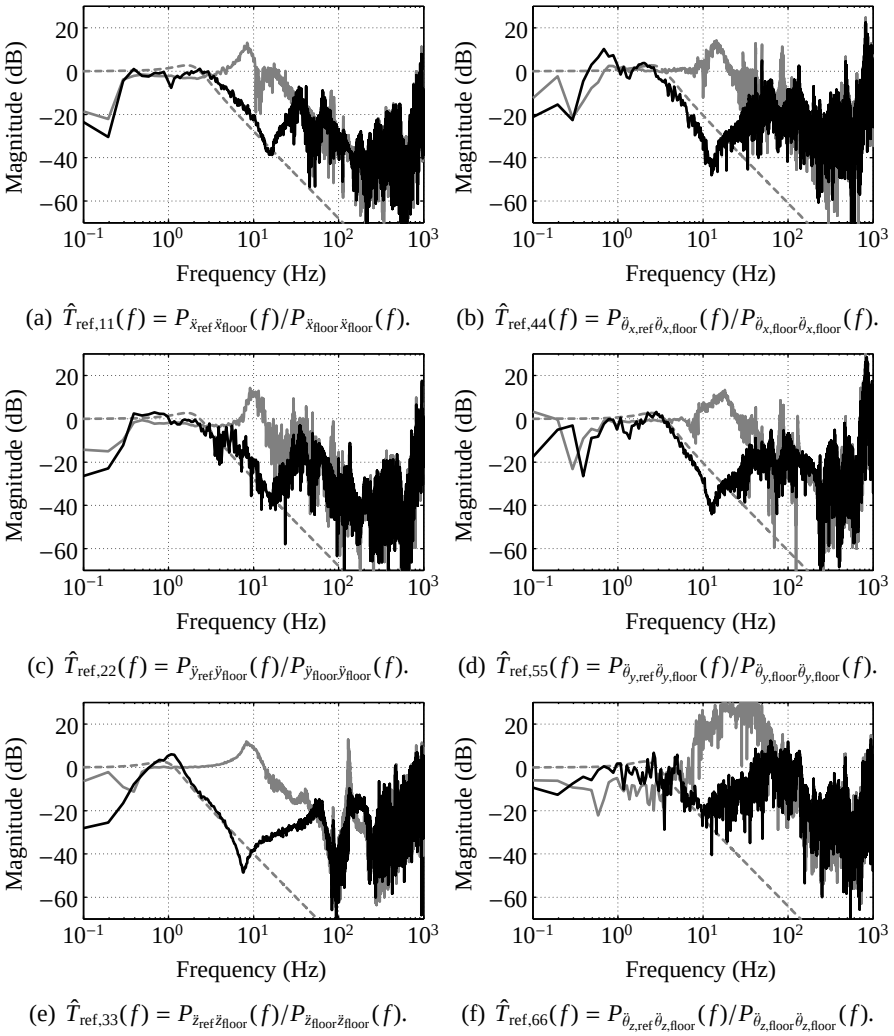

(a) $\hat{T}_{\mathrm{ref},11}(f) = P_{\ddot{x}_{\mathrm{ref}}\ddot{x}_{\mathrm{floor}}}(f)/P_{\ddot{x}_{\mathrm{floor}}\ddot{x}_{\mathrm{floor}}}(f)$.

(b) $\hat{T}_{\mathrm{ref},44}(f) = P_{\ddot{\theta}_{x,\mathrm{ref}}\ddot{\theta}_{x,\mathrm{floor}}}(f)/P_{\ddot{\theta}_{x,\mathrm{floor}}\ddot{\theta}_{x,\mathrm{floor}}}(f)$.

(c) $\hat{T}_{\mathrm{ref},22}(f) = P_{\ddot{y}_{\mathrm{ref}}\ddot{y}_{\mathrm{floor}}}(f)/P_{\ddot{y}_{\mathrm{floor}}\ddot{y}_{\mathrm{floor}}}(f)$.

(d) $\hat{T}_{\mathrm{ref},55}(f) = P_{\ddot{\theta}_{y,\mathrm{ref}}\ddot{\theta}_{y,\mathrm{floor}}}(f)/P_{\ddot{\theta}_{y,\mathrm{floor}}\ddot{\theta}_{y,\mathrm{floor}}}(f)$.

(e) $\hat{T}_{\mathrm{ref},33}(f) = P_{\ddot{z}_{\mathrm{ref}}\ddot{z}_{\mathrm{floor}}}(f)/P_{\ddot{z}_{\mathrm{floor}}\ddot{z}_{\mathrm{floor}}}(f)$.

(f) $\hat{T}_{\mathrm{ref},66}(f) = P_{\ddot{\theta}_{z,\mathrm{ref}}\ddot{\theta}_{z,\mathrm{floor}}}(f)/P_{\ddot{\theta}_{z,\mathrm{floor}}\ddot{\theta}_{z,\mathrm{floor}}}(f)$.

Fig. 8.7: Diagonal entries of transmissibility matrix $\hat{\mathbf{T}}_{\mathrm{ref}}(f)$ using acceleration feedback.
- - - - reference transmissibility
——— open loop
——— closed loop using acceleration feedback

of actuator noise and sensor noise, since the actual motion levels of the payload are very small. Therefore above 100 Hz, the transmissibilities are not reliable, in particular these of the rotations. Each of the curves of the closed loop coincides well with the curve of the corresponding reference transmissibility, up to

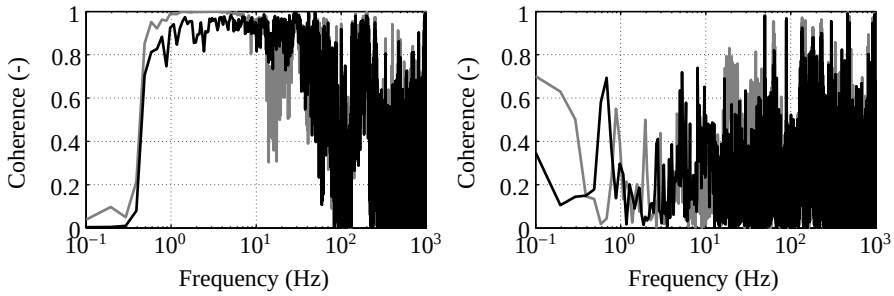

(a) Coherence between $\ddot{Z}_{\text{floor}}(f)$ and $\ddot{Z}_{\text{ref}}(f)$. (b) Coh. between $\ddot{\Theta}_{\text{z,floor}}(f)$ and $\ddot{\Theta}_{\text{z,ref}}(f)$.

Fig. 8.8: Coherence functions for transmissibility matrix $\hat{\mathbf{T}}_{\text{ref}}(f)$ in: (a) z-translation; (b) z-rotation; open loop (——) and closed loop using acceleration feedback (——).

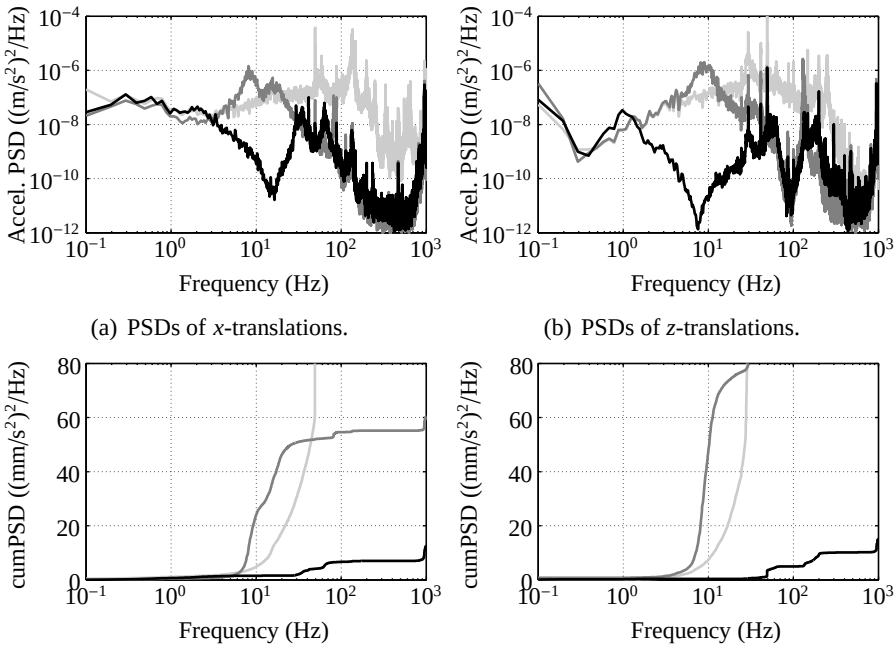

(a) PSDs of x-translations. (b) PSDs of z-translations.

(c) cumPSDs of x-translations. (d) cumPSDs of z-translations.

Fig. 8.9: (a,b) PSDs and (c,d) cumulative PSDs of measured vibrations: floor (——); payload in open loop (——); and in closed loop using acceleration feedback (——).

a frequency that is close to the corner frequency of the corresponding second-order low-pass filter in $\mathbf{F}_{\text{r}}(s)$ of Eq. (7.32). Each reference transmissibility is

Table 8.1: RMS acceleration levels of the floor and payloads using acceleration feedback.

i	mode shape	unit	$\lvert\ddot{x}_{\text{floor}}\rvert_{\text{RMS}}$	ol: $\lvert\ddot{x}_{\text{ref}}\rvert_{\text{RMS}}$	cl: $\lvert\ddot{x}_{\text{ref}}\rvert_{\text{RMS}}$	ol: $\lvert\ddot{x}_{\text{d,ref}}\rvert_{\text{RMS}}$	cl: $\lvert\ddot{x}_{\text{d,ref}}\rvert_{\text{RMS}}$
1	x_{ref}	mm/s^2	13.0	2.4	1.1	7.4	2.7
2	y_{ref}	mm/s^2	9.3	2.8	1.5	7.3	3.3
3	z_{ref}	mm/s^2	11.5	3.8	1.2	2.5	1.0
4	$\theta_{x,\text{ref}}$	mrad/s^2	50.0	34.5	16.3	103.5	45.1
5	$\theta_{y,\text{ref}}$	mrad/s^2	92.1	53.3	34.8	99.5	35.7
6	$\theta_{z,\text{ref}}$	mrad/s^2	29.4	52.1	19.2	69.9	32.5

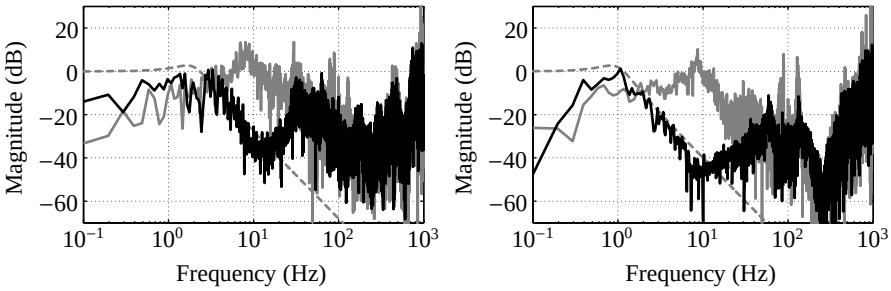

(a) $\hat{T}_{\text{d,ref},11}(f) = P_{\ddot{x}_{\text{ref}}\ddot{x}_{\text{floor}}}(f)/P_{\ddot{x}_{\text{floor}}\ddot{x}_{\text{floor}}}(f)$. (b) $\hat{T}_{\text{d,ref},33}(f) = P_{\ddot{z}_{\text{ref}}\ddot{z}_{\text{floor}}}(f)/P_{\ddot{z}_{\text{floor}}\ddot{z}_{\text{floor}}}(f)$.

Fig. 8.10: Diagonal entries of transmissibility matrix $\hat{\mathbf{T}}_{\text{d,ref}}(f)$ using acceleration feedback.
- - - - reference transmissibility
— open loop
— closed loop using acceleration feedback

a second-order low-pass filter constructed using the desired suspension frequency for the corner frequency of the filter and the corresponding damping ratio. Similar as for the modeling results, there are some resonance peaks in the closed loop transmissibilities in-between 30 and 300 Hz that are due to small phase margins in the CL of the corresponding loop gain matrix. However, it is concluded that the desired transmissibilities can be realized.

Instead of using the transmissibilities to analyze the performance, the plots of the PSDs can also be used for this. The PSDs of the x- and z-translations are shown in Figs. 8.9(a) and (b) for floor vibrations (light gray lines), payload vibrations in open loop (dark gray lines) and payload vibrations in closed loop (black lines). Since the plots of the PSDs become noisy at high frequencies, the plots of the cumulative PSDs can also be used. The cumulative PSDs are calculated as

$$\text{cum}P_{\bullet\bullet}(f) = \int_0^f P_{\bullet\bullet}(\varphi)\text{d}\varphi, \tag{8.5}$$

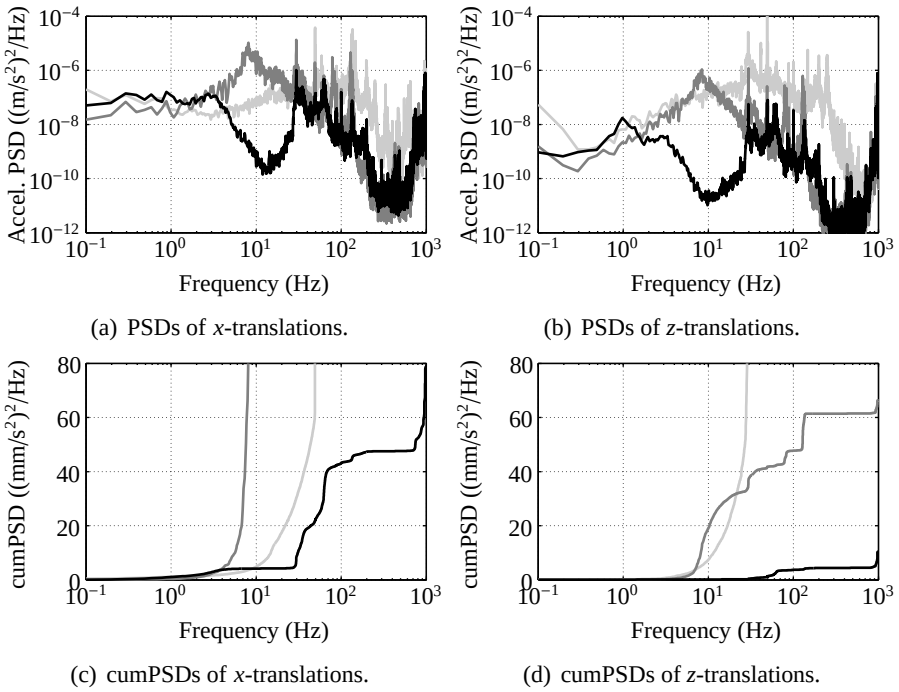

(a) PSDs of *x*-translations.

(b) PSDs of *z*-translations.

(c) cumPSDs of *x*-translations.

(d) cumPSDs of *z*-translations.

Fig. 8.11: (a,b) PSDs and (c,d) cumulative PSDs of measured vibrations: floor (———); large flexible payload (p2a) in open loop (———); and in closed loop using acceleration feedback (———).

where the final value cum$P_{\bullet\bullet}(f)$ is just the total power. The cumulative PSDs of *x*- and *z*-translations are shown in Figs. 8.9(c) and (d). These plots are smoother than those of the PSDs. It is observed that the main contributions to the total power are because of the peaks in the closed loop transmissibility due to small phase margins in the CL of the corresponding loop gain matrix. There is an additional contribution due to the peak around 900 Hz caused by the wire flexure dynamics. The sensor and actuator noise that appear at high-frequencies have almost no contribution to the total power.

The RMS acceleration levels in-between 0 and 1 kHz of the floor plate and payload can be calculated using Eq. (2.2). These are listed in Table 8.1. The levels of the closed loop are about a factor 2 or 3 smaller than those of the open loop. This is not a large improvement, but it is mainly due to the small phase margins obtained with the modified acceleration feedback controller.

Figs. 8.10(a) and (b) show two diagonal entries of the identified deformation transmissibility matrix, of the *x*- and *z*-translation. It is observed that these

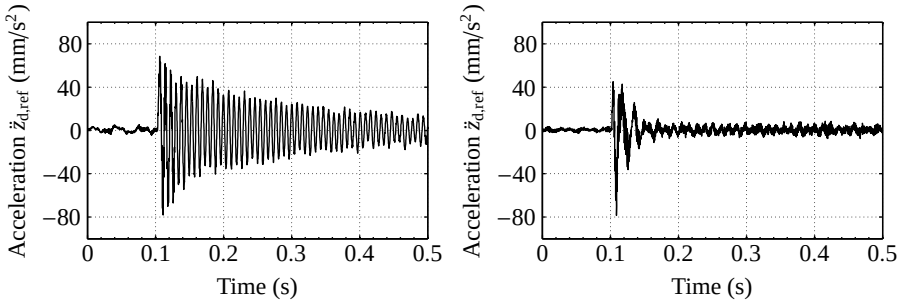

(a) Open loop. (b) Closed loop using acceleration feedback.

Fig. 8.12: Impulse response of the vertical acceleration $\ddot{z}_{d,ref}(t)$ of large flexible payload body (p2a): (a) in open loop; (b) in closed loop using acceleration feedback.

plots are more noisy than the plots of the corresponding entries of the identified transmissibility matrix. The other diagonal entries of the deformation transmissibility matrix are even more noisy. All coherence functions are very small. Therefore, it is better to use the corresponding PSDs of the measured accelerations of the large flexible payload body (p2a), shown in Figs. 8.11(a) and (b), and their cumulative PSDs, shown in Figs. 8.11(c) and (d). It is observed that the total power of the *x*-translation is due to many resonance peaks, while the total power of the *z*-translation is very small. The RMS acceleration levels are calculated as listed in Table 8.1 as well. The levels of the closed loop are also about a factor 2 to 3 smaller than those of the open loop.

To illustrate how much damping is added to the internal modes, the impulse responses of the large flexible payload body (p2a) in open loop and in closed loop are determined, see Figs. 8.12(a) and (b). Therefore, an impulse force with an amplitude of 0.1 N and a duration of 5 ms is added to all actuators simultaneously and the acceleration of the large flexible payload body (p2a) is measured in vertical direction. It is visible that the decay rate in closed loop is much smaller than in open loop, which means that significant damping is added to the internal mode. By counting the number of periods of the vibration mode it is calculated that the resonance frequency of this mode drops from 128 Hz to 88 Hz.

8.4.2 Sensor fusion

The diagonal entries of the identified transmissibility matrix using sensor fusion are plotted in Fig. 8.13. The gray solid lines represent the open loop, the black solid lines the closed loop using sensor fusion. In-between 1 and 100 Hz,

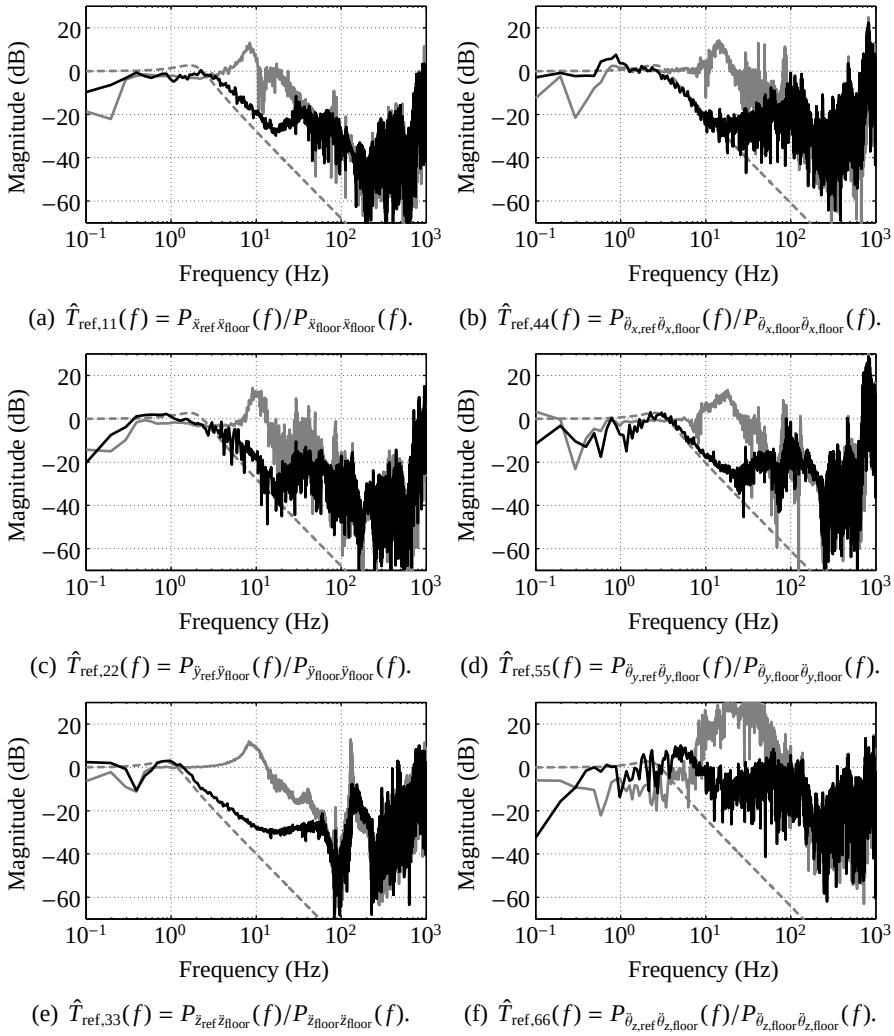

(a) $\hat{T}_{\mathrm{ref},11}(f) = P_{\ddot{x}_{\mathrm{ref}}\ddot{x}_{\mathrm{floor}}}(f)/P_{\ddot{x}_{\mathrm{floor}}\ddot{x}_{\mathrm{floor}}}(f)$.

(b) $\hat{T}_{\mathrm{ref},44}(f) = P_{\ddot{\theta}_{x,\mathrm{ref}}\ddot{\theta}_{x,\mathrm{floor}}}(f)/P_{\ddot{\theta}_{x,\mathrm{floor}}\ddot{\theta}_{x,\mathrm{floor}}}(f)$.

(c) $\hat{T}_{\mathrm{ref},22}(f) = P_{\ddot{y}_{\mathrm{ref}}\ddot{y}_{\mathrm{floor}}}(f)/P_{\ddot{y}_{\mathrm{floor}}\ddot{y}_{\mathrm{floor}}}(f)$.

(d) $\hat{T}_{\mathrm{ref},55}(f) = P_{\ddot{\theta}_{y,\mathrm{ref}}\ddot{\theta}_{y,\mathrm{floor}}}(f)/P_{\ddot{\theta}_{y,\mathrm{floor}}\ddot{\theta}_{y,\mathrm{floor}}}(f)$.

(e) $\hat{T}_{\mathrm{ref},33}(f) = P_{\ddot{z}_{\mathrm{ref}}\ddot{z}_{\mathrm{floor}}}(f)/P_{\ddot{z}_{\mathrm{floor}}\ddot{z}_{\mathrm{floor}}}(f)$.

(f) $\hat{T}_{\mathrm{ref},66}(f) = P_{\ddot{\theta}_{z,\mathrm{ref}}\ddot{\theta}_{z,\mathrm{floor}}}(f)/P_{\ddot{\theta}_{z,\mathrm{floor}}\ddot{\theta}_{z,\mathrm{floor}}}(f)$.

Fig. 8.13: Diagonal entries of transmissibility matrix $\hat{\mathbf{T}}_{\mathrm{ref}}(f)$ using sensor fusion.
- reference transmissibility
- open loop
- closed loop using sensor fusion

the transmissibilities of the closed loop match well with those of the blue lines in Fig. E.4 obtained with the flexible body model, except for the z-rotation, see Fig. 8.13(f), which is due to the same reason as for acceleration feedback. Similar as for the modeling results, the parasitic stiffness is the reason why

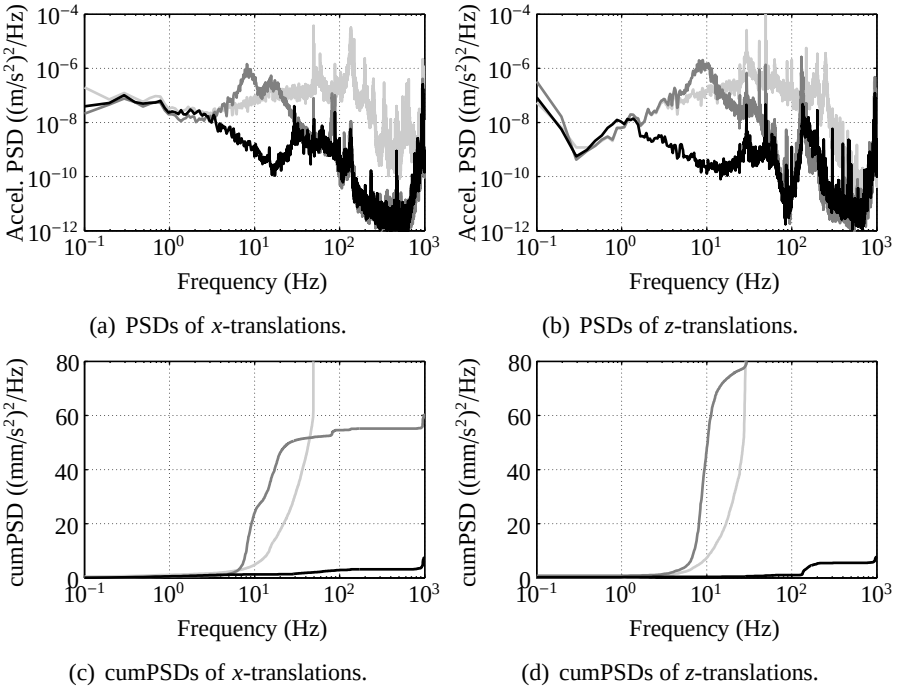

(a) PSDs of *x*-translations.

(b) PSDs of *z*-translations.

(c) cumPSDs of *x*-translations.

(d) cumPSDs of *z*-translations.

Fig. 8.14: (a,b) PSDs and (c,d) cumulative PSDs of measured vibrations: floor (——); payload in open loop (——); and in closed loop using sensor fusion (——).

that the closed loop transmissibility curves do not coincide with those of the reference transmissibilities. This can be observed in particular for the transmissibilities of the *x*- and *z*-translation, which deviate from their corresponding reference transmissibilities and show a roll-off rate that is slightly less than the desired −40 dB/decade, see Figs. 8.13(a) and (e). This indicates that the desired mode shapes, and therefore also the desired transmissibilities, cannot be realized using sensor fusion. This is because the contribution of the parasitic stiffness to the total stiffness matrix is not considered in the eigenvalue problem of Eq. (7.10) that is used to determine the desired mode shapes.

The plots of the PSDs and cumulative PSDs of *x*- and *z*-translations are shown in Figs. 8.14(a) and (b) and 8.15(a) and (b). These are calculated for floor vibrations (light gray lines), payload vibrations in open loop (dark gray lines) and closed loop (black lines), and large flexible payload (p2a) vibrations in open loop (dark gray lines) and closed loop (black lines). The results are quiet similar to those obtained with acceleration feedback, however with values of the total power that are lower. Especially the cumulative power at 100 Hz of

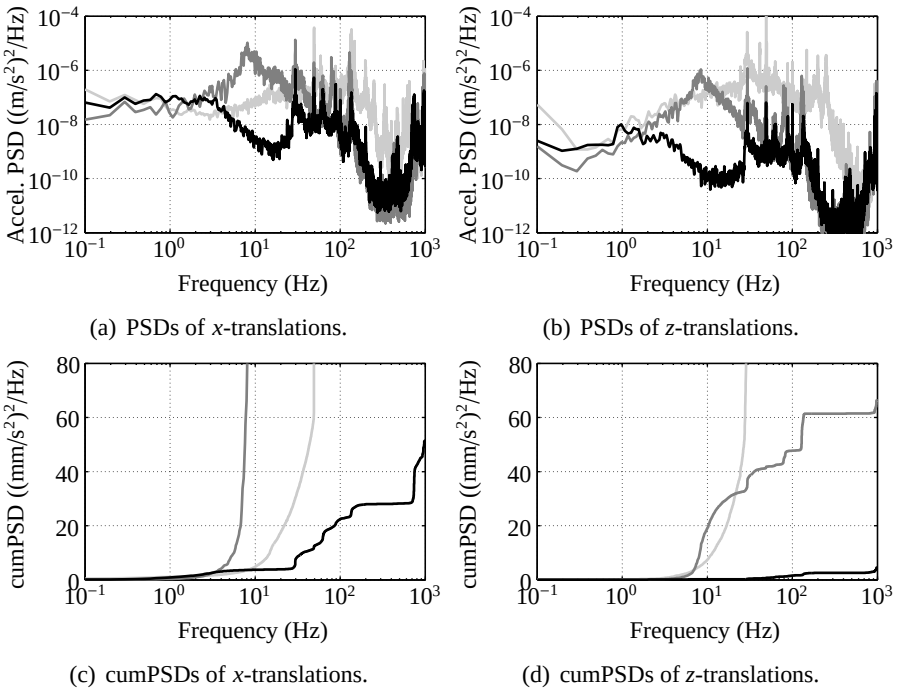

(a) PSDs of x-translations.

(b) PSDs of z-translations.

(c) cumPSDs of x-translations.

(d) cumPSDs of z-translations.

Fig. 8.15: (a,b) PSDs and (c,d) cumulative PSDs of measured vibrations: floor (———); large flexible payload (p2a) in open loop (———); and in closed loop using sensor fusion (———).

Table 8.2: RMS acceleration levels of the floor and payloads using sensor fusion.

i	mode shape	unit	$\lvert\ddot{x}_{\text{floor}}\rvert_{\text{RMS}}$	ol: $\lvert\ddot{x}_{\text{ref}}\rvert_{\text{RMS}}$	cl: $\lvert\ddot{x}_{\text{ref}}\rvert_{\text{RMS}}$	ol: $\lvert\ddot{x}_{\text{d,ref}}\rvert_{\text{RMS}}$	cl: $\lvert\ddot{x}_{\text{d,ref}}\rvert_{\text{RMS}}$
1	x_{ref}	mm/s^2	13.0	2.4	0.9	7.4	2.2
2	y_{ref}	mm/s^2	9.3	2.8	1.0	7.3	2.2
3	z_{ref}	mm/s^2	11.6	3.8	0.9	2.5	0.7
4	$\theta_{x,\text{ref}}$	mrad/s^2	50.0	34.5	11.7	103.5	28.3
5	$\theta_{y,\text{ref}}$	mrad/s^2	92.1	53.3	25.4	99.5	24.9
6	$\theta_{z,\text{ref}}$	mrad/s^2	29.4	52.1	10.9	69.8	29.2

the large flexible payload acceleration of the x-translation is about two times smaller than for acceleration feedback. This means that the internal modes of the payload are much better damped for sensor fusion as for acceleration feedback. This can also be concluded from the RMS acceleration levels in-between 0 and 1 kHz, see Table 8.2. These are about a factor 1.5 lower than for acceleration feedback, so a factor 3 to 5 lower than for the open loop.

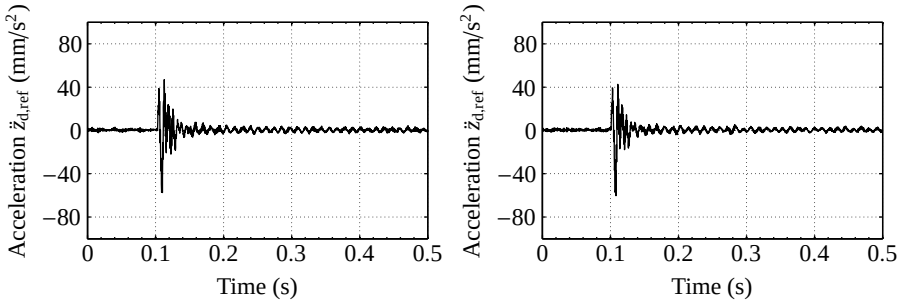

(a) Closed loop using sensor fusion. (b) Closed loop using two-sensor control.

Fig. 8.16: Impulse response of the vertical acceleration $\ddot{z}_{d,ref}(t)$ of large flexible payload body (p2a): (a) in closed loop using sensor fusion; (b) in closed loop using two-sensor control.

To illustrate how much damping is added to the internal modes, the impulse response of the large flexible payload body (p2a) in closed loop using sensor fusion is determined, see Fig. 8.16(a). By comparing it to Fig. 8.12(b), it is visible that the decay rate in closed loop using sensor fusion is only a little bit smaller than in closed loop using acceleration feedback. This means that the damping added to the internal mode is even larger. The resonance frequency of this mode is calculated as 88 Hz, the same value as for acceleration feedback.

8.4.3 Two-sensor control

The diagonal entries of the identified transmissibility matrix using two-sensor control are plotted in Fig. 8.17. The gray solid lines represent the open loop, the black solid lines the closed loop using two-sensor control. In-between 1 and 100 Hz, the transmissibilities of the closed loop match well with those of the red lines in Fig. E.4 obtained with the flexible body model, except for the z-rotation, which is due to the same reason as for acceleration feedback, see Fig. 8.17(f). There are no resonance peaks in the transmissibilities in-between 30 and 300 Hz due to larger phase margins in the loop gains of two-sensor control as compared to those of acceleration feedback. The closed loop transmissibility curves coincide with those of the reference transmissibilities, although there are small deviations for the x- and y-rotation, see Figs. 8.17(b) and (d). This is probably due to the parasitic stiffness which affects the force feedback controller of the two-sensor control strategy. However, it is concluded that the desired mode shapes and thus the desired transmissibilities can be realized using two-sensor control.

The plots of the PSDs and cumulative PSDs of x- and z-translations are

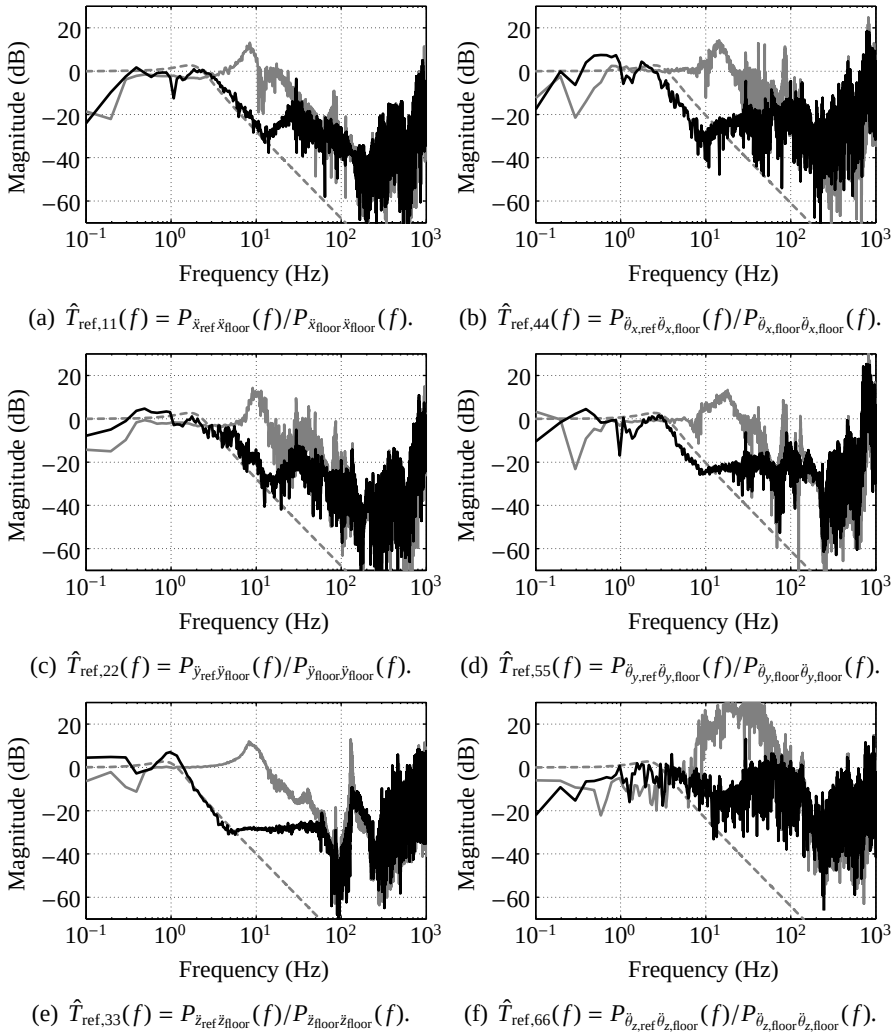

(a) $\hat{T}_{\mathrm{ref},11}(f) = P_{\ddot{x}_{\mathrm{ref}}\ddot{x}_{\mathrm{floor}}}(f)/P_{\ddot{x}_{\mathrm{floor}}\ddot{x}_{\mathrm{floor}}}(f)$.

(b) $\hat{T}_{\mathrm{ref},44}(f) = P_{\ddot{\theta}_{x,\mathrm{ref}}\ddot{\theta}_{x,\mathrm{floor}}}(f)/P_{\ddot{\theta}_{x,\mathrm{floor}}\ddot{\theta}_{x,\mathrm{floor}}}(f)$.

(c) $\hat{T}_{\mathrm{ref},22}(f) = P_{\ddot{y}_{\mathrm{ref}}\ddot{y}_{\mathrm{floor}}}(f)/P_{\ddot{y}_{\mathrm{floor}}\ddot{y}_{\mathrm{floor}}}(f)$.

(d) $\hat{T}_{\mathrm{ref},55}(f) = P_{\ddot{\theta}_{y,\mathrm{ref}}\ddot{\theta}_{y,\mathrm{floor}}}(f)/P_{\ddot{\theta}_{y,\mathrm{floor}}\ddot{\theta}_{y,\mathrm{floor}}}(f)$.

(e) $\hat{T}_{\mathrm{ref},33}(f) = P_{\ddot{z}_{\mathrm{ref}}\ddot{z}_{\mathrm{floor}}}(f)/P_{\ddot{z}_{\mathrm{floor}}\ddot{z}_{\mathrm{floor}}}(f)$.

(f) $\hat{T}_{\mathrm{ref},66}(f) = P_{\ddot{\theta}_{z,\mathrm{ref}}\ddot{\theta}_{z,\mathrm{floor}}}(f)/P_{\ddot{\theta}_{z,\mathrm{floor}}\ddot{\theta}_{z,\mathrm{floor}}}(f)$.

Fig. 8.17: Diagonal entries of transmissibility matrix $\hat{\mathbf{T}}_{\mathrm{ref}}(f)$ using two-sensor control.
- - - - reference transmissibility
——— open loop
——— closed loop using two-sensor control

shown in Figs. 8.18(a) and (b) and 8.19(a) and (b). These are calculated for floor vibrations (light gray lines), payload vibrations in open loop (dark gray lines) and closed loop (black lines), and large flexible payload (p2a) vibrations in open loop (dark gray lines) and closed loop (black lines). The results

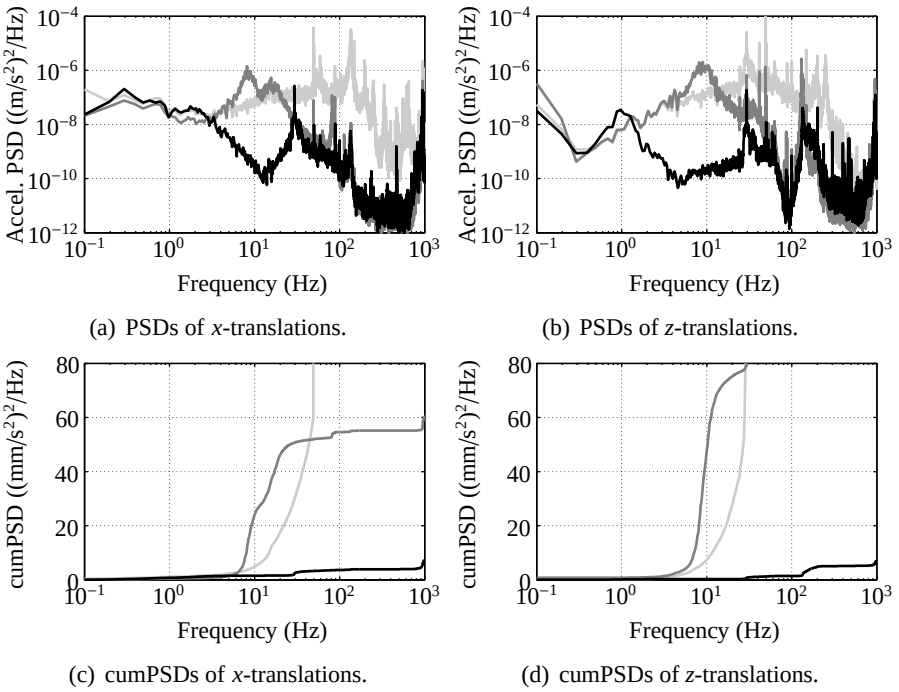

(a) PSDs of *x*-translations.

(b) PSDs of *z*-translations.

(c) cumPSDs of *x*-translations.

(d) cumPSDs of *z*-translations.

Fig. 8.18: (a,b) PSDs and (c,d) cumulative PSDs of measured vibrations: floor (——); payload in open loop (——); and in closed loop using two-sensor control (——).

are quiet similar to those obtained with sensor fusion, with values of the total power that are almost the same. It means that the internal modes of the payload are also well damped using two-sensor control. This can also be concluded from the RMS acceleration levels in between 0 and 1 kHz, see Table 8.3. These are almost the same as for sensor fusion, so a factor 3 to 5 lower than for the open loop.

To illustrate how much damping is added to the internal modes, the impulse response of the large flexible payload body (p2a) in closed loop using two-sensor control is determined, see Fig. 8.16(b). The result is similar to two-sensor control. This means that the damping added to the internal mode is very large. The resonance frequency of this mode is calculated as 88 Hz, which is the same value as for acceleration feedback and sensor fusion.

Based on the observation that with two-sensor control the desired transmissibilities can be realized, there are no resonance peaks in the transmissibilities and deformation transmissibilities due to small phase margins, and the RMS acceleration levels of the payload bodies are very small, it is concluded that

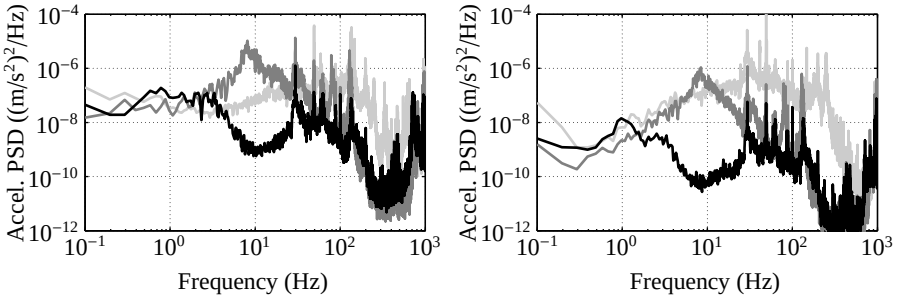

(a) PSDs of x-translations. (b) PSDs of z-translations.

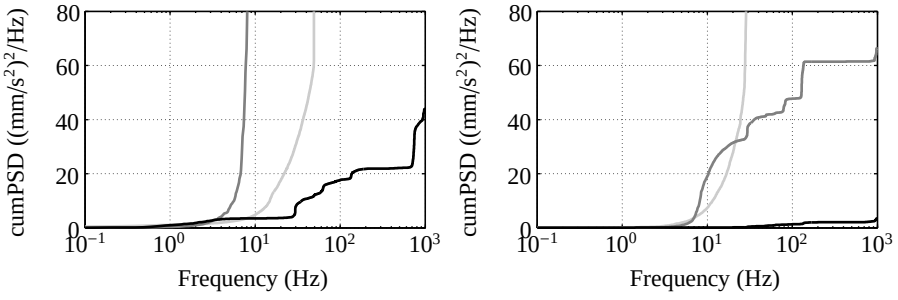

(c) cumPSDs of x-translations. (d) cumPSDs of z-translations.

Fig. 8.19: (a,b) PSDs and (c,d) cumulative PSDs of measured vibrations: floor (———); large flexible payload (p2a) in open loop (———); and in closed loop using two-sensor control (———).

Table 8.3: RMS acceleration levels of the floor and payload using two-sensor control.

i	mode shape	unit	$\lvert\ddot{x}_{\text{floor}}\rvert_{\text{RMS}}$	ol: $\lvert\ddot{x}_{\text{ref}}\rvert_{\text{RMS}}$	cl: $\lvert\ddot{x}_{\text{ref}}\rvert_{\text{RMS}}$	ol: $\lvert\ddot{x}_{\text{d,ref}}\rvert_{\text{RMS}}$	cl: $\lvert\ddot{x}_{\text{d,ref}}\rvert_{\text{RMS}}$
1	x_{ref}	mm/s^2	13.0	2.4	0.8	7.4	2.1
2	y_{ref}	mm/s^2	9.3	2.8	1.0	7.3	2.1
3	z_{ref}	mm/s^2	11.6	3.8	0.8	2.5	0.6
4	$\theta_{x,\text{ref}}$	mrad/s^2	50.0	34.5	9.7	103.5	24.4
5	$\theta_{y,\text{ref}}$	mrad/s^2	92.1	53.3	22.0	99.5	22.1
6	$\theta_{z,\text{ref}}$	mrad/s^2	29.4	52.1	10.0	69.8	28.7

the two-sensor control strategy results in the best performance. With two-sensor control the damping ratio of internal modes can be increased significantly, which is also one of the performance objectives stated in section 2.5. The best isolation performance is obtained for z-translation, with a reduction from the suspension frequency of 10 Hz in open loop to 1 Hz in closed loop and a lower transmissibility limit of −30 dB, see Fig. 8.17(e).

8.5 Discussion

In section 8.2 it is shown that in each leg of the develop demonstrator setup the loss of collocation between the actuator and sensors, together with the continuous structural dynamics of the suspended payload limits the available control bandwidth. As a consequence additional loop shaping filters are required to obtain a stable closed loop, in particular for acceleration feedback. For acceleration feedback, additional loop shaping filters are required even if there would be no loss of collocation. This is explained below.

The magnitudes of the CL of the transfer function matrix from actuator forces to accelerometer signals show large increases at high frequencies, see Fig. 6.2. These are due to many resonances and anti-resonances in this frequency range, with relative large separations between each resonance and anti-resonance, causing increases in the magnitudes. These increases are less apparent in the magnitudes of the CL of the transfer function matrix from actuator forces to force sensor signals, see Fig. 6.9. This results in higher crossover frequencies in the loop gains of acceleration feedback as compared to force feedback. Hence, acceleration feedback results in a higher control bandwidth than force feedback. This is also visible in the loop gains of acceleration feedback and force feedback of the one-axis vibration isolator shown in Fig. 3.3.

In chapter 7 it is shown that a higher roll-off rate for the acceleration feedback controller is used for sensor fusion and two-sensor control as compared to acceleration feedback. So, at high frequencies the relative contribution of acceleration feedback to the loop gains is smaller and that of the force feedback controller is larger. Therefore, the increases at high frequencies in the loop gain matrix from actuator forces to accelerometers signals are less important for sensor fusion and two-sensor control. This is an additional advantage of sensor fusion and two-sensor control over acceleration feedback.

However, it is suggested to improve the mechanical design of the six-axes active hard mount vibration isolator such that in each leg the actuator and sensors are collocated, or at least that the frequency at which collocation is lost, is much higher. In chapter 5 it is demonstrated that in the developed demonstrator setup the wire flexure dynamics is causing the loss of collocation. The wire flexures are used to make each leg of the vibration isolator compliant in all parasitic directions in order to obtain a low parasitic stiffness. Unfortunately, its axial stiffness is also limited and a trade-off between a high axial stiffness and a low parasitic stiffness has to be made. In section 5.3.1 it is shown that the parasitic stiffness introduced by the wire flexures is still high, resulting in a lower performance of sensor fusion, see section 8.4.2. Therefore, it is rec-

ommended to change the design of the legs such that the wire flexures can be omitted and are replaced by an alternative design solution. This solution must provide a much higher axial stiffness and a much lower parasitic stiffness as compared to wire flexures. The interested reader is referred to [47] for an example of a leg design without wire flexures.

The measured acceleration signals used to determine the performance also contain contributions of actuator noise and sensor noise of the accelerometers, in particular at high frequencies and at frequencies below 1 Hz. Their contributions become more important if the level of floor excitation is lower. Therefore, it is suggested to replace the accelerometers with some that have a lower noise level. References [33] and [59] present some comparisons between various accelerometers with ultra-low noise levels. It is shown that the noise PSD of an Endevco 87-10 piezoelectric accelerometer is about 100 times lower than that of an Endveco 7703A-1000 piezoelectric accelerometer, which are used for the demonstrator setup. The usable bandwidth of the Endevco 87-10 is at least 400 Hz which is still sufficient for the control strategies presented in chapter 7. In addition, these sensors do not contain high-pass filters in the charge amplifiers and as a consequence it is possible to obtain larger phase margins at the lowest crossover frequencies in the loop gains. Therefore, higher damping ratios of the suspension modes can be realized. More information about the modeling of noise in piezoelectric accelerometers can be found in [30–33].

The noise level of piezoelectric force sensors is in general well below that of the high-end piezoelectric accelerometers and therefore does not contribute to the total noise level, see [45, 53]. Actuator noise is mainly due to noise of the power amplifiers. Therefore, it is suggested to match the power amplifiers with the expected power consumption of the actuators [59].

Finally, it is suggested to add two horizontally placed piezoelectric actuators to the rigid floor plate such that the y-translation and z-rotation can be excited as well. Then it is possible to obtain more reliable estimates of the corresponding transmissibilities. It is also suggested to mount six accelerometers at the large flexible payload body instead of one, such that the deformation transmissibility matrix can be identified in one shot, which improves the estimates of the deformation transmissibilities.

8.6 Conclusions

The control strategies that are presented in chapter 7 are successfully implemented on the demonstrator setup of the six-axes active hard mount vibration

isolator, although with modified control parameters. It is shown that it is not possible to obtain closed loop stability using the desired high control bandwidth. This is due to the loss of collocation between actuator and sensors at about 900 Hz, together with the high-frequency structural dynamics of the demonstrator setup. In contrast to the one-axis vibration isolator, the notch filter used in the loop shaping filters in chapter 7 is not effective in compensating for the loss in collocation in the six-axes vibration isolator. Therefore, alternative loop shaping filters are designed.

Demanding a lower isolation performance and using the alternative loop shaping filters, closed loop stability can be obtained. It is shown that the performance of the vibration isolator regarding the transmissibilities and deformation transmissibilities match well with the modeling results of appendix E that are obtained using the same modified control parameters on the flexible body model described in section 5.3. The desired mode shapes can be successfully realized using the identification model obtained in chapter 6.

The best results are obtained using two-sensor control, since the desired mode shapes, and therefore the desired transmissibilities, are realized, as well as the desired suspension frequencies and damping ratios. This is the first performance objective stated in section 2.5. The best isolation performance is obtained for the z-translation, with a reduction of the suspension frequency from 9.8 Hz in open loop to 1 Hz in closed loop and a lower transmissibility limit of -30 dB, which is close to the transmissibility of the ideal active soft mount vibration isolator of section 2.5. The damping ratios of the internal modes can also be increased, which is the second performance objective, as is demonstrated by showing plots of the impulse response. The third objective, which is providing a stiff suspension, has already been realized by using hard mounts. The suspension modes are required to be at least 5 Hz. This requirement is fulfilled since the frequencies of the suspension modes of the demonstrator setup range from 7.0 to 18.1 Hz. Finally, the lowest RMS acceleration levels are obtained with two-sensor control. For the z-translation, the floor acceleration of 11.6 mm/s^2 RMS has been reduced to 0.6 mm/s^2 at the payload, which is a reduction of about 25 dB.

Suggestions for improving the design of the six-axes vibration isolator to obtain collocation between actuator and sensors are made. It is also suggested to use accelerometers with a lower noise level to improve the isolation performance in case of very low levels of floor vibrations.

Conclusions and recommendations

Chapter 9

9.1 Conclusions

The aim of this thesis is to develop an active hard mount vibration isolator for precision equipment. It is designed to obtain sufficient isolation of both floor vibrations and direct disturbance forces as well as to add damping to the internal modes of the suspended equipment. It is capable of fulfilling all these functions while simultaneously providing a stiff suspension to the equipment. First, several feedback control strategies for a one-axis active hard mount vibration isolator have been presented. Both modeling results and experimental results have demonstrated that all these functions can be fulfilled simultaneously. Next, the design, modeling and system identification of a demonstrator setup of a six-axes active hard mount vibration isolator have been discussed. A modal controller has been derived that can be used for tuning the suspension frequencies, damping ratios and mode shapes of the vibration isolator's suspension modes. The modal controller can only be derived if the mass, damping and stiffness matrices are known, which are obtained from either the model or system identification. Finally, the applicability of the modal controller has been demonstrated by performing closed loop experiments with the demonstrator setup. In the remainder of this section, the conclusions of the previous chapters are summarized.

In chapter 3 several control strategies for a one-axis vibration isolator have been proposed using acceleration feedback, force feedback or a combination of both. It has been shown that acceleration feedback outperforms force feedback in lowering the transmissibility and providing a stiff suspension. However, both acceleration and force feedback are not capable of increasing the damping ratio of the internal modes. For that reason, two novel control strategies have been derived. A sensor fusion strategy has been proposed in which

the acceleration signal is used at low frequencies and the force signal at high frequencies. A two-sensor control strategy has been proposed in which the force feedback controller is 90° out of phase with the acceleration feedback controller in the frequency range where damping of the internal modes is desired. It has been shown that the maximum achievable damping ratio of an internal mode is determined by the ratio of the anti-resonance frequencies for acceleration and force feedback. All three performance objectives stated in chapter 2 have been realized simultaneously using either sensor fusion or two-sensor control. The transmissibility of floor vibrations has been made comparable to that of an ideal active soft mount vibration isolator with a suspension frequency of 1 Hz and a lower transmissibility limit of −52 dB. Furthermore, the damping ratio of the internal mode has been increased to 43% at maximum and the suspension stiffness has been increased >150 times as compared to the ideal active soft mount. An additional advantage of both control strategies is that the system's susceptibility to direct disturbance forces is significantly decreased in the frequency range between 0 and 120 Hz as compared to the ideal active soft mount.

In chapter 4 the control strategies presented in chapter 3 have successfully been implemented on an experimental setup of a one-axis active hard mount vibration isolator. The experimental results match well with the modeling results in the frequency range from 1 to 250 Hz. Below 1 Hz and above 250 Hz sensor and actuator noise make the estimates of the performance transfer functions less reliable. It has been observed that for all control strategies except for acceleration feedback, it is not possible to compensate for vibrations that are being transmitted onto the suspended payload by means of parasitic stiffness paths. These vibrations result in a higher transmissibility and deformation transmissibility. For a successful implementation of the control strategies, it has been necessary to add a loop shaping filter to the controllers to compensate for the dynamics of the actuator and charge amplifiers of the accelerometer and force sensor as well as for the loss of collocation between actuator and sensors.

Chapter 5 describes the design and realization of a six-axes active hard mount vibration isolator and a demonstrator setup suspending a 10.9 kg payload. A rigid body model describing its suspension dynamics has been derived to get insight in how the six suspension modes depend on the mass and inertia properties of the payload, as well as on the axial stiffness of the legs and several other design parameters. A flexible body model has been presented, which can be used to analyze the effect of the payloads flexibilities. From this model, a reduced order model has been derived using Guyan reduction. The reduced

order model is a more accurate representation of the suspension dynamics than the approximate model, since the bending and torsional stiffness of the legs as well as the effect of an asymmetric payload are taken into account. The models describing the suspension dynamics have been used to derive the mass, damping and stiffness matrices that are used to design the modal controller explained in chapter 7.

In chapter 6 a novel three-steps method for the system identification of the active hard mount vibration isolator has been proposed. It has been used to validate the models of chapter 5 and to identify the reduced stiffness, damping and mass matrices that are used to design the modal controller of chapter 8. For the system identification several methods described in literature have been combined. In the first step, characteristic loci have been used for the estimation of poles. This allows to separate modes with closely spaced poles from each other. It has been shown that the proposed method outperforms the widely used LSCF estimator for the identification of closely spaced poles. In the second step, a state-space model describing accelerance transfer functions has been derived. In the third step, the reduced mass, damping and stiffness matrices have been calculated. The proposed system identification method has successfully been applied to experimental data from the demonstrator setup.

In chapter 7 a mode shaping modal controller has been derived for the six-axes active hard mount vibration isolator. With this modal controller, the resonance frequency, damping ratio and mode shape for each suspension mode can be tuned. The mode shapes can be chosen arbitrarily, provided that the modal matrix containing the mode shape vectors is of full rank. It can be used with both acceleration and force feedback, although force feedback requires the parasitic stiffness and damping being small and negligible. The modal controller can be simplified to a diagonal controller using an input and output decoupling matrix that (approximately) decouple the system's plant. This allows to use additional filtering for each suspension mode individually, and to extend the sensor fusion and two-sensor control strategy from the one-axis vibration isolator to the six-axes vibration isolator. It has been shown that the best performance is obtained for acceleration feedback and two-sensor control.

In chapter 8 the applicability of the mode shaping modal controller has successfully been demonstrated by performing closed loop experiments on the developed demonstrator setup, although with modified control parameters. It has been shown that closed loop stability cannot be obtained using the control parameters of chapter 7. This is due to the loss of collocation between actuator and sensors, together with the high-frequency structural dynamics of the

demonstrator setup. Demanding a lower isolation performance and using additional loop shaping filters, closed loop stability can be obtained. It has been shown that the performance of the vibration isolator regarding the transmissibilities and deformation transmissibilities matches well with the modeling results. The best results have been obtained using two-sensor control.

Based on the presented work in this thesis it is concluded that two-sensor control as proposed in sections 3.4 and 7.6 is the best control strategy for an active hard mount vibration isolator. The desired mode shapes and therefore the desired transmissibilities can be realized, as well as the desired suspension frequencies and damping ratios. It is possible to increase the damping ratios of the internal modes. The best isolation performance of the developed demonstrator has been obtained for the z-translation, with a reduction of the suspension frequency from 9.8 Hz in open loop to 1 Hz in closed loop and a lower transmissibility limit of -30 dB, which is close to the transmissibility of the ideal active soft mount vibration isolator as has been defined in chapter 2. The damping ratios of the internal modes can be increased as well as has been demonstrated in chapter 8. A stiff suspension has already been realized by using hard mounts. The requirement that the suspension modes are at least 5 Hz, has been fulfilled since the frequencies of the suspension modes of the demonstrator setup range from 7.0 to 18.1 Hz. The control experiments have demonstrated that the lowest RMS acceleration levels of the payload are obtained with two-sensor control. For the z-translation, the floor acceleration of 11.6 mm/s^2 RMS has been reduced to 0.6 mm/s^2 at the payload, which is a reduction of about 25 dB. It has been motivated that with two-sensor control a lower control bandwidth is required as compared to acceleration feedback.

The achievable performance of the demonstrator setup has been limited for mainly two reasons: due to the loss of collocation between the actuator and sensor in each leg, the control bandwidth is limited; due to actuator and sensor noise, the RMS acceleration levels of the suspended payload are limited.

9.2 Recommendations

Some recommendations for further research are proposed:

- The mechanical design of the six-axes active hard mount vibration isolator needs to be improved. Since all control strategies require a high-bandwidth controller, it should be aimed for a mechanical design such that in each leg the actuator and sensors are collocated or at least that the

frequency at which collocation is lost, is much higher (at least 2 kHz). Furthermore, a lower parasitic stiffness is desired, since this limits the performance for sensor fusion and two-sensor control.

- Active vibration isolators for precision equipment are used to isolate the equipment from very quiet floors, with acceleration levels that may be below that of a VC-E curve. Sensor noise of the accelerometers may limit the performance regarding the acceleration level of the suspended equipment. Therefore, it is suggested to use accelerometers with ultra-low noise levels, such as the Endevco 87-10 [32]. This accelerometer combines an ultra-low noise level with a usable bandwidth of at least 400 Hz.

- To obtain a reliable identification of the transmissibility and deformation transmissibility matrix in all degrees of freedom, it is recommended to be able to excite the rigid floor plate of the developed demonstrator setup in all directions. In the current setup, the y-translation and z-rotation cannot be excited. Therefore, two horizontally placed piezoelectric actuators should be added to the setup.

- In [10] the use of two-sensor control for active soft mount vibration isolators is investigated. The proposed control strategy is based on a combination of acceleration and displacement feedback. Therefore, an accelerometers is placed on the equipment and a displacement sensor is mounted between the floor and the suspended equipment. It is thought that with a lower control bandwidth the same performance objectives can be realized as for active hard mount vibration isolators. This simplifies the mechanical design of the vibration isolator.

REFERENCES

[1] K. Alvin, L. Peterson, and K. Park, "Method for determining minimum-order mass and stiffness matrices from modal test data". *AIAA Journal* **33** (1): 128–135, 1995.

[2] H. Amick, M. Gendreau, T. Busch, and C.G. Gordon, "Evolving criteria for research facilities: I - Vibration". In *Proc. SPIE* **5933**: 593303, 2005.

[3] M.D. Angelis, H. Lus, R. Betti, and R.W. Longman, "Extracting physical parameters of mechanical models from identified state-space representations". *J. Appl. Mech.* **69** (5): 617–625, 2002.

[4] H. van der Auweraer, P. Guillaume, P. Verboven, and S. Vanlanduit, "Application of a fast-stabilizing frequency domain parameter estimation method". *J. Dyn. Syst. Meas. Contr.* **123** (4): 651–658, 2001.

[5] B. Bakker and J. van Seggelen, "The revolutionary Hummingbird technology". *Mikroniek* **50** (3): 14–20, 2010.

[6] E. Balmès, "Frequency domain identification of structural dynamics using the pole-residue parameterization". In *Proc. IMAC*: 540–546, 1996.

[7] E. Balmès, "New results on the identification of normal modes from experimental complex modes". *Mech. Syst. Signal Proc.* **11** (2): 229–243, 1997.

[8] A. Beard, D. Schubert, and A. von Flotow, "A practical product implementation of an active/passive vibration isolation system". In *Proc. SPIE* **2264**: 38–49, 1994.

[9] M.A. Beijen, D. Tjepkema, and J. van Dijk, "Two-sensor control in active

vibration isolation using a single-axis hard mount system". Submitted, 2012.

[10] M.A. Beijen, *Multi-sensor control in active vibration isolation*. MSc thesis, University of Twente, 2012.

[11] B. Cauberghe, P. Guillaume, P. Verboven, S. Vanlanduit, and E. Parloo, "On the influence of the parameter constraint on the stability of the poles and the discrimination capabilities of the stabilization diagrams". *Mech. Syst. Signal Proc.* **19** (5): 989–1014, 2005.

[12] B. Cauberghe, P. Guillaume, R. Pintelon, and P. Verboven, "Frequency-domain subspace identification using FRF data from arbitrary signals". *J. Sound Vibr.* **290** (3-5): 555–571, 2006.

[13] C. Collette, S. Janssens, K. Artoos, and C. Hauvillerr, "Active vibration isolation of high precision machines". In *Diamond Light Source Proc.* **1** (e1): 1–5, 2010.

[14] M. Ford, J. Maciejowski, and J. Boyle, *Multivariable frequency domain toolbox: User's guide*. Cambridge Control Ltd. (Cambridge), 1988.

[15] P. Gardonio, S.J. Elliott, and R.J. Pinnington, "Active isolation of structural vibration on a multiple-degree-of-freedom system, part ii: Effectiveness of active control strategies". *J. Sound Vibr.* **207** (1): 95–121, 1997.

[16] C.G. Gordon, "Generic vibration criteria for vibration-sensitive equipment". In *Proc. SPIE* **3786**: 22–33, 1999.

[17] R.J. Guyan, "Reduction of stiffness and mass Matrices". *AIAA Journal* **3** (2): 380, 1965.

[18] Halcyonics, "Nano/Micro/Vario Series". http://www.halcyonics.de, last accessed July 2012.

[19] G.S. Hauge and M.E. Campbell, "Sensors and control of a space-based six-axis vibration isolation system". *J. Sound Vibr.* **269**: 913–931, 2004.

[20] M. Heertjes, K. de Graaff, and J.-G. van der Toorn, "Active vibration isolation of metrology frames; a modal decoupled control design". *J. Vibr. Acoust.* **127**: 223–233, 2005.

[21] V. Hollander, *Design of a hybrid hard mount setup for application of vibration isolation*. MSc thesis, University of Twente, 2008.

[22] V. Hollander, J.B. Jonker, J. van Dijk, “Design of mechatronic systems using a flexible multibody system approach”. In *Proc. ECSC*: 375–382, 2008.

[23] J. Holterman, *Vibration control of high-precision machines with active structural elements*. PhD thesis, University of Twente, 2002.

[24] J. Holterman and T.J.A. de Vries, “Active damping based on decoupled collocated control”. *IEEE/ASME Trans. Mechatr.* **10** (2): 135–145, 2005.

[25] M.E. Hoque, T. Mizuno, Y. Ishino, and M. Takasaki, “A six-axis hybrid vibration isolation system using active zero-power control supported by passive weight support mechanism”. *J. Sound Vibr.* **329** (17): 3417–3430, 2010.

[26] W. Hua, D.B. DeBra, C.T. Hardham, and B.T. Lantz, “Polyphase FIR complementary filters for control systems”. In *Spr. Top. Meet. Contr. Prec. Syst.* **32**: 109–114, 2004.

[27] D.J. Inman, “Active modal control for smart structures”. *Phil. Trans. Royal Soc. London A* **359**: 205–219, 2001.

[28] J.B. Jonker; R.G.K.M. Aarts, and J. van Dijk, “A linearized input-output representation of flexible multibody systems for control synthesis”. *Multibody Syst. Dyn.* **21**: 99–122, 2009.

[29] D. Karnopp and A. Trikha, “Comparative study of optimization techniques for shock and vibration isolation”. *J. Engin. Industry, series B* **91** (4): 1128–1132, 1969.

[30] F.A. Levinzon, “Fundamental noise limit of piezoelectric accelerometer”. *IEEE Sens. J.*, **4** (1): 108-111, 2004.

[31] F.A. Levinzon, “Noise of piezoelectric accelerometer with integral FET amplifier”. *IEEE Sens. J.* **5** (6): 1235–1242, 2005.

[32] F.A. Levinzon, “Ultra-low-noise 10 V/g compact IEPE seismic accelerometer”, in *Proc. IMAC* paper 27, 2008.

[33] F.A. Levinzon, “Ultra-low-noise seismic piezoelectric accelerometer with integral FET amplifier”. *IEEE Sens. J.* **12** (6): 2262–2268, 2012.

[34] L. Ljung, *System identification: Theory for the user*. Prentice Hall (Englewood Cliffs, NJ), 1999.

[35] H. Lus, M.D. Angelis, and R. Betti, “A new approach for reduced order modeling of mechanical systems using vibration measurements”. *J. Appl. Mech.* **70** (5): 715–723, 2003.

[36] K. Ma and M.N. Ghasemi-Nejhad, “Frequency-weighted adaptive control for simultaneous precision positioning and vibration suppression of smart structures”. *Smart Materials Struct.* **13** (5): 1143–1154, 2004.

[37] J. Maciejowski, *Multivariable feedback design*. Addison-Wesley (Boston, MA), 1989.

[38] T. McKelvey, H. Akcay, and L. Ljung, “Subspace-based multivariable system identification from frequency response data”. *Trans. Autom. Contr.* **41** (7): 960–979, 1996.

[39] Minus K Technology, “Superior, leading-edge negative-stiffness, cost-effective vibration isolation”. http://www.minusk.com, last accessed July 2012.

[40] D.K. Miu, “Physical interpretation of transfer function zeros for simple control systems with mechanical flexibilities”. *J. Dyn. Syst. Meas. Contr.* **113** (3): 419–424, 1991.

[41] P.G. Nelson, “Supporting active electro-pneumatic vibration isolation systems on platforms supported by STACIS™ hard-mount piezoelectric isolation systems”. TMC (Boston, MA), 2002.

[42] A.I. Olivayz, . Aguilary, and V. Sosa,“Low- and high-frequency vibration isolation for scanning probe microscopy”. *Meas. Sc. Tech.* **9**: 383-390, 1998.

[43] R. Pintelon and J. Schoukens, *System Identification: a Frequency Domain Approach*. IEEE Press (Piscataway, NJ), 2001.

[44] R. Politiek, *Design of a 3D experimental vibration isolation setup using active hard mounts*. MSc thesis, University of Twente, 2007.

[45] A. Preumont, *Vibration control of active structures*. Springer-Verlag (Berlin Heidelberg), 2011.

[46] A. Preumont, A. Franois, F. Bossens, and A. Abu-Hanieh, "Force feedback versus acceleration feedback in active vibration isolation". *J. Sound Vibr.* **257** (4): 605–613, 2002.

[47] A. Preumont, M. Horodinca, I. Romanescu, B. de Marneffe, M. Avraam, A. Deraemaeker, F. Bossens, and A.A. Hanieh, "A six-axis single-stage active vibration isolator based on Stewart platform". *J. Sound Vibr.* **300**: 644–661, 2007.

[48] R.M.G. Rijs, *Floor vibrations: Measurements and specifications*. Philips CFT(Eindhoven): CTB534-04-1362, 2004.

[49] H.M.J.R. Soemers, *Design principles for precision mechanisms*. T-Point Print VoF (Enschede), 2010.

[50] P. Sjövall, T. McKelvey, and T. Abrahamsson, "Constrained state-space system identification with application to structural dynamics". *Automatica* **42** (9): 1539–1546, 2006.

[51] J. Spanos, Z. Rahman, and G. Blackwood, "A soft 6-axis active vibration isolator". In *Proc. ACC* **1**: 412–416, 1995.

[52] Technical Manufacturing Corporation (TMC), "TMC STACIS™ active piezoelectric vibration cancellation system". http://www.techmfg.com, last accessed July 2012.

[53] D. Tjepkema, J. van Dijk, and H.M.J.R. Soemers, "Performance limits of active vibration isolation systems for precision equipment", in *Proc. EUSPEN*: 23–26, 2011.

[54] D. Tjepkema, J. van Dijk, and H.M.J.R. Soemers, "Active vibration isolation in precision machines using sensor fusion", in *Proc. ICSV*: 1–8, 2011

[55] D. Tjepkema, J. van Dijk, and H.M.J.R. Soemers, "Sensor fusion for active vibration isolation in precision equipment". *J. Sound Vibr.* **331** (4): 735–749, 2012.

[56] D. Tjepkema, J. van Dijk, and H.M.J.R. Soemers, ”A mode shaping modal controller for six DOFs active vibration isolation”. In Proc. Actuator: 455–458, 2012.

[57] H.D. Trinh, *Feedback control design for models of two hard mount vibration isolation setups*. MSc thesis, University of Twente, 2011.

[58] H. van der Auweraer, P. Guillaume, P. Verboven, and S. Vanlanduit, “Application of a fast-stabilizing frequency domain parameter estimation method”. *J. Dyn. Syst. Meas. Contr.* **123** (4): 651–658, 2001.

[59] G.W. van der Poel, *An exploration of active hard mount vibration isolation for precision equipment*. PhD thesis, University of Twente, 2010.

[60] J. van Dijk, “Mechatronic design of hard-mount concepts for precision equipment”. In *Motion and vibration control*: 315–324. Springer-Verlag (Berlin Heidelberg), 2009.

[61] J. van Eijk, D. Laro, J. Eisinger, W. Aarden, T. Michielsen, and S. van den Berg, “The “ultimate performance” in floor vibration isolation”. *Mikroniek* **51** (2): 13–19, 2011.

[62] P. Verboven, B. Cauberghe, E. Parloo, S. Vanlanduit, and P. Guillaume, “User-assisting tools for a fast frequency-domain modal parameter estimation method”. *Mech. Syst. Signal Proc.* **18** (4): 759–780, 2004.

[63] M.J. Vervoordeldonk, T.A.M. Ruijl, R.M.G. Rijs, ”Development of a novel active isolation concept”. In *Proc. ASPE*: 121–126, 2004.

[64] M. Vervoordeldonk, J. van Eijk, and N. Roozen, “Active structural damping in high-precision equipment”. In *Proc. ICNVE*: 573–581, 2006.

[65] E. Wernholt, and S. Gunnarsson, “Analysis of methods for multivariable frequency response function estimation in closed loop”. In *Proc. IEEE CDC*: 4881–4888, 2007.

Maximum achievable damping for sensor fusion

Appendix A

In this appendix a formula is derived to calculate the maximum achievable damping ratio of the internal mode using the control strategy of chapter 3 that is based on sensor fusion.

How the damping ratio of the internal mode depends on the filter pole ω_p is determined by the location of the closed loop poles in the complex plane. The closed loop poles can be calculated from the solution of the characteristic equation

$$1 + L_{r,(\ddot{x}_1,F_a)}(s) = 0, \tag{A.1}$$

where $L_{r,(\ddot{x}_1,F_a)}(s)$ is the loop gain for sensor fusion given by

$$L_{r,(\ddot{x}_1,F_s)}(s) = H_r(s)(LF(s)G_{\ddot{x}_1F_a}(s) + \frac{1}{m_1+m_2}HF(s)G_{F_sF_a}(s)), \tag{A.2}$$

which is the same equation as Eq. (3.27). $H_r(s)$ is the improved controller given by Eq. (3.19), $LF(s)$ and $HF(s)$ are the first-order low-pass and high-pass filters given by Eq. (3.26). Plant transfer functions $G_{\ddot{x}_1F_a}(s)$ and $G_{F_sF_a}(s)$ are given by Eqs. (3.17) and (3.23) respectively.

To calculate the closed loop poles corresponding to the internal mode it is sufficient to use the approximation of $L_{r,(\ddot{x}_1,F_a)}(s)$ around $s = j\omega_R$ where ω_R is the resonance frequency of the internal mode, which is 93 Hz. Using the mass and stiffness properties of the hard mount and the controller parameters as in chapter 3, the following approximations can be made:

$$\begin{aligned} G_{\ddot{x}_1F_a}(s \approx j\omega_R) &\approx \frac{s^2(m_2s^2+k_2)}{(m_1s^2+k_2)(m_2s^2+k_2)-k_2^2} \\ &\approx \frac{s^2(m_2s^2+k_2)}{s^2(m_1m_2s^2+k_2(m_1+m_2))} = \frac{1}{m_1}\frac{s^2+\omega_{a,\ddot{x}_1}^2}{s^2+\omega_{a,F_s}^2} \end{aligned} \tag{A.3}$$

$$G_{F_sF_a}(s \approx j\omega_R) \approx 1, \tag{A.4}$$

where $\omega_{a,\ddot{x}_1}$ and ω_{a,F_s} are given by Eqs. (3.18) and (3.24) respectively. Substituting Eqs. (A.3) and (A.4) into Eq. (A.2) yields for Eq. (A.1)

$$1 + H_r(s \approx j\omega_R)\left(\frac{\omega_p}{s+\omega_p}\frac{1}{m_1}\frac{s^2+\omega_{a,\ddot{x}_1}^2}{s^2+\omega_{a,F_s}^2} + \frac{1}{m_1+m_2}\frac{s}{s+\omega_p}\right) = 0. \tag{A.5}$$

In Fig. 3.5(b) the loop gain for sensor fusion is shown as the black dashed line. It is observed that around the resonance frequency of the internal mode, the loop gain is much larger than 1, so $L_{r,(\ddot{x}_1,F_a)}(s \approx j\omega_R) \gg 1$. This means that Eq. (A.5) can be approximated by

$$\begin{aligned} H_r(s \approx j\omega_R)\left(\frac{\omega_p}{s+\omega_p}\frac{1}{m_1}\frac{s^2+\omega_{a,\ddot{x}_1}^2}{s^2+\omega_{a,F_s}^2} + \frac{1}{m_1+m_2}\frac{s}{s+\omega_p}\right) &= 0 \\ H_r(s \approx j\omega_R)\frac{1}{s+\omega_p}\left(\frac{\omega_p}{m_1}\frac{s^2+\omega_{a,\ddot{x}_1}^2}{s^2+\omega_{a,F_s}^2} + \frac{s}{m_1+m_2}\right) &= 0. \end{aligned} \tag{A.6}$$

So the closed loop poles corresponding to the internal mode depend only on the part between brackets in Eq. (A.6). These closed loop poles are found by solving

$$\frac{\omega_p}{m_1}\frac{s^2+\omega_{a,\ddot{x}_1}^2}{s^2+\omega_{a,F_s}^2} + \frac{s}{m_1+m_2} = 0. \tag{A.7}$$

This equation can also be written as

$$\frac{g}{s}\frac{s^2+\omega_{a,\ddot{x}_1}^2}{s^2+\omega_{a,F_s}^2} + 1 = 0 \tag{A.8}$$

where gain $g = \omega_p(m_1+m_2)/m_1$. The solution of Eq. (A.8) is given in for example [45] as

$$g = \omega_{a,F_s}\sqrt{\frac{\omega_{a,F_s}}{\omega_{a,\ddot{x}_1}}}, \text{ such that } \omega_p = \frac{m_1}{m_1+m_2}\omega_{a,F_s}\sqrt{\frac{\omega_{a,F_s}}{\omega_{a,\ddot{x}_1}}} \tag{A.9}$$

This solution is obtained for $s = j\sqrt{\omega_{a,\ddot{x}_1}\omega_{a,F_s}}$ and the maximum achievable damping ratio is found as

$$\zeta_{max} = \frac{1}{2}\left|\frac{\omega_{a,F_s}}{\omega_{a,\ddot{x}_1}} - 1\right|. \tag{A.10}$$

INTERNAL DEFORMATION RESPONSE

Appendix B

In this appendix a relation is derived between the open loop response of the internal deformation $\Delta X(s)$ and the closed loop response in case of a two-sensor control strategy. It follows that the closed loop performance equals the open loop performance scaled with the sensitivity function $1/(1+L(s))$, which is the same relation as in single-input single-output systems.

Consider the control scheme for the two-sensor control strategy with the closed loop plant in Fig. B.1. When neglecting the direct disturbance force $F_d(s)$, the output $\Delta X(s)$ can be written as

$$\Delta X(s) = G_{\Delta x \ddot{x}_0}(s)\ddot{X}_0(s) + G_{\Delta x F_\mathrm{a}}(s)F_\mathrm{a}(s). \tag{B.1}$$

The actuator force equals

$$F_\mathrm{a}(s) = -(H_{\ddot{x}_1}(s)\ddot{X}_1(s) + H_{F_\mathrm{s}}(s)F_\mathrm{s}(s)). \tag{B.2}$$

The sensor outputs can be expressed as

$$\ddot{X}_1(s) = G_{\ddot{x}_1\ddot{x}_0}(s)\ddot{X}_0(s) + G_{\ddot{x}_1 F_\mathrm{a}}(s)F_\mathrm{a}(s), \tag{B.3}$$

$$F_\mathrm{s}(s) = G_{F_\mathrm{s}\ddot{x}_0}(s)\ddot{X}_0(s) + G_{F_\mathrm{s}F_\mathrm{a}}(s)F_\mathrm{a}(s). \tag{B.4}$$

The sensor outputs of Eqs. (B.3) and (B.4) are substituted into Eq. (B.2)

$$\begin{aligned} F_\mathrm{a}(s) = &-H_{\ddot{x}_1}(s)(G_{\ddot{x}_1\ddot{x}_0}\ddot{X}_0(s) + G_{\ddot{x}_1 F_\mathrm{a}}(s)F_\mathrm{a}(s)) \\ &-H_{F_\mathrm{s}}(s)(G_{F_\mathrm{s}\ddot{x}_0}(s)\ddot{X}_0(s) + G_{F_\mathrm{s}F_\mathrm{a}}(s)F_\mathrm{a}(s)) \end{aligned} \tag{B.5}$$

Rewriting Eq. (B.5) gives the closed loop transfer function from floor vibrations to actuator force

$$F_\mathrm{a}(s) = -\frac{H_{\ddot{x}_1}(s)G_{\ddot{x}_1\ddot{x}_0}(s) + H_{F_\mathrm{s}}(s)G_{F_\mathrm{s}\ddot{x}_0}(s)}{1 + H_{\ddot{x}_1}(s)G_{\ddot{x}_1 F_\mathrm{a}}(s) + H_{F_\mathrm{s}}(s)G_{F_\mathrm{s}F_\mathrm{a}}(s)}\ddot{X}_0(s). \tag{B.6}$$

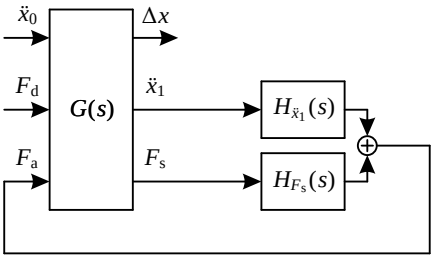

Fig. B.1: Control scheme of two-sensor control.

This expression for $F_a(s)$ is substituted into Eq. (B.1):

$$\Delta X(s) = (G_{\Delta x \ddot{x}_0}(s) - G_{\Delta x F_a}(s)\frac{H_{\ddot{x}_1}(s)G_{\ddot{x}_1\ddot{x}_0}(s) + H_{F_s}(s)G_{F_s\ddot{x}_0}(s)}{1 + H_{\ddot{x}_1}(s)G_{\ddot{x}_1 F_a}(s) + H_{F_s}(s)G_{F_s F_a}(s)})\ddot{X}_0(s). \tag{B.7}$$

This means that the closed loop transfer function from floor vibrations $\ddot{X}_0(s)$ to internal deformation $\Delta X(s)$ can be written as

$$\frac{\Delta X(s)}{\ddot{X}_0(s)} = G_{\Delta x \ddot{x}_0}(s) - G_{\Delta x F_a}(s)\frac{H_{\ddot{x}_1}(s)G_{\ddot{x}_1\ddot{x}_0}(s) + H_{F_s}(s)G_{F_s\ddot{x}_0}(s)}{1 + L_{2,(\ddot{x}_1,F_s)}(s)}. \tag{B.8}$$

In Eq. (B.8) the loop gain $L_{2,(\ddot{x}_1,F_s)}(s) = H_{\ddot{x}_1}(s)G_{\ddot{x}_1 F_a}(s) + H_{F_s}(s)G_{F_s F_a}(s)$. To simplify Eq. (B.8) a substitution for $G_{\Delta x F_a}(s)$ is derived

$$G_{\Delta x F_a}(s) = \frac{\Delta X(s)}{F_a(s)} = \frac{\Delta X(s)}{\ddot{X}_0(s)}\frac{\ddot{X}_0(s)}{\ddot{X}_1(s)}\frac{\ddot{X}_1(s)}{F_a(s)} = \frac{G_{\Delta x \ddot{x}_0}(s)G_{\ddot{x}_1 F_a}(s)}{G_{\ddot{x}_1\ddot{x}_0}(s)}. \tag{B.9}$$

Eq. (B.9) is substituted into Eq. (B.8) yielding

$$\frac{\Delta X(s)}{\ddot{X}_0(s)} = G_{\Delta x \ddot{x}_0}(s)(1 - \frac{H_{\ddot{x}_1}(s)G_{\ddot{x}_1 F_a}(s) + H_{F_s}(s)G_{F_s\ddot{x}_0}(s)/G_{\ddot{x}_1\ddot{x}_0}(s) \cdot G_{\ddot{x}_1 F_a}(s)}{1 + L_{2,(\ddot{x}_1,F_s)}(s)}). \tag{B.10}$$

In a similar way it can be shown that $G_{F_s\ddot{x}_0}(s)/G_{\ddot{x}_1\ddot{x}_0}(s) \cdot G_{\ddot{x}_1 F_a}(s) = G_{F_s F_a}(s)$, which means that the nominator in (B.10) equals the loop gain $L_{2,(\ddot{x}_1,F_s)}(s)$. This leads to the final result:

$$\frac{\Delta X(s)}{\ddot{X}_0(s)} = G_{\Delta x \ddot{x}_0}(s)\frac{1}{1 + L_{2,(\ddot{x}_1,F_s)}(s)}, \tag{B.11}$$

which states that the closed loop internal deformation is equal to the open loop internal deformation $G_{\Delta x \ddot{x}_0}(s)$ scaled with the sensitivity $1/(1 + L_{2,(\ddot{x}_1,F_s)}(s))$.

COHERENCE FUNCTIONS

Appendix C

Coherence functions for the experiments with the one-axis vibration isolator.

Acceleration feedback

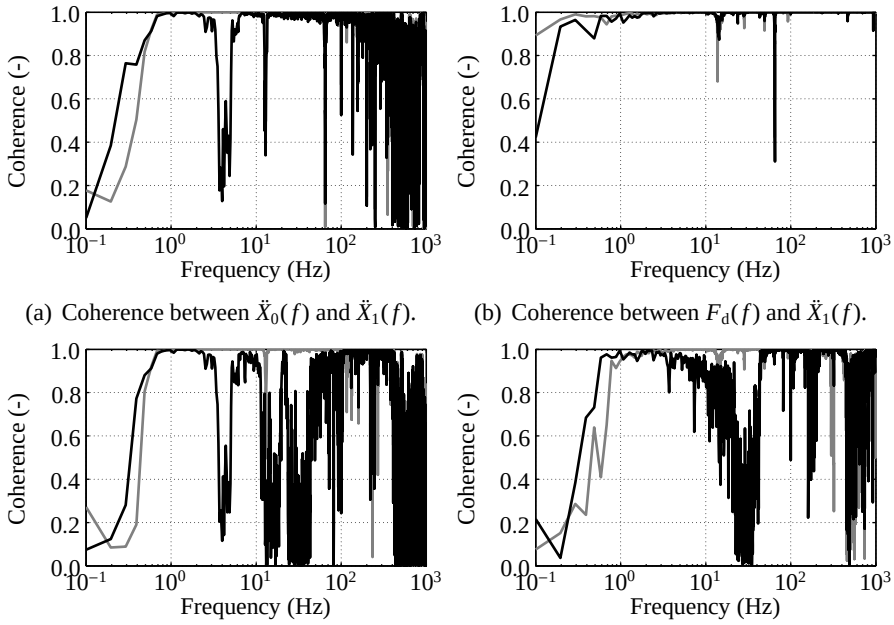

(a) Coherence between $\ddot{X}_0(f)$ and $\ddot{X}_1(f)$.

(b) Coherence between $F_d(f)$ and $\ddot{X}_1(f)$.

(c) Coherence between $\ddot{X}_0(f)$ and $\ddot{X}_2(f)$.

(d) Coherence between $F_d(f)$ and $\ddot{X}_2(f)$.

Fig. C.1: Coherence functions corresponding to: (a) transmissibility $\hat{T}(f)$; (b) compliance $\hat{C}(f)$; (c) deformation transmissibility $\hat{T}_d(f)$; (d) deformability $\hat{D}(f)$; open loop (——) and closed loop using acceleration feedback (——).

Force feedback

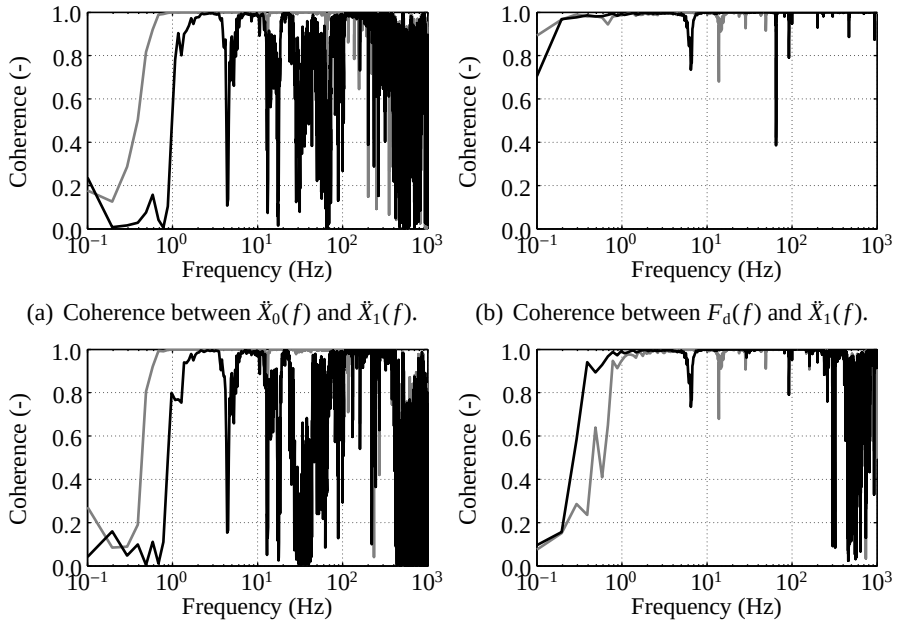

(a) Coherence between $\ddot{X}_0(f)$ and $\ddot{X}_1(f)$.

(b) Coherence between $F_d(f)$ and $\ddot{X}_1(f)$.

(c) Coherence between $\ddot{X}_0(f)$ and $\ddot{X}_2(f)$.

(d) Coherence between $F_d(f)$ and $\ddot{X}_2(f)$.

Fig. C.2: Coherence functions corresponding to: (a) transmissibility $\hat{T}(f)$; (b) compliance $\hat{C}(f)$; (c) deformation transmissibility $\hat{T}_d(f)$; (d) deformability $\hat{D}(f)$; open loop (——) and closed loop using force feedback (——).

Sensor fusion

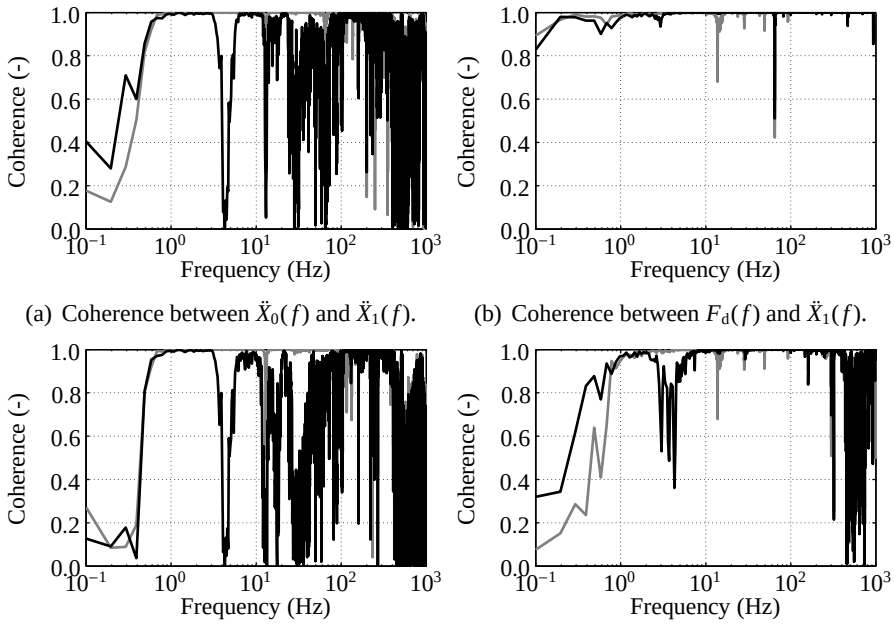

(a) Coherence between $\ddot{X}_0(f)$ and $\ddot{X}_1(f)$.

(b) Coherence between $F_\mathrm{d}(f)$ and $\ddot{X}_1(f)$.

(c) Coherence between $\ddot{X}_0(f)$ and $\ddot{X}_2(f)$.

(d) Coherence between $F_\mathrm{d}(f)$ and $\ddot{X}_2(f)$.

Fig. C.3: Coherence functions corresponding to: (a) transmissibility $\hat{T}(f)$; (b) compliance $\hat{C}(f)$; (c) deformation transmissibility $\hat{T}_\mathrm{d}(f)$; (d) deformability $\hat{D}(f)$; open loop (——) and closed loop using sensor fusion (——).

Two-sensor control

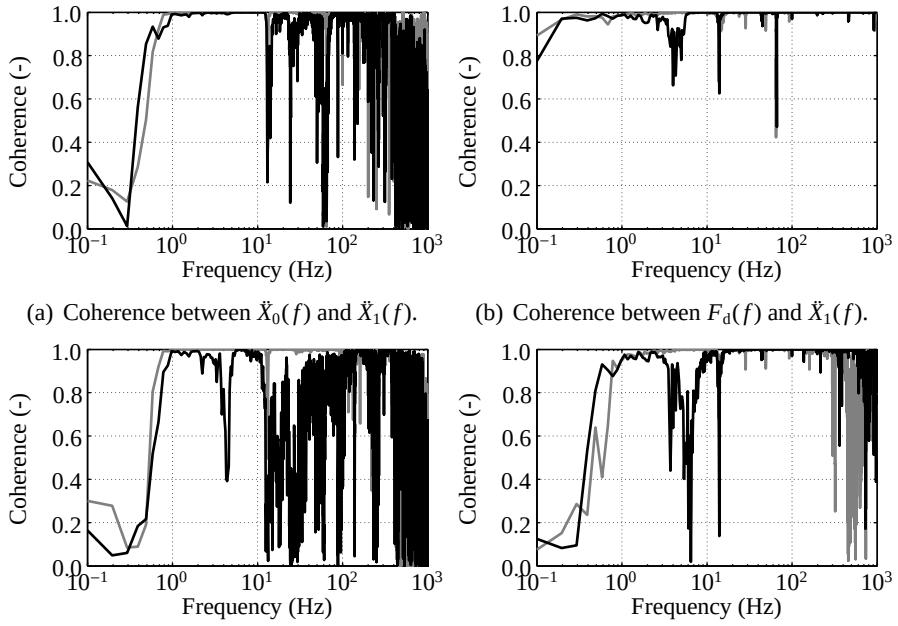

(a) Coherence between $\ddot{X}_0(f)$ and $\ddot{X}_1(f)$.

(b) Coherence between $F_d(f)$ and $\ddot{X}_1(f)$.

(c) Coherence between $\ddot{X}_0(f)$ and $\ddot{X}_2(f)$.

(d) Coherence between $F_d(f)$ and $\ddot{X}_2(f)$.

Fig. C.4: Coherence functions corresponding to: (a) transmissibility $\hat{T}(f)$; (b) compliance $\hat{C}(f)$; (c) deformation transmissibility $\hat{T}_d(f)$; (d) deformability $\hat{D}(f)$; open loop (——) and closed loop using two-sensor control (——).

Simplification of the mode shaping modal controller

Appendix D

In this appendix it is shown that the mode shaping modal controller derived in chapter 7, which is a centralized controller (each actuator interacts will all sensors), can be simplified to a centralized controller (each actuator interacts only with its collocated sensor and for each actuator-sensor-pair the same controller is used). However, with this centralized controller it is no longer possible to individually tune suspension frequency and damping ratio of each mode.

The expressions for proportional gain matrix $\mathbf{K}_\mathrm{a}$ of Eq. (7.18) and integral gain matrix $\mathbf{K}_\mathrm{v}$ of Eq. (7.19) of the mode shaping modal controller for acceleration feedback simplify significantly for the choice $\mathbf{\Omega}_\mathrm{n} = \omega_\mathrm{n}\mathbf{I}_6$, $\mathbf{\Xi}_\mathrm{n} = 2\zeta_\mathrm{n}\omega_\mathrm{n}\mathbf{I}_6$ and $\mathbf{\Phi}_\mathrm{n} = \mathbf{\Phi}_\mathrm{o}$ such that $\mathbf{P}_\mathrm{n} = \mathbf{P}_\mathrm{o}$:

$$\mathbf{K}_\mathrm{a} = \mathbf{B}_\mathrm{o}^{-1}(\bar{\mathbf{K}}\omega_\mathrm{n}^{-2} - \bar{\mathbf{M}})\mathbf{C}_\mathrm{o}^{-1} \tag{D.1}$$

and

$$\mathbf{K}_\mathrm{v} = 2\zeta_\mathrm{n}\omega_\mathrm{n}(\mathbf{B}_\mathrm{o}^{-1}\bar{\mathbf{M}}\mathbf{C}_\mathrm{o}^{-1} + \mathbf{K}_\mathrm{a}) - \mathbf{B}_\mathrm{o}^{-1}\bar{\mathbf{D}}\mathbf{C}_\mathrm{o}^{-1}. \tag{D.2}$$

These expressions are equal to the ones derived in [60], which are based on the modal decoupling approach described in [27]. For this particular choice, the suspension frequencies of the six suspension modes are the same. Hence the corresponding mode shapes can be any linear combination of the orthogonal coordinates $\boldsymbol{x}_\mathrm{ref}$ and there is no need to tune the mode shapes.

Further simplification is possible if ω_n is chosen to be much lower than the smallest open loop suspension frequency, which results in $\bar{\mathbf{K}}\omega_\mathrm{n}^{-2} \gg \bar{\mathbf{M}}$, such that $\bar{\mathbf{M}}$ can be omitted in Eqs. (D.1)–(D.4). To guarantee an exact constrained design (see section 5.1), the off-diagonal elements of $\bar{\mathbf{K}}$ are much smaller compared to the diagonal elements, since a diagonal element represents the axial

stiffness of a leg, k, which is designed to be stiff in the axial direction. Therefore, $\bar{\mathbf{K}} \approx k\mathbf{I}_6$. If $\mathbf{D}$ is negligible, Eqs. (D.1) and (D.2) reduce to:

$$\mathbf{K}_\mathrm{a} = \omega_\mathrm{n}^{-2} k \mathbf{B}_\mathrm{o}^{-1} \mathbf{C}_\mathrm{o}^{-1}, \tag{D.3}$$

$$\mathbf{K}_\mathrm{v} = 2\zeta_\mathrm{n} \omega_\mathrm{n}^{-1} k \mathbf{B}_\mathrm{o}^{-1} \mathbf{C}_\mathrm{o}^{-1}. \tag{D.4}$$

This means that a very simple decentralized feedback strategy already results in approximate modal decoupling. However, both simplifications described in Eqs. (D.1)–(D.4) do not allow to change the mode shapes of the closed loop system with respect to the open loop system or to set the suspension frequency of each suspension mode individually. So the mode shapes of the vibration isolator in closed loop are the same as those in open loop.

In a similar way the simplified expressions for the proportional and integral gain matrices corresponding to the mode shaping modal controller for force feedback can be obtained.

MODELING RESULTS FOR THE MODIFIED CONTROL SETTINGS

Appendix E

In this appendix the modeling results for the modified control settings described in section 8.3 are presented. Next to the plots of the characteristic loci (CL) that are used to check closed loop stability, the diagonal elements of the (deformation) transmissibility matrix are shown.

The results are obtained with the mode shaping modal control strategy presented in section 7.4 using the flexible body model described in section 5.3. The following control settings are defined. The reduced mass, damping and stiffness matrices $\bar{\mathbf{M}}$, $\bar{\mathbf{D}}$ and $\bar{\mathbf{K}}$ are available from this model. Input and output matrices $\mathbf{B}_o$ and $\mathbf{C}_o$ are identity: $\mathbf{B}_o = \mathbf{C}_o = \mathbf{I}_6$, since the actuators and sensors are co-aligned with the degrees of freedom (DOFs) $\boldsymbol{q}_o$, which are the leg extensions. The reference frame (x, y z) is located in point p at the elastic center of the payload and the desired suspension mode shapes are chosen as pure translations and rotations of p in the directions of x, y and z, hence $\mathbf{\Phi}_n = \mathbf{I}_6$.

The control parameters for the mode shaping modal controller are listed in Table E.1. These are equal to those in Table 7.1 except for the values of ω_{fi} which are all three times lower compared to Table 7.1. The values for the filter poles of the low-pass and high-pass filters used for sensor fusion listed in Table 7.2 are repeated in Table E.2. The controller gains for the force feedback

Table E.1: Control parameters for the mode shaping modal controller.

i	mode shape	ω_{ni} (rad/s)	ζ_{ni} (-)	ω_{fi} (rad/s)	ζ_{fi} (-)
1	x	$2\pi\cdot3$	0.4	$2\pi\cdot15$	0.07
2	y	$2\pi\cdot3$	0.4	$2\pi\cdot15$	0.07
3	z	$2\pi\cdot1$	0.4	$2\pi\cdot7.5$	0.07
4	θ_x	$2\pi\cdot2.5$	0.4	$2\pi\cdot12.5$	0.07
5	θ_y	$2\pi\cdot2.5$	0.4	$2\pi\cdot12.5$	0.07
6	θ_z	$2\pi\cdot2$	0.4	$2\pi\cdot10$	0.07

Table E.2: Frequencies of the anti-resonances and poles, and controller gains.

i	mode shape	$\omega_{ai,\ddot{x}_1}$ (rad/s)	ω_{ai,F_s} (rad/s)	ω_{pi} (rad/s)	k_{fi} (-)
1	x	$2\pi\cdot$ 68.5	$2\pi\cdot$ 75.1	$2\pi\cdot$64.4	$6.1\cdot10^{-4}$
2	y	$2\pi\cdot$ 72.9	$2\pi\cdot$ 80.9	$2\pi\cdot$69.2	$5.8\cdot10^{-4}$
3	z	$2\pi\cdot$107.4	$2\pi\cdot$142.4	$2\pi\cdot$93.3	$17.7\cdot10^{-4}$
4	θ_x	$2\pi\cdot$ 56.4	$2\pi\cdot$ 80.6	$2\pi\cdot$47.2	$9.0\cdot10^{-4}$
5	θ_y	$2\pi\cdot$ 56.4	$2\pi\cdot$ 75.1	$2\pi\cdot$48.9	$9.0\cdot10^{-4}$
6	θ_z	$2\pi\cdot$ 79.7	$2\pi\cdot$ 81.4	$2\pi\cdot$78.9	$7.9\cdot10^{-4}$

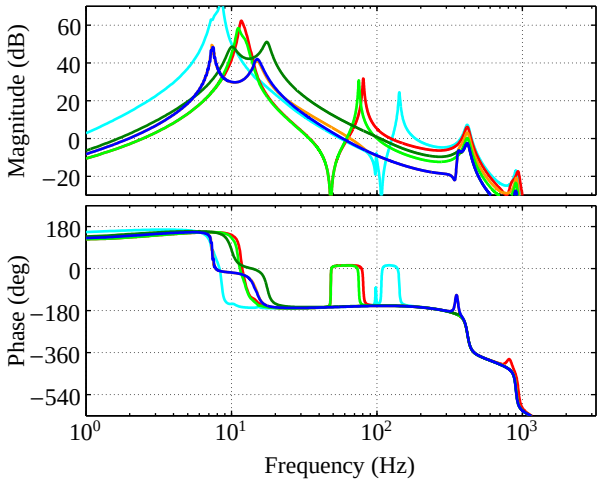

Fig. E.1: Characteristic loci of loop gain matrices $\mathbf{L}_{r,\ddot{x}_1}(s)$ for acceleration feedback.

controller used with two-sensor control are also listed in Table E.2. These are different than those in Table 7.2 and are calculated using Eq. (7.58) together with the values listed in Table E.2 and $\beta = 1$.

Next, the loop shaping filter $F_{\text{ext}}(s)$ is defined. For acceleration feedback, it is chosen as

$$F_{\text{ext}}(s) = \frac{s+\omega_1}{\omega_1}\frac{\omega_2^2}{s^2+2\zeta_2\omega_2 s+\omega_2^2}\frac{\omega_3}{s+\omega_3}\frac{\omega_4}{s+\omega_4}, \tag{E.1}$$

where $\omega_i = 2\pi f_i$ with $f_1 = 392$ Hz, $f_2 = 425$ Hz, $f_2 = 450$ Hz and $f_1 = 1$ kHz, and $\zeta_2 = 0.4$. This filter compensates for the first-order low-pass filter formed by the impedance of the voice coil actuator, and it increases the roll-off rate of the controller by adding one second-order low-pass filter and two first-order low-pass filters to it.

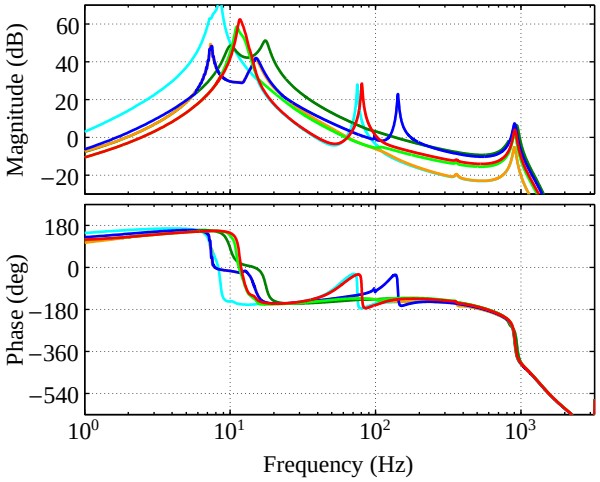

Fig. E.2: Characteristic loci of loop gain matrices $\mathbf{L}_{\mathrm{r},(\ddot{\mathbf{x}}_1,F_\mathrm{s})}(s)$ for sensor fusion.

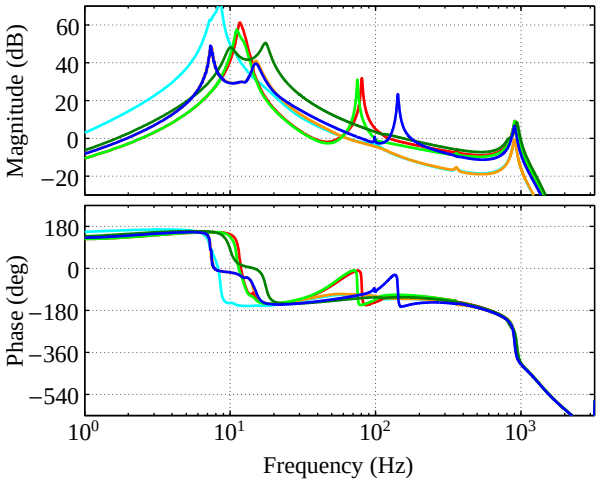

Fig. E.3: Characteristic loci of loop gain matrices $\mathbf{L}_{\mathrm{t},(\ddot{\mathbf{x}}_1,F_\mathrm{s})}(s)$ for two-sensor control.

For sensor fusion and two-sensor control, one of the first-order low-pass filters in the loop shaping filter $F_\mathrm{ext}(s)$ of Eq. (E.1) is replaced by a lead filter:

$$F_\mathrm{ext}(s) = \frac{s+\omega_1}{\omega_1}\,\frac{\omega_2}{s+\omega_2}\,\frac{\omega_3^2}{s^2+2\zeta_3\omega_3 s+\omega_3^2}\,\frac{s+\omega_4}{s+\omega_5}\,\frac{\omega_5}{\omega_4}, \tag{E.2}$$

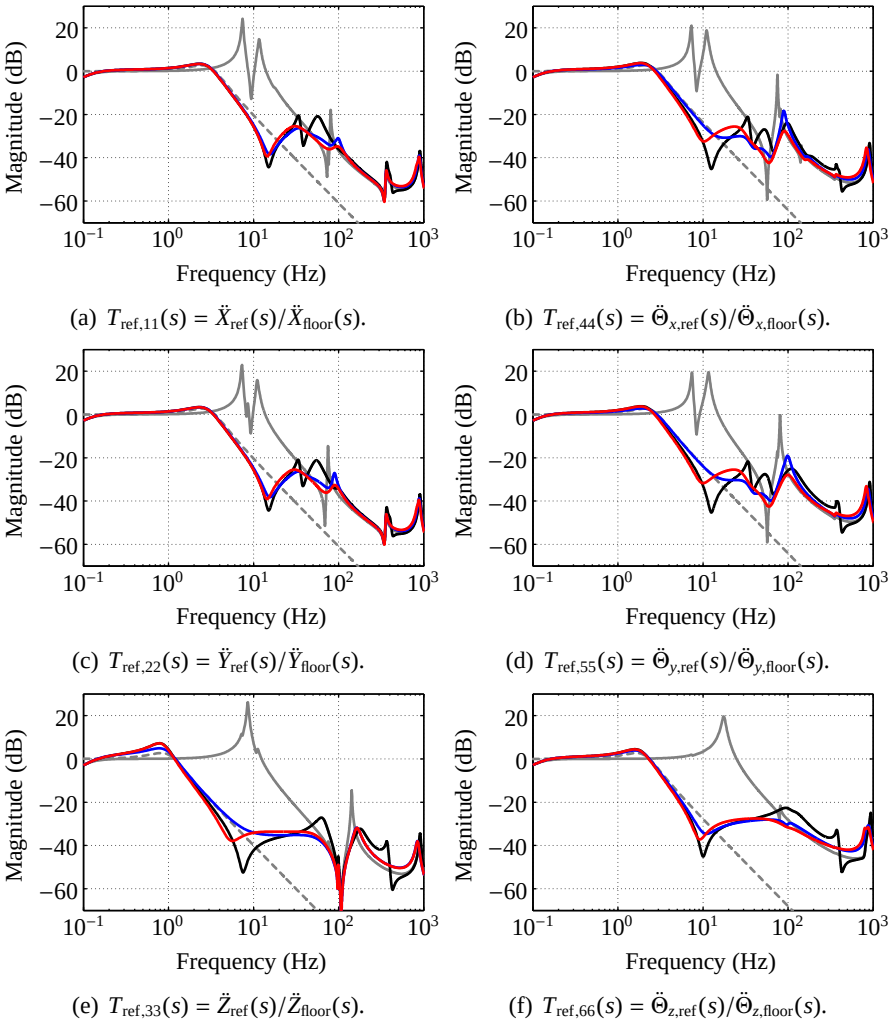

(a) $T_{\mathrm{ref},11}(s) = \ddot{X}_{\mathrm{ref}}(s)/\ddot{X}_{\mathrm{floor}}(s)$.

(b) $T_{\mathrm{ref},44}(s) = \ddot{\Theta}_{x,\mathrm{ref}}(s)/\ddot{\Theta}_{x,\mathrm{floor}}(s)$.

(c) $T_{\mathrm{ref},22}(s) = \ddot{Y}_{\mathrm{ref}}(s)/\ddot{Y}_{\mathrm{floor}}(s)$.

(d) $T_{\mathrm{ref},55}(s) = \ddot{\Theta}_{y,\mathrm{ref}}(s)/\ddot{\Theta}_{y,\mathrm{floor}}(s)$.

(e) $T_{\mathrm{ref},33}(s) = \ddot{Z}_{\mathrm{ref}}(s)/\ddot{Z}_{\mathrm{floor}}(s)$.

(f) $T_{\mathrm{ref},66}(s) = \ddot{\Theta}_{z,\mathrm{ref}}(s)/\ddot{\Theta}_{z,\mathrm{floor}}(s)$.

Fig. E.4: Diagonal entries of transmissibility matrix $\mathbf{T}_{\mathrm{ref}}(s)$.
- reference transmissibility
- open loop
- closed loop using acceleration feedback
- closed loop using sensor fusion
- closed loop using two-sensor control

where $\omega_i = 2\pi f_i$ with $f_1 = 392$ Hz, $f_2 = 1$ kHz, $f_3 = 1.5$ kHz, $f_4 = 70$ Hz and $f_5 = 141$ Hz, and $\zeta_3 = 0.4$. The lead filter is chosen such that around 100 Hz some phase lead is obtained. In the frequency range around 100 Hz several

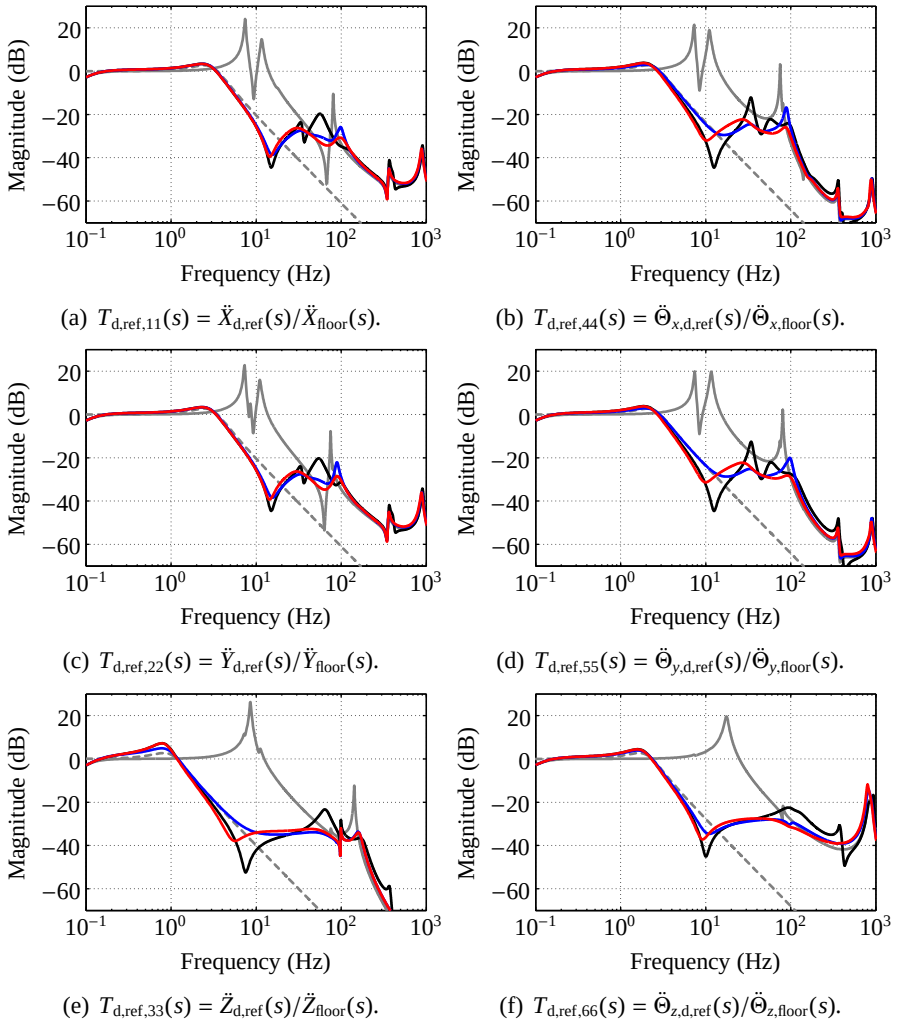

(a) $T_{\mathrm{d,ref},11}(s) = \ddot{X}_{\mathrm{d,ref}}(s)/\ddot{X}_{\mathrm{floor}}(s)$.

(b) $T_{\mathrm{d,ref},44}(s) = \ddot{\Theta}_{x,\mathrm{d,ref}}(s)/\ddot{\Theta}_{x,\mathrm{floor}}(s)$.

(c) $T_{\mathrm{d,ref},22}(s) = \ddot{Y}_{\mathrm{d,ref}}(s)/\ddot{Y}_{\mathrm{floor}}(s)$.

(d) $T_{\mathrm{d,ref},55}(s) = \ddot{\Theta}_{y,\mathrm{d,ref}}(s)/\ddot{\Theta}_{y,\mathrm{floor}}(s)$.

(e) $T_{\mathrm{d,ref},33}(s) = \ddot{Z}_{\mathrm{d,ref}}(s)/\ddot{Z}_{\mathrm{floor}}(s)$.

(f) $T_{\mathrm{d,ref},66}(s) = \ddot{\Theta}_{z,\mathrm{d,ref}}(s)/\ddot{\Theta}_{z,\mathrm{floor}}(s)$.

Fig. E.5: Diagonal entries of deformation transmissibility matrix $\mathbf{T}_{\mathrm{d,ref}}(s)$.
- reference transmissibility
- open loop
- closed loop using acceleration feedback
- closed loop using sensor fusion
- closed loop using two-sensor control

internal modes are present. The lead filter results in larger phase margins at the crossover frequencies in this frequency range. The crossover frequencies are present in the characteristic loci (CL) of the corresponding loop gain matrices.

Therefore, it is expected that the internal modes can be better damped than without the lead filter.

Closed loop stability is checked using the generalized Nyquist criterion [37]. This can be done by plotting the CL of the corresponding loop gain matrix. The plots of the CL for acceleration feedback, sensor fusion and two-sensor control are shown in Figs E.1–E.3. In all plots it is observed that the phase angles of the CL cross the -180° phase line at a frequency where the corresponding magnitudes are smaller than 0 dB and the phase angles are all below -180° at the six highest crossover frequencies. Hence, closed loop stability is obtained for all three control strategies.

Finally, the transmissibility matrix $\mathbf{T}_{\text{ref}}(s)$ and deformation transmissibility matrix $\mathbf{T}_{\text{d,ref}}(s)$ are calculated for each control strategy. Their diagonal entries are plotted in Figs. 7.9 and E.5. It is observed that these figures do not differ much from Figs. 7.8 and 7.9 except with a lower performance. It is clearly visible that for acceleration feedback some peaks in the (deformation) transmissibilities appear. These are due to a small phase margin around the frequencies of these peaks in the CL of the corresponding loop gain matrix. For sensor fusion there are also some peaks, while for two-sensor control there are no peaks. Hence, the best performance is obtained with two-sensor control.

SUMMARY

Environmental disturbances such as floor vibrations, may limit the performance of precision equipment. Therefore, the equipment is commonly mounted on vibration isolators that are used to isolate the equipment from floor vibrations. A vibration isolator can be considered as a mechanical low-pass filter, which provides isolation above $\sqrt{2}$ times the suspension frequency. This frequency is calculated as the square root of the suspension stiffness divided by the mass of the suspended equipment. By tuning these mechanical parameters, the desired suspension frequency can be obtained. Most industrial vibration isolators are designed as a soft mount with a low suspension stiffness to aim for a low suspension frequency and therefore a low transmission of floor vibrations.

However, the low suspension stiffness introduces problems with leveling of the equipment and it increases its susceptibility to disturbance forces acting directly on it, due to for example acoustic excitation. Both problems can be circumvented by using active hard mounts, which provide a much higher suspension stiffness. Its performance objectives can be formulated as: lowering the transmissibility of floor vibrations to make it comparable to that of an ideal active soft mount vibration isolator, increasing the damping ratios of the internal modes of the equipment, and reducing the equipment's sensitivity for direct disturbances. All parts required to realize the three performance objectives, in fact the suspension stiffness, actuators and sensors, can be located in the mount; there is no need for modification of the equipment's design.

Several feedback control strategies for a one-axis active hard mount vibration isolator are presented. It is shown that all three objectives cannot be realized simultaneously by using either acceleration or force feedback. However, with a novel control strategy based on sensor fusion, using acceleration feedback at low frequencies and force feedback at high frequencies, it is possible to realize all objectives simultaneously. In addition, a two-sensor control strategy

is derived in which acceleration feedback is used to obtain a low transmissibility and force feedback is added afterwards to increase the damping ratio of the internal mode. All control strategies are successfully validated on an experimental setup of a one-axis active hard mount vibration isolator.

A demonstrator setup of a six-axes active hard mount vibration isolator is developed. Its design is described and a novel system identification method is presented that is used to obtain a state-space model describing both its suspension dynamics and its flexible body dynamics. From the state-space model, the reduced order mass, damping, and stiffness matrices can be derived.

These matrices are used for designing a modal controller for the six-axes active hard mount vibration isolator is presented, such that for each suspension mode not only its resonance frequency and damping ratio but also its mode shape can be tuned. The possibility of tuning the suspension mode shapes provides an additional tool for designers of active vibration isolators to obtain the desired isolation performance. It is shown how the modal controller can be used to extend the derived control strategies from the one-axis vibration isolator to the six-axes vibration isolator.

The control strategies using the model controller are validated on the demonstrator setup. Due to hardware limitations, the desired performance objectives are not realized to their full extent. The hardware limitations are mainly due to a loss of collocation between the actuator and sensors, which limits the available control bandwidth, and due to actuator and sensor noise, that limit the RMS acceleration levels of the suspended equipment. The best isolation performance is obtained for the z-translation, with a transmissibility close to that of the ideal active soft mount vibration isolator. The floor acceleration of 11.6 mm/s^2 RMS has been reduced to 0.6 mm/s^2 at the suspended equipment, which is a reduction of about 25 dB. The damping ratio in closed loop is significantly increased with respect to that in open loop. The suspension stiffness is about 100 times higher as compared to the ideal active soft mount.

Further research should focus on improving the mechanical design of the six-axes active hard mount vibration isolator, such there will be no loss of collocation between the actuator and sensors, and on using sensors with ultra-low noise levels.

SAMENVATTING

De werking van precisie apparatuur kan worden beperkt door vloertrillingen. Daarom wordt zulke apparatuur meestal ondersteund door een trillingsisolator, die de doorgifte van deze vloertrillingen naar de ondersteunde apparatuur verlaagt. Zo'n trillingsisolator kan worden beschouwd als een mechanisch laagdoorlaatfilter, waarbij isolatie wordt verkregen boven $\sqrt{2}$ maal de ondersteuningsfrequentie. Deze frequentie kan worden berekend als de wortel uit de ondersteuningstijfheid gedeeld door de massa van de ondersteunde apparatuur. Door deze massa en stijheid te kiezen, kan de gewenste ondersteuningsfrequentie worden verkregen. De meeste industriële trillingsisolatoren zijn slap ondersteund om een lage ondersteuningsfrequentie en daarom een lage doorgifte van vloertrillingen te realiseren.

Echter, de slappe ondersteuning leidt tot problemen met de nivellering van de apparatuur en het vergroot de gevoeligheid voor directe stoorkrachten, bijvoorbeeld vanwege akoestische aanstoting. Beide problemen kunnen worden voorkomen door een actieve trillingsisolator met een stijve ondersteuning toe te passen. De doelstellingen ervan kunnen worden geformuleerd als: het verlagen van de doorgifte van vloertrillingen zodat deze vergelijkbaar wordt met die van een ideale actieve trillingsisolator met een slappe ondersteuning, het verhogen van de demping van interne trillingsvormen van de apparatuur en het verkleinen van de gevoeligheid van de apparatuur voor directe stoorkrachten. Alle onderdelen die nodig zijn om deze drie doelstellingen te realiseren kunnen in de ondersteuning zelf worden geplaatst; het is niet nodig om het ontwerp van de apparatuur hiervoor te veranderen.

In het proefschrift worden een aantal feedback regelstrategieën voor een eenassige actieve trillingsisolator met een stijve ondersteuning gepresenteerd. Het wordt duidelijk gemaakt dat het niet mogelijk is alle drie doelstellingen tegelijkertijd te realiseren door alleen versnellings- of krachtfeedback te gebruiken. Echter, met een vernieuwende regelstrategie gebaseerd op sensor-

fusie, waarbij laagfrequent versnellingsfeedback en hoogfrequent krachtfeedback wordt toegepast, is dit wel mogelijk. Daarnaast is een twee-sensor regelstrategie afgeleid waarbij versnellingsfeedback wordt gebruikt om een lage doorgifte van vloertrillingen te verkrijgen en krachtfeedback om de demping van interne trillingsvormen te verhogen. Alle regelstrategieën zijn succesvol gevalideerd met een experimentele opstelling van een eenassige actieve trillingsisolator met een stijve ondersteuning.

Tevens is er een demonstratieopstelling van een zesassige actieve trillingsisolator met een stijve ondersteuning ontwikkeld. Het ontwerp ervan wordt beschreven en er is een vernieuwende methode ontwikkeld voor de systeemidentificatie van deze demonstratieopstelling en het afleiden van de massa-, demping- en stijfheidsmatrices.

Vervolgens zijn deze matrices gebruikt voor het ontwerpen van een modale regelaar voor de zesassige trillingsisolator met een stijve ondersteuning, zodanig dat voor iedere trillingsvorm de ondersteuningfrequentie, demping en trillingsvorm zelf kunnen worden afgesteld. Dit biedt ontwerpers van actieve trillingsisolatoren een aanvullend gereedschap om de gewenste isolatieprestatie te verkrijgen. De modale regelaar kan ook worden gebruikt om de eerder afgeleide regelstrategieën van de eenassige trillingsisolator uit te breiden naar de zesassige trillingsisolator.

Deze regelstrategieën zijn gevalideerd door middel van experimenten met de demonstratieopstelling. Vanwege hardwareproblemen kunnen de gewenste doelstellingen niet volledig worden gerealiseerd. Deze problemen zijn veroorzaakt door een verlies aan collocatie tussen actuator en sensoren, waardoor de beschikbare bandbreedte van de regelaar beperkt is, en door actuator- en sensorruis, waardoor de RMS versnellingsniveaus van de ondersteunde apparatuur worden beperkt. De beste isolatieprestatie is verkregen voor de z-verplaatsing, met een doorgifte van vloertrillingen die in de buurt komt van die van een ideale actieve trillingsisolator met een slappe ondersteuning. De vloerversnellingen van 11.6 mm/s^2 RMS zijn gereduceerd tot 0.6 mm/s^2 op de ondersteunde apparatuur, wat een reductie van 25 dB betekent. De demping van de interne trillingsvormen in gesloten lus is aanzienlijk hoger dan die in open lus. De ondersteuningsstijfheid is ongeveer 100 keer hoger in vergelijking met die van een slap ondersteunde trillingsisolator.

Verder onderzoek zou zich moeten richten op het verbeteren van het mechanisch ontwerp van de zesassige trillingsisolator met een stijve ondersteuning, zodanig dat het verlies aan collocatie tussen de actuator en sensoren beperkt wordt, en op het gebruik van sensoren met een ultra-laag ruisniveau.

Dankwoord

Bedankt! Iedereen die de afgelopen jaren bewust of onbewust heeft bijgedragen aan mijn promotie en de totstandkoming van dit proefschrift wil ik hiervoor hartelijk bedanken. Jullie verdienen het om hieronder te worden genoemd.

In de eerste plaats wil ik Herman en Johannes bedanken voor het begeleiden van mijn promotie. Herman, bedankt voor jouw industriële blik op dit onderzoek en de interessante discussies die wij hebben gevoerd. Johannes, fijn dat jouw deur altijd open stond om met vragen binnen te komen of om over nieuwe ideeën te discussiëren. Jan Peters, ik wil jou bedanken voor het coördineren van alles wat met SmartPie te maken heeft. Succes met het blijven promoten van piëzotechnologie in de wereld.

Tjeerd, binnen onze vakgroep mijn voorganger op het gebied van onderzoek naar actieve trillingsisolatie, dankjewel voor de twee jaren waarin wij samen aan dit interessante onderzoek hebben gewerkt. Wouter, dankjewel voor alle discussies over regeltechniek en systeemidentificatie. Steven, dankjewel voor alle uitleg over wiskundige problemen waarmee ik heb geworsteld.

Leo, bedankt voor het realiseren van de twee experimentele opstellingen en het repareren van alle dingen die stuk gingen. Martina, bedankt voor het regelen van de zaken omtrent mijn promotie die niets met de inhoud ervan te maken hebben, en dat waren er nogal wat. Mensen zoals jullie zijn onmisbaar als het gaat om wetenschappelijk onderzoek.

Ik wil Hieu en Michiel bedanken omdat ze met hun afstudeeropdrachten hebben bijgedragen aan het onderzoek. Michiel, ook bedankt voor jouw leergierigheid en nieuwsgierigheid, alle discussies die we hebben gevoerd, en de interessante ideeën voor vervolgonderzoek. Heel veel succes met de uitvoering hiervan.

Verder wil ik iedereen van de vakgroep WA bedanken die tijdens de koffiepauzes, kerstdiners en andere uitjes voor de nodige ontspanning heeft gezorgd.

Johann, good luck with defending your title as the best PhD student of the group. Daarnaast wil ik iedereen succes wensen die zich inzet om regeltechniek en mechatronisch ontwerpen een solide plek te geven in het toekomstig werktuigbouwkundig onderwijs aan de Universiteit Twente.

Marc en Kim, Timo en Liliane, Robert en Aafke, Dennis en alle andere vrienden, bedankt voor de gezelligheid na het werk en in het weekend. Kim, ook bedankt voor het mede-organiseren van de maandelijkse vrijdagmiddagborrels. Laten we deze traditie voortzetten bij Demcon! Mijn ouders, broer en toekomstige schoonfamilie, bedankt voor jullie niet aflatende belangstelling voor mijn promotie maar vooral ook voor het bieden van een warme plek om op terug te kunnen vallen.

Marleen, tenslotte wil ik jou bedanken voor jouw steun en vertrouwen, voor alle leuke dingen die wij samen hebben meegemaakt en bovenal voor jouw liefde.

Enschede, oktober 2012,

Dirk Tjepkema

About the author

Dirk Tjepkema was born on March 23, 1983, in Leeuwarden, The Netherlands, and raised in the small villages Oude Bildtzijl and Sint Annaparochie. He attended the Christelijk Gymnasium Beyers Naudé in Leeuwarden, from which he graduated in 2001. He then entered the study Mechanical Engineering at the University of Twente. In 2004 he joined the Solar Team Twente and participated in the 2005 World Solar Challenge in Australia. After his return, he started with the master's curriculum at the department of Mechanical Automation and Mechatronics of prof. dr. ir. J.B. Jonker. As part of the curriculum he did an internship at MTU Aero Engines GmbH in Munich, Germany, in October 2006. Here he worked on the modeling of a fuel system in an aero engine. In March 2008 he obtained his master degree under supervision of dr. ir. R.G.K.M. Aarts with thesis title: "Identification of the Stäubli RX90B robot using accelerometers".

From April 2008 to July 2008 he worked for four months as a design engineer at Sensata Technologies in Almelo, The Netherlands. In August 2008 he started his PhD research at the department of Mechanical Automation and Mechatronics of the University of Twente of which the content is described in this thesis. Parts of this work were presented at the EUSPEN 11^{th} International Conference in Como, Italy (2011), the 18^{th} International Congress of Sound and Vibration in Rio de Janeiro, Brazil (2011), and the 13^{th} International Conference on New Actuators in Bremen, Germany (2012).

He will continue his career at Demcon in Oldenzaal, The Netherlands, and is still active in the Solar Team Twente project.